CORA Cork Open Research Archive
Cartlann Taighde Oscailte Chorcaí

Title	Energy storage systems for wave energy converters and microgrids
Authors	Murray, Dónal B.
Publication date	2013
Original Citation	Murray, D.B. 2013. Energy storage systems for wave energy converters and microgrids. PhD Thesis, University College Cork.
Type of publication	Doctoral thesis
Rights	© 2013. Dónal Brendan Murray - http://creativecommons.org/licenses/by-nc-nd/3.0/
Download date	2026-11-02 09:02:06
Item downloaded from	https://hdl.handle.net/10468/1137



UCC
University College Cork, Ireland
Coláiste na hOllscoile Corcaigh

Energy storage systems for wave energy converters and microgrids

Dónal Brendan Murray



A thesis submitted to the National University of Ireland, Cork

for the degree of Doctor of Philosophy

March 2013

Supervised by Dr. John G. Hayes and Dr. Michael G. Egan

Head of Department: Professor Nabeel A. Riza

Department of Electrical and Electronic Engineering

University College Cork

Ireland

Table of contents

Table of contents III

Declaration IX

Abstract XI

Acknowledgements XIII

Associated publications XV

List of figures XVII

List of tables XXIII

Nomenclature XXV

Chapter 1 Introduction 1

1.1 Thesis introduction 1

1.2 Why research wave energy and wave energy converters (WECs)? 2

1.2.1 The global energy demand 2

1.2.2 Energy and electricity from fossil fuels 2

1.2.3 Nuclear technology 3

1.2.4 Renewable energy 3

1.2.5 Ocean energy 4

1.3 What are the motivations for including energy storage on-board? 5

1.3.1 Power smoothing 5

1.3.2 Low-voltage ride-through (LVRT) 8

1.3.3 Ancillary services 8

1.4 Approaches to the implementation of energy storage 9

1.4.1 Approaches to energy storage implementation for a farm of WECs 9

1.4.2 Approaches to energy storage implementation for individual WECs 10

1.5 Energy storage strategies in the electrical power take-off systems of offshore WECs 19
1.6 Electrical energy storage – technology overview 20
1.6.1 Superconducting magnetic energy storage (SMES) 20
1.6.2 Batteries 20
1.6.3 Supercapacitors (SCs) 21
1.6.4 Capacitors 22
1.6.5 Technology comparison 22
1.7 Why lithium-ion (Li-ion) batteries are examined in particular? 23
1.8 Why supercapacitors (SCs) are examined in particular? 25
Chapter 2 Variable speed strategies for offshore WECs 27
2.1 Introduction 27
2.2 The wave energy converter (WEC) 27
2.3 The system model 28
2.4 Sea-state data 28
2.5 The effect of speed on pneumatic power interaction block 30
2.6 The OWC turbine model 31
2.7 The examined variable speed strategies 34
2.7.1 Strategy A: Fixed speed 36
2.7.2 Strategy B: Loose PI 37
2.7.3 Strategy C: dTem/dt 38
2.7.4 Strategy D: ω^2 40
2.7.5 Strategy E: Efficient Φ 41
2.7.6 Strategy F: ω^{β} 46
2.8 Comparison of variable speed schemes 50
2.9 Results 51
2.10 Conclusion 54

Chapter 3 Supercapacitor (SC) testing and supercapacitors (SCs) for power smoothing 57

3.1 Objectives.....57

3.2 Introduction.....57

3.3 Supercapacitors (SCs) as an offshore energy storage device for power smoothing in conjunction with turbine inertia.....60

3.4 Standard cycle lifetime testing at ambient temperature.....64

3.5 Standard cycle lifetime testing at rated temperature 68

3.6 Application testing at ambient temperature 68

3.7 Results.....70

3.7.1 Standard cycle lifetime testing at ambient temperature.....70

3.7.2 Standard cycle lifetime testing at rated temperature 75

3.7.3 Investigation of the temperature effect on supercapacitor (SC) cycle lifetime 77

3.7.4 Application testing at ambient temperature.....79

3.7.5 Overall comparison plots of supercapacitor (SC) testing 82

3.8 Conclusion 83

Chapter 4 Supercapacitor (SC) applications in an offshore WEC.....87

4.1 Introduction.....87

4.2 Objectives.....87

4.3 Supercapacitors (SCs) for power smoothing 88

4.4 Turbine start-up with supercapacitors (SCs) 90

4.5 Low-voltage ride-through (LVRT) utilising supercapacitors (SCs).....90

4.6 OWC system model 92

4.6.1 Overview.....92

4.6.2 Turbine model.....94

4.6.3 Machine-side converter model.....94

4.6.4 Grid-side converter model.....101

4.6.5 Supercapacitor (SC) converter and control 106
4.7 Turbine start-up control scheme 109
4.8 Low-voltage ride-through (LVRT) control scheme 110
4.9 Results 111
4.9.1 Turbine start-up utilising supercapacitors (SCs) 111
4.9.2 Low-voltage ride-through utilising supercapacitors (SCs) 113
4.10 Conclusions 117
Chapter 5 Integration and testing of a high-voltage lithium-ion battery into a microgrid 119
5.1 Introduction 119
5.1.1 Motivation 119
5.1.2 Battery overview 121
5.1.3 Power converter overview 122
5.2 Objectives 123
5.3 Device operation 124
5.3.1 Safety features of the lithium-ion (Li-ion) battery 124
5.3.2 Lithium-ion (Li-ion) battery 125
5.3.3 Controller Area Network (CAN) 126
5.3.4 Initial battery testing 128
5.3.5 Power converter operation 129
5.4 Integration of the power converter and battery to the microgrid 131
5.4.1 Floating the battery and isolation 131
5.4.2 The battery panel 132
5.4.3 Cabling and cable terminations 136
5.4.4 Microgrid control 137
5.5 Battery modelling and characterisation 137
5.5.1 Battery charge and discharge tests 137
5.5.2 Battery step test 139

5.6 Results 139
5.6.1 The battery and power converter integrated into the microgrid 139
5.6.2 Test plots 142
5.6.3 Charge/discharge curves 143
5.6.4 Step test 146
5.6.5 Model performance 149
5.6.6 Creation of piecewise equation to describe discharge profile 151
5.7 Conclusions 153
Chapter 6 Conclusions 155
6.1 Conclusion summary 155
6.2 Future work 158
Appendix A Examination of power loss due to I^2R in a WEC with and without energy storage 159
A.1 Normal peak to average input power analysis 159
A.1.1 Grid power and energy with and without an energy storage device for power smoothing 159
A.1.2 Net flow of energy to the energy storage system 163
A.1.3 Transmission I^2R losses from output grid power with and without energy storage for power smoothing 164
A.1.4 Net output grid power with and without energy storage for power smoothing taking account of transmission I^2R losses 169
A.2 Large peak to average input wave power profile analysis 174
A.2.1 Transmission I^2R losses from output grid power with and without energy storage used for power smoothing 174
A.2.2 Net output grid power with and without energy storage used for power smoothing taking account of transmission I^2R losses 176
Appendix B Derivation of PI anti-integral control block equations 183
Appendix C Derivation of strategy F: ω^{β} control equation from [26] 185

Appendix D BCAP0005 P270 supercapacitor (SC) datasheet from Maxwell Technologies 191

Appendix E Matlab code used for supercapacitor (SC) #11 (standard testing) 193

Appendix F Matlab code used for supercapacitor (SC) #16 (thermal testing) 201

Appendix G Matlab code used for supercapacitor (SC) #26 (application testing) 211

Appendix H Derivation of the inertia of a Wells turbine with NACA 0015 turbine blades 223

Appendix I High-voltage lithium-ion (Li-ion) battery specifications 227

Bibliography 229

Declaration

I hereby declare that the thesis submitted is my own work and has not been submitted for another degree either at University College Cork or elsewhere.

Work carried out by others has been duly acknowledged in the thesis.

Signed: _____

Date: _____

Abstract

The thesis initially gives an overview of the wave industry and the current state of some of the leading technologies as well as the energy storage systems that are inherently part of the power take-off mechanism. The benefits of electrical energy storage systems for wave energy converters are then outlined as well as the key parameters required from them. The options for storage systems are investigated and the reasons for examining supercapacitors and lithium-ion batteries in more detail are shown.

The thesis then focusses on a particular type of offshore wave energy converter in its analysis, the backward bent duct buoy employing a Wells turbine. Variable speed strategies from the research literature which make use of the energy stored in the turbine inertia are examined for this system, and based on this analysis an appropriate scheme is selected.

A supercapacitor power smoothing approach is presented in conjunction with the variable speed strategy. As long component lifetime is a requirement for offshore wave energy converters, a computer-controlled test rig has been built to validate supercapacitor lifetimes to manufacturer's specifications. The test rig is also utilised to determine the effect of temperature on supercapacitors, and determine application lifetime. Cycle testing is carried out on individual supercapacitors at room temperature, and also at rated temperature utilising a thermal chamber and equipment programmed through the general purpose interface bus by Matlab. Application testing is carried out using time-compressed scaled-power profiles from the model to allow a comparison of lifetime degradation.

Further applications of supercapacitors in offshore wave energy converters are then explored. These include start-up of the non-self-starting Wells turbine, and low-voltage ride-through examined to the limits specified in the Irish grid code for wind turbines. These applications are investigated with a more complete model of the system that includes a detailed back-to-back converter coupling a permanent magnet synchronous generator to the grid.

Supercapacitors have been utilised in combination with battery systems for many applications to aid with peak power requirements and have been shown to improve the performance of these energy storage systems. The design, implementation, and construction of coupling a 5 kW h lithium-ion battery to a microgrid are described. The high voltage battery employed a continuous power rating of 10 kW and was designed for the future EV market with a controller area network interface. This build gives a general insight to some of the engineering, planning, safety, and cost requirements of implementing a high power energy storage system near or on an offshore device for interface to a microgrid or grid.

Acknowledgements

There are many people who have supported and helped me during the creation of this thesis and my time as a PhD student. I would like to thank a few who have been very special to me.

To my supervisors John Hayes and Michael Egan, whose mix of technical expertise, infectious positivity, careful planning, career and personal development awareness and continued support are traits I will always admire and strive to. Their support style allowed independent growth and development of sustainable, healthy life habits. They helped with any technical problems and supported an on-going thirst for knowledge, and also quickly dealt with many of the administrative details that are common in a university where continued improvement is sought and implemented in academic and bureaucratic procedures.

To Dara O'Sullivan who continues to offer guidance and expertise in the wave industry and for collaborating on much of my work, I thank him.

I wish to acknowledge and show my appreciation to the Irish Research Council for Science Engineering and Technology (IRCSET) for funding this research under the Embark Initiative, and to the United Technologies Research Centre Ireland (UTRCI) for funding the microgrid power converter and battery integration project.

I would like to express my gratitude to James Griffiths for his continued advice and help on all issues. Also, I would like to thank the staff of the Department of Electrical and Electronic Engineering in University College Cork. I would like to thank the mechanical workshop staff Michael O'Shea and Timothy Power. A special word of appreciation goes to the administrative staff Geraldine Mangan, Ralf O'Flaherty, Niamh O'Sullivan, Mary Costello, and Rita Sarteschi. I'd also like to thank Dr. Gordon Lightbody, Hilary Mansfield, and Dr. Ray Foley. Also for allowing me access to the facilities of the department, I'd like to thank Professor Nabeel A. Riza and Professor Patrick Murphy.

To Judy Rea and the staff of the Hydraulics and Maritime Research Centre (HMRC), particularly Darren, Tom, Niall, Sarah, and James, I thank you for all your help. I would especially like to thank you for help and advice during the work on the integration of a lithium-ion battery to a microgrid.

To those in the Power Electronics Research Laboratory (PERL) who have helped me: David Cashman, Jason Hannon, Marek Rylko, Naveen Boggarapu, Jack Bermingham, Diarmaid Hogan, Brendan Barry, and last but by no means least Kevin Hartnett. To my other laboratory co-demonstrators, Kieran Beausang, Mark Hamilton, and Naoise MacSuibhne, thank you.

To my parents Brendan and Eibhlín, and my brothers and sisters Éamonn, Séamus, Áine and Gráinne, I'd like to thank you all for your unwavering support, patience and encouragement.

To my friends, especially the members of UCC Ultimate Frisbee club and Rebel Ultimate Frisbee club who I got to know during my time as a PhD student and from whom I learned many life lessons. A special mention goes to Brian, James, Gráinne and Mairéad.

Finally, to Celine Larkin who has helped me through so much of this, in all aspects, thank you for everything.

Associated publications

- D. B. Murray, M. G. Egan, J. G. Hayes, D. L. O'Sullivan, "Applications of Supercapacitor Energy Storage for a Wave Energy Converter System", 8th European Wave and Tidal Energy Conference, Uppsala, Sweden, September 7-10, 2009, pp. 786-795.

- D. B. Murray, J. G. Hayes, M. G. Egan, D. L. O'Sullivan, "Supercapacitor Testing for Power Smoothing in a Variable Speed Offshore Wave Energy Converter", 26th Annual IEEE Applied Power Electronics Conference & Exposition (APEC), Fort Worth, Texas, USA, March 6-9, 2011, pp. 1933-1939.

- D. O'Sullivan, D. Murray, J. Hayes, M. G. Egan, A. W. Lewis (2011). "The Benefits of Device Level Short Term Energy Storage in Ocean Wave Energy Converters", in "Energy Storage in the Emerging Era of Smart Grids", Rosario Carbone (Ed.), ISBN: 978-953-307-269-2, InTech.

- D. B. Murray, J. G. Hayes, D. L. O'Sullivan, M. G. Egan, "Supercapacitor Testing for Power Smoothing in a Variable Speed Offshore Wave Energy Converter", IEEE Journal of Oceanic Engineering, Volume 37, Issue 2, April 2012, pp. 301-308.

- D. B. Murray, D. L. O'Sullivan, M. G. Egan, J. G. Hayes, "Electrical Energy Storage Systems" in chapter 4 of, "Electrical Design for Ocean Wave and Tidal Energy Systems", edited by Ray Alcorn, Dara O'Sullivan, Darren Mollaghan, to be published by the Institution of Engineering and Technology (IET).

List of figures

Figure 1.1: Global annual mean wave power density (colour) and annual mean best direction (→). The land buffers used to quantify the resource are also shown, coloured by continent (see [9] for more details). 4
Figure 1.2: Wind speed short term variability 5
Figure 1.3: Wave elevation short term variability [11] 6
Figure 1.4: BBDB OWC WEC overview 11
Figure 1.5: OWC WEC power transfer overview 12
Figure 1.6: Attenuator WEC overview 13
Figure 1.7: Attenuator WEC power transfer overview 14
Figure 1.8: Overtopping device WEC overview 15
Figure 1.9: Overtopping device WEC power transfer overview 15
Figure 1.10: The PowerBuoy from Ocean Power Technologies (www.oceanpowertechnologies.com) 17
Figure 1.11: Original AWS prototype before submersion [31] 17
Figure 1.12: The Oyster 1 from Aquamarine Power [32] 18
Figure 1.13: Electrical power transfer overview 19
Figure 1.14: Cycle life versus depth of discharge (DOD) at 25 °C for a fixed DOD and varying charging rates, for the Saft Synerion 48E Li-ion module [41] 24

Figure 2.1: BBDB OWC WEC overview 27
Figure 2.2: Overview of the system model 28
Figure 2.3: Relative occurrence and average pneumatic power produced in the WEC for a given sea-state 29
Figure 2.4: Example pneumatic power profile of a sea-state over a 200 second window 30
Figure 2.5: Pneumatic power gain versus speed for the examined WEC 30
Figure 2.6: Characteristic non-dimensional torque versus flow coefficient curve for the tested data 33

Figure 2.7: Overview of the OWC model parameters evaluation 34
Figure 2.8: Simulink turbine model used from [21] 34
Figure 2.9: Generator power and speed for a given pneumatic power for fixed speed control 37
Figure 2.10: Generator power and speed for a given pneumatic power for variable speed strategy B: Loose PI 37
Figure 2.11: Loose PI control strategy control block diagram 38
Figure 2.12: PI model block 38
Figure 2.13: Generator power and speed for a given pneumatic power for variable speed strategy C: dTem/dt 39
Figure 2.14: Generator torque versus turbine speed profile for strategy D: ω^2 40
Figure 2.15: Generator power and speed for a given pneumatic power for variable speed strategy D: ω^2 41
Figure 2.16: Generator power and speed for variable speed strategy D: ω^2, showing operation near maximum speed 41
Figure 2.17: Efficiency versus non-dimensional flow coefficient, Φ, for the model, fixing the turbine speed and using a ramp pneumatic power input 43
Figure 2.18: Efficiency versus non-dimensional flow coefficient, Φ, for the model, fixing the pneumatic power input and varying the turbine speed. 43
Figure 2.19: Ppneu, Pelec and Phi versus time for pneumatic power profile with an absolute sine wave shape 44
Figure 2.20: Ppneu, Pelec and Phi versus time for pneumatic power profile with a sine squared shape 45
Figure 2.21: Ppneu, Pelec and Phi versus time for fixed speed 1,100 rpm with pneumatic power profile 46
Figure 2.22: Average mechanical power versus fixed speed for two sea-states and maximum power curve 47
Figure 2.23: Maximum average power versus fixed speed for the examined sea-states and maximum power curve 47
Figure 2.24: Speed control power curve of generator power versus speed 49
Figure 2.25: Generator power and speed for a given pneumatic power for variable speed strategy F: ω^{β} 49
Figure 2.26: Generator power and speed with the switched controller to prevent chattering for a given input pneumatic power 50

Figure 3.1: Results of available lifecycle testing of SCs at 2.5 V and 2.7 V from Maxwell Technologies [52] 58
Figure 3.2: Results of available lifecycle testing of SCs from Maxwell Technologies [53] 59
Figure 3.3: Generator power and speed for variable speed strategy F: ω^{β} with the switched controller to prevent chattering for a given input pneumatic power profile from sea-state 6 60
Figure 3.4: Input pneumatic power, grid power and turbine speed with SCs and the switched controller added to prevent chattering for a given input pneumatic power profile 63
Figure 3.5: Generator power, grid power, SC power and SC voltage with the switched controller and SCs added for the most frequently occurring sea-state 63
Figure 3.6: SC current and voltage during characterisation 66
Figure 3.7: Histogram of measured ESR from characterisation tests of 30 SCs 66
Figure 3.8: Histogram of measured capacitance from characterisation tests of 30 SCs... 67
Figure 3.9: SC lifecycle test setup 67
Figure 3.10: Application test power demand of the SC before voltage limits 69
Figure 3.11: SC current and voltage from application testing 70
Figure 3.12: Capacitance versus cycle number during cycle lifetime testing at 25°C ambient 71
Figure 3.13: ESR versus cycle number during cycle lifetime testing at 25°C ambient 71
Figure 3.14: Manufacturer generic curve of capacitance evolution over lifetime from Maxwell Technologies, without time scale provided [53] 72
Figure 3.15: Capacitance for cycle lifetime testing at 25°C ambient with log scale 73
Figure 3.16: ESR for cycle lifetime testing at 25°C ambient with log scale 73
Figure 3.17: Cycle lifetime testing capacitance over one day at 25°C ambient 74
Figure 3.18: Cycle lifetime testing ESR over one day at 25°C ambient 74
Figure 3.19: Ambient and SC temperature for the cycle lifetime setup over one day 74
Figure 3.20: Capacitance versus cycle number during standard testing at 65°C 75
Figure 3.21: ESR versus cycle number during standard testing at 65°C 76
Figure 3.22: Capacitance versus cycle number during cycle lifetime testing at 65°C with log scale 76
Figure 3.23: ESR versus cycle number during cycle lifetime testing at 65°C with log scale 77
Figure 3.24: Capacitance versus cycle number during application testing at 25°C 80

Figure 3.25: ESR versus cycle number during application testing at 25°C 80
Figure 3.26: Capacitance versus cycle number during application testing at 25°C with log scale 81
Figure 3.27: ESR versus cycle number during application testing at 25°C with log scale . 81
Figure 3.28: Capacitance versus cycle number for the three tested SCs 82
Figure 3.29: Capacitance versus cycle number for the three tested SCs with log scale ... 82
Figure 3.30: ESR versus cycle number for the three tested SCs 83
Figure 3.31: ESR versus cycle number for the three tested SCs with log scale 83

Figure 4.1: WEC grid-connected system 88
Figure 4.2: Eirgrid LVRT requirement [63] 91
Figure 4.3: Pneumatic power and resultant turbine torque from typical sea-state data for the full-scale device 94
Figure 4.4: Block diagram of permanent magnet machine and controller 97
Figure 4.5: Speed control loop assuming an ideal current loop 99
Figure 4.6: Simulink schematic of the machine-side converter 100
Figure 4.7: Block diagram of grid filter and controller 103
Figure 4.8: Dc-link voltage control strategy 105
Figure 4.9: Simulink schematic of the grid-side converter 106
Figure 4.10: SC equivalent circuit used 107
Figure 4.11: Speed, input torque and electromagnetic torque versus time during turbine start-up with typical sea-state data 112
Figure 4.12: SC voltage and current during turbine start-up 112
Figure 4.13: Grid voltage during LVRT event 114
Figure 4.14: Grid current during LVRT event 114
Figure 4.15: Grid power and reactive power during LVRT event 115
Figure 4.16: Inverter voltage during LVRT event 115
Figure 4.17: Turbine speed and input torque during LVRT event without SCs 116
Figure 4.18: Turbine speed and input torque during LVRT event with SCs 116
Figure 4.19: SC voltage and current during LVRT event 117

Figure 5.1: Li-ion battery 121
Figure 5.2: Battery side with high and low voltage connectors 122
Figure 5.3: Battery side with MSD 122

Figure 5.4: Power converter electrical circuit overview 123
Figure 5.5: Overview of microgrid to battery connection with the main power and communication lines 124
Figure 5.6: Li-ion battery voltage over approximately 20% to 90% state of charge (SOC) 129
Figure 5.7: Triphase power converter cabinet layout 131
Figure 5.8: Electrical drawing of the battery electronics of the battery panel enclosure 134
Figure 5.9: Front view of the high voltage battery enclosure including panel with associated control electronics 140
Figure 5.10: Battery panel internal view 140
Figure 5.11: Battery enclosure internal view 141
Figure 5.12: Microgrid panel and Triphase panel installations 141
Figure 5.13: Standard operation of the Triphase IGBT based power converter with the set-point for Iinv_q at 10 A 142
Figure 5.14: Power converter and battery standard operation with current from the battery raised from 0 to 5 A 143
Figure 5.15: Battery voltage during complete discharge at 10 A recorded from the BMS 144
Figure 5.16: Battery SOC during complete discharge at 10 A recorded from the BMS 144
Figure 5.17: Battery voltage during complete charge at 10 A recorded from the BMS 144
Figure 5.18: Battery SOC during complete charge at 10 A recorded from the BMS 145
Figure 5.19: Voltage versus time for battery step test 146
Figure 5.20: Dc-bus voltage response to a step in battery current from -10 A (discharge) to 0 A 148
Figure 5.21: Dc-bus voltage response to a step in battery current from 10 A (charge) to 0 A 148
Figure 5.22: Battery voltage during complete discharge comparing experimental profile to model profile 149
Figure 5.23: Simulation and datasheet results from discharge of a 1.2 V NiMH battery (HHR650D from Panasonic) [80] 150
Figure 5.24: Battery voltage versus SOC for charge and discharge tests comparing model performance to experimental data 150
Figure 5.25: Battery voltage versus SOC for piecewise fitted equation with discharge profile 152

Figure 5.26: Battery voltage versus SOC for charge and discharge tests comparing model performance to experimental data to piecewise equation 153

Figure A.1: Wave power and resultant grid power over time for an idealised wave 161
Figure A.2: Plot of power from an idealised energy storage device and grid power before and after power smoothing 163
Figure A.3: I^2R power loss without an energy storage device assuming unity voltage and an arbitrary value of 0.2 Ω for R 167
Figure A.4: Comparing power loss due to I^2R of grid power output with and without energy storage assuming unity voltage and an arbitrary value of 0.2 Ω for R 168
Figure A.5: Normalised difference in net power output for cases where energy storage is and isn't used to smooth the grid output power and taking into account the resultant power loss due to I^2R in the transmitted power 173
Figure A.6: Grid power with and without energy storage employed for a large peak to average profile 175
Figure A.7: Normalised difference in net power output for cases where energy storage is and isn't used. Also taking into account the resultant power loss due to I^2R in the transmitted power, and comparing with large peak to average input power 181

Figure B.1: PI model block 183

Figure C.1: Regulation curves for several values of AJ MW kg m^2/s, where $A = |dP_e/dt|$ is the maximum value of the time-derivative of the electrical power allowed by the grid. 189

Figure H.1: Wells turbine 223
Figure H.2: Profile of the NACA0015 turbine blade 224

List of tables

Table I: Electrical energy storage technology comparison 23
Table II: Summary of sea-state data details 29
Table III: Comparison of the examined variable speed strategies 52
Table IV: Generator power peaks for each sea-state using control strategy F: ω^{β} with the switched controller 61
Table V: Parameters of the large SC module [54] 62
Table VI: Performance data of variable speed strategy with SCs from simulations 62
Table VII: Initial characterisation results of 30 BCAP0005 P270 SCs from Maxwell Technologies 65
Table VIII: SC modules scaled to values relevant to the tested SC 69
Table IX: Initial parameters of the SCs under test conditions 70
Table X: Table examining temperature effects on SCs based on applying an Arrhenius equation to testing results at 25°C and 65°C 78
Table XI: BCAP0005 P270 SC testing results summary 84
Table XII: Permanent magnet machine model parameters 93
Table XIII: Grid connection model parameters 101
Table XIV: Parameters of the SC module [54] 108
Table XV: Energy supplied and lost in the system during turbine start-up (assuming an ideal converter) 113
Table XVI: Triphase power converter specifications 123
Table XVII: Low voltage connector pin-out 126
Table XVIII: D-sub 9-pin connector pin-out 126
Table XIX: CAN message example sent from the Li-ion battery 128
Table XX: Explanation of items in the electrical drawing of the battery panel enclosure 135
Table XXI: Cables from the battery to the battery panel 136
Table XXII: Cables from the battery panel to the microgrid system 136
Table XXIII: Groundings of cables from the panel box to the system 137

Table XXIV: Parameter extrapolation from the battery discharge curve for the battery model 146
Table XXV: Evaluation of battery resistance 147
Table XXVI: Evaluation of battery response time 147

Nomenclature

A	Area of overlap of capacitor plates (m^2)
A	Exponential zone amplitude (V)
A_{init}	Exponential zone amplitude of initial portion of piecewise equation (V)
A_{end}	Exponential zone amplitude of end portion of piecewise equation (V)
A_a	Annular area (m^2)
A_D	Duct area (m^2)
AWS	Archimedes Wave Swing
B	Exponential zone time constant inverse $(A\ h)^{-1}$
B	Viscous damping (N s/m)
B_A	Parameter to be determined
B_r	Turbine damping ratio
$B_t(t)$	Applied turbine damping (kg/(s m^4))
BBDB	Backward Bent Duct Buoy
BMS	Battery Management System
c	Parameter to be optimised
c_v	Specific heat of gas at constant volume
C	Capacitance (F)
C	Unit specifying charge rate of battery, where a unit is the charge/discharge rate equal to the capacity of the battery in one hour
C_{cm}	Ac common mode filter effective capacitance (F)

CAES	Compressed Air Energy Storage
CAN	Controller Area Network
d	Separation distance between capacitor plates (m)
d	Direct axis
D	Turbine diameter (m)
DFIG	Doubly-Fed Induction Generator
DOD	Depth of Discharge
E_a	Activation energy (e V)
E_0	Battery constant voltage (V)
EDLC	Electric Double Layer Capacitor
ESL	Equivalent Series Inductance
ESR	Equivalent Series Resistance
EU	European Union
EV	Electric Vehicle
g	Gravitational constant of 9.81 (m/s^2)
GPIB	General Purpose Interface Bus
h	Falling height (m)
HVIL	High Voltage Interlock Loop
I	Current (A)
i	Battery current (A)
i^*	Filtered current (A)
$\hat{\imath}_a(t)$	Peak phase a current (A)
I_a	Inverter current on phase a (A)

I_{avg}	Average current (A)
I_{base}	Base current for controller (A)
I_c	Capacitor current (A)
$i_{d_g}(t)$	Direct-axis current in the grid circuit (A)
$i_{d_m}(t)$	Direct-axis current in the stator windings (A)
$I_{d_m}*$	Desired direct-axis current in stator windings (A)
I_{dc_link}	Dc-link current (A)
$i_{q_g}(t)$	Quadrature-axis current in the grid circuit (A)
$i_{q_m}(t)$	Quadrature-axis current in the stator windings (A)
I_{rated}	Rated current (A)
$I_{rms}(t)$	Rms current (A)
IEC	International Electrotechnical Commission
IGBT	Insulated Gate Bipolar Transistor
IPCC	Intergovernmental Panel on Climate Change
J	Inertia (kg m^2)
k	Constant
K	Polarisation constant (V/(A h)) or polarisation resistance (Ω)
K_{new}	Slope of linear portion of piecewise curve (V/SOC%)
k_B	Boltzmann's constant (J/K)
k_m	Machine constant (V s)
$k_{p_g_cur}$	Gain of the PI controller for the grid current loop
$k_{p_m_cur}$	Gain of the PI controller for the machine current loop
k_{p_speed}	Gain of the PI controller for the machine speed loop

$k_{p_g_volt}$	Gain of the PI controller for the grid dc-bus voltage loop
L	Inductance (H)
L_1	Filter inductance (H)
L_2	Optional filter inductance (H)
L_{cm}	Ac common mode filter inductance (H)
L_{d_m}	Direct-axis armature inductance (H)
L_g	Grid side filter inductance (H)
L_{q_m}	Quadrature-axis armature inductance (H)
LED	Light Emitting Diode
Li-ion	Lithium ion
LVRT	Low-Voltage Ride Through
m	Mass
MSD	Manual Service Disconnect
N	Total number of data points in the measurement
OEA	Ocean Energy Association
OWC	Oscillating Water Column
p	Pole pairs
$p(t)$	Pressure (Pa)
$P(t)$	Power (W)
$P_{em}(t)$	Electromagnetic power (W)
$P_{gen}(t)$	Generator power (W)
$P_{loss}(t)$	Power loss (W)
P_{max}	Maximum power (W)

$P_{mech}(t)$	Mechanical power (W)
$\mathrm{P}_{pneu}(t)$	Pneumatic power (W)
P_{max}	Maximum power (W)
PG	Parameter Group
PGN	Parameter Group Number
PM	Permanent Magnet
PMSM	Permanent Magnet Synchronous Machine
PTO	Power Take-Off
PV	Photovoltaic
q	Quadrature axis
Q	Battery capacity (A h)
$Q(t)$	Reactive power (V Ar)
Q_{exp}	Energy of initial exponential drop-off region (A h)
$Q_f(t)$	Axial flowrate (m^3/s)
$Q_{f_avg}(t)$	Average flowrate (m^3/s)
Q_{nom}	Capacity to the end of the nominal zone voltage (A h)
R	Internal resistance (Ω)
R	Equivalent series resistance of capacitor (Ω)
R_{epr}	Equivalent parallel resistance (Ω)
R_{esr}	Equivalent series resistance (Ω)
R_g	Grid side filter resistance (Ω)
R_s	Stator phase resistance (Ω)
R_{sys}	System resistance (Ω)

r_t	Radius of turbine (m)
RCBO	Residual-current Circuit Breaker with Overload protection
s	Laplace domain complex argument
SAE	Society of Automotive Engineers
SC	Supercapacitor
SMES	Superconducting Magnetic Energy Storage
t	Time (s)
T	Period (s)
$T(t)$	Turbine torque (N m)
t_1	Time at instant 1 (s)
T_1	Absolute temperature of data point 1 (K)
t_2	Time at instant 2 (s)
T_2	Absolute temperature of data point 2 (K)
t_d	Time to discharge (s)
$T_{em}(t)$	Electromagnetic torque (N m)
t_i	Reaction time of data point (hours)
T_i	Absolute temperature of data point (K)
$T_{loss}(t)$	Torque loss (N m)
$T_{mech}(t)$	Mechanical torque (N m)
T_{ND}	Non-dimensional torque
$TF_{curr_closed_loop}$	Closed loop transfer function for the machine current circuit
$TF_{speed_closed_loop}$	Closed loop transfer function for the machine speed circuit
$TF_{volt_open_loop}$	Open loop transfer function for the grid dc-bus voltage circuit

$U_t(t)$	Tip velocity of the turbine (m/s)
UN	United Nations
v	Wind speed (m/s)
V	Voltage (V)
V	Volume (m^3)
V_1	Voltage at point 1 (V)
V_2	Voltage at point 2 (V)
$V_{90\%}$	Battery voltage at 90% SOC (V)
$V_{0\%}$	Battery voltage at 0% SOC (V)
V_a	Output voltage from the inverter on phase a (V)
$\hat{V}_a(t)$	Peak phase a voltage (V)
V_{agrid}	Grid voltage on phase a (V)
V_{base}	Base voltage for controller (V)
V_{batt}	Battery voltage (V)
$v_{control}(t)$	Control voltage (V)
$v_{d_g}(t)$	Direct-axis inverter voltage to the grid (V)
$v_{d_m}(t)$	Direct-axis terminal voltage of the permanent magnet machine (V)
V_{dc_link}	Dc-link voltage (V)
$V_{dc_link}*$	Desire dc-link voltage (V)
$v_{dgrid}(t)$	Direct axis grid voltage (V)
V_{diff}	Difference in voltages (V)
V_{diff_max}	Difference in maximum voltages (V)
V_{diff_min}	Difference in minimum voltages (V)

V_{end}	Voltage at end of rest period (V)
V_{exp}	Voltage at end of initial exponential drop-off region (V)
V_{finish}	Final voltage (V)
V_{full}	Full voltage at 100% SOC (V)
$\hat{V}_{inv}(t)$	Peak inverter voltage (V)
V_{max}	Maximum voltage (V)
$V_{max_with_R}$	Maximum voltage taking account of voltage across series resistance (V)
V_{min}	Minimum voltage (V)
$V_{min_with_R}$	Minimum voltage taking account of voltage across series resistance (V)
V_{nom}	Voltage at end of nominal zone (V)
$v_{phase}(t)$	Phase voltage from inverter leg (V)
$v_{q_g}(t)$	Quadrature-axis inverter voltage to the grid (V)
$v_{q_m}(t)$	Quadrature-axis terminal voltage of the permanent-magnet machine (V)
$v_{qgrid}(t)$	Quadrature-axis grid voltage (V)
V_{start}	Starting voltage (V)
$v_{tri}(t)$	Triangular waveform voltage (V)
W_{gas}	Energy of gas accumulator (J)
$W_{reservoir}$	Energy contained in reservoir (J)
W_{SC}	Energy contained in supercapitors (J)
W_{SMES}	Energy in superconducting magnetic energy storage device (J)
$W_{turbine}$	Energy of rotating turbine (J)
WEC	Wave Energy Converter
X_g	Grid filter reactance (Ω)

x_i	A discrete data point
α	Parameter to be optimised
β	Parameter to be optimised
ε	Permittivity (F/m)
η	Efficiency
θ	Parameter to be optimised
λ_{fd}	Flux linkage established by magnets (V s)
μ	Mean value
ν	Parameter to be optimised
$\Pi(t)$	Non-dimensional power
ρ	Density (kg/m^3)
ρ_a	Air density (kg/m^3)
σ	Standard deviation
Φ	Non-dimensional flow coefficient
$\Phi_{avg}(t)$	Average non-dimensional flow
Φ_{avg_max}	Maximum average non-dimensional flow
Φ_{avg_min}	Minimum average non-dimensional flow
$\Psi(t)$	Non-dimensional pressure
$\omega(t)$	Turbine speed (rad/s)
ω_1	Particular rotational speed (rad/s)
ω_2	Particular rotational speed (rad/s)
$\omega_{avg}(t)$	Average speed (rad/s)
ω_{avg_max}	Maximum average speed (rad/s)

ω_{avg_min}	Minimum average speed (rad/s)
ω_{cg}	Grid controller cut-off frequency (Hz)
ω_{des}	Desired speed (rad/s)
$\omega_e(t)$	Speed of rotation of the flux in the machine (rad/s)
$\omega_g(t)$	Frequency of the grid (rad/s)
$\omega_{i_g_cur}$	Zero of the PI controller for the gird current loop
$\omega_{i_m_cur}$	Zero of the PI controller for the machine current loop
ω_{i_speed}	Zero of the PI controller for the machine speed loop
$\omega_{i_g_volt}$	Zero of the PI controller for the grid dc-bus voltage loop
ω_{max}	Maximum speed (rad/s)

Chapter 1 Introduction

1.1 Thesis introduction

This thesis examines the potential for on-board energy storage in offshore wave energy converters (WECs) with a focus on supercapacitors (SCs), turbine inertia and lithium-ion (Li-ion) batteries, and to this end investigates experimentally energy storage in a microgrid application.

This chapter outlines the motivation for this research and presents the benefits of utilising energy storage in an offshore WEC application. Various WEC technologies are explored as well as their inherent energy storage mechanisms. The WEC examined in this thesis is an Oscillating Water Column (OWC) of the backward bent duct design utilising a Wells turbine.

Energy storage options and technologies are compared, and a literature review identifies a gap in the available research and a need for this work. The motivations for examining SCs and Li-ion batteries in particular are given with reference to WECs, electric vehicles (EVs), and microgrids.

Chapter 2 presents variable speed strategies for offshore WECs. A number of strategies described and suggested for OWCs from different authors are examined and compared using models developed, based on the Matlab/Simulink platform.

Chapter 3 describes SCs as an offshore energy storage device for power smoothing in conjunction with turbine inertia. A novel control scheme is suggested and examined using a Matlab/Simulink model. SC testing is outlined and described. Lifecycle testing at ambient and elevated temperatures, and application testing at ambient temperature, aim to give an insight into SCs' robustness and suitability for the harsh offshore environment with long maintenance intervals. Previous testing results from the available literature are shown to be incomplete.

Chapter 4 investigates other applications of SC energy storage for use in offshore WEC installations. These applications include turbine start-up for offshore WECs utilising

Wells turbines, and low-voltage ride-through (LVRT) to help with grid stability. A more complete electrical model using the Matlab/SimPowerSystems platform is developed for the power converters and generator in the analysis of these applications.

SCs have been utilised in combination with battery systems for many applications to aid with peak power requirements and have been shown to improve the performance of these energy storage systems. The design, build, and integration of a 5 kW h Li-ion battery to a microgrid are discussed in Chapter 5. This build gives an insight into some of the engineering, planning, safety, and cost requirements of implementing a high power energy storage system, near or on an offshore device for interface to a microgrid or grid.

Finally conclusions, a brief summary, and future work are outlined in Chapter 6.

1.2 Why research wave energy and wave energy converters (WECs)?

1.2.1 The global energy demand

The United Nations (UN) projects human global population to grow from about 7 billion today to about 9.3 billion by 2050 [1]. This exponential growth brings an increased global energy and electricity demand. The two main sources of electricity production by conventional means today are fossil fuels and nuclear power.

1.2.2 Energy and electricity from fossil fuels

Fossil fuels are the chief source of electricity production worldwide but fossil fuel reserves are a source of concern. In addition, it is evident that emissions from the combustion of fossil fuels are the main contributor to the greenhouse effect. The Intergovernmental Panel on Climate Change's (IPCC) 2007 report states with very high confidence (more than 90% certainty) that the net effect of human activities on the planet since 1750 has been one of environmental warming [2]. The investigation into global warming has led to many, albeit contentious, agreements on the reduction of carbon emissions for nations. For example, in 2007 EU leaders made a unilateral commitment to cut their carbon emissions by at least 20% of 1990 levels by the year 2020 [3].

1.2.3 Nuclear technology

While nuclear power makes a significant contribution to the global energy mix, there are still safety concerns. The dangers of nuclear power plants themselves have been demonstrated in the Chernobyl (1986), and more recent Fukushima (2011) disasters, as well as the Three Mile Island accident (1979). The processing and disposal of hazardous nuclear waste is another drawback of the technology. These issues have led to reluctance among many countries to opt for this source of energy.

1.2.4 Renewable energy

Research and development into renewable energy technologies has increased in the last decade because of the aforementioned issues with fossil fuels and nuclear power, coupled with national requirements for security of supply. EU Directive 2009/28/EC [4] outlines targets for the share of energy from renewable sources in gross final consumption of energy for 2020 and compares them to the 2005 figures. Ireland has ambitious targets, renewable sources had 5.5% of the share of energy in 2010 with 16% the target for 2020 [5]. Electricity generated from renewable energy (normalised) reached 14.8% of gross electricity consumption in 2010 [5].

The three main renewable energy sources are hydro energy, wind energy, and solar energy from photovoltaic technology. Hydro-electrical power generation is an established and proven technology, with a total installed capacity of 136 GW in the EU-27. Although, most of Europe's best suited sites have already been developed [6].

Over the past decade wind energy has emerged as a successful and economical renewable energy source. In 2010/2011 the cumulative installed wind power in the EU was 93,957 MW, of which 9,616 MW was installed in 2011 [7]. The industry appears to have fixed on the three-bladed horizontal-axis wind turbine as the industry-standard solution. Most installed wind turbines are located onshore, although offshore installations are becoming more common and in 2011 there was 866 MW of new installed offshore capacity [7], reflecting a gradual market change to the offshore environment.

Photovoltaic (PV) technology implements the generation of electrical power directly from solar energy. Interestingly, the EU installed an estimated 17 GW of solar PV in 2011, and solar PV capacity in operation at the end of 2011 was about 10 times the global total just five years earlier [8]. Advantages include noiseless operation, no carbon dioxide emission during operation, and simple maintenance. Some disadvantages of the

technology are its sensitivity to shading and dirt, and output and life degradation with increased temperature. In 2011, solar PV manufacturers struggled to make profits or survive with excess inventory, falling prices, and declining government support [8]. Also module manufacturing continued its marked shift to Asia, mainly at the expense of European firms [8].

1.2.5 Ocean energy

Offshore ocean wave energy has the potential to contribute significantly to this renewable energy mix. There has been a rapid acceleration in recent years in research and development funding, infrastructure creation, foreshore license policy streamlining, and general policy development. The industry itself is still in the embryonic stages of development, with many technologies competing for this, as yet, untapped market and many scaled prototypes are either operating or under development. There are in reality though, very few full scaled devices built or producing power to the grid.

The global wave atlas is shown in Figure 1.1. It is seen that Ireland and the western shores of Europe are ideally positioned to exploit some of the most energetic waves in the world: the locations for most available power for WECs are on the west coast of land masses, as waves primarily flow from west to east [9]. It is predicted that as much as 237 GW is the available wave resource off Europe, with 29 GW off Ireland [9]. Basing figures on an available WEC (the Pelamis), it is estimated that the total extractable wave power from ocean-facing coastlines of the world (neglecting certain islands and the poles) is approximately 97 GW [9].

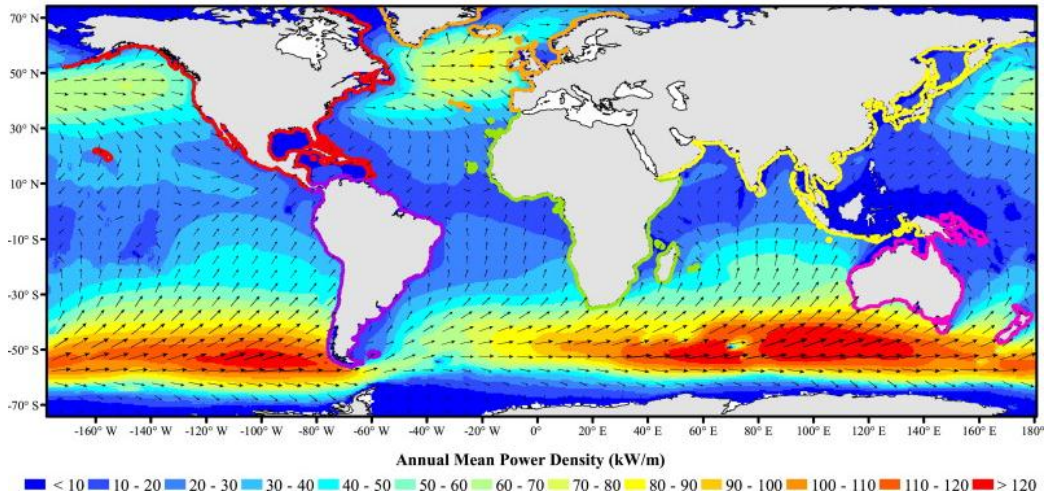


Figure 1.1: Global annual mean wave power density (colour) and annual mean best direction (→). The land buffers used to quantify the resource are also shown, coloured by continent (see [9] for more details).

The European Union Ocean Energy Association (EU-OEA) created a 2010-2050 roadmap for the development of the ocean energy industry in Europe, which aims to enable the industry to realise 3.6 GW of installed capacity by 2020 (0.5 GW from Ireland), and close to 188 GW by 2050 [10]. The development of such an industry would bring economic benefits such as job creation and would be suitable to contribute to regional development in Europe especially in remote and coastal areas.

1.3 What are the motivations for including energy storage on-board?

1.3.1 Power smoothing

Ocean waves are formed from the wind and depend mainly on wind speed, duration, direction and fetch (distance over which the wind blows across water and the wave travels). This energy transfer from the wind to the ocean extends deep below the surface of the water and in areas of deep water, ocean waves lose energy very slowly. A plot of wind speed versus time and wind power versus time is shown in Figure 1.2. Power fluctuations are seen to occur rapidly as divergence around a mean value, and as wind power is proportional to the cube of wind speed, there is a dramatic increase in the standard deviation compared to the wind speed profile.

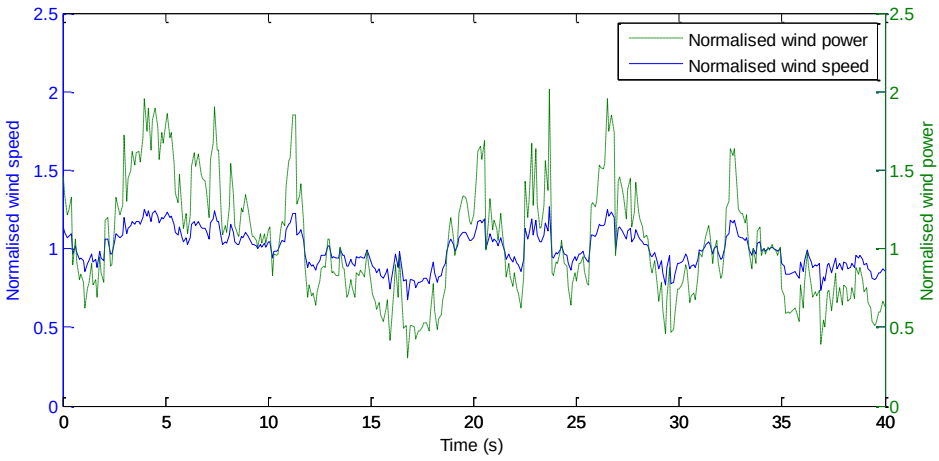


Figure 1.2: Wind speed short term variability

During the transfer of energy from wind to waves, many of these rapid power fluctuations are smoothened out. As waves are effectively an integration of wind

power, their available power and direction is steadier and can be forecasted and predicted to a better degree than with wind; this is one of the principal advantages of wave power.

As sea water is almost 1,000 times denser than air, the available power is thus more concentrated than with wind energy. Accordingly, the oscillating water column (OWC) wave energy converter (WEC) can convert this concentrated power into a focussed oscillating air stream, although it is clear that such devices are exposed to a very harsh environment and hence have component lifetime issues. A sample plot of normalised wave elevation over time is shown in Figure 1.3. Wave power is a function of the wave height and comparing Figure 1.2 and Figure 1.3 it is seen that the energy transfer of wind to wave smoothens out much of the rapid power changes. An inherent large power fluctuation still exists as the wave power transitions through zero twice during each wave period. This input power variation is experienced as the input power to many WECs.

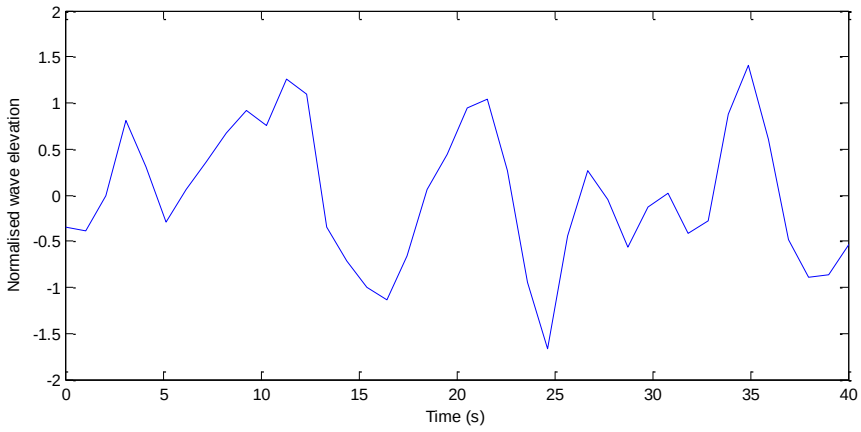


Figure 1.3: Wave elevation short term variability [11]

Ocean wave periods typically vary from one to twenty seconds, and without some form of energy storage or power smoothing, the output grid power from the device will display this same power fluctuation over this time period.

A power source with large variations will have increased cost and decreased system lifetime due to elevated power losses and larger ratings required for equipment. If the WEC is connected to a weak grid, flicker and voltage and frequency deviation issues arise, as the varying current may interact with the grid impedance to affect the local voltage levels [12]. Flicker is related to the voltage changes in the supply which result in

variations to the light output of lighting sources. The human perceptibility to this varying light intensity prompted the definition of a mechanism for calculating flicker severity on which IEC standards are based. Humans are most sensitive at a frequency of 8.8 Hz. At lower WEC input power frequencies and with WECs' large input power variations, it is expected that flicker and local voltage levels will still vary at a noticeable rate to the human eye if power smoothing is not implemented.

The issue of equipment rating is related to the peak to average power output ratio as opposed to fault conditions. Larger power rated equipment clearly costs more. For example, increased conductor area is required to handle the increased currents, and increased insulation is required to handle the increased voltage rating. A peak to average power output ratio of 1:1 allows the equipment to be used optimally and most cost effectively. Much equipment like generators, transformers, cables etc., will be able to handle transient peak ratios of up to 3:1 to 5:1, where the time at which the equipment is operated at peak power is limited by the thermal time constant. Power electronic equipment usually has a much lower time constant, which effectively results in rated power and peak power being very close. To achieve full controllability, power electronic converters are typically utilised to control the electrical power flows. The power electronic converters will experience this input peak power and need to be rated accordingly unless power smoothing equipment is inherent in the power take-off system.

Due to the power fluctuations, the system losses fluctuate and dissipate heat cyclically. This thermal cycling for equipment with different temperature coefficients and different coefficients of thermal expansion degrades interconnections throughout the system, for example between wire bonds and silicon in power electronic converter modules. Component, and hence system, lifetime is directly related to the amplitude and frequency of the power fluctuations, most especially for power electronic devices with their very short thermal time constants.

Comparing two power sources with the same average power, but one with a constant power output and the other with a fluctuating power output, will show that there are increased power losses in the fluctuating power output case. This additional power loss component is described in equation (1.1).

$$P_{loss} = R_{sys}\left[\frac{1}{T}\int_0^T {I_{rms}}^2(t)dt - {I_{avg}}^2\right] \quad (1.1)$$

It should be noted that using an energy storage device to smooth output power and remove this power loss component is unlikely to increase the overall efficiency of the WEC, due to the losses in the energy storage system. This issue is examined for a power source with an ideal sine wave input in Appendix A.

1.3.2 Low-voltage ride-through (LVRT)

As well as power smoothing, energy storage can help with low-voltage ride-through (LVRT) in grid connected WECs. In a grid low-voltage event (short circuit conditions), the ability to transfer power to the grid is limited as it is a function of the grid voltage. If this occurs when the wave energy converter (WEC) is experiencing high input power without damping, there will be a transient power imbalance unless real energy storage is employed. This energy storage device will be required to handle large power flows. If the input wave power is exported to the grid without an energy storage device via a power converter, the dc-link voltage of this converter will rise dangerously unless controlled. As well as using energy storage to ride through this fault, another option would be to burn off excess energy in a controlled manner using a power electronic converter and a dissipative load bank circuit.

1.3.3 Ancillary services

Energy storage might also help with the operation of specific WECs. For example in offshore WECs employing Wells turbines, energy storage can provide the energy to accelerate these non-self-starting, high inertia devices from rest. While the power converter used in the power-take off mechanism is often bi-directional and could theoretically be employed to start the machine, it is preferable to allow power flow in one direction only to help with ratings and minimise cost of safety and protective equipment. This also has advantages from a grid operator perspective, by limiting starting current surge from the grid as well as in terms of the import capacity of the grid connection.

Electrical power is needed in offshore WECs for lighting, communications, equipment monitoring, and control purposes. Heating and ventilation equipment may also need to be powered. Thus, some form of energy storage is required. Due to the high energy

density values of batteries, as seen in Section 1.6, these seem ideal devices for this application.

1.4 Approaches to the implementation of energy storage

There are many different technologies and approaches to extracting power from the ocean waves and there are many methods of employing energy storage in the system. Energy storage implementation can be examined for wave energy converters (WECs) on an individual basis, where installation would probably take place on-board the individual WEC, as well as on a collective basis, where the power output from a wave farm is connected to an energy storage system on or offshore.

1.4.1 Approaches to energy storage implementation for a farm of WECs

As outlined in Section 1.3, a motivation for including energy storage in a WEC system is to help with power smoothing. Aggregating the output power from many WECs in a wave farm has been examined in [13] where three WECs (SEAREV point absorbers) were operated over 20 days, and the standard deviation of the power reduced by 80% compared to single device operation. According to a study, power smoothing is independent of array layout and sea-state conditions, but instead depends on the number of systems in the array [14]. Simulations also conclude that less electrical energy storage will be needed for a centralized energy storage device for a wave farm, compared to individual WEC energy storage [15]. The power smoothing effect of combining many WECs in a wave farm is also discussed in [16], where the power variation is reduced for a farm of uncorrelated devices, although it is possible that power peaks may occur simultaneously in many WECs resulting in large export power fluctuations. This effect is partly shown in [15]. Clearly, a smoother output from an individual WEC would improve this smoothing by aggregation process.

If an energy storage system is sized for a farm of WEC devices, it will be required to handle a large power throughput. Presently, no commercial wave farms are in existence and the industry is still in the development stage. Grid code requirements will have to be fulfilled as power quality to the grid from a wave farm will be of greater importance compared to single device operation.

Energy storage options for the scenario where the storage system is placed onshore are not limited by size and space constraints. The power quality to the grid can be greatly enhanced by large scale systems which provide long-term energy storage. These long-term options include pumped hydro, compressed air energy storage (CAES) and large

scale battery installations. This thesis will focus on short-term energy storage options for on-board WEC devices.

1.4.2 Approaches to energy storage implementation for individual WECs

There are many different types of WECs currently in development, and full scale prototypes are rare. Recent reviews identified about 100 projects at various stages of development and this number seems to be increasing as new concepts outnumber those that are being abandoned [17]. Indeed, 110 developers are listed in [18].

This large number of WECs encompasses devices with a wide range of technologies utilizing a variety of methods to extract energy from the ocean waves and some with inherent energy storage built into the power take-off mechanism. There have been several methods of subdividing the devices according to various criteria. In [19], the following four commonly used classifications are employed to differentiate WECs and brief details are given on only a few important devices:

1. Operating principle.
2. Location.
3. Power take-off system.
4. Directional characteristics.

Energy storage may be inherent and built into the power take-off mechanisms of these WECs. The following device classifications that are used in this chapter to examine devices with inbuilt energy storage are representative of the majority of ocean energy devices [20].

- Oscillating water column (OWC).
- Attenuator.
- Overtopping device.
- Point absorber.
- Submerged pressure differential.
- Oscillating wave surge converter.

The energy contained in ocean waves is greatest offshore where wave interaction and friction with the local geometry is minimised. This chapter will primarily focus on offshore WECs.

The level of energy storage utilised, as well as the efficiency of the device, is dependent on the control system implemented. For oscillating-body and OWC converters, if the device is to be an efficient absorber, its own frequency of oscillation should match the frequency of the incoming wave, i.e. it should operate at near-resonance conditions [21]. Clearly, a control scheme utilising energy storage will likely reduce the output power fluctuation. However, some control methods aimed at maximising the power output can result in significantly larger power fluctuations, e.g. the "latching" control scheme implemented in some point absorbers.

1.4.2.1 Oscillating water column (OWC) – inertial energy storage

In an OWC, incident waves compress and expand the air within a chamber causing airflow across a turbine. These turbines are generally Wells turbines or impulse turbines and they convert the bidirectional pneumatic power to unidirectional, but pulsating, mechanical power from which a generator produces electricity.

In terms of offshore OWCs, an example of an offshore floating device that has proven successful at scaled testing is the OE Buoy. This is based on the backward bent duct buoy (BBDB) principle and is developed by OceanEnergy (www.oceanenergy.ie). A quarter-scale device had been successfully operating in Galway Bay off Ireland for over two years and also employs a Wells turbine [22], [23]. In the BBDB, the OWC inlet is oriented away from the wave direction which was found to be an improvement over inlets oriented into the wave direction.

A diagram of the BBDB OWC WEC is shown below in Figure 1.4.

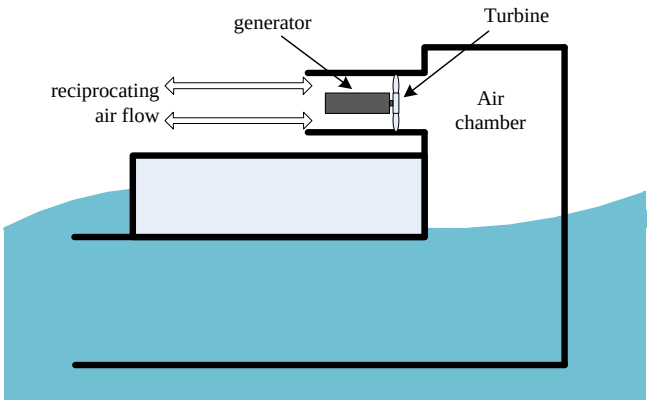


Figure 1.4: BBDB OWC WEC overview

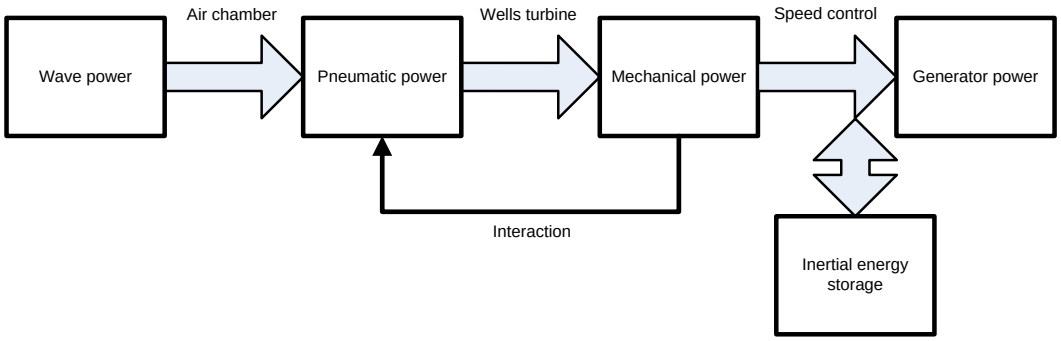


Figure 1.5: OWC WEC power transfer overview

The power transfer overview is displayed in Figure 1.5. This reveals where the flywheel energy storage effect of the turbine inertia is experienced in the power take-off system. The feedback interaction of the power take-off is also noted.

Fixed shoreline structures have been built in Portugal (Pico, Azores, 1999, [24]) and Scotland (LIMPET, island of Islay, 2000, [25]). The device in Portugal is rated at 400 kW. It uses a Wells turbine with an inertia of 595 kg m^2 and a speed range of 750 rpm to 1,500 rpm [26]. The LIMPET contains two 250 kW Wells turbines each with speed ranges of 700 rpm to 1,500 rpm and inertias of 1,250 kg m^2 per unit [27].

Utilising the rotating Wells turbines in a variable speed strategy offers significant energy storage due to the flywheel effect of the turbine inertia. For example, the difference in energy stored in a rotating turbine with inertia J, between two speeds ω_1 and ω_2 is:

$$W_{turbine} = \frac{1}{2} J({\omega_1}^2 - {\omega_2}^2) \tag{1.2}$$

This gives a figure of 1.5 kW h of energy storage for the Pico device which equates to almost 14 seconds of rated power. For the LIMPET device, the energy stored per turbine is 3.2 kW h, giving over 46 seconds of operation at rated power.

It is noted from the power transfer overview diagram of Figure 1.5 that if there is no mechanical power produced on the turbine, the control scheme may allow the generator to continue exporting power to the grid. This input to output power differential is balanced utilising the inertial energy storage of the Wells turbine and this will cause the turbine speed to reduce. Conversely, if there is excess mechanical power produced on the Wells turbine of which the generator exports a fraction to the grid, the

excess mechanical power will cause the turbine speed to increase. These power flows are described by equations (1.3) and (1.4):

$$P_{mech}(t) = P_{gen}(t) + P_{loss}(t) + J\omega(t)\frac{d\omega(t)}{dt} \tag{1.3}$$

$$P_{mech}(t) = P_{gen}(t) + P_{loss}(t) + \frac{d}{dt}\left(\frac{1}{2}J\,\omega^2\right) \tag{1.4}$$

1.4.2.2 Attenuator – hydraulic accumulator energy storage

Attenuators are multi-segment floating devices that align with the wave direction. The differing heights of waves along the length of the device cause the floating segments to move relative to each other. The resulting motion at the joints between segments is converted into electrical power through hydraulic or other means.

An example of an attenuator is the Pelamis device developed by Pelamis Wave Power (www.pelamiswave.com). This semi-submerged device consists of four or five cylindrical segments where hydraulic rams at the segment joints pump oil through hydraulic motors driving three electrical generators. This power take-off includes high pressure storage gas accumulators providing some in-built energy storage. A Pelamis P2 machine was installed offshore at Orkney in Scotland in 2010. Also, three Pelamis machines were installed and operated at Agucadoura in Portugal, five kilometres offshore in 2008 to become the world's first wave farm. Due to technical difficulties attributed to excessive wear on bearings, they have since been removed though the manufacturer has since identified a solution. Each device had a capacity of 750 kW in total from its three 250 kW generators.

An overview diagram of an attenuator WEC is shown below in Figure 1.6.

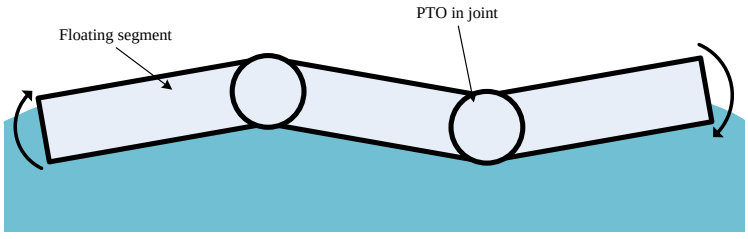


Figure 1.6: Attenuator WEC overview

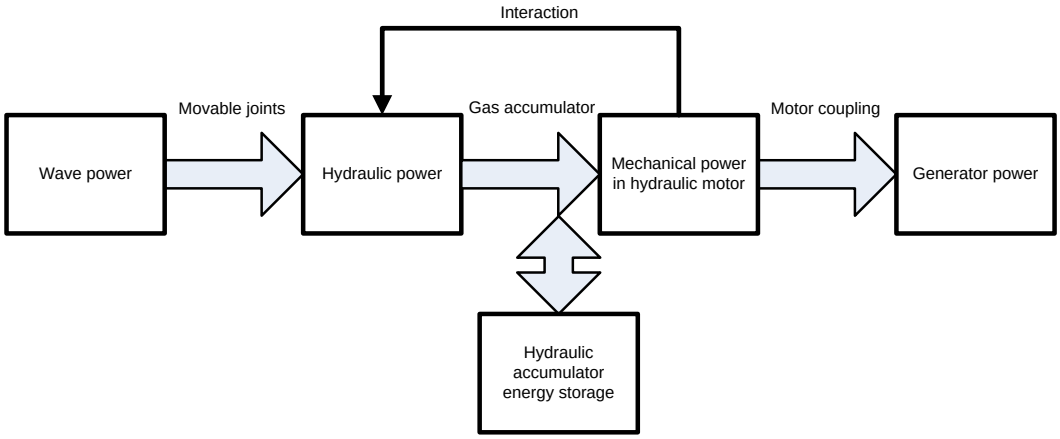


Figure 1.7: Attenuator WEC power transfer overview

The approximate power transfer overview diagram in Figure 1.7 gives a graphical representation of where the high pressure accumulator energy storage is in the power take-off system. Again it should be noted, the power take-off is a highly coupled system where the control strategy greatly influences the feedback and interaction between stages of this simplified power transfer process as well as the extractable power.

The short term energy storage of the accumulator pressure in each joint is set by the difference between the primary transmission energy intake and the secondary transmission outlet. The primary transmission consists of a hydraulic system which converts the wave power into stored energy in the accumulators, while the secondary transmission consists of hydraulic motors coupled to three-phase asynchronous generators which converts this stored energy to electricity exported to shore [19], [28]. The hydraulic control system is achieved through electronically-controlled valves which control fluid flow between the hydraulic cylinders in the movable joints, and the high pressure accumulator and low pressure reservoir.

The energy transfer of the accumulator gas in expansion is given in equation (1.5), assuming the ideal gas law is obeyed and the process is isentropic (constant entropy) [29].

$$W_{gas} = mc_v(T_1 - T_2) \tag{1.5}$$

where m is the mass of the gas, c_v is the specific heat at constant volume, T_1 is the absolute temperature in Kelvin before expansion, and T_2 is the absolute temperature in Kelvin after expansion. Further information on gas accumulators as an energy storage device in WECs is found in [29].

1.4.2.3 Overtopping device – hydro energy storage

Overtopping devices direct ocean waves and the sea water up over a structure and store this water above sea level in a reservoir. This potential energy of the water is converted first to kinetic and then to electrical energy using a conventional low-head hydro turbine when releasing the water back into the sea. The reservoir itself forms a large energy storage mechanism which allows for the smoothing of the short term power variability of the waves.

An overview of an overtopping WEC is shown below in Figure 1.8 and the power transfer overview in Figure 1.9 shows where the energy storage mechanism is in relation to the overall power take-off system.

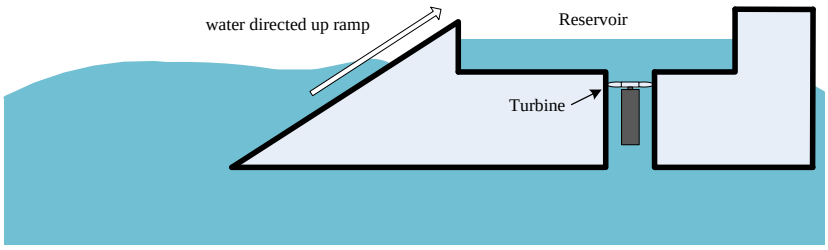


Figure 1.8: Overtopping device WEC overview

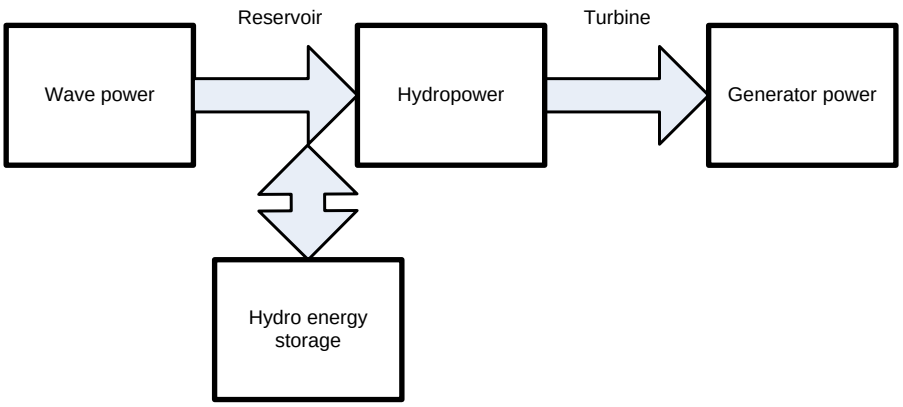


Figure 1.9: Overtopping device WEC power transfer overview

An example of an overtopping device is the Wave Dragon developed by Wave Dragon Ltd. (www.wavedragon.net). This offshore device employs ramps and reflectors to help focus the waves into the reservoir. A 1:4.5 scaled prototype is operating in Nissum Bredning, Denmark and is rated at 20 kW. It contains seven low-head Kaplan turbines each connected to 2.3 kW permanent magnet generators. It is designed for a site with a low power wave climate of 0.4 kW/m. This has a reservoir capacity of 55 m^3 with a ramp height of 3.6 m above sea level. The largest wave dragon specified would be designed for a wave climate of 48 kW/m, have a reservoir of 14,000 m^3 and a ramp height of 19 m. These are relatively large devices: The 0.4 kW/m device has a total length of 33 m, a width of 55 m, and weight of 237 tonnes. The 48 kW/m device has a total length of 220 m, a width of 390 m, and a weight of 54,000 tonnes. These large devices contain significant energy storage in their reservoirs above sea level. For example, the potential energy stored in a reservoir of water of density ρ (1000 kg/m^3), volume V, and falling height h is:

$$W_{reservoir} = \rho g h V \tag{1.6}$$

where g is the gravitational constant of 9.81 m/s^2. Assuming the total volume of water is at the ramp heights specified above (a large over approximation) of 3.6 m for the 0.4 kW/m device and 19 m for the 48 kW/m device, allows evaluation of the total energy contained in the full reservoirs. This evaluates to 0.54 kW h and 725 kW h respectively for the two systems described above.

1.4.2.4 Point absorber

Point absorbers have horizontal dimensions much smaller than the incident wave length and often absorb energy in all directions. They usually consist of two main components, a buoyant displacer which moves with the wave height, and a stationary or slow-moving reactor. The movement between these two bodies is converted into electrical power.

An example of a point absorber is the PowerBuoy from Ocean Power Technologies (www.oceanpowertechnologies.com). A 40 kW scaled prototype was operated over a kilometre offshore and grid-connected via an onshore substation in Hawaii from 2009-2011. In 2011, they tested a 150 kW device more than 50 km offshore from Invergordan off the Scottish North East coast. This device uses a linear permanent magnet generator driven by a piston [22], [30] and is shown Figure 1.10.



Figure 1.10: The PowerBuoy from Ocean Power Technologies (www.oceanpowertechnologies.com)

1.4.2.5 Submerged pressure differential

This device is completely under the surface of the water and operates in a similar way to a point absorber. It contains two main parts; the bottom part is fixed, while the top part moves in response to differences in pressure caused by the varying wave heights above the device.

An example of this device is the Archimedes Wave Swing (AWS) developed by AWS Ocean Energy (www.awsocean.com). The original prototype has an air-filled cylindrical steel chamber whose bottom part is fixed to the sea-bed. The top part, called the floater, is a vertically moving body that operates in resonance with the sea waves. A direct-drive permanent-magnet linear synchronous generator is used as the power take-off. The original 2 MW Dutch AWS 1 prototype was tested in 2004, five kilometres off the northern coast of Portugal. At the end of testing a severe failure occurred and the device sank [19]. This original prototype is shown in Figure 1.11.



Figure 1.11: Original AWS prototype before submersion [31]

Future device prototypes will be slack moored and arranged in wave farm configurations where each device will be connected to a central offshore substation via a high voltage link. The new PTO is also different, with the linear generator being replaced by a hydraulic/pneumatic power take-off [14].

1.4.2.6 Oscillating wave surge converter

The oscillating wave surge converter operates near the shore and exploits the back and forth motion of the waves. The devices are typically secured to the sea-bed and consist of a surge displacer. Energy is extracted from the waves using hydraulic converters at the hinge point of the surge displacer and fixed base.

An example of an oscillating wave surge converter is the Oyster developed by Aquamarine Power (www.aquamarinepower.com). The surge displacer is a buoyant, hinged flap which drives two hydraulic pistons which in turn pump high pressure water through a pipe network to an onshore hydroelectric turbine. A 315 kW device (Oyster 1) was tested at EMEC in 2009 – 2011, and an 800 kW device (Oyster 800) is currently undergoing testing at EMEC and was grid connected in June 2012. An image of the Oyster 1 device is shown here.



Figure 1.12: The Oyster 1 from Aquamarine Power [32]

Oscillating wave surge converters typically contain energy storage in on-board accumulators or onshore in pumped hydro devices in similar strategies to the attenuator or overtopping energy storage systems shown previously.

1.5 Energy storage strategies in the electrical power take-off systems of offshore WECs

After the generator stage of the WEC power take-off (PTO), further electrical stages may be implemented in the system before electricity is delivered to the grid. Typically a back-to-back converter is used, which decouples the frequency of the generator from the fixed voltage and fixed (50 or 60 Hz) frequency of the electrical grid, and allows the generator to operate at variable speeds. This back-to-back converter contains a dc-link whose dc voltage is sustained by a capacitor bank. In a standard control scheme the grid-coupled converter delivers power to the grid to maintain this dc-link voltage close to its set-point. The capacitor operational voltage range as well as its capacitance determines the energy stored in the dc-link stage of the PTO.

Further electrical energy storage control may be implemented using a dc-dc converter connected between the dc-link and the electrical storage device; typically a battery, supercapacitor (SC) module, or capacitor bank. This dc-dc converter allows control of the power flows to and from the electrical energy storage system. This electrical PTO schematic after the generator is shown in Figure 1.13, similar to a schematic given in [33], and also similar to the full power converter topology for a wind turbine [34]. This power electronic topology is also given in [35] for a battery energy storage system. This layout is valid for most generator types, except for a doubly-fed induction generator (DFIG), where the converter is placed on the rotor windings allowing for converter de-rating [33].

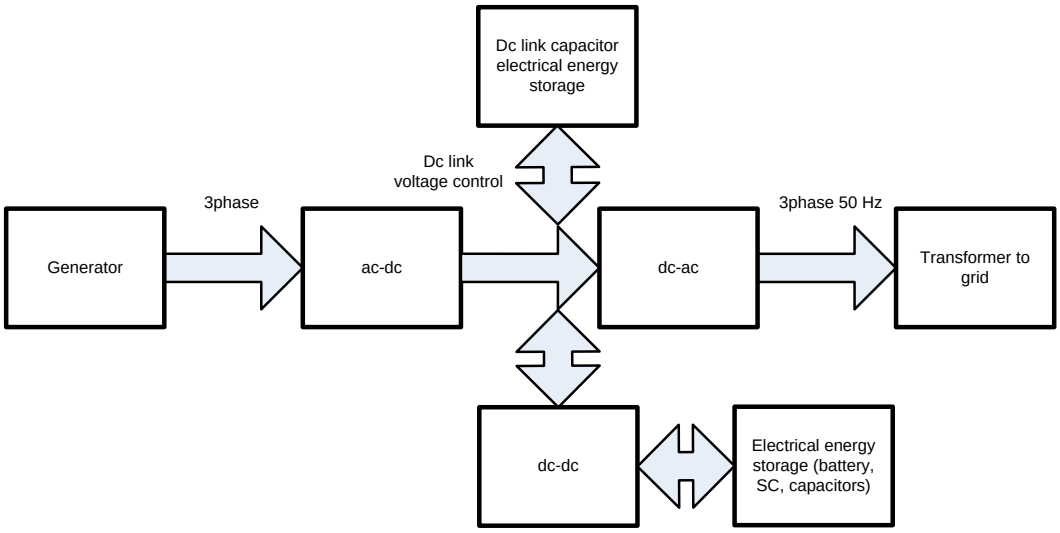


Figure 1.13: Electrical power transfer overview

1.6 Electrical energy storage – technology overview

Viable electrical energy storage technologies for off-shore wave energy applications include batteries, supercapacitors (SCs), capacitors, and superconducting magnetic energy storage (SMES) devices. A summary of each technology is given with a focus of utilisation on-board an offshore WEC.

1.6.1 Superconducting magnetic energy storage (SMES)

SMES systems store energy in the magnetic field around a superconducting coil created by the flow of dc current. The coil achieves superconductivity when cooled to a temperature below its superconducting critical temperature. Once charged, the current is sustained with very low losses and the magnetic field energy can be stored according to the following equation.

$$W_{SMES} = \frac{1}{2} L I^2 \tag{1.7}$$

where I is the magnitude of the current and L is the associated inductance at this current level.

SMES is currently costly and has not yet fully emerged from the development stage [36], [37]. It consists of many essential parts, including a cryogenically-cooled refrigerator that increases breakdown vulnerability in the harsh offshore wave climate as well as increasing the necessary space and mechanical support. For these reasons, SMES is not practical and has not yet been considered for offshore ocean energy applications.

1.6.2 Batteries

Batteries are high energy density electrical storage devices that have undergone significant development in recent times. With the increased research into electric vehicles, rechargeable batteries are undergoing continuous development. Currently lithium-ion (Li-ion) batteries are the technology of choice being installed in new electric vehicles as their improved performance over NiMH batteries are now being realised as production costs decrease. Some Li-ion batteries for electric and hybrid electric

vehicles have energy densities as high as 140 W h/kg and power densities of up to 745 W/kg [38].

1.6.3 Supercapacitors (SCs)

Supercapacitors (SCs) are known variously as electric double layer capacitors (EDLC), ultracapacitors, and electrochemical double layer capacitors. This variety of names comes from a number of market leaders or from the physical composition that effectively contains a double layer that increases capacitance. They have a high power density and are governed by the same equations as all capacitors. The value of capacitance is given in equation (1.8) and the energy stored at a particular voltage is given in equation (1.9).

$$C = \frac{\varepsilon A}{d} \tag{1.8}$$

$$W_{SC} = \frac{1}{2} C V^2 \tag{1.9}$$

SCs use a porous carbon-based electrode with a large surface area typically between 1 million m^2/kg to 2 million m^2/kg. The charge separation distance, less than 10 angstroms (10 x 10^{-10} metres), is much smaller than what can be accomplished using conventional dielectric materials. These properties give SCs their extremely high capacitance in accordance with equation (1.8), with values ranging from a few farads up to 5,000 farads. However, critically, due to the very small charge separation distance in the 'double layer', voltage ratings are low; typically close to 2.7 V. To achieve higher voltages, strings of series connected SCs are created. Consequently voltage balancing circuits are usually added due to the relatively large capacitance variations of individual SCs.

SCs have a demonstrated robustness in applications with photovoltaics where the SCs complemented battery storage devices and improved system performance and battery lifetime [39], [40]. They also demonstrated operating at sea for long periods of time [40]. SCs have also been used in wind turbine pitch systems, hybrid vehicles, trains, buses, and lift trucks. The time constant of SCs is typically around one second. Their small energy density but large power density suggest they are ideal short term energy

storage options, especially for ocean energy applications if their lifetimes can be shown to be compatible with the required service life of such equipment in an offshore WEC.

1.6.4 Capacitors

The three main capacitor technologies are ceramic capacitors, electrolytic and film capacitors.

Ceramic capacitors are typically utilised for high frequency applications and have very low equivalent series resistance (ESR) ratings but have poor aging characteristics.

Electrolytic capacitors are typically used to store large amounts of energy with a relatively high capacitance compared to other capacitors (not SCs). Electrolytics are often utilised in dc-link applications in power converters to help maintain the bus-voltage during any large power deviations. Drawbacks include poor tolerances and poor high-frequency characteristics.

Film capacitors are larger and more expensive than electrolytic capacitors, but they have higher surge or pulse load capabilities, high rated voltages (up to kV range), lower aging, and higher ripple current capability. They have very low ESR and equivalent series inductance (ESL) values.

As capacitors are typically situated very close to the power electronics in power converters to help maintain the dc-bus voltage, reduce wire lengths and minimise parasitic inductance, they are not offered in modules normally but are integrated into the power converter during design and construction. For this reason the technology comparison does not include a capacitor module.

1.6.5 Technology comparison

It is difficult to make a comparison of technologies that encompass many manufacturers' products and their slight differences. For this reason, leading products of each technology are chosen. A large SC module from Maxwell Technologies is compared with a high energy Li-ion battery module from SAFT batteries, a large electrolytic capacitor from EPCOS and a high performance lead acid battery from Enersys. Comparisons are made typically using modules to take into account any control, safety, and cooling equipment that might also be needed when using the technology, and allow a comparison of these standalone modular devices.

Table I: Electrical energy storage technology comparison

	Maxwell Technologies BMOD0063 P125	**SAFT Synerion 48E**		**Epcos B41456 B8150M**	**Enersys genesis EP 12VG 12V70EP**
Technology	SC module	Li-ion battery module		Aluminium electrolytic capacitor	Lead acid battery
Voltage (V)	125	48		63	12
Capacitance (F)	63			0.15	
Energy (W h)	137	2,200 (70% DOD)	71 (3.2% DOD)	0.083	644 (1C)
Max cont. power (W)	15,000	1,150		1600	644 (1C)
Volume (l)	70	17		1.0	10
Weight (kg)	61	19		1.3	24
Cycle life (cycles)	1,000,000 (75% DOD)	10,000 (70% DOD)	1,000,000 (3.2% DOD)		400 (80% DOD)
Energy density (W h/L)	2.0	130	4.2	0.081	64
Specific energy (W h/kg)	2.3	120	3.7	0.064	27
Power density (W/L)	210	68	68	1500	64
Specific power (W/kg)	250	61	61	1200	27

1.7 Why lithium-ion (Li-ion) batteries are examined in particular?

Li-ion batteries cycle life is in the range of several thousand cycles at present, although SAFT (www.saftbatteries.com) show cycle life increasing for a lower depth of discharge (DOD) for their Synerion 48E module. They specify over 1,000,000 cycles for 3% to 6% DOD (determined by extrapolation) depending on charge rates as seen in the Figure 1.14.

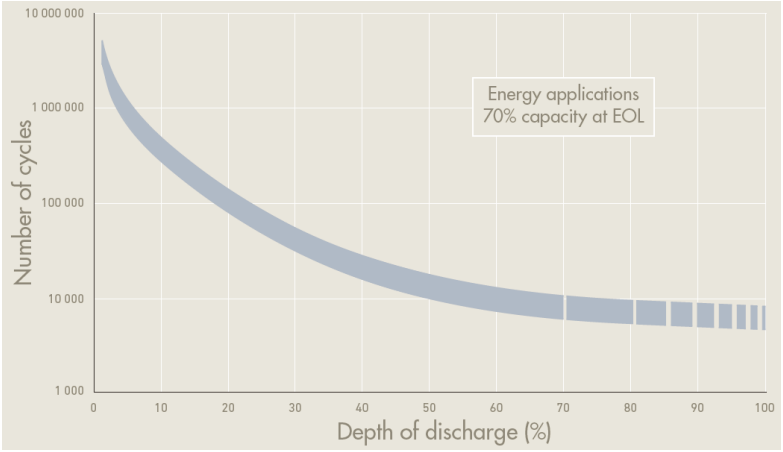


Figure 1.14: Cycle life versus depth of discharge (DOD) at 25 °C for a fixed DOD and varying charging rates, for the Saft Synerion 48E Li-ion module [41]

The lifecycle analysis is determined using an end of life definition of 70% of the initial capacity remaining. As determined from Figure 1.14, the nominal 2,200 W h Saft Synerion 48E module would only have an effective usable energy of 71 W h at a DOD of 3.2% corresponding to 1 million cycles. This would produce effective energy densities and specific energies in the ranges of 4 W h/L and 4 W h/kg. While charging rates are not given for the above figure, using the lower limit of 3% DOD (71 W h) at the maximum continuous discharge capacity of 1,150 W, gives a cycle time of almost 450 seconds. This would take over 14 years to complete 1 million cycles if operated continuously at this charge/discharge rate.

Desired intervals for non-routine, disruptive maintenance, for offshore WECs are specified in Chapter 2 as 5 to 10 years. The evaluated lifetime of 14 years demonstrates the Li-ion battery robustness and effective high cycle lifetime if operated within specified limits, provided the battery is oversized sufficiently to achieve the required DOD figure.

While Chapter 2, Chapter 3, and Chapter 4 explore turbine inertia and SCs as energy storage devices, Li-ion batteries are explored in Chapter 5. Li-ion batteries are gaining market share in EV and renewable applications and are currently employed in the Nissan Leaf, Mitsubishi iMieV, Ford Fusion, and Chevy Volt. It is proposed in [42], [43], [44] to improve battery performance with SCs to assist in high power events, thus increasing the battery lifetime and improving efficiency.

With the increased proportion of renewable generation and smaller generators on the grid, many systems are of yet not well integrated with nearby renewables or to the external grid. Also, overall system performance is not optimised for efficient and sustainable operations in the event of power outages or periods of high stress on the grid [45]. This has led to an increased focus on microgrids to help manage these areas encompassing local generation and local loads. In Chapter 5, the integration of a high voltage Li-ion battery into a microgrid is described. An examination of the Li-ion battery parameters is carried out and compared to the inbuilt Matlab/Simulink battery model which has so far been validated for a low-voltage individual Li-ion cell.

1.8 Why supercapacitors (SCs) are examined in particular?

While SCs cannot compete with batteries in terms of energy density, their much longer cycle life, power density, operational temperature range, and ability to fully discharge make them an energy storage option that must be considered in many applications. A typical SC has an energy density of over 5 W h/kg, a power density of over 6,000 W/kg, and a rated lifetime of 1 million cycles (www.maxwell.com). This high cycle-lifetime value has not yet been demonstrated in available literature. Table I demonstrates that SCs' power and energy densities lie in a range between capacitors and batteries. Coupled with this, SCs have charge/discharge efficiencies ranging from 0.85 to 0.98 [46]. These characteristics are very complementary to those of batteries and thus appear ideal for a WEC application.

Chapter 2 Variable speed strategies for offshore WECs

2.1 Introduction

This chapter investigates variable speed control strategies from leading papers, for a full-scale offshore Oscillating Water Column (OWC) Wave Energy Converter (WEC) incorporating a Wells turbine. A developed Simulink model of the examined WEC is utilised to compare five different control schemes as well as comparing them to fixed speed cases. This model is based on experimental data from an offshore WEC scaled prototype. Complete sea-state data, encompassing 30 minute power profiles for 13 different sea-states, gives the input pneumatic power to the model and is utilised to help evaluate each strategy. The control schemes are compared in terms of efficiency, power smoothing, and speed limit constraints. Practical concerns are also addressed.

2.2 The wave energy converter (WEC)

The OWC WEC considered utilises a Wells turbine and it is assumed that blow-off valves are not employed. Incident waves compress and expand the air within a chamber causing airflow across the Wells turbine. This converts the bidirectional pneumatic power to unidirectional, but pulsating mechanical power from which a generator produces electricity. A simplified schematic of the WEC is shown in Figure 2.1.

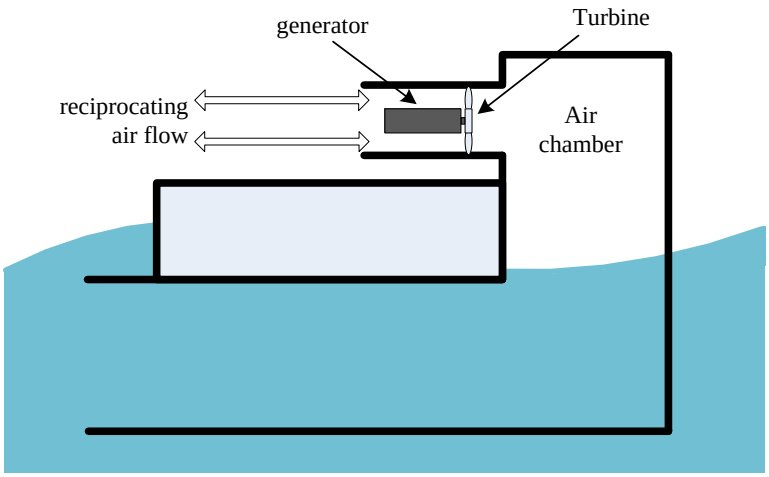


Figure 2.1: BBDB OWC WEC overview

2.3 The system model

An overview of the system model is shown in Figure 2.2.

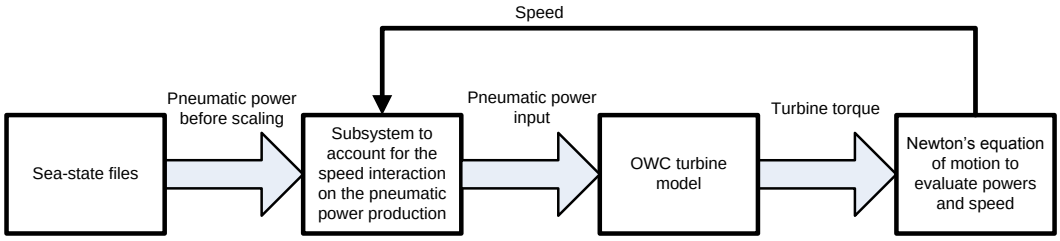


Figure 2.2: Overview of the system model

The sea-state files which produce a pneumatic power profile are described in Section 2.4. The subsystem which accounts for the speed interaction on the pneumatic power production is described in Section 2.5, while the turbine model which outputs the turbine torque for a given pneumatic input is detailed in Section 2.6.

2.4 Sea-state data

The performance of this WEC model and any associated control scheme is examined using pneumatic power profiles produced from the ocean waves inside the WEC at a particular site. Sea-state data was obtained for 13 sea-states shown below in Figure 2.3. These encompass over 99.9% of the waves occurring at a site throughout the year.

The OWC device shown in Figure 2.1 was tested at a scale of 1:50 in the Hydraulics and Maritime Research Centre (HMRC) wave basin. Data from this testing were scaled and utilized as the input pneumatic power time series for the model [47]. The actual wave elevation time series applied to the scaled model in the wave basin are based on Bretschneider type irregular sea-states, typical of open-ocean conditions [47].

Table II shows the percentage occurrence of each sea-state as well as the average pneumatic power produced in the backward bent duct buoy.

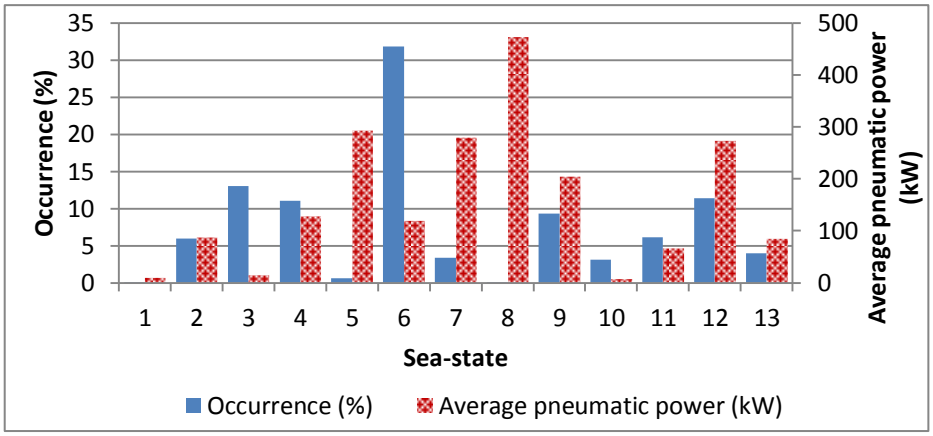


Figure 2.3: Relative occurrence and average pneumatic power produced in the WEC for a given sea-state

Table II: Summary of sea-state data details

Sea-state	Avg Ppneu (kW)	Occurrence (%)
1	10	0.05
2	87	5.95
3	16	13.04
4	128	11.04
5	294	0.64
6	119	31.85
7	280	3.41
8	473	0.02
9	205	9.32
10	8	3.08
11	66	6.11
12	274	11.42
13	85	4

An example full-scale pneumatic power profile produced over a 30 minute window with a sample step size of 0.44 seconds (2.3 Hz) is taken for each sea-state. This can then be utilised as an input to the WEC model. A typical 200 second excerpt of the power profile for the most commonly occurring sea-state is shown in Figure 2.4.

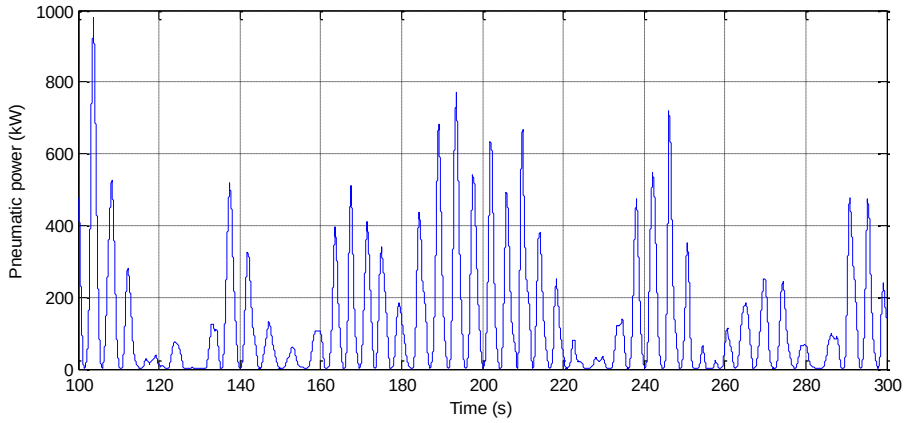


Figure 2.4: Example pneumatic power profile of a sea-state over a 200 second window

2.5 The effect of speed on pneumatic power interaction block

For the examined WEC, the pneumatic power produced from the waves is dependent on the turbine speed. This effect of turbine speed on the average pneumatic power production in the experimental data was examined by staff in the HMRC. The experimental data from a quarter scale prototype operating offshore was collated. Data from matching sea-states were examined where the turbine was operated at different speeds, or data was investigated from one sea-state where the turbine fixed speed was changed several times. The effect of the turbine speed on the average pneumatic power production was estimated. This lead to the creation of a subsystem model in the Matlab/Simulink environment which applied a per unit damping gain to the pneumatic power input based on instantaneous speed. The gains and corresponding speeds are shown in Figure 2.5. There is a range where speed does not have a significant effect on the pneumatic power production and here the gain is set to unity. Above and below this region the gain reduces linearly (an approximation).

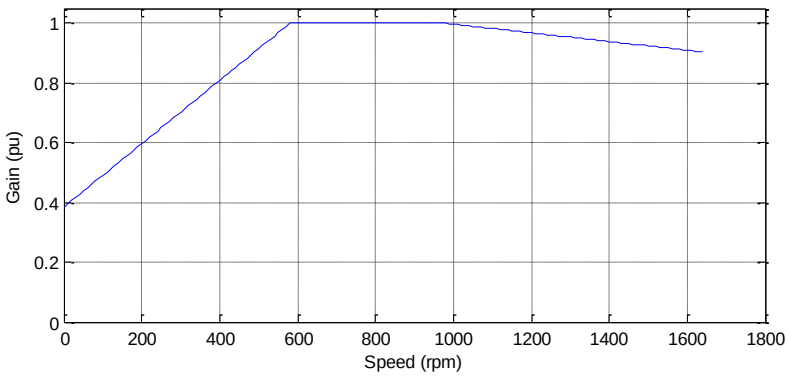


Figure 2.5: Pneumatic power gain versus speed for the examined WEC

2.6 The OWC turbine model

To extract realistic power take-off (PTO) information for the device at variable speed, the Simulink model created in [21] was utilised. This was based on data from a quarter-scale prototype operated offshore in an Atlantic test site, as well as from equations defined in [48]. The model inputs are pneumatic power and turbine speed, and the output is turbine torque. Non-dimensional quantities are used which allows scaling to full size.

The independent variable for the first part of the model is pneumatic power $\mathrm{P}_{pneu}(t)$ while the dependent variable is Φ, the non-dimensional flow coefficient. Experimental data allowed development of a non-dimensional torque T_{ND} characteristic curve from a measurement of pressure. This facilitated evaluation of the non-dimensional flow coefficient, Φ, using turbine damping.

Pneumatic power is the input to the model and is described by the equation (2.1), where $p(t)$ is the pressure in the chamber and $Q_f(t)$ is the axial flow-rate.

$$\mathrm{P}_{pneu}(t) = p(t)\, Q_f(t) \tag{2.1}$$

The following expressions describe the non-dimensional quantities for pressure, flow and power:

$$\Psi(t) = \frac{p(t)}{\rho_a \omega(t)^2 D^2} \tag{2.2}$$

$$\Phi(t) = \frac{Q_f(t)}{A_a\, U_t(t)} \tag{2.3}$$

$$\Pi(t) = \frac{P(t)}{\rho_a \omega(t)^3 D^5} \tag{2.4}$$

where $\Psi(t)$ is non-dimensional pressure, $\Phi(t)$ is the non-dimensional flow coefficient, and $\Pi(t)$ is non-dimensional power. D is the turbine diameter, $\omega(t)$ is the turbine

speed, and ρ_a is the air density. U_t is the tip velocity of the turbine given in equation (2.5), where r_t is the radius of the turbine.

$$U_t(t) = \omega(t)\, r_t \tag{2.5}$$

It is shown in [26] that non-dimensional pressure, $\Psi(t)$, and non-dimensional flow, $\Phi(t)$, have a linear relationship. The slope of this is known as the damping ratio of the turbine represented by B_r.

The applied turbine damping, $B_t(t)$, is given by the following expression:

$$B_t(t) = \frac{2\, \rho_a\, D\, \omega(t)\, B_r}{A_a} \tag{2.6}$$

where A_a is the annular area which is equal to the duct area minus the hub area.

The flow inside the chamber was thus derived using the following expression from [21]:

$$Q_f(t) = \frac{p(t)}{B_t(t)} \tag{2.7}$$

The relationship in equation (2.7) combined with equation (2.1) and is used to give an expression for the flow-rate $Q_f(t)$ as shown in equation (2.8).

$$Q_f(t) = \sqrt{\frac{P_{pneu}(t)}{B_t(t)}} \tag{2.8}$$

From the input pneumatic power $\mathrm{P}_{pneu}(t)$, and using given values of r_t, D, B_r, A_a, ρ_a for the turbine, the non-dimensional flow coefficient, Φ, can be evaluated with a measure of turbine speed. The non-dimensional torque is then produced using a lookup table of Φ versus T_{ND}. A plot of this lookup table is shown in Figure 2.6.

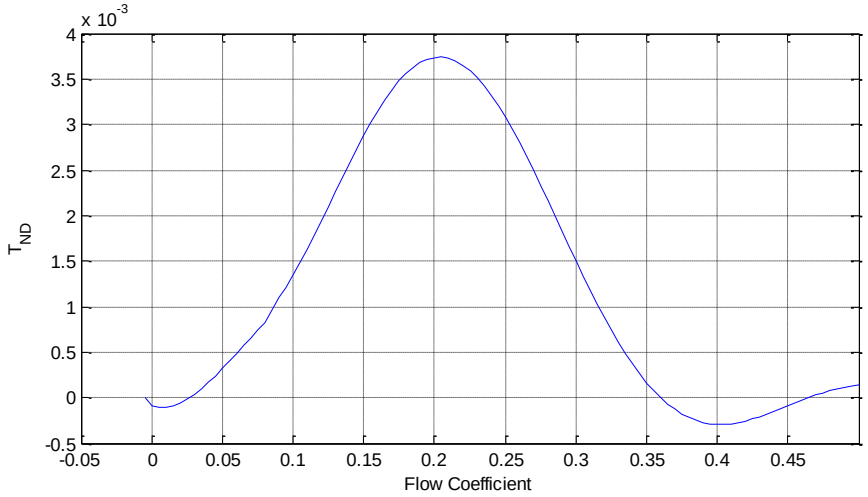


Figure 2.6: Characteristic non-dimensional torque versus flow coefficient curve for the tested data

This non-dimensional characteristic curve was developed in [21] assuming the speed of the system was constant. Therefore, the experimental data used to develop the curve was sorted into speed bins of 20 rpm intervals and a best fit curve was applied. The curve was formulated by taking a mean torque at each flow coefficient, but this leads to inaccuracies in the instantaneous torque prediction [21]. Also noise in measurements affected accuracy. The model is a first order model and does not take into account higher order aerodynamic effects, for example hysteresis in the turbine. Also, it is assumed that the same flow regions occur for inflow and outflow. In [21], the model was able to predict the electrical energy generated from their system within 20% of the actual experimental value.

From the non-dimensional torque versus flow coefficient curve in Figure 2.6 the turbine torque is evaluated according to equation (2.9).

$$T(t) = T_{ND}\ \rho_a\ \omega(t)^2\ D^5 \tag{2.9}$$

The overall model strategy is shown in Figure 2.7.

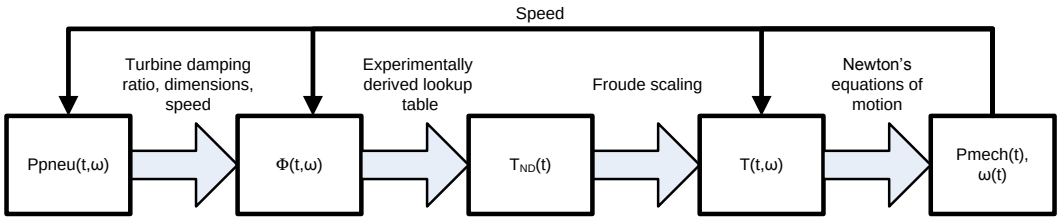


Figure 2.7: Overview of the OWC model parameters evaluation

The OWC Simulink model is shown in Figure 2.8.

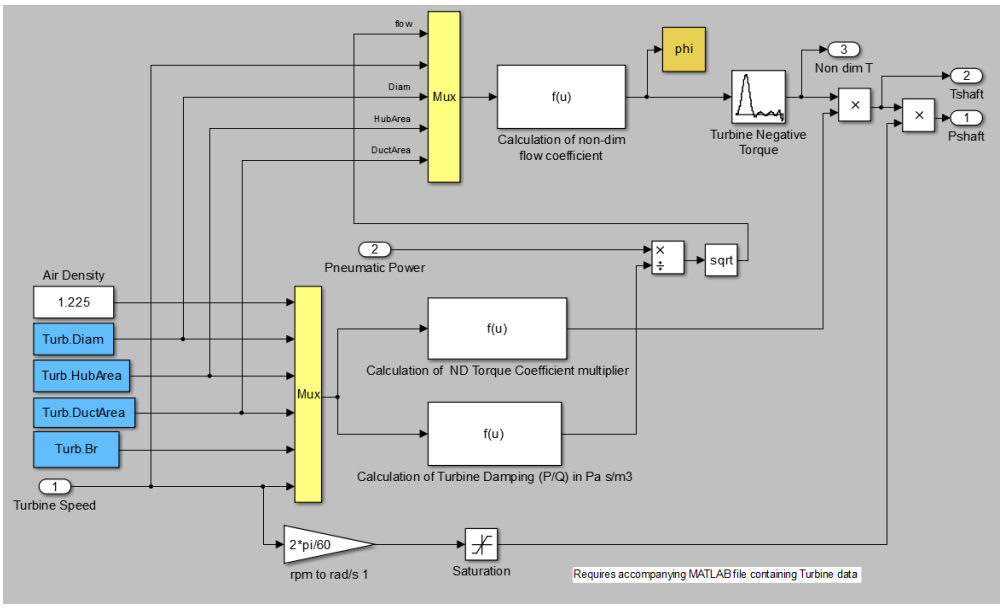


Figure 2.8: Simulink turbine model used from [21]

2.7 The examined variable speed strategies

Variable speed strategies have been examined for WECs in [26], [49], and [50], and key features to all include attempting to maximise the energy output and smoothing power fluctuations. Wind turbines maximise efficiency for a particular wind velocity on an instantaneous basis by varying the turbine speed and blade pitch. In the OWC WEC, the input power invariably goes through zero twice during every wave period, and a low inertia device would be needed to track the maximum PTO point. This would reduce the capability of power smoothing with turbine inertia. Instead WEC variable speed strategies are based on average values over periods of multiple waves to sea-states.

With so many WECs in development, it is recognised that variable speed strategies will be unique to each device and its location. Factors to be considered when devising a control strategy are discussed in [49] and consist of:

I. Remaining within speed limits.
II. Efficient performance.
III. Power quality to the grid.
IV. Utilising a realistic control procedure, where measurable quantities are used.

Power flow and speed variation is governed by Newton's equation of motion for the shaft:

$$P_{mech}(t) = T_{mech}(t)\,\omega(t) = P_{em}(t) + P_{loss}(t) + J\,\omega(t)\,\frac{d\omega(t)}{dt} \qquad (2.10)$$

Here, $P_{mech}(t)$ is the mechanical power on the turbine and $P_{em}(t)$ is the electrical power drawn from the generator.

Six strategies were considered and compared using the turbine model described above with sea-state data.

- **A: Fixed speed** fixes the turbine speed to allow performance comparisons with the other control strategies.
- **B: Loose PI** allows speed fluctuation about a set-point by decreasing the bandwidth of the speed PI controller.
- **C: dTem/dt** relates the derivative of torque to the derivative of speed. An extra factor is included which is proportional to the deviation from a speed set-point to remove dependence on initial conditions.
- **D: ω^2** relates torque to speed squared, as per the non-dimensional torque equation, shown in equation (2.9). Additional terms are added to ensure operation between speed limits.
- **E: Efficient Φ** controls speed to keep the average value of non-dimensional flow in the high efficiency region of the WEC.
- **F: ω^β** is based on stochastic modelling of OWC performance to set the turbine torque to the most efficient value based on turbine speed as well as considering the maximum rate of change of power to the grid to help prevent over-speed.

For the modelling work the turbine inertia was set at 595 kg m^2 in line with other full-scale OWC Wells turbines [26]. The value utilised for the turbine viscous friction coefficient B was nominally set at 0.25 N m s after consultation with HMRC and coulomb friction was ignored. No electrical losses were taken into account and electrical performance was assumed ideal, matching the evaluated $T_{em}(t)$ from the control strategy.

A saturation block was included on the evaluated $T_{em}(t)$ in the model based on power converter and electrical machine limits and is constrained from 0 to 10,000 Nm to avoid drawing power from the grid in the control scheme.

As shown in Figure 2.7, parameters such as pneumatic power and turbine torque are functions of speed and the pneumatic power input profile was evaluated at a turbine damping corresponding to a fixed speed. While the effect of speed on the pneumatic power production is approximated and described in Section 2.5, this is not ideal when comparing variable speed strategies and hopefully this will be improved on in future comparison work.

2.7.1 Strategy A: Fixed speed

To evaluate the advantages and disadvantages of a variable speed strategy, a perfect infinite bandwidth fixed speed control scheme was modelled to use as a comparison. This is done by setting the turbine speed as a constant in the simulation. Various fixed speeds were modelled to get a complete picture of the strategy performance. In reality the control system would implement a strategy such as a fast PI controller on the current loops of the power take off electrical machine. This would prevent significant deviations from a fixed speed by adjusting the generator torque.

Neglecting speed deviations, the previously stated equation (2.10) simplifies to the generated electrical power being equal to the mechanical input power minus losses.

A plot of the resultant electrical power is shown below in Figure 2.9 for the sample sea-state pneumatic power input. It is seen that due to turbine stall a further power deviation is introduced into the output power profile. Turbine stall occurs when at a certain speed and pneumatic power on the turbine, any further increase in pneumatic power actually results in less aerodynamic interaction with the turbine and therefore a subsequent output power drop. This effect of turbine stall on the power output is highlighted in the plots below.

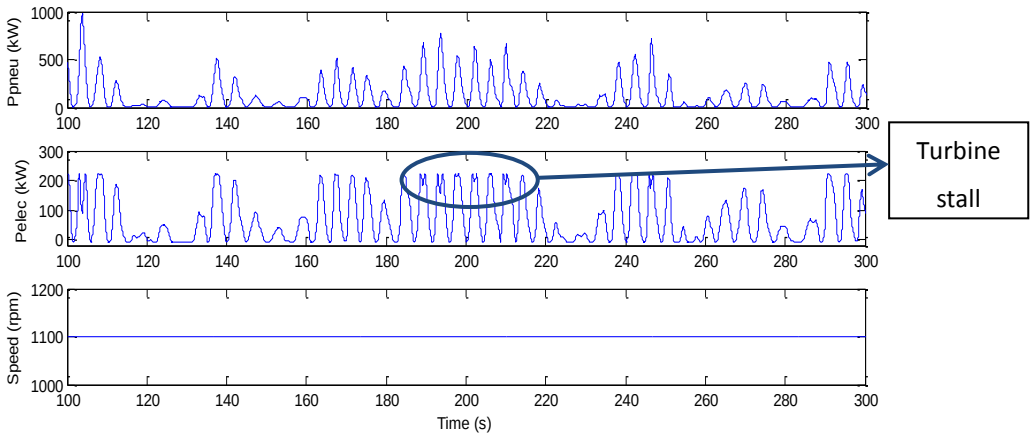


Figure 2.9: Generator power and speed for a given pneumatic power for fixed speed control

2.7.2 Strategy B: Loose PI

This method decreases the response speed of the speed PI controller which uses a speed error as the input. Power smoothing is achieved utilising the large inertia of the Wells turbine and allowing the speed to fluctuate according to equation (2.10). This strategy can be developed further by setting the desired speed at the value which maximises energy extraction for that sea-state (found to be 1,282 rpm for the sample sea-state). As the generator developed torque, $T_{em}(t)$, is prevented from entering motoring mode, this strategy results in a generated electrical power profile where the power frequently transitions to zero.

An extract of the power and speed profiles are shown in Figure 2.10. The pneumatic power profile before scaling due to the effect of turbine speed is shown for comparison.

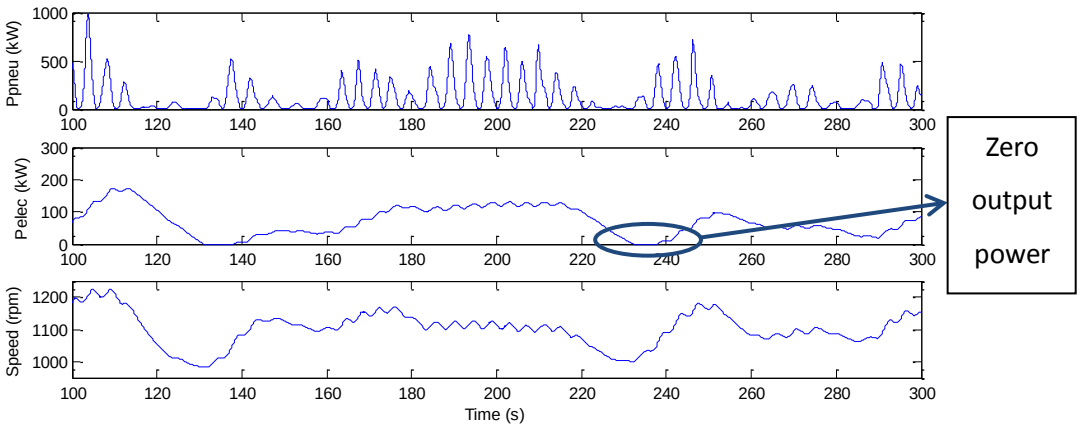


Figure 2.10: Generator power and speed for a given pneumatic power for variable speed strategy B: Loose PI

The overall control block diagram for this control strategy is shown in Figure 2.11.

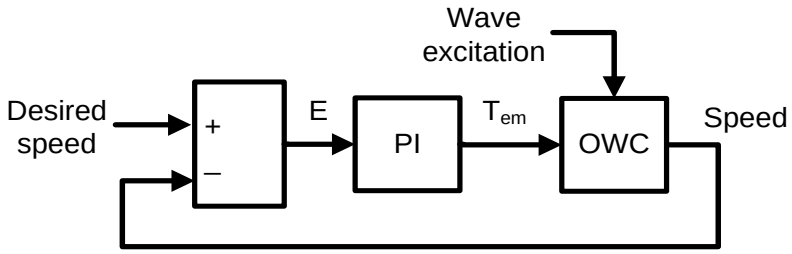


Figure 2.11: Loose PI control strategy control block diagram

The PI block used was of the following form which includes the benefits of anti-integral windup. The proportional gain is represented by K_p. The gain W_i is equal to K_i/K_p, where K_i is the integral gain in the conventional description of a PI controller. The derivations of these gain terms are evaluated in Appendix B. The values used in the modelling work were 4 for K_p and 0.167 for W_i.

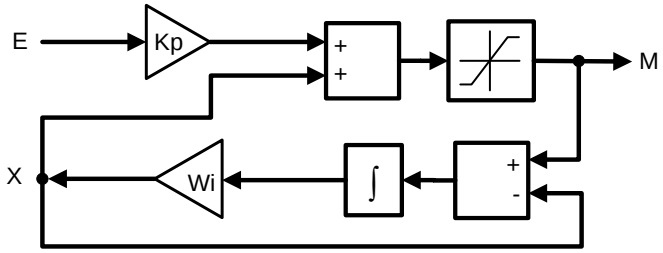


Figure 2.12: PI model block

2.7.3 Strategy C: dTem/dt

This was developed in [49] after initially examining a speed control strategy where the objective was to maintain the electric torque piecewise constant along given time intervals in the order of several wave periods. Speed was allowed to fluctuate about an average value $\hat{\omega}$ (depending on the sea-state) that ensured the best aerodynamic performance for the turbine. Results from simulations with a mathematical model for the OWC device indicated that speed limits were not maintained and fluctuations were unacceptably high from the grid perspective.

This algorithm from [49] sets the time derivative of electromagnetic torque, proportional to the rate of change of speed. An additional term is included to prevent large deviations from the set-point speed. This algorithm is shown in equation (2.11):

$$\frac{dT_{em}(t)}{dt} = k\,T_{em}\frac{|\omega(t)-\omega_{des}|}{\omega_{des}}\frac{d\omega(t)}{dt} \tag{2.11}$$

This is equivalent to equation (2.12).

$$T_{em}(t) = \int k\,T_{em}\frac{|\omega(t)-\omega_{des}|}{\omega_{des}}\frac{d\omega(t)}{dt}\,dt \tag{2.12}$$

where k is a constant, T_{em} is the electromagnetic torque of the generator, $\omega(t)$ is the turbine speed, and ω_{des} is the desired speed.

An initial non-zero value for T_{em} is set by the user. Various values of k were modelled to determine the value which maximises the efficiency for the control scheme with a given sea-state (equal to 1 for the sample sea-state). Acting on ω_{des} it is possible to establish an average speed matching the sea-state, giving a similar meaning of ω_{des} to $\widehat{\omega}$ mentioned previously.

An extract of the power and speed profiles are shown below in Figure 2.13. Like strategy B: Loose PI, this strategy requires a set-point speed. It is shown in Figure 2.13 that the further the speed deviates from this set speed (1,100 rpm for this figure), the higher the generated extracted power fluctuation in accordance with equation (2.12).

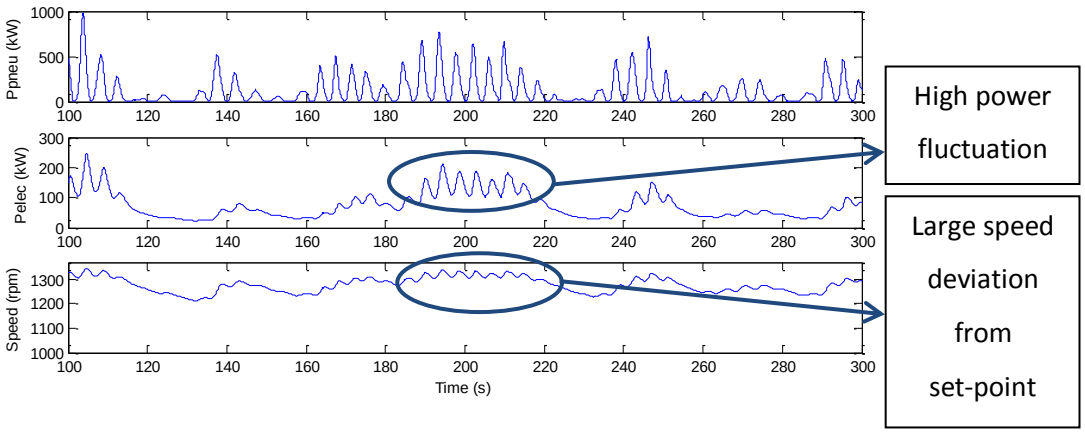


Figure 2.13: Generator power and speed for a given pneumatic power for variable speed strategy C: dTem/dt

2.7.4 Strategy D: ω²

The recommended control strategy from [49] sets the instantaneous dimensionless torque coefficient (which can be derived from equation (2.9)) to a constant. For fixed values of ρ_a this is equivalent to setting torque to a constant times speed squared. Additional terms are added to the algorithm ensuring operation within speed limits.

$$T_{em}(t) = c\left[1 + \left(\frac{\alpha\omega_{max}}{\omega_{max} - \omega(t)}\right)^{\beta}\right]\left[1 - \left(\frac{\nu\omega_{min}}{\omega(t) - \omega_{min}}\right)^{\theta}\right]\omega(t)^2 \qquad (2.13)$$

The (positive) parameters c, α, β, ν, and θ are to be optimised for a given sea-state. Setting the torque to a constant times speed squared is equivalent to setting the dimensionless torque coefficient equal to a constant.

A value of c was determined by setting α and ν to zero, eliminating the terms in brackets and determining the value of c which maximised efficiency. The values of α, β, ν, and θ, should be chosen in principle such that the terms between the square brackets remain close to unity except when $\omega(t)$ becomes close to ω_{max} or ω_{min}. These values are 0.03 for c, and the same values as those utilised in [49] for α, β, ν, and θ are selected specifically as; 0.076, 1.5, 0.019, and 4.0 respectively. The resultant profile of generator torque versus turbine speed is shown in Figure 2.14.

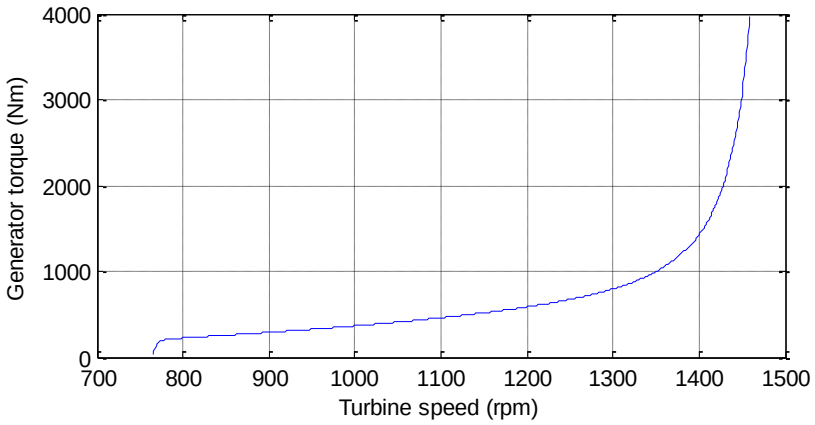


Figure 2.14: Generator torque versus turbine speed profile for strategy D: ω²

It is noted in [49] that choosing parameters that resulted in smaller oscillations of generator torque and consequently electrical power, reduced overall efficiency.

An extract of the power profiles and turbine speed are shown in Figure 2.15. Examination of the full power profile shows that the generator power increases rapidly near the maximum set speed of 1,500 rpm as shown in Figure 2.16.

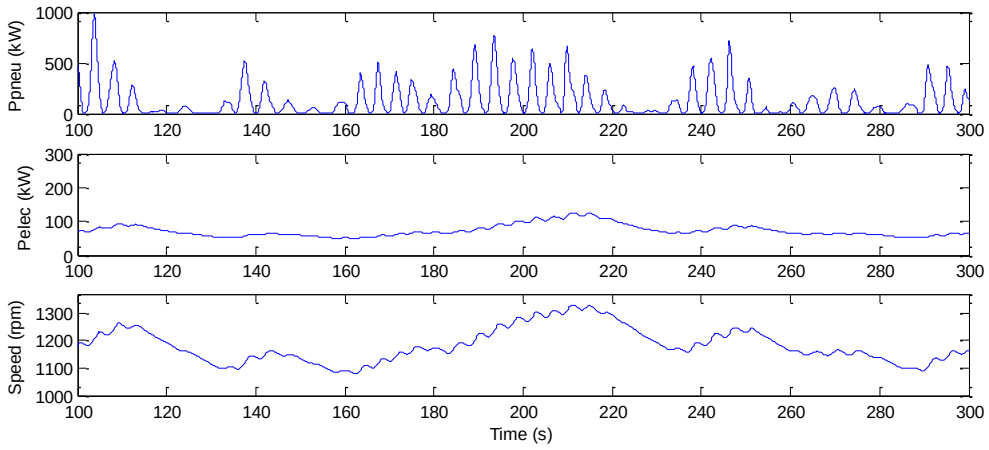


Figure 2.15: Generator power and speed for a given pneumatic power for variable speed strategy D: ω^2

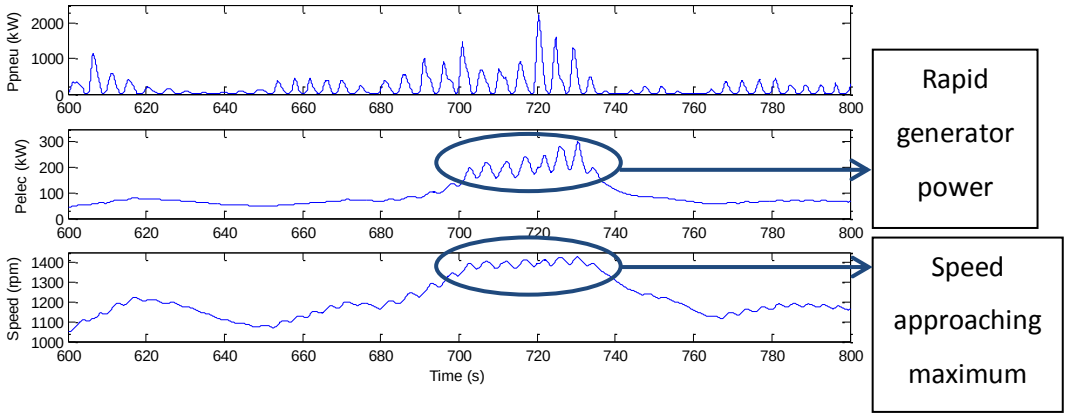


Figure 2.16: Generator power and speed for variable speed strategy D: ω^2, showing operation near maximum speed

2.7.5 Strategy E: Efficient Φ

A strategy was suggested in [50] but had not been fully modelled. This strategy is based on the efficiency curve of a Wells turbine measured over its airflow regime. The mechanical power developed in [50] is given by:

$$P_{mech} = P_{pneu}\eta \tag{2.14}$$

where η is efficiency. In this strategy, the average value of the non-dimensional flow coefficient, Φ, is maintained in the high efficiency region by controlling the speed according to equation (2.15), derived from equation (2.3).

$$\Phi_{avg}(t) = \frac{Q_{f_avg}(t)}{r_t A_D \omega_{avg}(t)} \tag{2.15}$$

where:

$$Q_{f_avg}(t) = \left(\frac{p(t)}{B_t(t)}\right)_{avg} \tag{2.16}$$

B_t is the applied turbine damping which is a constant times the instantaneous speed. The average values are moving averages and the set point average speed is adjusted using $T_{em}(t)$ as mentioned in strategy A.

A plot of the efficiency versus flow coefficient, Φ, for the turbine model was generated to determine the high efficiency operating region. The flow coefficient, Φ, is dependent on turbine speed and flow (hence pneumatic power) according to equation (2.15). Plots of efficiency versus flow coefficient were generated in the model by fixing one variable and varying the other. Figure 2.17 was obtained by fixing the turbine speed, using a ramp input of pneumatic power, and measuring the resulting non-dimensional flow and efficiency. Figure 2.18 was obtained by fixing the pneumatic power input and varying the turbine speed. The efficiency measure was obtained from the output mechanical power developed on the turbine after viscous friction losses, divided by the input pneumatic power to the turbine.

The efficiency in Figure 2.17 and Figure 2.18 is seen to increase up to a certain value, after which it decreases due to turbine stall. At lower flowrates aerodynamic drag predominates and efficiency becomes negative.

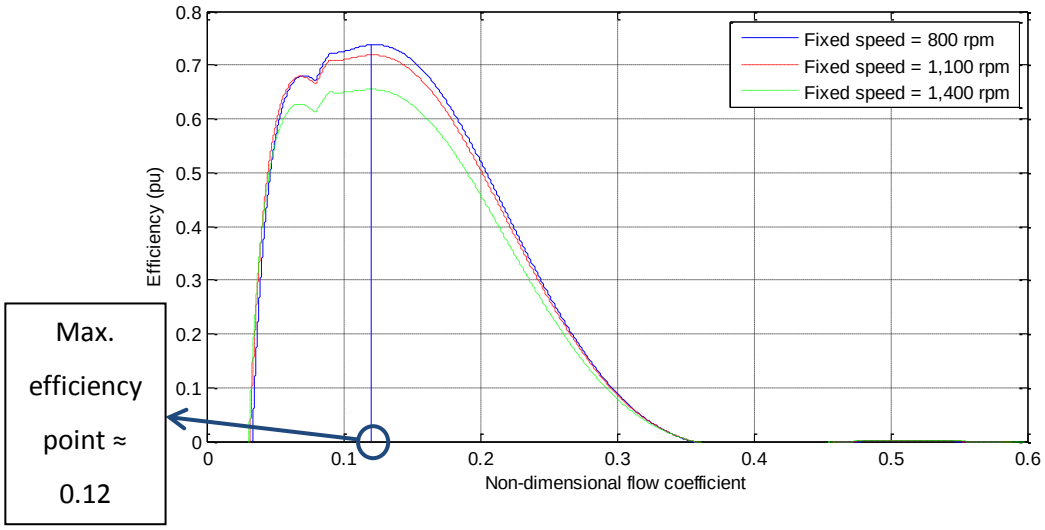


Figure 2.17: Efficiency versus non-dimensional flow coefficient, Φ, for the model, fixing the turbine speed and using a ramp pneumatic power input

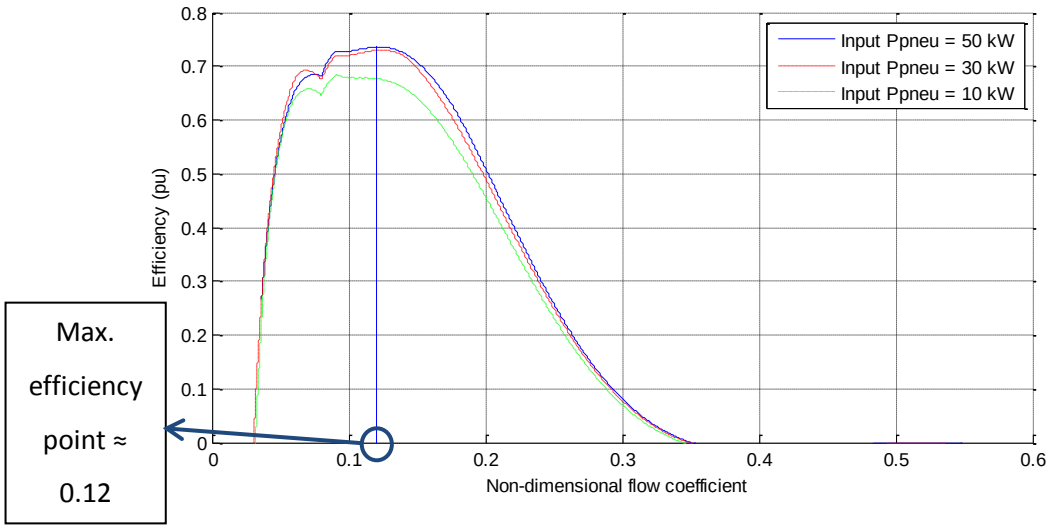


Figure 2.18: Efficiency versus non-dimensional flow coefficient, Φ, for the model, fixing the pneumatic power input and varying the turbine speed.

While slightly different profiles of efficiency versus flow coefficient are extracted dependent on the fixed speed or fixed input pneumatic power utilised, the profile is very similar in each plot and a clear high efficiency operating range can be seen. These graphs suggests that by controlling the average value of the non-dimensional flow coefficient, Φ, to be close to 0.12, that maximum efficiency will result. It is also suggested in the algorithm that different constant values could be assigned for different

sea-states for the desired $\omega_{avg}(t)$ from equation (2.15). The control strategy uses the following boundary conditions:

- $\Phi_{avg_min} \leq \Phi_{avg}(t) \leq \Phi_{avg_max}$
- $\omega_{avg_min} \leq \omega_{avg}(t) \leq \omega_{avg_max}$

If the boundary conditions are not satisfied, the generator torque will be adjusted until $\Phi_{avg}(t)$ returns to the optimum point and the system will then operate at a new $\omega_{avg}(t)$.

Preliminary modelling work was performed to test the validity of this strategy on the turbine model utilising two different ideal input pneumatic power profiles described below.

1. The first input pneumatic power profile is the absolute value of a sine wave with amplitude 100 kW and frequency 0.15 Hz. Maximum efficiency occurred at an average Φ of 0.102 and a speed of 890 rpm. A plot is shown in Figure 2.19 with a running 30 second average value for Φ.

2. A squared sinusoid was inserted with an amplitude of 100 kW and a frequency of 0.15 Hz as the second input pneumatic power profile. Maximum efficiency occurred at an average Φ of 0.088 and a speed of 870 rpm. A plot of this profile is shown in Figure 2.20 with a running 30 second average of Φ.

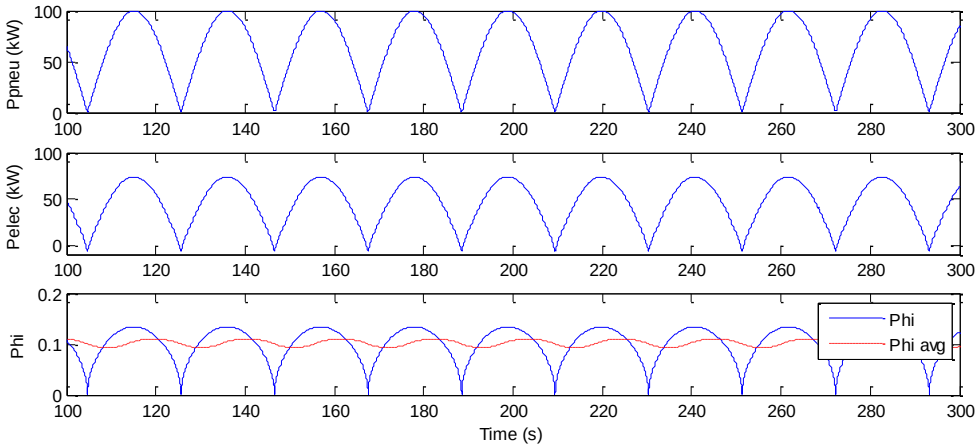


Figure 2.19: Ppneu, Pelec and Phi versus time for pneumatic power profile with an absolute sine wave shape

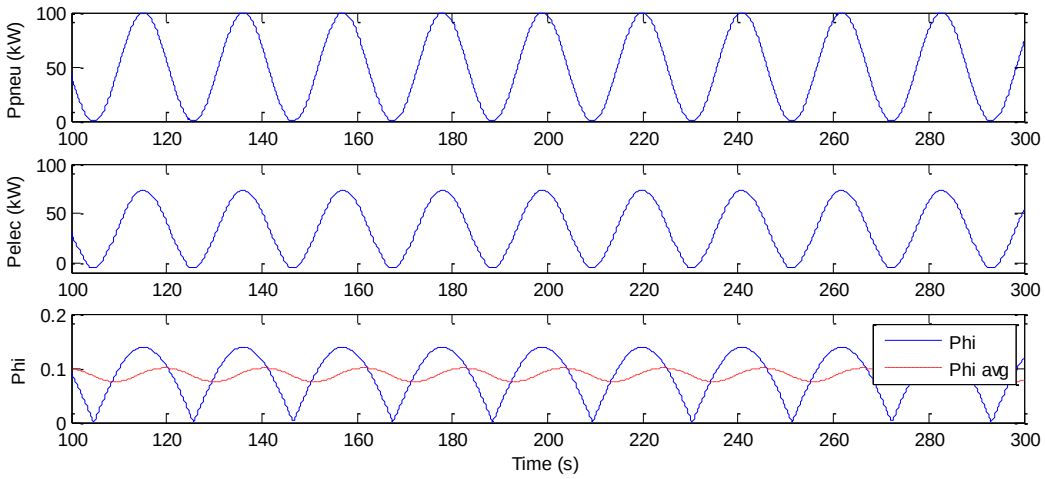


Figure 2.20: Ppneu, Pelec and Phi versus time for pneumatic power profile with a sine squared shape

These differences in what is the most efficient value of Φ (phi) to use are dramatic when we compare two different basic power profiles. The initial work suggested that the most efficient value to use for Φ_{avg} was 0.12 (from Figure 2.17 and Figure 2.18), while the two different pneumatic power inputs above were most efficient at Φ_{avg} values of 0.102 and 0.088, 15% and 27% respectively of a difference from the initial value. The efficiency versus flow coefficient curves in Figure 2.17 and Figure 2.18 were extracted using a fixed value or fixed slope for pneumatic power input, whereas the pneumatic power input profiles examined in Figure 2.19 and Figure 2.20 are absolute sine waves or squared sine waves. The efficiency curves are also seen to vary in Figure 2.17 with different speeds and to vary in Figure 2.18 with different values of pneumatic power. This might explain the maximum efficiency occurring at different values for Φ_{avg} in Figure 2.19 and Figure 2.20 than to the expected 0.12. Also, it is noted that if the set speed is changed to 700 rpm to produce a Φ_{avg} of 0.12 (max. efficiency according to Figure 2.17 and Figure 2.18), for the squared sinusoid power profile, 11% less electrical power is extracted from modelling.

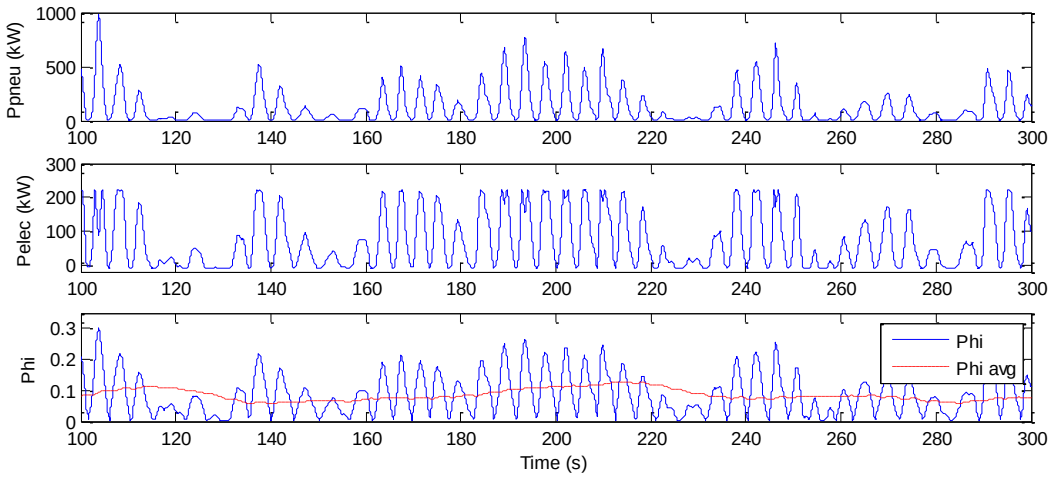


Figure 2.21: Ppneu, Pelec and Phi versus time for fixed speed 1,100 rpm with pneumatic power profile

The above plots indicate that a running average value of non-dimensional flow, Φ, is not well suited as waves often occur in groups, and a running average introduces a delay and a decrease in bandwidth. This would lead to a system that is too slow to respond and take advantage of these waves.

For these reasons and the practical difficulty in implementing an efficient measurement of flow in a device, further simulation work was not carried out and this variable speed strategy was disregarded from analysis.

2.7.6 Strategy F: ω^{β}

This was developed in [26], after first examining the control strategy proposed in [49] and described in Section 2.7.4 describing Strategy D: ω^2 which is based on dimensional analysis. It is stated in [26] that if incompressible air flow is assumed and the effects due to Reynolds number and Mach number variation are neglected, the instantaneous value of the aerodynamic efficiency of a given turbine is known to be a function only of T_{mech}/ω^2, where T_{mech} is the aerodynamically produced torque on the turbine rotor and ω is rotational speed. This was used in [49] to propose a control algorithm of $T_{em}(t) = c\,\omega(t)^2$. This approach aimed at keeping the time-averaged value of the turbine aerodynamic efficiency at its maximum, but ignored the effect of varying speed on the hydrodynamics of the wave energy converter, and did not propose any non-empirical method for determining the value of the proportionality constant c. If the

effect of varying speed on the wave energy absorption is to be considered, the relationship between T_{em} and ω is expected to become more complicated [26].

The control strategy then developed in [26] consists of two parts where part one relates torque to a power of speed as shown in equation (2.17).

$$T_{em}(t) = k\omega(t)^{\beta} \tag{2.17}$$

This was developed by measuring the average mechanical power produced at a fixed machine speed. The fixed machine speed maximising the average power for each of the examined sea-states was found and these speeds and powers were plotted. Results from two sample sea-states are shown in Figure 2.22, and the maximum average powers for the full range of sea-states are shown in Figure 2.23 on a log plot.

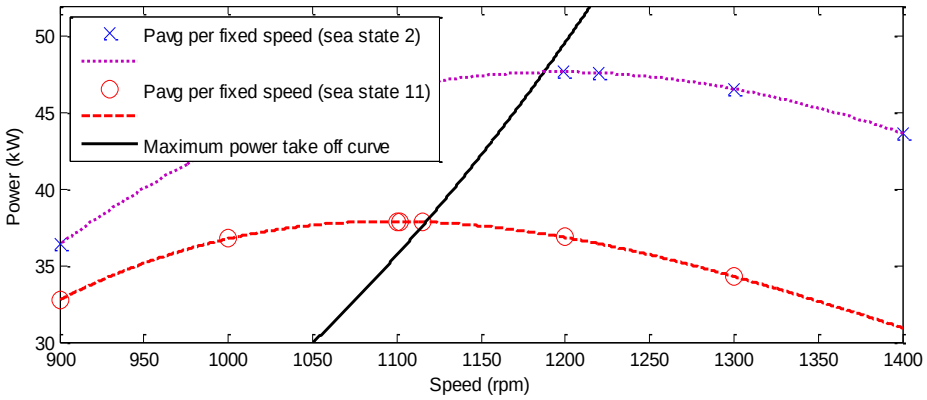


Figure 2.22: Average mechanical power versus fixed speed for two sea-states and maximum power curve

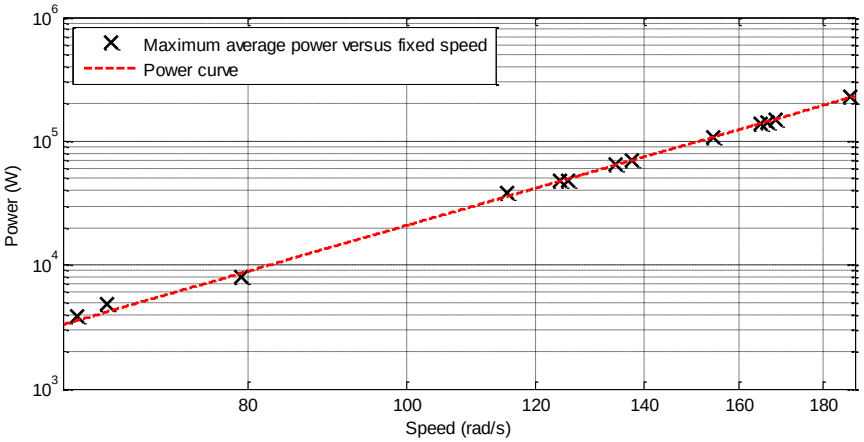


Figure 2.23: Maximum average power versus fixed speed for the examined sea-states and maximum power curve

Using the curve fitting tool in Matlab with these maximum average powers and corresponding fixed speeds, the empirical power coefficients in equation (2.18) were derived (producing an R-square value of 0.9996). This curve is also shown in Figure 2.22 and Figure 2.23.

$$P_{gen} = 0.0005307\omega^{3.797} \tag{2.18}$$

It is remarkable that this control law seems insensitive to wave climate. It is also noted there is a power factor difference in the control law of 3.797 from the cube in to the power available across a wind turbine of $P_{wind} = kv^3$, where v is the wind speed.

The motivation for this curve to be utilised as a control law could be discussed as follows: While the examined sea-states are representative of the wave climate for a given location, these sea-states could be replaced by a larger set of sea-states of smaller duration. It is expected that these shorter sea-states would also fit along the same curve. By setting the generator power to this curve according to turbine speed, the device will operate efficiently without need to predict and estimate the current sea-state.

The second part of the control scheme limits the generator power as shown in equation (2.19) and ensures that the turbine does not over-speed, avoiding mechanical stress and possible failure.

$$P_{gen}(t) = \left[{P_{max}}^2 - J\left|\frac{dP_{em}(t)}{dt}\right|({\omega_{max}}^2 - \omega(t)^2)\right]^{\frac{1}{2}} \tag{2.19}$$

The motivation and derivation of this equation is shown in Appendix C. The oscillations in electrical power output from an OWC WEC can easily be absorbed by a large electrical grid, but may introduce unacceptable disturbances into a small isolated grid. The maximum allowed rate of change of power onto the grid is specified in $\frac{dP_{em}(t)}{dt}$. The value used for $-J\left|\frac{dP_{em}(t)}{dt}\right|$ was set at 100 MW s^{-1} kg m^2 as per [26]. The maximum power rating for the generator was set at the peak mechanical input power at full speed (570 kW), to ensure no acceleration beyond this point.

The control algorithm sets the generator power to the maximum value evaluated from equation (2.18) and equation (2.19) according to the turbine speed, as shown in Figure 2.24.

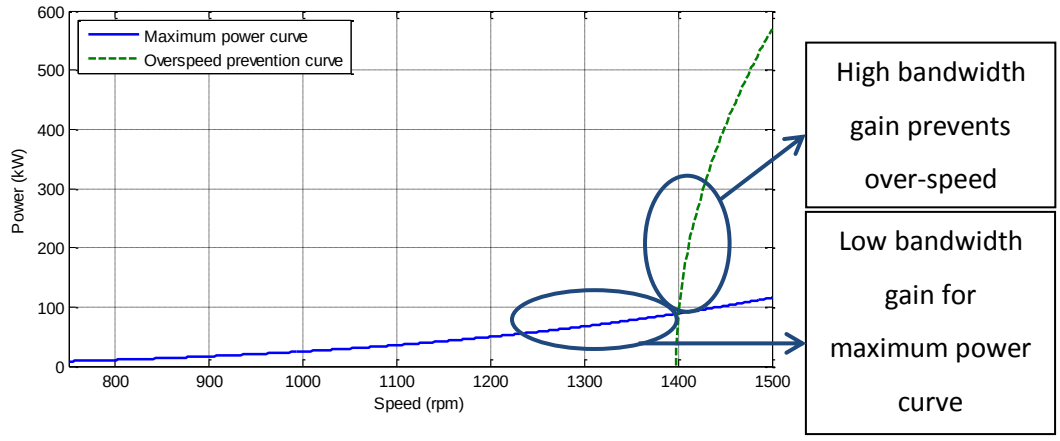


Figure 2.24: Speed control power curve of generator power versus speed

An extract of the power profiles and turbine speed are shown in Figure 2.25.

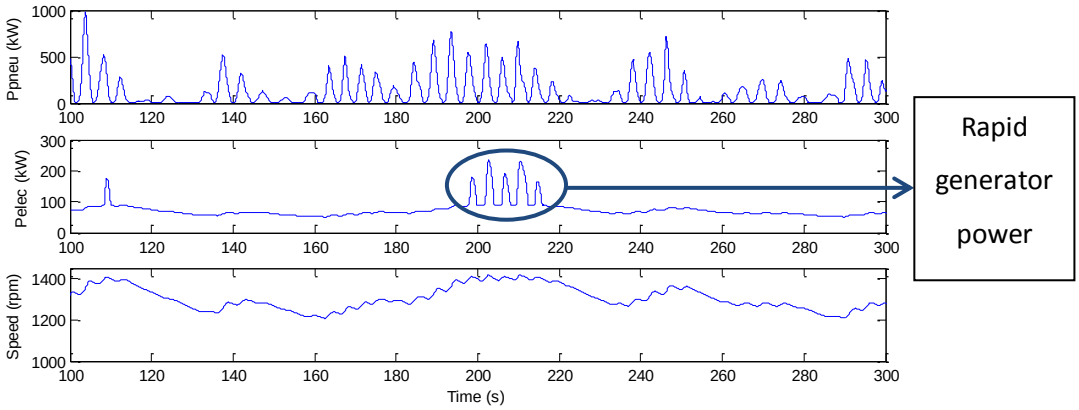


Figure 2.25: Generator power and speed for a given pneumatic power for variable speed strategy F: ω^{β}

The electrical power is relatively constant compared to the pneumatic input power, except for peaks when the maximum power deviation equation (2.19) comes into effect. This occurs at around 1,400 rpm. The increased power draw lowers the speed into the region governed by equation (2.18) and as the speed is now at this equation boundary, chattering occurs.

To prevent this chattering, a switched controller is used where the local maximum generator torque achieved is maintained until the speed drops by a predetermined level (this hysteresis value was set at 80 rpm). The resulting power profile and turbine speed are shown in Figure 2.26.

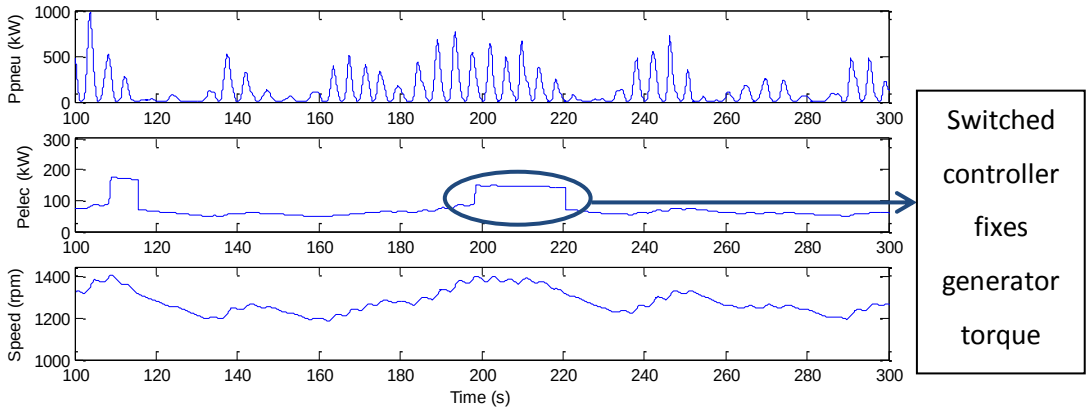


Figure 2.26: Generator power and speed with the switched controller to prevent chattering for a given input pneumatic power

2.8 Comparison of variable speed schemes

Each strategy was compared using the most frequently occurring sea-state as the input to each model. This had an average pneumatic power input of 119 kW, an occurrence percentage of 31.85%, and the data was over 30 minutes in duration. The peak to average value of input pneumatic power is 18.6 for this sea-state.

The level of power smoothing was indicated by measuring the standard deviations of the different powers in the system. The standard deviation is a measure of the variation of a quantity from the mean. It is given in equation (2.20) as:

$$\sigma = \sqrt{\frac{1}{N}\sum_{i=1}^{N}(x_i - \mu)^2} \tag{2.20}$$

where μ is the mean value, x_i is a discrete data point, and N is the total number of data points in the measurement. The mean value μ is found using equation (2.21).

$$\mu = \frac{1}{N}\sum_{i=1}^{N} x_i \tag{2.21}$$

While the standard deviation over a running time window can be a convenient, and perhaps a more appropriate measure in an ocean energy application where the available power varies over periods of waves and longer, it is felt that a single overall standard deviation figure is more useful and allows a valid comparison.

Another measure of power smoothing was the peak to average value of the output electrical power. Finally, maximum and minimum speeds were noted as well as the maximum generator torque. The results of the variable speed comparisons are given in the next section.

2.9 Results

To summarize: Each scheme was modelled using the same sea-state, the most frequent sea-state for the location examined. Turbine inertia was modelled at 595 kg m^2 and a viscous friction coefficient of 0.25 N m s was utilised. The desired speed was set at 1,100 rpm, and maximum and minimum speed limits were 1,500 rpm and 750 rpm respectively.

The modelling work produced the results shown in Table III. Fixed speed cases at the desired speed, the maximum rated speed, and the most efficient fixed speed for the sea-state were compared. Also loose PI control was modelled at the desired speed of 1,100 rpm as well as at the most efficient fixed speed of 1,282 rpm for comparison.

Once every strategy was tailored for the WEC and given sea-state, efficiency performance was similar for each. Some notes can be made for each strategy after examining the numbers and the earlier power and speed profiles.

- **Strategy A: Fixed speed**

  The higher the fixed speed, the higher the generator torque required to prevent further speed increase. This is due to turbine stall occurring at a higher value of input pneumatic power.

  To prevent speed deviations, the generator would need to operate in motoring mode to overcome friction losses in times of low wave energy. There is also the requirement to change the desired fixed speed dependent on the current sea-state.

Table III: Comparison of the examined variable speed strategies

Strategy	**A: Fixed speed**	**A: Fixed speed**	**A: Fixed speed**	**B: Loose PI**	**B: Loose PI**	**C: dT_{em}/dt**	**D: ω^2**	**E: Efficient Φ**	**F: ω^β**	**F: ω^β switched controller**
Description	1100 rpm	1282 rpm	1500 rpm	1100 rpm	1282 rpm	$\frac{d\omega}{dt}$	$c\,\omega^2$	Φ_{avg}	$k\omega^\beta$	$k\omega^\beta$
Efficiency (%)	50.7	55.0	50.4	53.0	56.2	55.6	54.0		54.9	**55.0***
Peak to average P_{elec}	3.7	5.4	9.4	3.6	4.5	4.9	4.6		5.5	**4.6***
SD of P_{mech} (pu)	0.42	0.54	0.62	0.45	0.56	0.55	0.49		0.55	0.55
SD of P_{elec} (pu)	0.42	0.54	0.62	0.29	0.37	0.29	0.16		0.21	**0.23***
Measured ω_{max} (rpm)	1100	1282	1500	1240.2	1457.9	1356.4	1427.3		1440.4	1427.7
Measured ω_{min} (rpm)	1100	1282	1500	939	1111.9	1096.2	814.8		940.7	940.7
Measured T_{em_max} (Nm)	1951.9	2651.3	3629.6	1812.7	2074.9	2303.5	2001.1		2408	2028.9

**These values show the simulated power smoothing performance of the chosen variable speed scheme*

No power smoothing is achieved with this strategy as the standard deviations of mechanical and electrical power are the same.

- **Strategy B: Loose PI**

This strategy is seen to be the most efficient when the set speed is set to the value which corresponds to efficient PTO operation for that sea-state. This could prove difficult to implement practically but the strategy is simple to design and is a robust control method that will likely remain an appealing option for many WEC developers.

- **Strategy C: dTem/dt**

While this strategy demonstrated good efficiency, determining the correct set speed, and value for the constant k, would be difficult in real-time. Also, the control equation contains a derivative that is very susceptible to noise, reducing the power smoothing capability.

- **Strategy D: ω^2**

This demonstrated excellent power smoothing performance, but parameters might need to be tuned for each sea-state. When the speed approaches a turbine speed limit, the power variance is seen to increase dramatically and mirror the input wave profile.

- **Strategy E: Efficient Φ**

Practical difficulties in measuring Φ, the very low response time, and sensitivity to small changes in Φ on performance with slightly different wave profiles, prevented complete tuning and full simulation work. Therefore, this suggested variable speed strategy was disregarded from analysis

- **Strategy F: ω^β**

This is seen to be a very efficient strategy, and has the advantage that once the gain and power of the control equation are determined, is applicable for all sea-states in the given location.

Chattering of the output electrical power occurred with the original strategy when the speed tended towards the boundary of control equations (2.18) and (2.19). A

switched controller was introduced to remove some of these peaks and this was found to further smooth the power profile as seen in Figure 2.26. This smoothing capability is not captured in the standard deviation measure of 0.23 pu for electrical power which was an increase on the standard deviation of 0.21 pu before the switched controller was added. This is because the switched controller introduces a large smooth peak of significant duration which is far from the mean power. Before the switched controller was added, the rapid power fluctuations were closer to the mean power resulting in a smaller standard deviation measure according to equation (2.20). The smoothing effect of the switched controller is observed by comparing Figure 2.25 and Figure 2.26.

2.10 Conclusion

It is clear from these results that major variations in power are an inevitable feature of OWC WEC devices.

This chapter investigated variable speed control strategies from leading papers, for a full-scale offshore Oscillating Water Column (OWC) Wave Energy Converter (WEC) incorporating a Wells turbine. A developed Simulink model of the examined WEC was utilised to compare five different control schemes as well as comparing them to fixed speed cases.

The variable speed strategy that produced the best performance, when comparing each using sea-state data from the most frequently occurring sea-state as an input to the model, was variable speed strategy F: ω^{β}. This is based on [26] and consists of two parts, where part one relates torque to a power of speed, and the second part limits the generator power and ensures that the turbine does not over-speed. Chattering of output power occurs when the speed tends towards the boundary of the control equations. A switched controller was used to remove this power chattering and resulted in only occasional large smooth peaks in the output generator electrical power profile.

This variable speed strategy produced an efficiency of 55% for the sea-state comparing input pneumatic power to output electrical power for an ideal generator, and taking account of friction. The measured standard deviation was 0.23 pu, using the standard deviation of the pneumatic power profile as a reference. The peak to average electrical power was 4.6 while the peak to average value of input pneumatic power is 18.6 for this

sea-state. These figures demonstrate the power smoothing performance of this strategy from modelling of this examined WEC.

Over the past number of years, significant progress has been made in both the performance and cost of supercapacitor (SC) devices, to such an extent that they may now be viable for application in high power renewable energy systems such as this.

It will be suggested in the next chapter to further smooth out these power peaks using SCs.

Chapter 3 Supercapacitor (SC) testing and supercapacitors (SCs) for power smoothing

3.1 Objectives

This chapter investigates power smoothing in a full-scale offshore oscillating water column (OWC) wave energy converter (WEC) by integrating supercapacitors (SCs) with the inertia of a Wells turbine controlled at variable speed. Modelling work is extended beyond that carried out in Chapter 2, where variable speed schemes were examined, and a SC system is sized to smooth and reduce the grid peak power for a 570 kW (peak) system. Long component lifetime is a requirement for offshore WECs. Hence, a computer-controlled test rig has been built to evaluate and validate SC lifetimes to manufacturer's specifications and determine application lifetime. Cycle testing is carried out on individual SCs at room temperature and also at rated temperature utilizing a thermal chamber and equipment interconnected by the general purpose interface bus (GPIB) and programmed by the MathWorks computing environment Matlab. Application testing is carried out using time-compressed scaled-power profiles from the model to allow a comparison of lifetime degradations. The SCs, under standard testing at ambient and rated temperature, and application testing at ambient temperature, have undergone approximately 10 million, 9 million, and 1 million cycles respectively. The results demonstrate cycle lifetimes in excess of manufacturer specifications and potential for integration into a WEC.

3.2 Introduction

This chapter examines power smoothing in a single offshore WEC by developing an energy storage system (ESS) utilizing the turbine inertia in a variable-speed strategy as described in Chapter 2 and smoothing the generator output power with SCs. Actual sea-state data is used with an experimentally derived WEC model to obtain the full-scale power flows and system speed response. From this, a SC system is sized and integrated into the model developed in the MathWorks simulation environment Simulink.

While it has been shown that variable-speed operation of WEC turbines can contribute to power smoothing, this application with SCs has yet to be examined. SCs are a proven robust technology characterized by a large power density that is currently unavailable from batteries. However, by comparison, SCs have a significantly lower energy density. Practical operation at sea has been demonstrated in wave measurement buoys [40].

Offshore systems require a high level of reliability due to the obvious difficulties and high cost associated with access for maintenance purposes [51]. These difficulties include working in an unstable environment for floating WECs, docking issues, and the ready availability of equipment and labour on days with an acceptably low sea-swell. Hence, all on-board subsystems should have long lifetime characteristics that at least match the typical desired intervals for non-routine, disruptive maintenance for offshore WECs. Over this time period the number of power cycles to be smoothed is quite large, and, while SC cycle lifetimes are specified from 500,000 to one million, results of documented cycle testing reached at most 150,000 [52] (or 450,000 without *y*-axis scaling [53]), as shown below in Figure 3.1 and Figure 3.2.

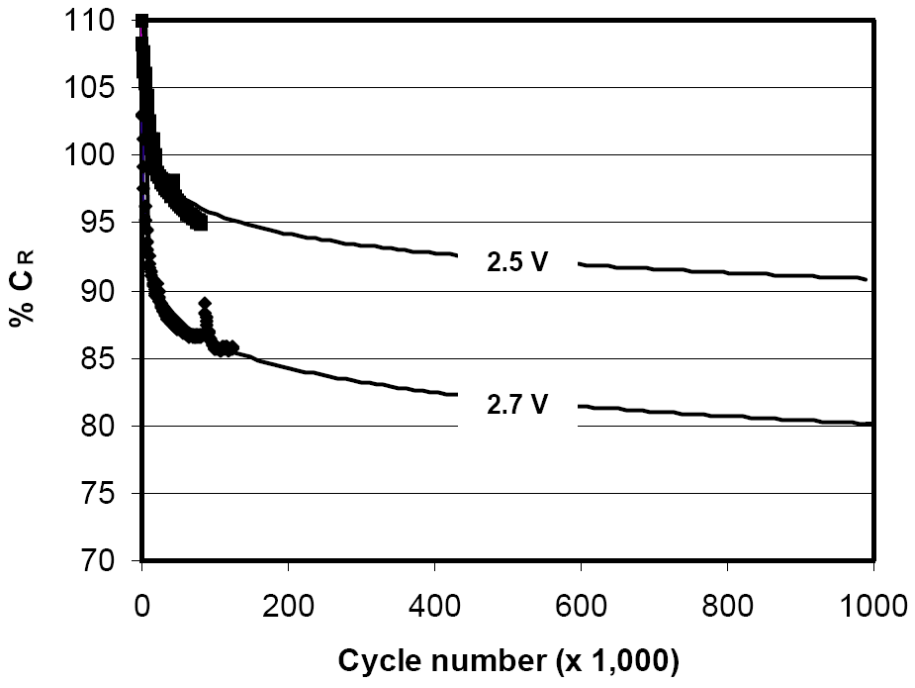


Figure 3.1: Results of available lifecycle testing of SCs at 2.5 V and 2.7 V from Maxwell Technologies [52]

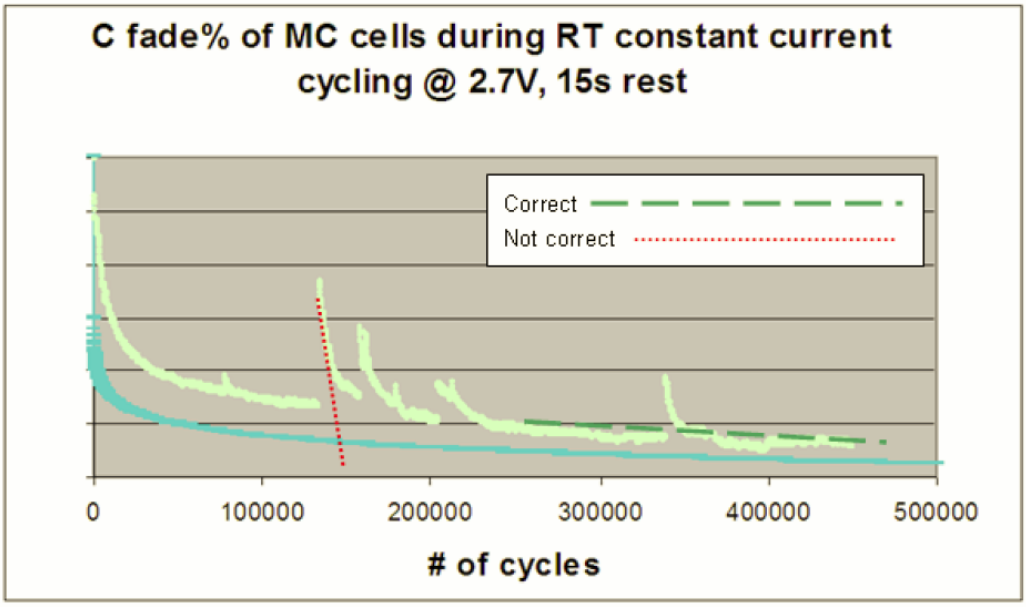


Figure 3.2: Results of available lifecycle testing of SCs from Maxwell Technologies [53]

Figure 3.2 shows the degradation of capacitance versus number of cycles available from the manufacturer of the SCs tested in this chapter. As rated cycle lifetime is generally specified as 20% below rated capacitance after 500,000 cycles, it is expected that the capacitance in Figure 3.2 agrees with this specification. Lifetime estimation based on linear trends of capacitance is also shown as the "correct" and "not correct" lines, and it is important to base this linear estimation after the initial exponential capacitance drop that occurs at the start of testing. This is discussed further in Section 3.7.1.

This chapter optimizes the energy storage system by integrating the turbine inertia and SCs using a Simulink model. Test setups are then built to establish the SC cycle lifetimes under the standard and application test conditions. SC standard testing at rated temperature is also carried out to determine the extent to which elevated temperatures affect lifetime. This life testing will help determine if SC cycle lifetime is a limiting factor in the application of power smoothing in offshore WECs.

Section 3.3 describes the system model and speed control system used in conjunction with a SC power smoothing strategy. The standard lifetime testing, standard lifetime testing at rated temperature, and application testing are presented in Section 3.4, Section 3.5, and Section 3.6 respectively. Experimental results are shown in Section 3.7 and conclusions are drawn in Section 3.8.

3.3 Supercapacitors (SCs) as an offshore energy storage device for power smoothing in conjunction with turbine inertia

The implemented variable speed control strategy is discussed in Chapter 2 in Section 2.7.6, and is termed Strategy F: ω^{β} with switched controller. As shown in Figure 3.3, the inherent nature of the OWC technology and implemented control strategy is such that the generator electrical power contains large peaks that occur only occasionally. It is proposed to further smooth this power with SCs connected, via a power electronic dc-dc converter, to the direct current (dc) bus of the back-to-back converter which couples the generator to the grid.

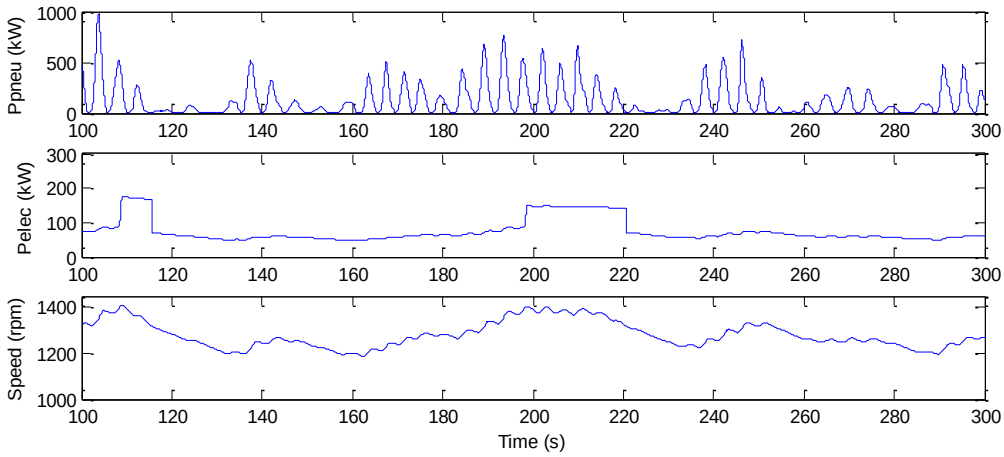


Figure 3.3: Generator power and speed for variable speed strategy F: ω^{β} with the switched controller to prevent chattering for a given input pneumatic power profile from sea-state 6

The number of generator power peaks using this control strategy for each sea-state was measured over the full simulation time of about 30 minutes. These numbers were multiplied by the sea-state's percentage occurrence to evaluate the total number of generator peaks expected over the 30 minute simulation time. The results in Table IV were obtained. The average wave power in each sea-state is also shown. It was assumed that the WEC would not be operational in very low or high energy sea-states, thus as shown in Table IV, some sea-states are not used. Therefore, the device would be functioning over 70% of the time.

Table IV: Generator power peaks for each sea-state using control strategy F: ω^{β} with the switched controller

Sea-state	Occurrence % of all sea-states	Pwave avg (kW)	Generator peaks from simulation	Total peaks due to sea-state over simulation time
2	5.95	257	2	0.12
4	11.04	309	15	1.66
5	0.64	858	57	0.36
6	31.85	386	11	3.50
7	3.41	1072	49	1.67
9	9.32	1286	40	3.73
11	6.11	515	2	0.12
13	4	1786	2	0.08
Total	72.34			11.24

Each sea-state file gives 1,809 seconds of real-time information and extending the average power peak rate from Table IV over the simulation time leads to 22.3 peaks per hour, and approximately 981,000 peaks of electrical power to be smoothed over the 5 year interval for non-routine disruptive maintenance. This number of peaks is within the specified cycle lifetime of some SC modules.

The control strategy attempts to maintain the SCs at their lowest operational voltage (half-rated voltage) to make available the SC energy capacity for absorbing power peaks. Once the generator power exceeds a predetermined value (dependent on the sea-state), the SCs prevent any excess power flowing to the grid and absorb the difference. Once the input power drops below this value, the SCs maintain this power to the grid until the minimum voltage is achieved. A voltage hysteresis band prevents discharge of the SCs until the band is exceeded to ensure no rapid charging and discharging cycles occur (this was set at 15 V above minimum).

The SCs are sized for the maximum energy sea-state of the WEC, which produces 294 kW of pneumatic power on average and 141 kW of mechanical power on average. Sizing was based on multiples of the large SC module, the BMOD0063 P125 63 F, available from Maxwell Technologies Inc. (a manufacturer and market leader in SCs), with parameters given in Table V. These modules utilise SCs of the same technology as the SCs under test (described in Sections 3.4, 3.5, and 3.6). Two modules in series give a voltage range of 125 V - 250 V and five of these parallel strings satisfy all module ratings, and limit the maximum output grid power to 175 kW for the sea-state producing

maximum energy. Due to the physical size and significant ballast of the WEC, the SC system size is not necessarily a constraint: Taking dimensions of 1 m for length (with space for air flow through fans), a width of 42.5 cm, and a height of 30.5 cm (allowing gaps between modules with legs removed) gives a total volume of 1.3 m^3 for 10 modules. The total SC system mass is approximately 600 kg.

Table V: Parameters of the large SC module [54]

The BMOD0063 P125 module from Maxwell Technologies Inc.	
Capacitance (F)	63
Max continuous current (A)	150
Max peak current, 1 second (A)	750
R_{esr}, DC (mΩ)	18
Cycle life (cycles)	1,000,000
Mass (kg)	59.5

The levels of power smoothing were indicated by measuring the standard deviations of the powers in the system over the simulation time, using the input pneumatic power as a reference. The modelling work produced the results in Table VI for the most commonly occurring sea-state with the grid power limited to 145 kW. This modelling work assumes an ideal generator and energy storage device. This assumption leads to higher efficiency data for the system from modelling than would be expected from experimental testing. The average pneumatic power is 119 kW for this sea-state.

Table VI: Performance data of variable speed strategy with SCs from simulations

Strategy	**F: ω^{β}**	**F: ω^{β} + switched controller**	**F: ω^{β} + switched controller + SCs**
Efficiency (%)	54.9	55.0	**55.0***
Peak to avg P_{mech}	6.9	6.8	6.8
Peak to avg P_{elec}	5.5	4.6	4.6
Peak to avg P_{grid}	5.5	4.6	**2.2***
SD of P_{elec} (pu)	0.21	0.23	0.23
SD of P_{grid} (pu)	0.21	0.23	**0.18***
Measured ω_{max} (rpm)	1440	1428	1428
Measured ω_{min} (rpm)	941	941	941
Measured T_{em_max} (Nm)	2408	2029	2029

**These values show the simulated power smoothing performance of the variable speed scheme*

The major advantage of integrating SCs and turbine inertia in this power smoothing scheme is the reduction of the peak-to-average grid power. An extract of the power profiles and turbine speed are shown in Figure 3.4.

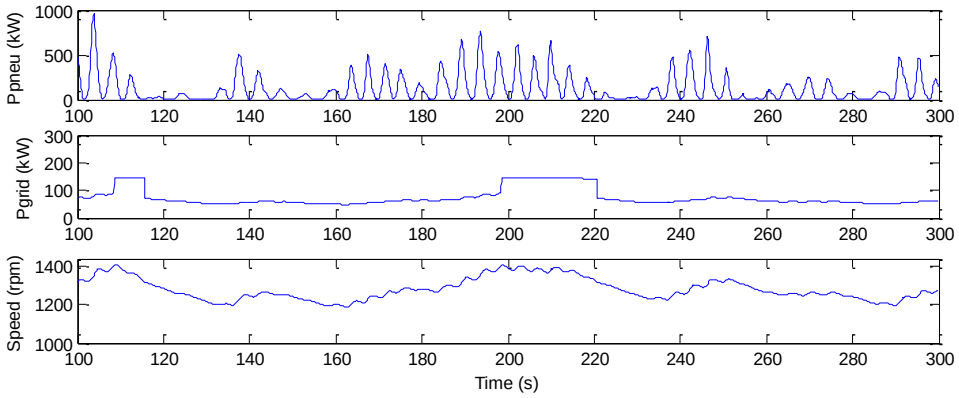


Figure 3.4: Input pneumatic power, grid power and turbine speed with SCs and the switched controller added to prevent chattering for a given input pneumatic power profile

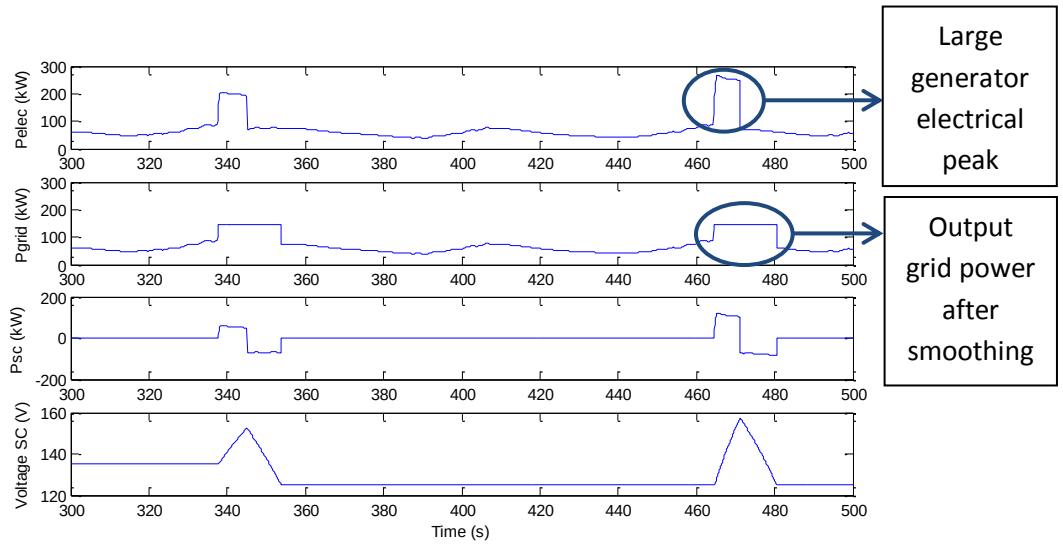


Figure 3.5: Generator power, grid power, SC power and SC voltage with the switched controller and SCs added for the most frequently occurring sea-state

The effect of the SC power smoothing strategy with the variable speed scheme including switched controller is not illustrated in Figure 3.4. However, Figure 3.5 shows the power profiles for the same sea-state over a different time period as well as the corresponding SC voltage. The hysteresis band of the SC controller is evident as it discharges back to the minimum voltage once the maximum value of (140 + 15) V is reached.

3.4 Standard cycle lifetime testing at ambient temperature

Supercapacitors (SCs) do not have a hard failure point to indicate end of life, but rather a maximum parameter deviation, typically a reduction of capacitance of 20% and an increase in the equivalent series resistance (ESR) of 100%. While SC lifetime has been tested before, it has typically been accelerated testing, where elevated voltages and temperatures were used. Based on changes in lifetime at small deviations of voltage and temperature at elevated values, typical lifetimes at normal conditions were determined from extrapolations [55], [56], [57]. Maxwell Technologies Inc. provide some results from its lifetime testing but only up to 150,000 cycles, and then extrapolate to one million [52], shown in Figure 3.1 (or up to 450,000 cycles without *y*-axis scaling [53], shown in Figure 3.2). Also, the company's testing procedure provided 15 seconds of rest between every cycle.

To decrease cycle testing time, the smallest capacitance SC available from Maxwell Technologies Inc. at the time (the BCAP0005 P270) was chosen for lifecycle testing. Maxwell Technologies Inc.'s range of SC capacitance is currently 1 F to 3000 F. The datasheet for this SC is shown in Appendix D. Thirty BCAP0005 P270 SCs were characterized and the results are shown in Table VII. Each SC is charged at the rated current of 1.6 A to the rated voltage of 2.7 V, undergoes a five second rest period (approximately five time constants), and the voltage and time are measured. The SC is then discharged at rated current to half rated voltage, and another five second rest period takes place before measuring the final voltage. Plots of this characterization profile are shown in Figure 3.6, and the capacitance and ESR are evaluated according to equations (3.1) and (3.2).

$$C = \frac{I_{rated} t_d}{V_{start} - V_{finish}} \tag{3.1}$$

$$R = \frac{V_{finish} - V_{rated}/2}{I_{rated}} \tag{3.2}$$

Table VII: Initial characterisation results of 30 BCAP0005 P270 SCs from Maxwell Technologies

SC number	ESR Ω (avg. over cycles 5 to 10)	Capacitance F (avg. over cycles 5 to 10)
1	0.116	5.60
2	0.101	5.71
3	0.110	5.87
4	0.103	5.87
5	0.111	5.64
6	0.098	5.77
7	0.105	5.71
8	0.105	5.86
9	0.108	5.59
10	0.099	5.70
11	0.108	5.79
12	0.101	5.76
13	0.108	5.77
14	0.101	5.91
15	0.104	5.83
16	0.105	5.75
17	0.108	5.72
18	0.112	5.66
19	0.106	5.76
20	0.105	5.72
21	0.103	5.74
22	0.100	5.77
23	0.109	5.72
24	0.103	5.77
25	0.108	5.80
26	0.103	5.76
27	0.103	5.83
28	0.107	5.95
29	0.106	5.80
30	0.107	5.72
Mean	**0.105**	**5.76**

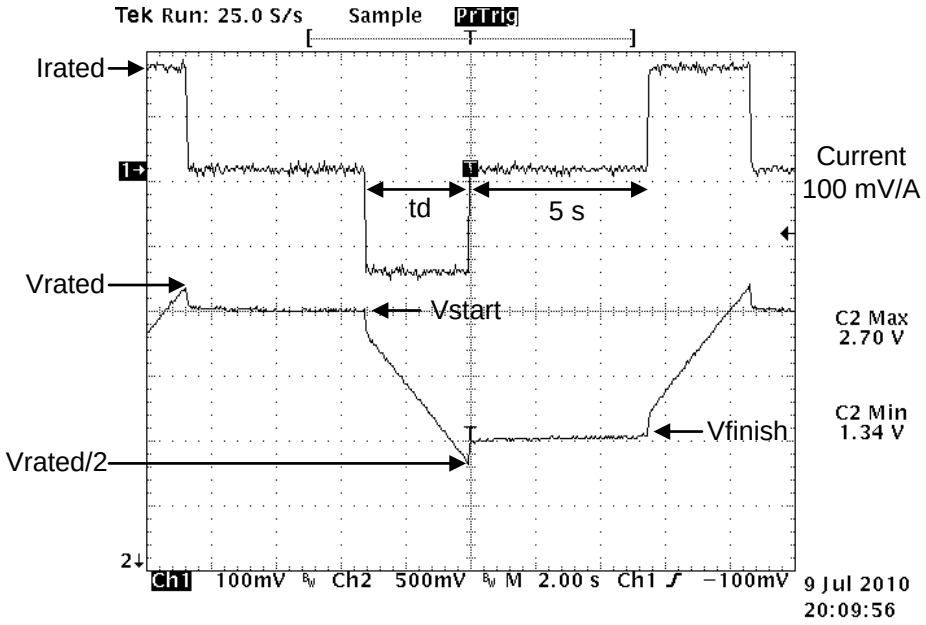


Figure 3.6: SC current and voltage during characterisation

Histograms of the above data were created, dividing the ESR and capacitance into 10 equally spaced bins. A normal density function is then fitted over the histogram. These histograms with normal density functions are shown in Figure 3.7 and Figure 3.8 respectively, and show the spread of capacitance and ESR for the 30 SCs. The ratio of maximum capacitance to minimum capacitance for the batch is approximately 1.06, while the ratio of maximum to minimum ESR is approximately 1.18.

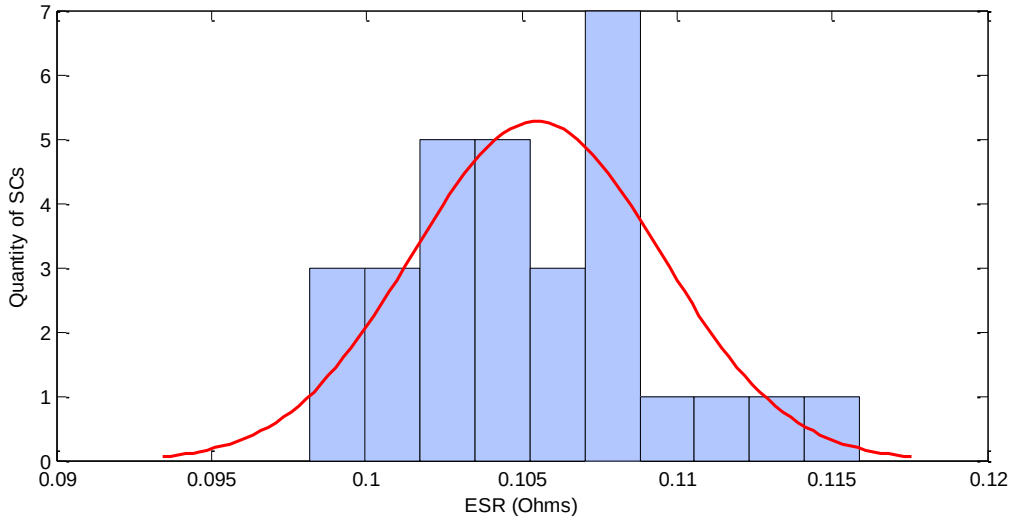


Figure 3.7: Histogram of measured ESR from characterisation tests of 30 SCs

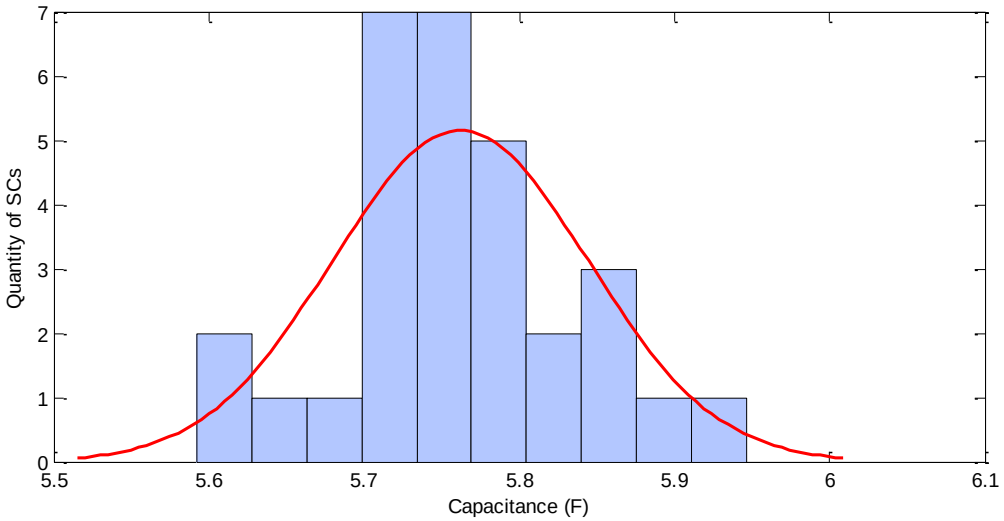


Figure 3.8: Histogram of measured capacitance from characterisation tests of 30 SCs

A SC with close to average specifications was chosen for testing. The test setup, shown in Figure 3.9, consists of a power supply to charge the SC, an electronic load, a high precision voltmeter, and a thermocouple monitor taking temperature readings of the top, body, and leg of the SC, as well as the ambient temperature. These devices are operated using hardware interconnected by the general purpose interface bus (GPIB) under the control of a Matlab file. The testing is carried out at ambient temperature with continuous rated current.

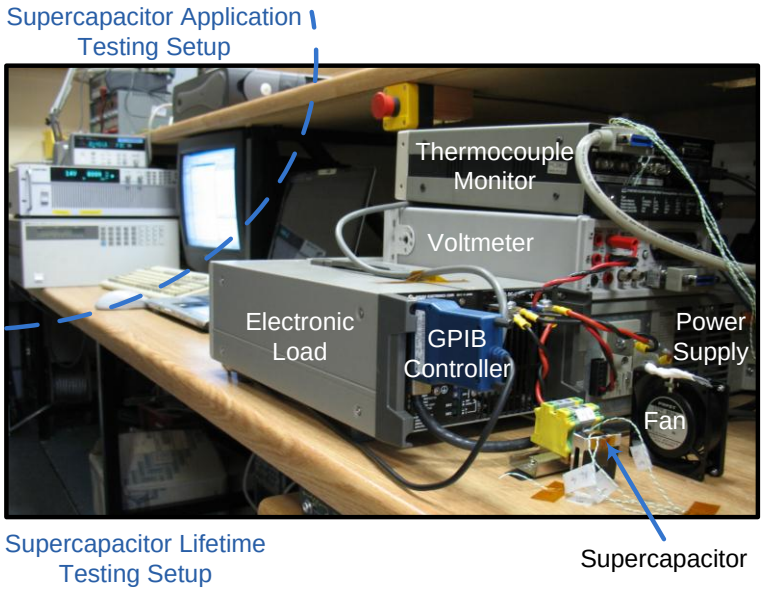


Figure 3.9: SC lifecycle test setup

Constant current cycling between rated and half rated voltage is carried out continuously. Characterization tests occur every 100 cycles and are performed over five consecutive cycles, from which average values are obtained giving more accurate readings. The BCAP0005 P270 SC from Maxwell Technologies Inc. has a specified cycle lifetime of 500,000, where end of life is specified as a 30% reduction of capacitance, or a 100% increase in ESR. The lifetime degradation of a single SC is shown in the results in Section 3.7.1 where over 10 million cycles are shown tested. The Matlab file used to control the GPIB interconnected equipment for this lifecycle testing is shown in Appendix E.

3.5 Standard cycle lifetime testing at rated temperature

While high-temperature testing has been performed before, it has typically been carried out in conjunction with high voltage testing. In an unmanned offshore WEC, the SCs will be utilized in modules which may also be placed inside on-board control rooms with poor thermal management, leading to operating temperature in excess of the tested 25°C room temperature. To test the extent to which elevated temperatures will adversely affect the SCs' cycle lifetime, a BCAP0005 P270 SC was placed inside a thermal chamber which was maintained at 64°C. Tests under constant current cycling conditions were performed on the device continuously, in accordance to the standard cycle lifetime specifications described above. The SC was placed in a heat sink under the airflow of a fan inside the chamber. This induced a temperature rise of about 1°C at the continuous current rating, allowing operation at the SC rated temperature of 65°C. The Matlab file used to the control the GPIB interconnected equipment for this lifecycle testing at rated temperature is shown in Appendix F.

3.6 Application testing at ambient temperature

From the modelling work, the full-scale demanded SC power profile is obtained (before voltage limits are encountered). Using Froude scaling [58], these powers are scaled down to values relevant to the BCAP0005 P270 SC under test. To scale time down, divide by scale to the power of 0.5, and to scale power down, divide by scale to the power of 3.5. A scale factor of 21.1 was chosen to match the continuous powers of the module scaled with the tested SC. The other relevant resultant scaled values closely match the tested SC ratings, as shown in Table VIII. As the resultant usable energy of the SC is lower than the scaled value, the maximum voltage limit is expected to be reached during testing.

Table VIII: SC modules scaled to values relevant to the tested SC

	SC module scaled	Tested SC
Continuous power (W)	4.32	4.32
1 sec power (W)	10.17	9.18
Usable energy (J)	18.5	13.7

The model SC power profile is developed from the most commonly occurring sea-state before voltage limits are encountered, with the grid power limited to 145 kW. This sea-state contains over 30 minutes of data and produces ten power peaks; this is also close to the average power peak rate over yearly operation.

The application SC test utilizes similar equipment as outlined in the lifecycle testing. Due to Froude scaling the applied power profile lasts 395 seconds, and a sample time of 0.109 seconds is utilised in the testing. This is looped three times before characterisation tests are carried out. Testing is performed continuously and the single SC selected for testing has specifications close to the SC in the lifecycle apparatus. The Matlab file used to control the GPIB interconnected equipment for this application testing is shown in Appendix G. A plot of this SC power demand profile before voltage limits are utilised is shown in Figure 3.10. A sample of the SC applied current and resultant voltage is presented in Figure 3.11.

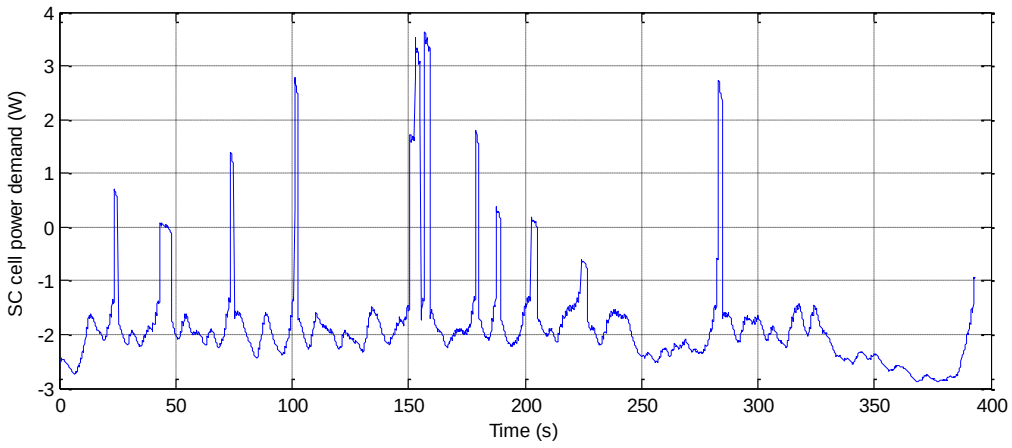


Figure 3.10: Application test power demand of the SC before voltage limits

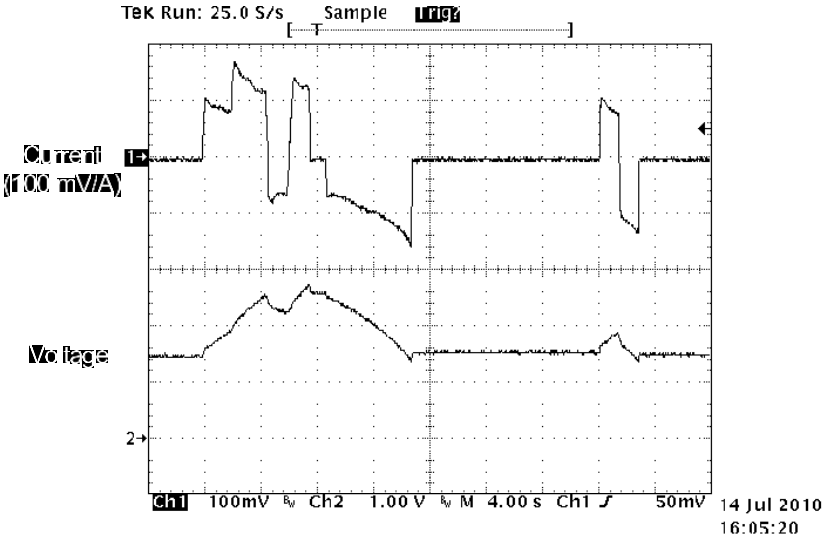


Figure 3.11: SC current and voltage from application testing

3.7 Results

Approximately 10 million cycles have been tested on the single SC under standard test, 9 million cycles on the single SC under standard test at rated temperature, and about 1 million cycles for the application test SC. The initial parameters and testing conditions of the SCs under test are shown in Table IX. Testing runs continuously for a few days at a time, after which data files are collected, equipment checked, and parameters noted before the computer controlled testing is started again. While most data points were very close to previous readings, rarely some data points were well outside the range due to apparent logging errors, a running average of the previous 30 data points were calculated and the current point was removed from analysis if not within 0.1 F or 0.01 Ω of this average.

Table IX: Initial parameters of the SCs under test conditions

	Cycle life SC	Thermal SC	Application SC
Initial *C* (F)	5.79	5.75	5.76
Initial R_{esr}, DC (mΩ)	0.11	0.11	0.10
Average ambient temperature (°C)	25	64	24

3.7.1 Standard cycle lifetime testing at ambient temperature

The degradations of capacitance and ESR for the SC under standard test are seen in Figure 3.12 and Figure 3.13 respectively.

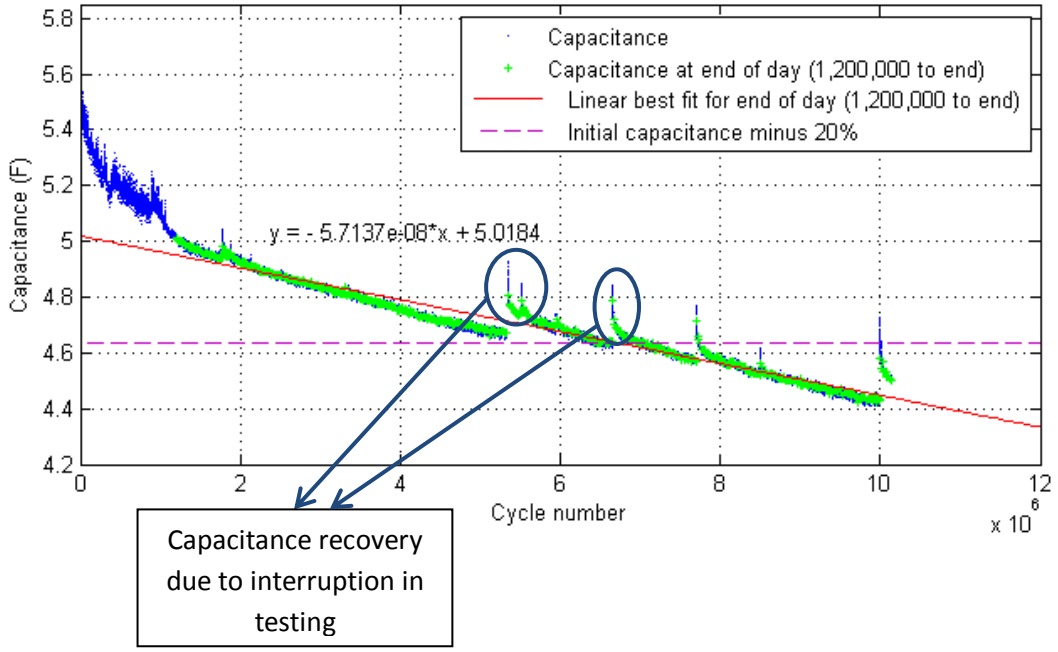


Figure 3.12: Capacitance versus cycle number during cycle lifetime testing at 25°C ambient

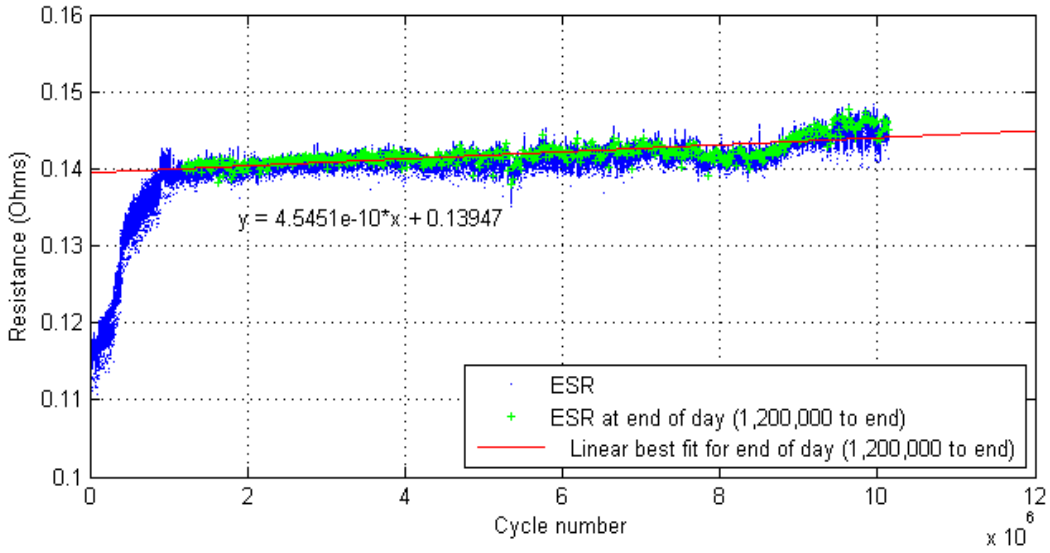


Figure 3.13: ESR versus cycle number during cycle lifetime testing at 25°C ambient

The SC itself is rated for 500,000 cycles, and over 10 million cycles are shown tested. Previous available testing data demonstrated operation up to 150,000 cycles [52] (or 450,000 without *y*-axis scaling [53]). Figure 3.12 and Figure 3.13 validate SC performance discussed in [53], where there is an exponential decrease of capacitance initially before capacitance degradation becomes more linear. It is expected that near

end of life a slow exponential fall off of capacitance will occur. This expected capacitance degradation over lifetime is shown in Figure 3.14.

The lifetime of the SC may be estimated using guidelines in [53], and noting that it is typical that capacitance will encounter the end of life limit before ESR. Lifetime may be estimated by plotting a trend-line along the linear portion of the capacitance degradation profile as seen in Figure 3.14. Estimating life based on linear trends during the exponential drop of capacitance will result in incorrect estimates as shown in Figure 3.14.

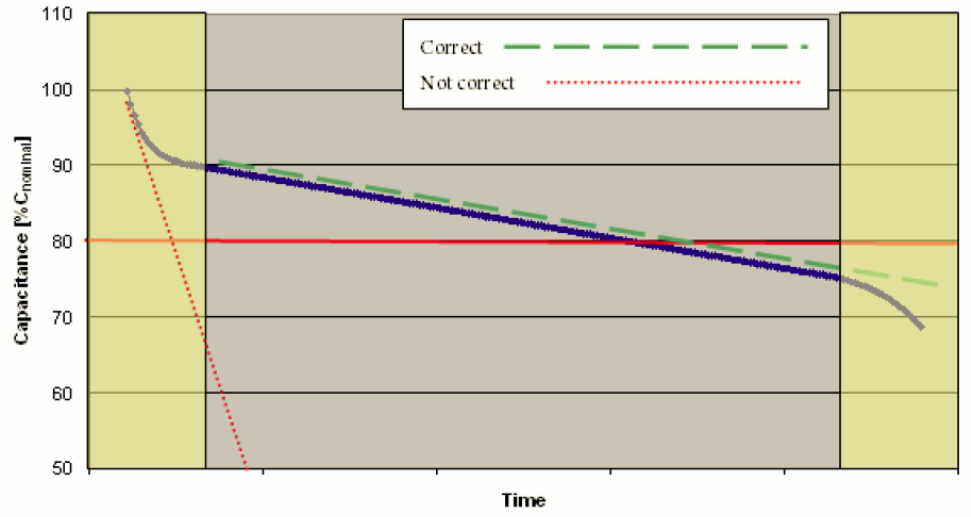


Figure 3.14: Manufacturer generic curve of capacitance evolution over lifetime from Maxwell Technologies, without time scale provided [53]

A phenomenon called recovery is observed if testing is interrupted on the SC after a long period of continuous usage (dc or voltage cycles). The capacitance and ESR measurements show recovery as a function of the rest time, and the measured capacitance increases and the measured resistance decreases. Therefore it is recommended to wait until the recovery has abated before executing another life estimate. It is stated in [53] that this could take as many as 30,000 or 40,000 cycles.

A linear best fit line is applied to the capacitance graph using points obtained at the end of each testing day, and from 1.2 million cycles onward. This prevents life estimation errors from the initial exponential decrease of capacitance and from capacitance recovery that occurs while testing stops. This capacitance recovery is seen in the available literature plots of Figure 3.1 and Figure 3.2 and is also in the experimental plot of Figure 3.12. Initially no testing occurs overnight, or on weekends (this weekend

recovery is clearly seen up to one million cycles in Figure 3.12), but eventually testing is carried out continuously. If these trends continue, capacitance will reach end of life first, in line with current literature [53]; capacitance will reach 70% of its nominal 5 F after 26.6 million cycles, although it is stated by Maxwell Technologies Inc. that there is an exponential decrease of capacitance near end of life which might affect this estimate.

A line showing the initial capacitance minus 20% is also given in Figure 3.12 and this is used for lifetime estimates described in Section 3.7.3.

Log plots based on Figure 3.12 and Figure 3.13 are shown below in Figure 3.15 and Figure 3.16 highlighting the initial exponential portions of the curves, as it is difficult to see the initial values of measured capacitance from Figure 3.12.

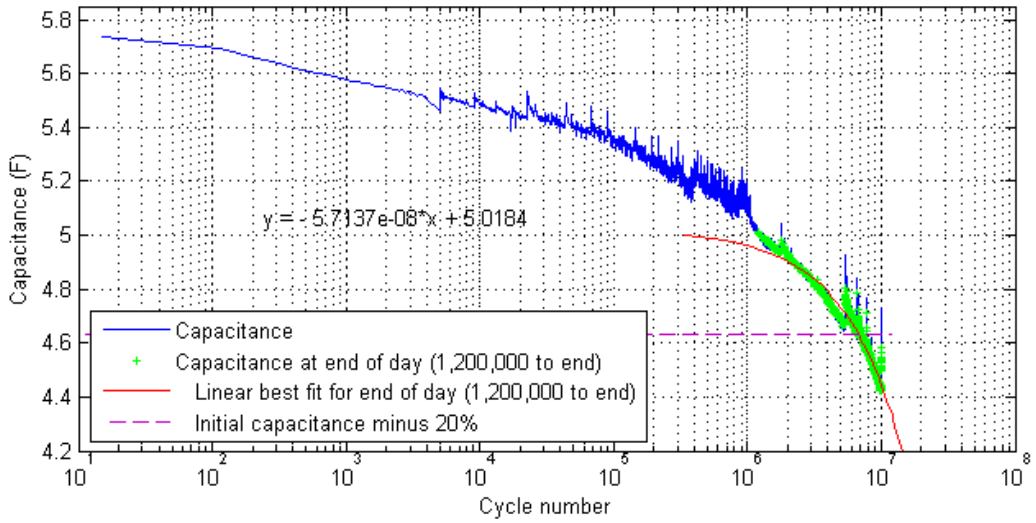


Figure 3.15: Capacitance for cycle lifetime testing at 25°C ambient with log scale

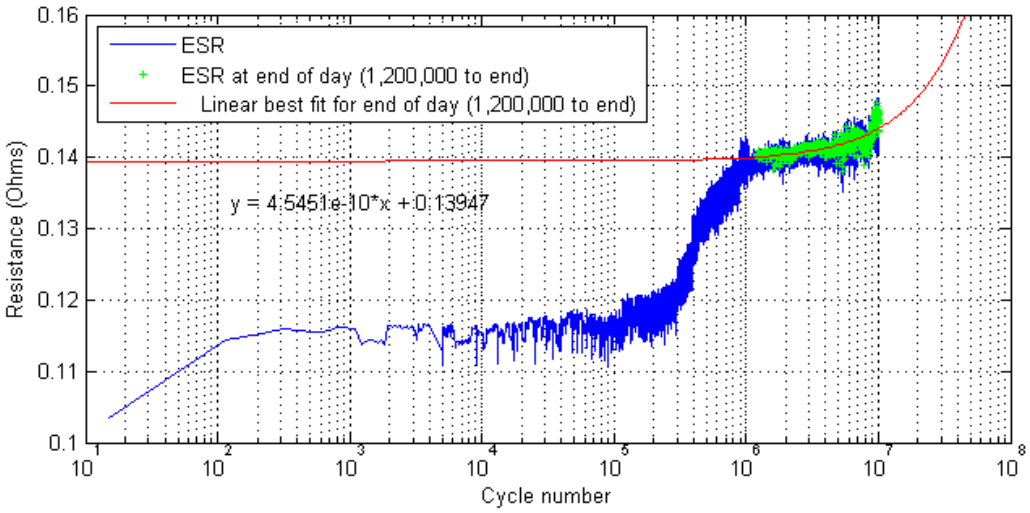


Figure 3.16: ESR for cycle lifetime testing at 25°C ambient with log scale

The variations of capacitance and ESR for the SC over one day of testing are shown in Figure 3.17 and Figure 3.18, and the variation of ambient temperature and SC temperature measured at the top, body, and leg is shown in Figure 3.19. SC temperature rises only slightly above ambient, due to the action of the heat sink and fan. Also, the first characterization point in Figure 3.17, Figure 3.18, and Figure 3.19 is taken before the SC has undergone any power cycles and after an overnight rest.

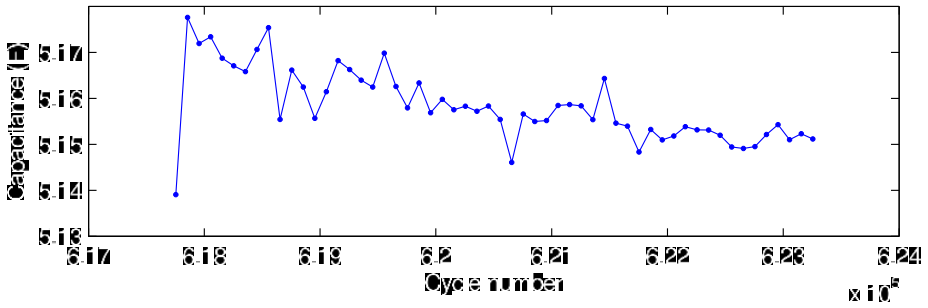


Figure 3.17: Cycle lifetime testing capacitance over one day at 25°C ambient

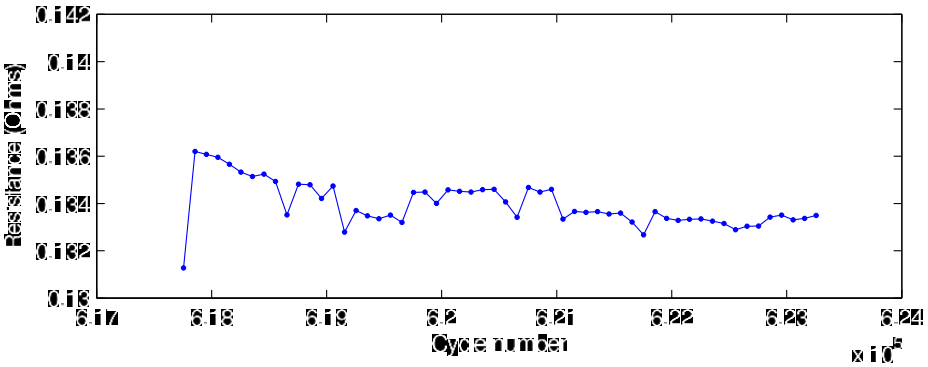


Figure 3.18: Cycle lifetime testing ESR over one day at 25°C ambient

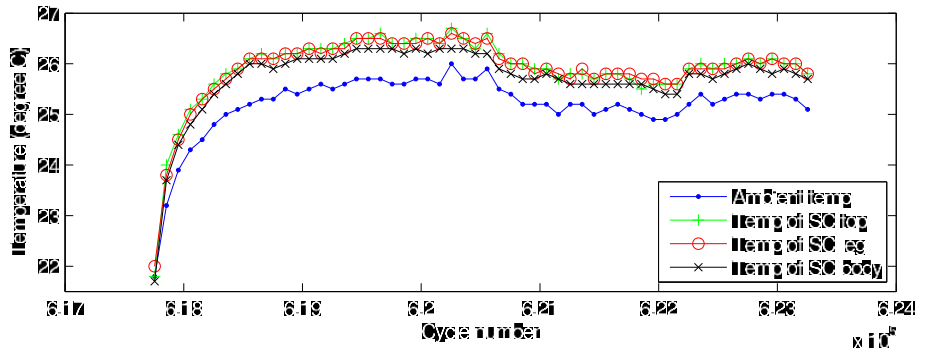


Figure 3.19: Ambient and SC temperature for the cycle lifetime setup over one day

Temperature has a significant effect on SC lifetime, and a typical reference is that an increase in 10°C will halve lifetime [52], [59]. From this it is expected that operation at the rated temperature of 65°C will lead to capacitance degradation at 16 times that which is experienced at a room temperature of 25°C.

3.7.2 Standard cycle lifetime testing at rated temperature

Standard cycle lifetime testing at rated temperature has achieved over 9 million cycles to date. The degradation of capacitance and ESR are seen in Figure 3.20 and Figure 3.21 respectively. These plots are smoother initially than the plots from the SC at ambient temperature, as due to added safety checks the testing could be carried out continuously from the start. During testing days of rest occurred and the resulting capacitance recovery is clearly seen. A linear best fit line is applied to the capacitance graph using points obtained at the end of each testing day, and from 1.2 million cycles onward. According to these trends, capacitance will reach end of life first after 12.8 million cycles. A line showing the initial capacitance minus 20% is also given in Figure 3.20, this is used for lifetime estimates described in Section 3.7.3.

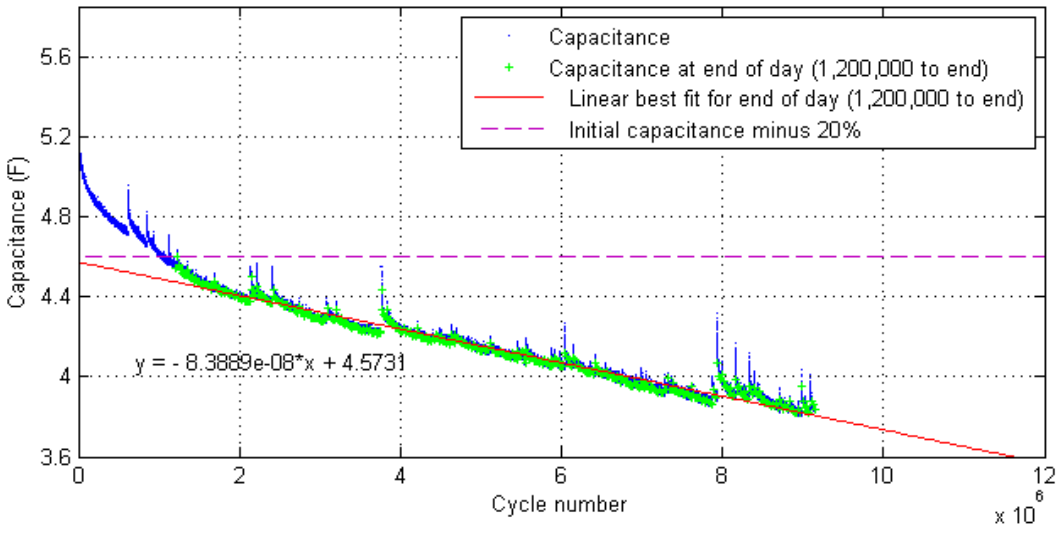


Figure 3.20: Capacitance versus cycle number during standard testing at 65°C

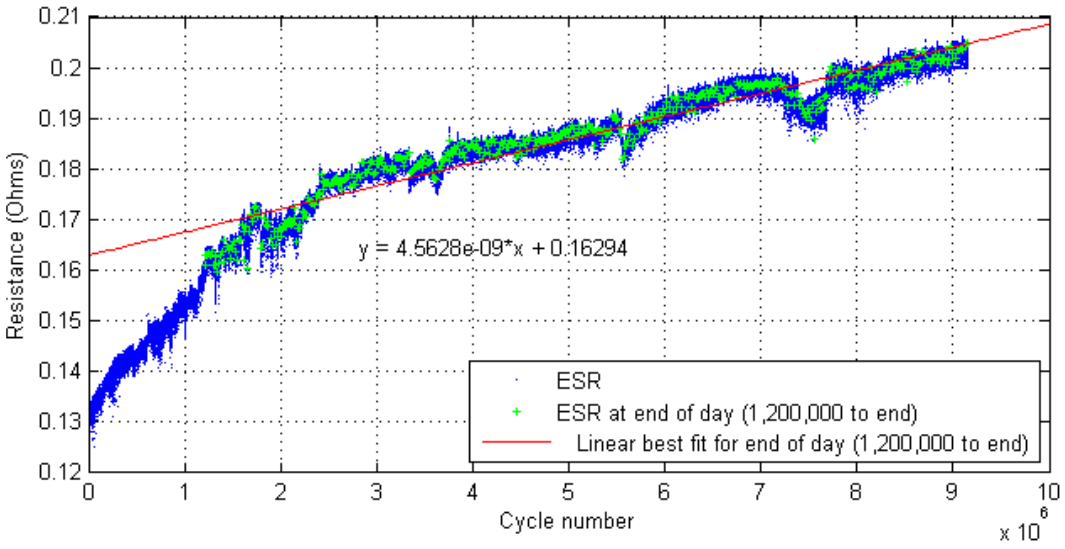


Figure 3.21: ESR versus cycle number during standard testing at 65°C

Log plots based on Figure 3.20 and Figure 3.21 are shown in Figure 3.22 and Figure 3.23, highlighting the exponential portions of the curves. The initial capacitance decay is not noticeable in Figure 3.20 but it is seen clearly in Figure 3.22.

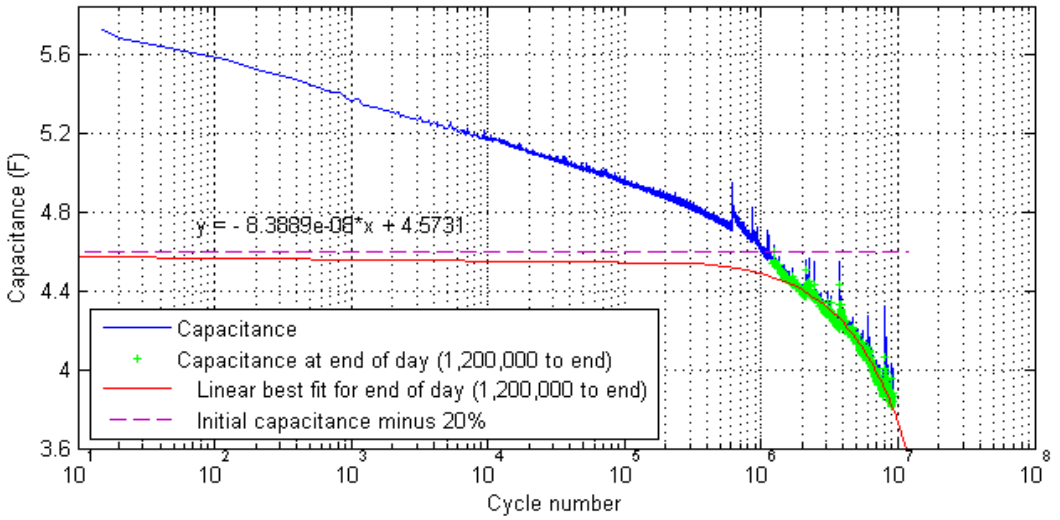


Figure 3.22: Capacitance versus cycle number during cycle lifetime testing at 65°C with log scale

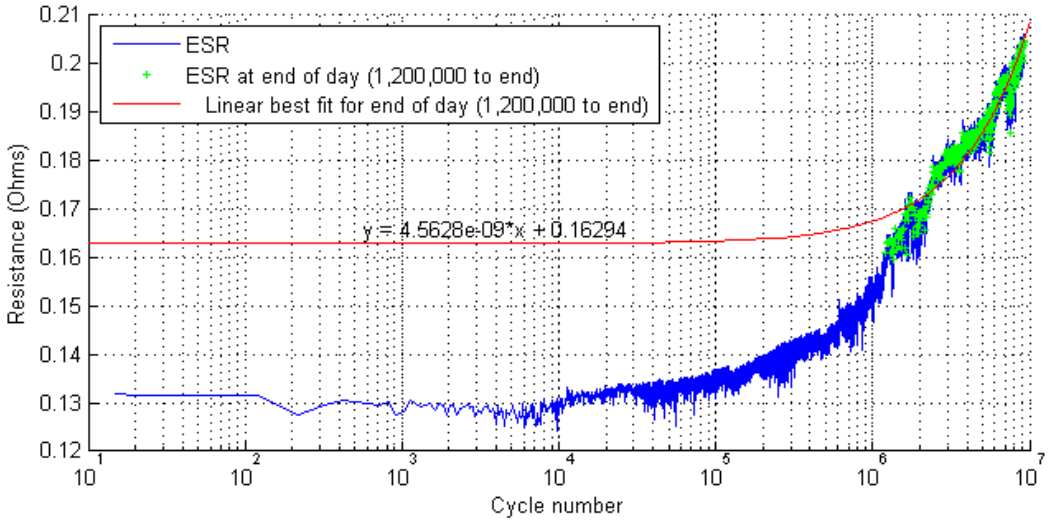


Figure 3.23: ESR versus cycle number during cycle lifetime testing at 65°C with log scale

3.7.3 Investigation of the temperature effect on supercapacitor (SC) cycle lifetime

To investigate the effect of temperature on the SC cycle lifetime, an Arrhenius equation which looks at the temperature dependence on the rate of a chemical reaction was applied to the trends of the two standard cycle lifetime tests. This was demonstrated in [60], where the aging of five large SCs from Maxwell Technologies Inc. was tested at constant rated voltage and at two different temperatures to determine the parameters for the lifetime model shown in equation (3.3).

$$t_i = B_A \, e^{\frac{-E_a}{k_B T_i}} \tag{3.3}$$

where T_i is the absolute temperature of interest in Kelvin, t_i is the reaction time in hours, k_B is Boltzmann's constant, B_A is a parameter to be determined, and E_a is the activation energy in eV given by equation (3.4). The time to end of life for the two test points is represented by t_1 and t_2, and the corresponding absolute temperatures are T_1 and T_2.

$$E_a = \frac{k ln(t_1/t_2)}{1/T_1 - 1/T_2} \tag{3.4}$$

Applying these equations to the work in this chapter and using the estimated time to end of life of 30% below nominal capacitance of 3.5 F produces an E_a of 0.16 eV and 86.7 hours for B_A. From this it is found that cycle lifetime is halved for an increase in temperature of around 37°C for the temperature range of interest (averaging two data points where one point finds the temperature which halves lifetime based on a SC at 25°C, and the other finds the temperature to double lifetime based on a SC at 65°C).

Applying the Arrhenius equations to two further points of 10% below initial nominal capacitance (4.5 F) and to 20% below initial tested capacitance, produces the results in Table X.

The temperature values which half lifetime are obtained from values of estimated lifetime based on trends which are assumed linear. These parameters were obtained from single sample testing of small capacitance SCs at 64.9°C and 25.8°C, and are only applicable at constant current cycling between rated and half rated voltage.

Table X: Table examining temperature effects on SCs based on applying an Arrhenius equation to testing results at 25°C and 65°C

Criteria	**Time to nominal capacitance minus 30% (3.5 F)**	
Cycles to 3.5 F	At standard temperature 26.6 million	At rated temperature 12.8 million
E_a (eV)	0.16	
B_A (hours)	86.7	
Temperature which halves lifetime (°C)	37.0	
Criteria	**Time to nominal capacitance minus 10% (4.5 F)**	
Cycles to 4.5 F	At standard temperature 9 million	At rated temperature 1.4 million
E_a (eV)	0.41	
B_A (hours)	0.0017	
Temperature which halves lifetime (°C)	14.6	
Criteria	**Time to initial measured capacitance minus 20% (≈4.61 F)**	
Cycles to minus 20% of initial C	At standard temperature 6.7 million	At rated temperature 1.1 million
E_a (eV)	0.40	
B_A (hours)	0.002	
Temperature which halves lifetime (°C)	15.0	

The SC temperature effects based on cycle lifetimes to -20% of the initial measured value, or 10% below nominal capacitance, seem the most applicable in this work. From this it is found that cycle lifetime is halved for an increase in temperature of around 15°C for the temperature range of interest. This is a reasonable correlation to the usual 10°C rule of thumb which is based on SCs maintained at a constant voltage [52].

It is noted from Table X that the temperature effect on SCs based on estimated time to end of life does not correlate with values based on tested lifetime values. The temperature effect based on complete lifetime estimates assume that lifetime is linear. Also, the effects of recovery in the capacitance testing may have affected the lifetime estimates.

3.7.4 Application testing at ambient temperature

The application lifetime test applied a scaled power profile to a single SC based on variable speed scheme F: ω^{β} with switched controller and SCs, described in Section 2.7.6 and Section 3.3. The application lifetime testing has achieved over 1 million cycles to date. This corresponds to over five years of operation at full scale. The degradation of capacitance and ESR are seen in Figure 3.24 and Figure 3.25 respectively. A linear best fit line is applied to the capacitance graph using points obtained at the end of testing each day, and from 240,000 cycles onward. Up until about 200,000 cycles, testing is stopped overnight and at weekends, and in accordance with [53], a lifetime estimate from a linearization should only be applied once the capacitance recovery resulting from breaks in testing has diminished. If these linear trends continue, capacitance will reach end of life first after 6.72 million cycles. The application work predicts about 1 million cycles to be experienced by an energy storage system of SC modules at full scale. If this SC system were to experience similar cycle lifetime degradation to the single SC tested (neglecting other ageing phenomena), an estimated 34 years of operation at sea could be achieved.

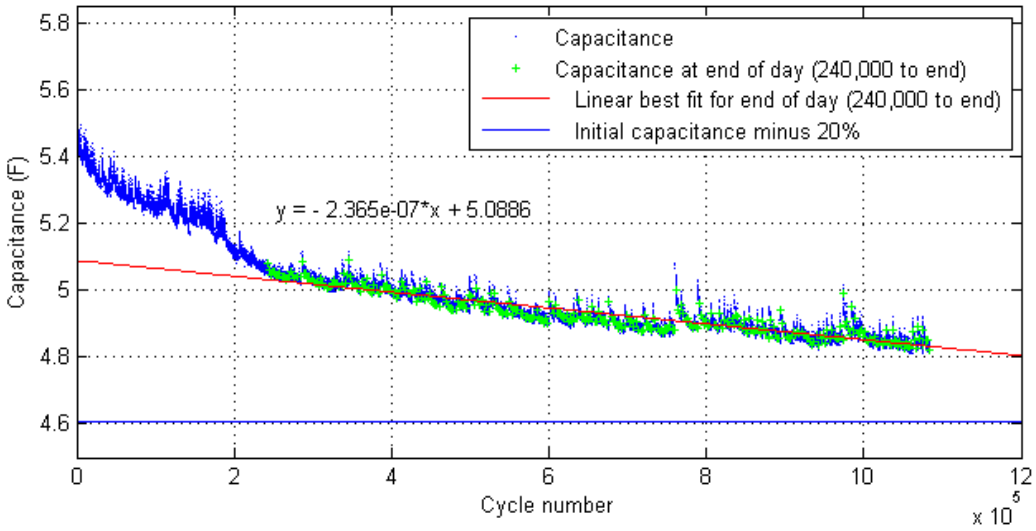


Figure 3.24: Capacitance versus cycle number during application testing at 25°C

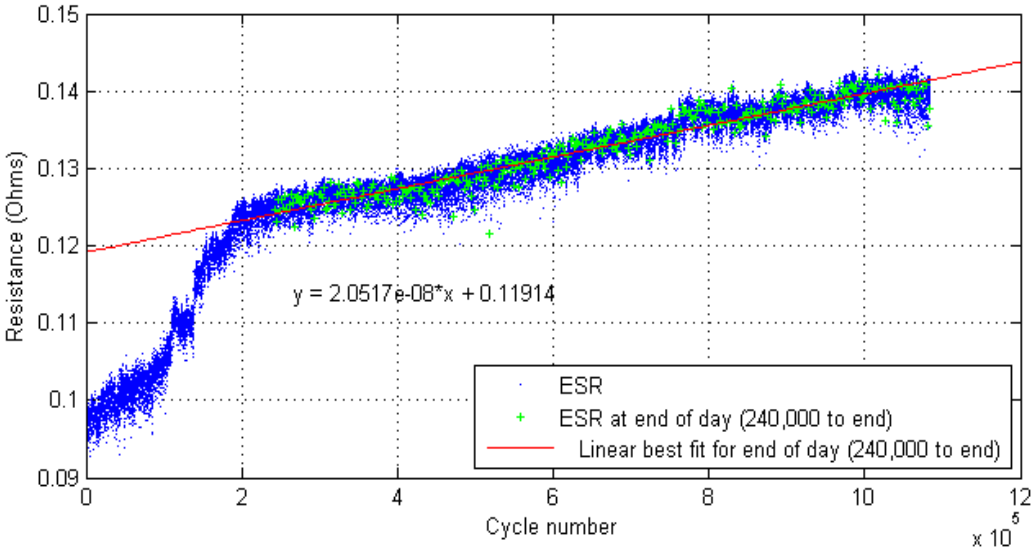


Figure 3.25: ESR versus cycle number during application testing at 25°C

Log plots based on Figure 3.24 and Figure 3.25 are shown in Figure 3.25 and Figure 3.26 highlighting the initial capacitance degradation.

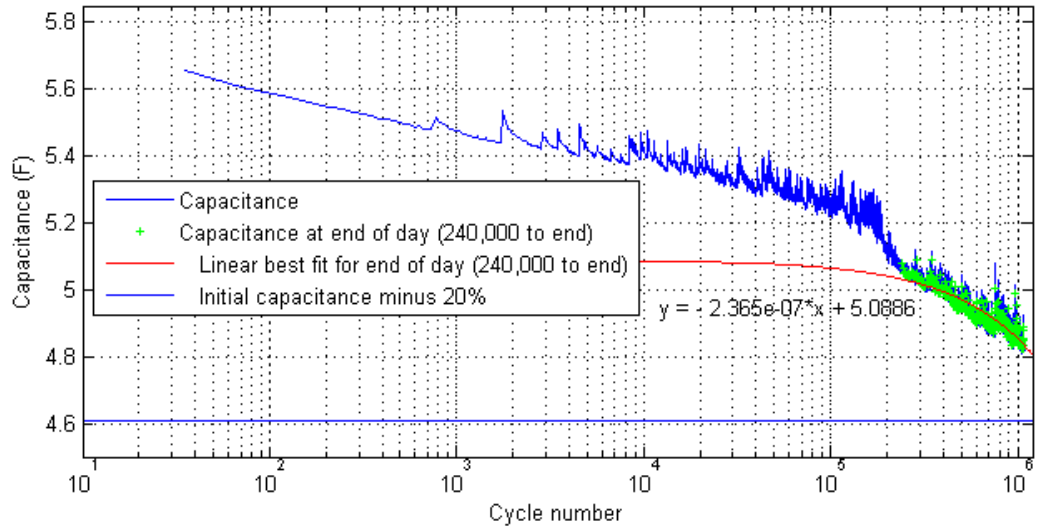


Figure 3.26: Capacitance versus cycle number during application testing at 25°C with log scale

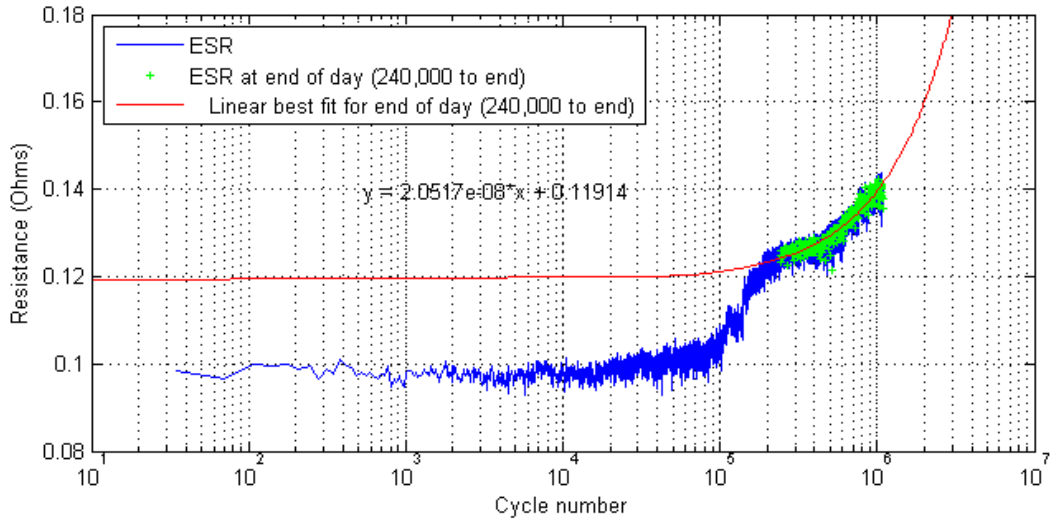


Figure 3.27: ESR versus cycle number during application testing at 25°C with log scale

The application test end of life estimate is 6.72 million cycles compared to 26.6 million cycles for the standard test. While it is difficult to compare projected lifetime degradations for the plots, it is interesting to note the testing time required. The application test would require 2,810 days of nonstop testing to achieve 6.72 million cycles, whereas the standard test would require 2,011 days of nonstop testing to achieve 26.6 million cycles.

3.7.5 Overall comparison plots of supercapacitor (SC) testing

The capacitance and ESR of the three tested SCs are plotted on the same plots with linear scales in Figure 3.28 and Figure 3.29, and on the same plots with log scales in Figure 3.30, and Figure 3.31 to highlight the test comparisons.

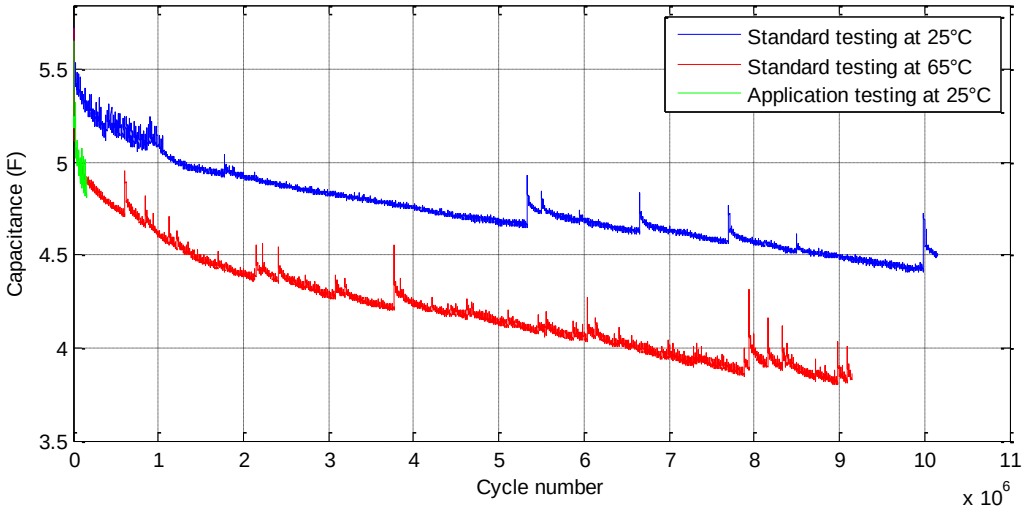


Figure 3.28: Capacitance versus cycle number for the three tested SCs

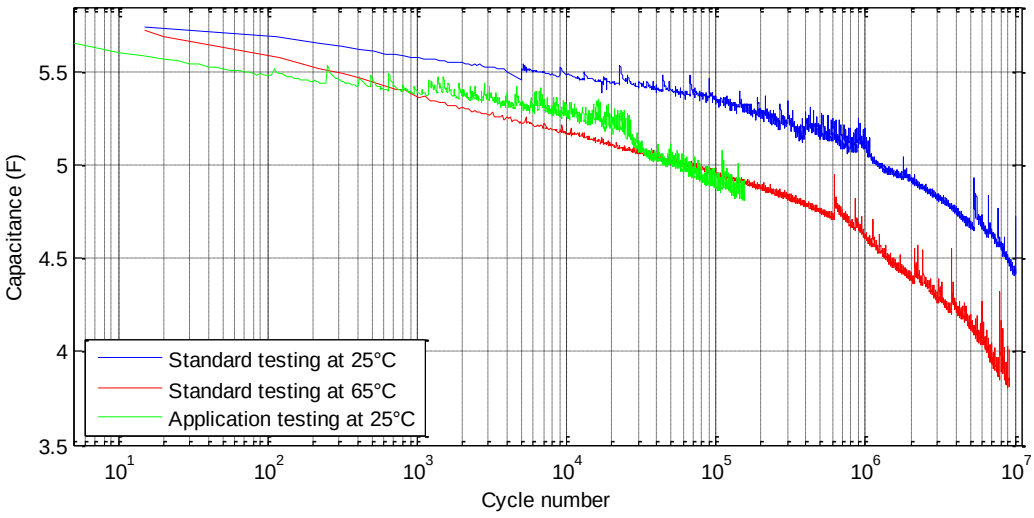


Figure 3.29: Capacitance versus cycle number for the three tested SCs with log scale

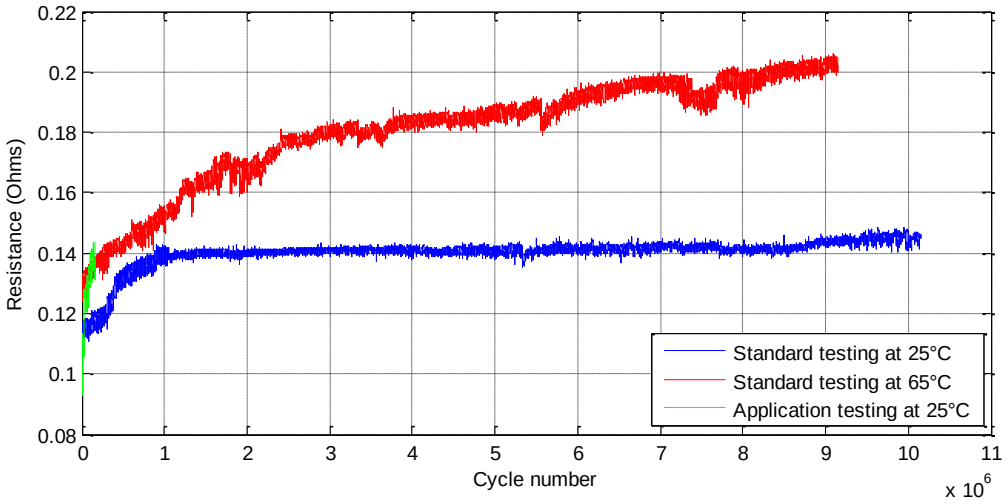


Figure 3.30: ESR versus cycle number for the three tested SCs

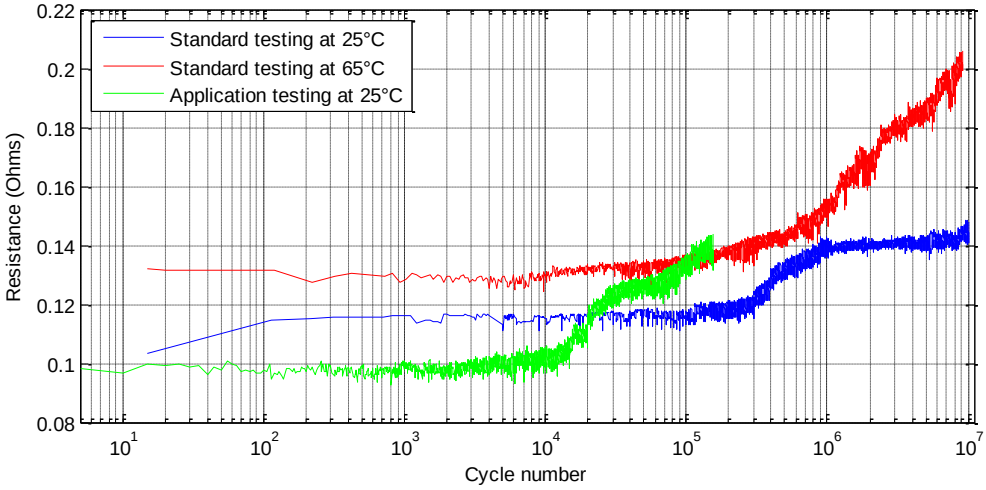


Figure 3.31: ESR versus cycle number for the three tested SCs with log scale

3.8 Conclusion

This chapter investigated power smoothing in a full-scale offshore OWC WEC by integrating SCs with the inertia of a Wells turbine controlled at variable speed. A Simulink model was developed for the WEC system utilizing sea-state data and a SC system was sized to smooth and reduce the grid peak power for a 570 kW (peak) system. The peak-to-average grid power improved to 2.2, compared to 4.6 without the SC system. The grid power standard deviation reduced to 0.18 pu using input pneumatic power as a reference, compared to 0.23 pu without the SC system.

As long component lifetime is a requirement for offshore WECs, computer-controlled lifetime testing setups have been built using GPIB equipment to validate SC lifetimes and determine application lifetime. Over 10 million cycles have been tested on the standard setup, over 9 million cycles at rated temperature, and over 1 million cycles on the application setup equivalent to over five years of full-scale operation. Previous results of available documented cycle testing reached at most 150,000 cycles [52] (or 450,000 without *y*-axis scaling [53]). A summary of these results is shown in Table XI. Expected cycle lifetime of an application SC tested at rated temperature is included. This assumes the SC would experience similar cycle lifetime degradation to the single application SC tested with other ageing phenomena neglected.

Table XI: BCAP0005 P270 SC testing results summary

Rated cycle lifetime at 25°C		**500,000**		
	Cycle life SC	**Thermal SC**	**Application SC**	**Application SC at rated temp**
Cycles tested	10 million	9 million	1 million	0
Equivalent full scale operation time			5 years	
Average ambient temperature	25 °C	64 °C	24 °C	64 °C
Tested cycle lifetime to 20% below initial capacitance	6.7 million	1.1 million		
Expected cycle lifetime to 30% below nominal capacitance	26.6 million	12.8 million	6.72 million	1.12 million
Equivalent full scale time of operation at the 30% end of life criterion			33.9 years	5.66 years
Testing time required for expected cycle lifetime	2,011 days	968 days	2,810 days	

An Arrhenius degradation was assumed to create an equation for the expected time of life based on operating temperature. Based on single sample testing at 26°C and 65°C on small capacitance SCs, a temperature increase of approximately 15°C halves lifetime (though linear trends for lifetime estimates suggest 37°C halves lifetime). According to [59], a temperature increase of 10°C reduces life expectancy by approximately half. Also, lifetime is halved for each 100 mV above nominal voltage [61]. In these tests the SC operating voltage was maintained at a constant value for a given temperature, and C and R_{esr} were measured over time.

Also, based on initial trends of single sample tests, the application tested SC appears to have a much smaller cycle life compared to the standard lifecycle tested SC, but it is interesting to note that the application test would require slightly more time to reach this end of life estimate.

This chapter has demonstrated that if SCs are utilised with turbine inertia for power smoothing in an offshore WEC with the algorithm described, then cycle lifetime of SCs appears not to be a limiting factor in the intervals for non-routine disruptive maintenance (typically five to ten years) that would be experienced, even if placed in a relatively high ambient temperature location.

It is planned to continue testing the SC operating at rated temperature until failure and to submit the results of this updated experimental data to IEEE transactions on industrial electronics, or a similar journal, for publication.

Chapter 4 Supercapacitor (SC) applications in an offshore WEC

4.1 Introduction

This chapter describes further applications of an energy storage system based on supercapacitors (SCs) when employed in a full-scale, grid-connected offshore WEC, to expand on power smoothing with turbine inertia examined in the previous chapter. An increased focus is placed on the electrical dynamics of the system and this is demonstrated through modelling in the Matlab/Simulink/SimPowerSystems environment. The following areas are examined:

i. Minimisation of the output power fluctuations.
ii. Start sequences for the machine.
iii. Low-Voltage Ride-Through (LVRT) capability.

An emphasis is placed on ensuring a component lifetime greater than the maintenance period of the WEC as before. The investigation is based on a Backward-Bent-Duct Buoy (BBDB) Oscillating Water Column (OWC) using a Wells turbine connected to a Permanent-Magnet Synchronous Machine (PMSM) as the power take-off generator. The full system is modelled in Simulink using real sea data, and results are shown.

4.2 Objectives

This chapter explores the use of SC energy storage in a full-scale grid-connected offshore OWC WEC. The overall topology is shown in Figure 4.1, where a Wells turbine utilising NACA0015 blades is coupled to a Permanent-Magnet Synchronous Machine (PMSM) as the power take-off generator. The transformer and transmission line system are not modelled but are shown in Figure 4.1 for completeness.

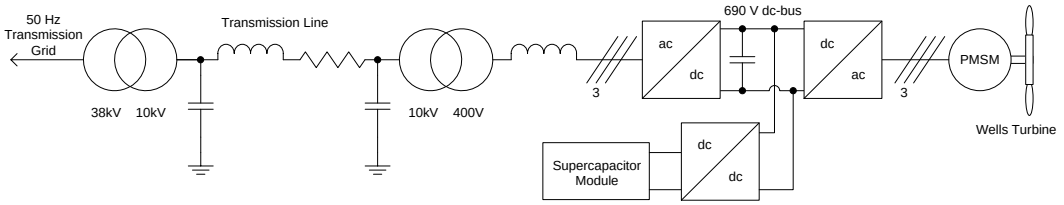


Figure 4.1: WEC grid-connected system

SC systems are reviewed and potential applications are discussed. Descriptions and results of Simulink modelling using real sea data are then presented.

4.3 Supercapacitors (SCs) for power smoothing

While a power smoothing scheme integrating turbine inertia and SCs is examined in Chapter 3, the energy stored in the turbine inertia will vary across OWC WEC devices, depending on the control strategy used, the inertia, and the allowable speed range. Thus any output power smoothing scheme with SCs will need to be re-examined.

Fixed speed operation is likely to remain an appealing option for WEC developers, especially in the prototype development stage where simple control and analysis of the performance at a variety of fixed speeds are key objectives. While fixed speed operation is assumed ideal in simulations in Chapter 2, in reality this would be achieved using a control scheme like fast PI control that prevents significant deviations from the desired fixed speed by adjusting generator torque.

A quick analysis of the power smoothing requirement of SCs, assuming worst case conditions of no available turbine inertia energy storage, is carried out.

From modelling work in Chapter 2, the average pneumatic input power for the most frequently occurring sea-state is 119 kW. The peak to average value for this input pneumatic power is 18.6. For a fixed speed of 1,100 rpm the conversion efficiency is 50.7%, the average electrical power is 60.5 kW and the peak to average electrical power is 3.7. This gives a rough indication of the expected power requirements for the storage device needed to smooth output power, neglecting power smoothing available from turbine inertia. A typical large SC power module has a rated power output in the range of 9 kW to 18 kW (the BMOD0063 P125 module from Maxwell Technologies Inc.). Therefore, by connecting a number of these modules together, the power requirements can be met.

As outlined in Chapter 3, maintenance intervals in offshore WECs are of necessity long with a typical desired interval for non-routine, disruptive maintenance of five to ten years [51]. This maintenance interval gives the desired minimum lifetime of any employed SC energy storage element. An indication of the operational time for an offshore WEC in that time is given in [62], where it is stated that their device is idle about one third of the year though it is difficult to define this value at the early stage of development for many WEC technologies.

Typical ocean wave periods can vary from one to twenty seconds or even higher. Using a wave period of about 10 seconds, for a typical full-scale WEC, gives a frequency of 0.1 Hz. If a short term SC energy storage device is to be utilised for power smoothing over each wave period it will need to survive power cycling for five years at close to this rate. The number of power cycles expected with these figures over the specified maintenance interval is:

Power cycles = 6 cycle/min = (6)(60)(24)(365.25)(5)(2/3) ≈10.5 million cycles/5 years

For a WEC that rectifies the input wave power, the power frequency to the energy storage device will be doubled. This results in 21 million cycles over 5 years if power smoothing is to take place over each wave period. This results in serious lifetime issues for any SC energy storage equipment that is likely to be cycled at every wave cycle.

From the previous chapter, results of power cycling on a single small capacitance SC indicate that this sort of cycle lifetime is possible even though rated cycle lifetimes are typically given by manufacturers as 500,000 to 1 million. However, it is unknown if large capacitance SCs or SCs placed in series and/or parallel in modules will exhibit this extended lifetime characteristic, and if SC modules can help attenuate normal operating output power fluctuations. According to [61], SC lifetime is halved for each 100 mV above nominal voltage. In these tests the SC operating voltage was maintained at a constant value for a given temperature and capacitance and ESR variation was measured over time. While it can be inferred that reducing the operating voltage will extend cycle lifetime, as yet no data on this topic is available, and it is unknown if 21 million power cycles are attainable.

Some SC modules require voltage balancing due to capacitive tolerances and equivalent resistance variations between SCs, to ensure no over-voltages take place. The reliability of each of these balancing circuits as well as each low voltage SC placed in series in a

module, are key concerns when investigating continued power cycling operation over five years.

More research is needed on these issues before this application of power smoothing can be examined for SCs. However, SCs can make a significant contribution to the development of offshore WECs in other areas.

4.4 Turbine start-up with supercapacitors (SCs)

Wells turbines are not self-starting. During start-up as high energy sea-states arise, considerable energy is required to accelerate the high inertia turbine from rest.

In offshore WEC prototypes currently in operation, this start-up has so far been implemented using on-board batteries. Batteries are high energy density, low power devices that do not exhibit the same cycle life as SCs. Also, high power drain and large depth of discharge (DOD) can significantly reduce their lifetime. To ensure the battery is not damaged, it is proposed to use the SC module as the start-up mechanism. This will ensure the WEC will start rapidly without a grid-side surge and begin generating power once an energetic sea-state is sensed (typically done for an OWC using a predefined value for rms pressure inside the chamber).

While the power converter used is bi-directional and could theoretically be employed to start the machine, it is preferable to allow power flow in one direction only to help with ratings and minimise cost of safety and protective equipment. This also has advantages from a grid operator perspective, by limiting starting current surge from the grid as well as in terms of the import capacity of the grid connection.

Turbine damping increases as speed increases and this allows the turbine to interact more efficiently with the oscillating air stream. Turbine stall is also reduced. As the turbine gathers speed, more and more input torque will be experienced which aids in the acceleration to the set speed where normal operation can occur.

4.5 Low-voltage ride-through (LVRT) utilising supercapacitors (SCs)

The increased proportion of wind turbines in the electrical grid has led to stricter grid codes for these devices. While the wave energy industry is still in the development stage, it is expected to eventually experience the same sort of growth that the wind

industry has had over the past ten years. If these expectations are realised, it is probable that similar grid codes will be put in place for wave energy converters.

A typical grid code can be seen in [63]. It states that wind farm power stations should remain connected to the transmission system for voltage dips on any or all three phases, where the transmission system phase voltage remains above the black line in Figure 4.2. In addition to this, these power stations must provide active power in proportion to the retained voltage and maximise reactive current to the transmission system without exceeding turbine limits.

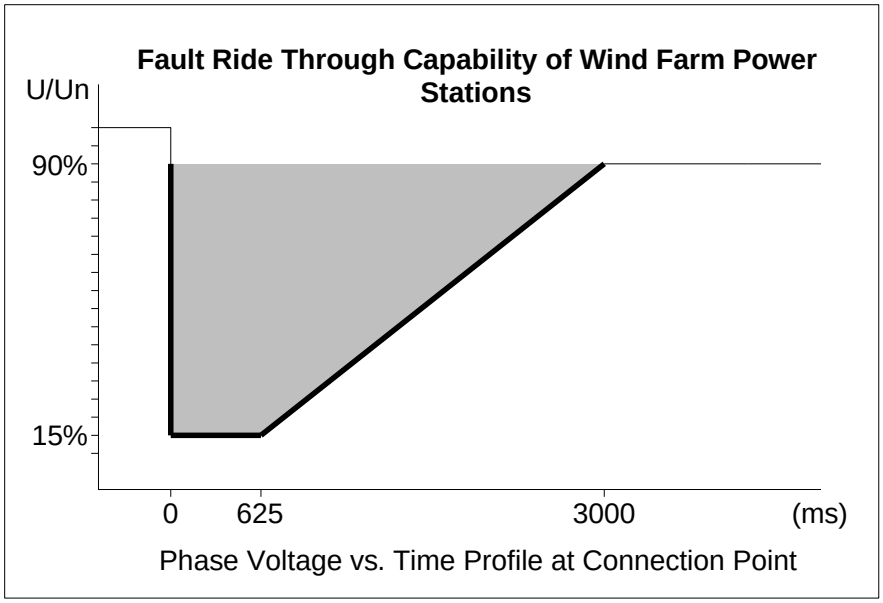


Figure 4.2: Eirgrid LVRT requirement [63]

In a low-voltage event, the ability to transfer power to the grid is limited as it is a function of the grid voltage. If this occurs when the turbine is experiencing high input power, there will be a transient power imbalance and the dc-link voltage may rise dangerously unless controlled. Four options to ride through the fault are:

1. Allow the turbine to speed up, increasing its kinetic energy and so curtailing power onto the dc-link.
2. Extract the excess power flow onto the dc-bus to an energy storage device.
3. Burn off excess energy in a controlled manner using a power electronic converter and a dissipative load bank circuit
4. A combination of these.

The option examined in this chapter is a combination of using SCs connected to the dc-link and allowing the turbine to accelerate.

4.6 OWC system model

4.6.1 Overview

One of the advantages of the system utilising a Wells turbine in an OWC is that the high speed bi-directional airflow facilitates the use of shaft speeds that are consistent with most generators and therefore eliminates the need for a gearbox [51] [64].

Wells turbines need to be robust to withstand the lift, drag and axial forces. They are generally high inertia devices, with a typical inertia of 595 kg m^2 in full-scale converters [26] used in the analysis in Chapter 2 and Chapter 3. These Wells turbines have pneumatic to mechanical peak power conversion efficiencies of 60-70%.

Using available dimensions, the inertia of a Wells turbine with NACA0015 blades was evaluated in Appendix H. These dimensions give an inertia of 91 kg m^2 and a mass of 195 kg for an aluminium device, and an inertia of 263 kg m^2 and a mass of 564 kg for a steel device. The work will assume worst case conditions, and as the LVRT scheme uses turbine inertia to help ride through the fault, the smaller inertia value is used.

It is assumed the shaft of the coupled PMSM has an inertia of 9 kg m^2, to give an overall inertia of 100 kg m^2 and the speed for the device is set at 1,100 rpm.

In order to draw conclusions from this work, a full-scale grid-connected system is simulated.

From Chapter 2, the average pneumatic input power for the most frequently occurring sea-state is 119 kW. The peak to average value for this input pneumatic power is 18.6. While the optimum rating of generators for use in WECs is an issue that has not yet been fully addressed, the accurate prediction of stall speed in a Wells turbine provides a maximum mechanical power value. In the turbine model used, it is found that there is a maximum input torque value for a given turbine speed before stall occurs and any further increase in input pneumatic power will lead to a torque reduction. In the previous chapter the maximum speed was chosen at 1,500 rpm, as mechanical stresses on the Wells turbine are a concern above this value. This produced a maximum stall at 3625 N m and a maximum power rating of 570 kW. This work used a lower speed range of 1,200 rpm which allowed less energy to be absorbed by the turbine inertia during a

grid low-voltage event. The model of this turbine predicts a maximum input torque of 2320 N m, and a maximum mechanical output power of 290 kW (assuming a control scheme that prevents the turbine speed exceeding the specified value). This estimated peak power rating, together with the time-varying sea-state data, enables an appropriately rated permanent-magnet machine to be selected, ensuring that the power fluctuations will not damage the permanent magnets in worst case conditions. Converter current ratings are also selected based on this maximum torque figure.

The permanent-magnet machine parameters are shown in the following table. The value utilised for the turbine viscous friction coefficient B was nominally set at 0.25 N m s and coulomb friction was ignored.

Table XII: Permanent magnet machine model parameters

Parameter	Value
Pole pairs	4
Stator phase resistance R_s	5 mΩ
Armature inductance (= L_{d_m} = L_{q_m})	0.55 mH
Flux linkage established by magnets	0.4 V s
Viscous damping B	0.25 N m s
Static friction	0 N m
Rotor type	Round
Back EMF waveform	Sinusoidal

A permanent-magnet machine is used due to its high efficiency brushless rotor structure and simple controllability. It is noted in [51], that a brushless machine is needed in offshore WECs due to impractical maintenance requirements associated with brush replacement. A two level back-to-back power converter decouples the machine from the 50 Hz grid. This brushless machine and converter layout is becoming the topology of choice in the offshore wind industry and therefore this design satisfies the reliability requirements of a WEC.

The full system topology is shown in Figure 4.1. The back-to-back converter feeds a local transformer which steps the voltage up to 10 kV. Power is transported to shore via an ac-transmission cable, where a larger transformer on land steps the voltage up to 38 kV and feeds power into the transmission grid, assumed to be an infinite bus. While the

work did not model the transformers and transmission line in the grid-connection, the full layout is however shown for completeness.

4.6.2 Turbine model

The turbine model described in Section 2.3, based on an offshore OWC utilising a Wells turbine, provided the input torque to the PM machine. This model utilised available data from the most frequently occurring sea-state, producing an average of 119 kW of pneumatic power.

The typical input pneumatic power and the resultant turbine torque when operated at 1,100 rpm are shown in Figure 4.3.

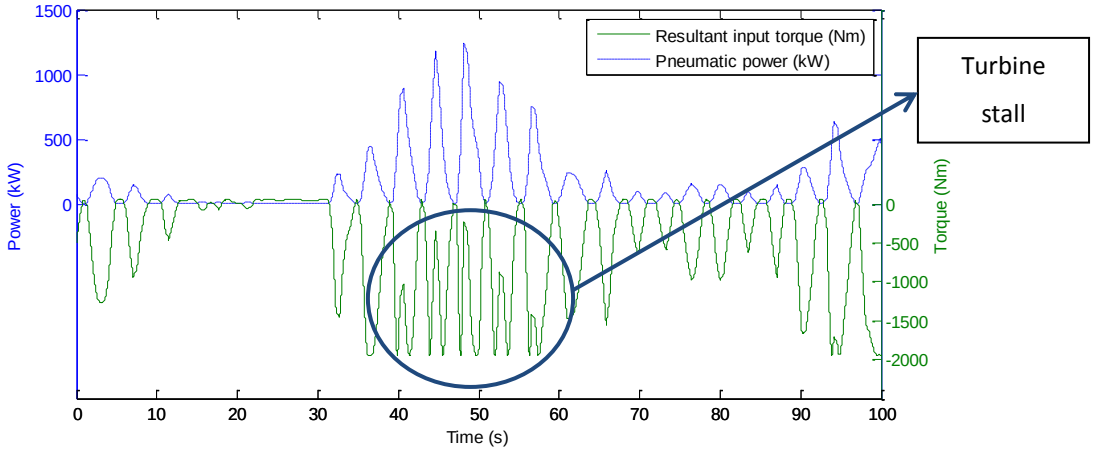


Figure 4.3: Pneumatic power and resultant turbine torque from typical sea-state data for the full-scale device

4.6.3 Machine-side converter model

4.6.3.1 Current loop

A field-oriented control (FOC) scheme was developed utilising cascaded speed and current PI loops. This was based on back-to-back converters both using sine wave Pulse-Width Modulation (PWM). The machine-side converter is used to maintain the speed of the turbine at the pre-set desired value of 1,100 rpm. Machine voltages and currents are transformed to *d* and *q*-axis (direct and quadrature) variables using the Park transformation. The equation for the electromagnetic torque in a PM machine is shown in equation (4.1)

$$T_{em}(t) = \frac{3p}{2}\,\lambda_{fd}\,i_{q_m}(t) \tag{4.1}$$

where λ_{fd} is the flux linkage of the stator direct-axis windings due to the flux from the rotor magnets, the *d*-axis is always aligned with the rotor magnetic axis, and i_{q_m} is the quadrature-axis current in the stator windings. This equation is valid for a non-salient machine (assumed in this analysis). Flux-weakening mode was not used due to the requirement for only a limited narrow band of speeds and hence i_{d_m} was set to zero.

The terminal voltages of a PM machine in the *d*-*q* (direct/quadrature) reference frame are represented by equations (4.2) and (4.3).

$$v_{d_m}(t) = R_s\, i_{d_m}(t) + L_{d_m}\, \frac{d}{dt}\, i_{d_m}(t) - \omega_e(t)\, L_{q_m}\, i_{q_m}(t) \tag{4.2}$$

$$\begin{aligned} v_{q_m}(t) = R_s\, i_{q_m}(t) + L_{q_m}\, \frac{d}{dt}\, i_{q_m}(t) \\ + \omega_e(t)\big(L_{d_m}\, i_{d_m}(t) + \lambda_{fd}\big) \end{aligned} \tag{4.3}$$

where R_s is the stator phase resistance and L_{q_m} and L_{d_m} are the q and *d*-axis inductances. In a round rotor PM machine, there is no saliency or variation in phase inductance so $L_{q_m} = L_{d_m}$ and this is called synchronous inductance. The term $\omega_e(t)$ describes the speed of rotation of the flux in the machine and is equal to the number of pole pairs in the machine times the mechanical speed of rotation of the generator and coupled turbine.

The terminal voltages in equations (4.2) and (4.3) may be set using a PWM strategy in an ideal inverter. The torque produced in the PM machine is described as a function of $i_{q_m}(t)$ in equation (4.1). Speed variation of the machine related to torque is described by Newton's equation of motion for the shaft. This is given in terms of power flows in equation (2.10), and it is shown in terms of torques in equation (4.4).

$$T_{mech}(t) = T_{em}(t) + T_{loss}(t) + J\, \frac{d\omega(t)}{dt} \tag{4.4}$$

The term $T_{loss}(t)$ may be represented by $B\, \omega(t)$ for the PM machine.

A PI controller uses a speed error to create a reference *q*-axis current which is directly proportional to machine torque as shown. The controller to the PWM inverter controls the terminal voltages to produce the *d* and *q*-axis currents. Equations (4.2) and (4.3) are rearranged in terms of *d* and *q*-axis current derivatives below.

$$\frac{d}{dt} i_{d_m} = \frac{1}{L_{d_m}} \left(v_{d_m} - R_s \, i_{d_m} + \omega_e \, L_{q_m} \, i_{q_m} \right) \tag{4.5}$$

$$\frac{d}{dt} i_{q_m} = \frac{1}{L_{q_m}} \left(v_{q_m} - R_s \, i_{q_m} - \omega_e \, L_{d_m} \, i_{d_m} - \omega_e \lambda_{fd} \right) \tag{4.6}$$

The machine-side converter controller design is based on [65] and [66]. For a field oriented control scheme, the maximum output voltage to one phase from the PWM converter is half the dc-bus voltage to create the desired full sine wave without distortion. The control voltage to the converter switches is compared to a triangular waveform to create the PWM signals. This is described in equation (4.7).

$$v_{phase}(t) = \frac{V_{dc_link}}{2} \frac{1}{v_{tri}(t)} v_{control}(t) \tag{4.7}$$

If the triangular waveform has a magnitude of 1, the gain of the control voltage is effectively $V_{dc_link}/2$. The output of the controller thus is a per unit value allowing ease of scaling.

Equations (4.5) and (4.6) contain cross coupled terms complicating controller design. These terms are cancelled from the above equations by feeding forward the machine currents and machine speed and using appropriate scaling as described in equations (4.8) and (4.9).

$$v_{d_m} = v_{d_m}{}' - \omega_e \, L_{q_m} \, i_{q_m} \tag{4.8}$$

$$v_{q_m} = v_{q_m}{}' + \omega_e \, L_{d_m} \, i_{d_m} + \omega_e \lambda_{fd} \tag{4.9}$$

The full system with controllers may now be shown as in Figure 4.4.

By using Laplace transforms and cancelling cross coupled terms that are fed forward, the system may be represented by the following equations:

$$V_{d_m}'(s) = \left(R_s + sL_{d_m}\right)I_{d_m}(s) \tag{4.10}$$

$$V_{q_m}'(s) = \left(R_s + sL_{q_m}\right)I_{q_m}(s) \tag{4.11}$$

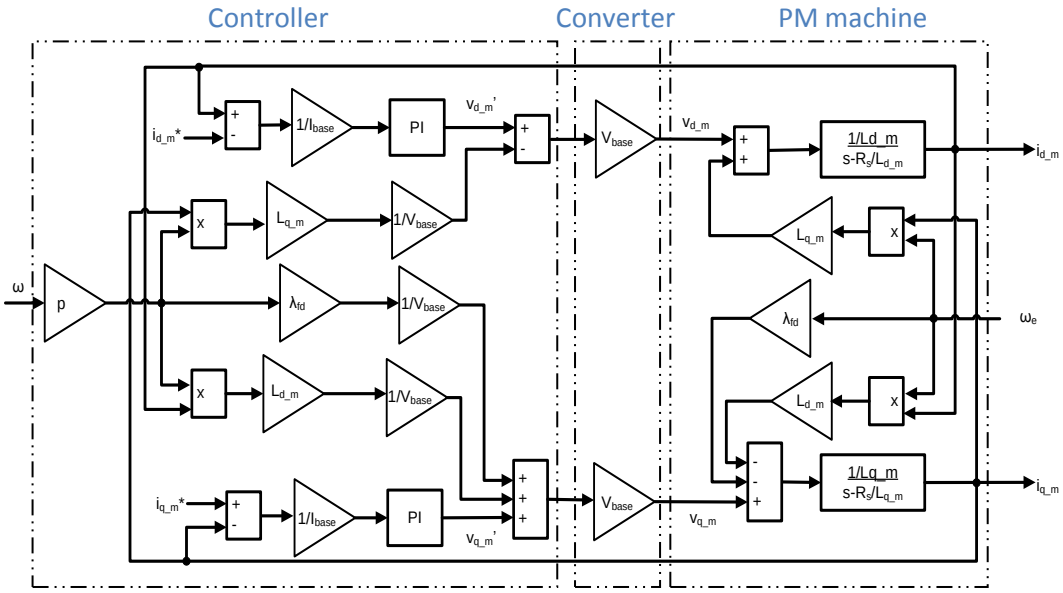


Figure 4.4: Block diagram of permanent magnet machine and controller

The gains of the PI controllers that control the *d-q* currents for the machine side converter are named $k_{p_m_cur}$ and $\omega_{i_m_cur}$. By using classical control design, the pole of the system is cancelled by the zero of the PI controller by setting $\omega_{i_m_cur} = R_s/L_{d_m}$.

The closed loop transfer function of these current control loops becomes:

$$TF_{curr_closed_loop}(s) = \frac{I_{d_m}}{I_{d_m}*} = \frac{\frac{1}{I_{base}}\frac{k_{p_m_cur}}{s}V_{base}\,1/L_{d_m}}{1 + \frac{1}{I_{base}}\frac{k_{p_m_cur}}{s}V_{base}\,1/L_{d_m}} \tag{4.12}$$

$$TF_{curr_closed_loop}(s) = \frac{I_{d_m}}{I_{d_m}*} = \frac{\frac{1}{I_{base}} k_{p_m_cur} V_{base}\, 1/L_{d_m}}{s + \frac{1}{I_{base}} k_{p_m_cur} V_{base}\, 1/L_{d_m}} \quad (4.13)$$

Equation (4.13) describes a first order system with $\omega_c = \frac{1}{I_{base}} k_{p_m_cur} V_{base}\, 1/L_{d_m}$ as the cut-off frequency. By choosing an appropriate value for ω_c the PI gain $k_{p_m_cur}$ may be determined. Choosing a cut-off frequency of 200 Hz, produces a $k_{p_m_cur}$of 1.93. This cut-off frequency of the current loop is an order of magnitude smaller than the switching frequency of the PWM converter. Therefore, switching dynamics are assumed ideal and the impact of PWM switch and frequency harmonics is neglected. The PI controllers in both channels are designed assuming that the inverter is ideal, and that the gain of the converter of $V_{dc_link}/2$ is constant. In reality this will change as the dc-link voltage is changed. Control of this dc-link voltage is described in Section 4.6.4 and Section 4.6.5.

4.6.3.2 Speed loop

The speed control strategy in this chapter consists of setting a desired speed for the turbine with the system responding to produce this speed using a PI controller.

Equation (4.4) describing the torques of the system is rearranged in terms of speed derivative, the input and output torque signs are inverted (to ease control design) to give equation (4.14).

$$\frac{d}{dt}\omega = \frac{1}{J}(T_{em} - T_{mech} - B\omega) \quad (4.14)$$

The input to this control scheme is electromagnetic torque T_{em} and the output is turbine speed ω. This electromagnetic torque is set by the quadrature machine current, i_q, according to equation (4.1). This may be rewritten as equation (4.15):

$$T_{em}(t) = \frac{3p}{2}\, \lambda_{fd}\, i_{q_m}(t) = k_m i_{q_m}(t) \quad (4.15)$$

To maximise the electromagnetic torque, outside of a field weakening zone, according to equation (4.1), i_{d_m} needs to be minimised and set to zero. It is assumed that this

tracking of i_{q_m} is ideal, when evaluating gains for the speed PI controller. The speed control loop is shown in Figure 4.5.

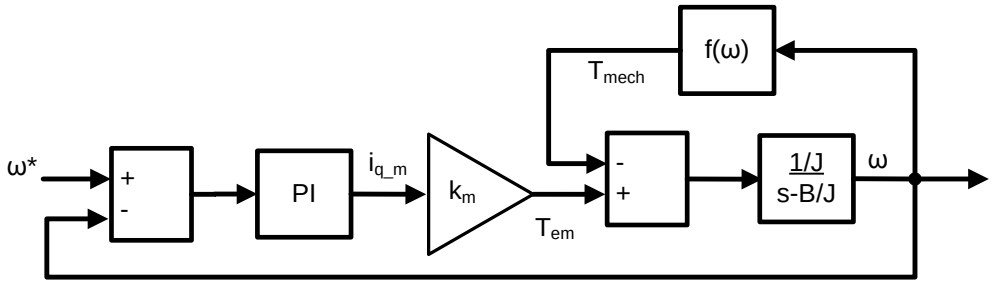


Figure 4.5: Speed control loop assuming an ideal current loop

The mechanical torque developed from the OWC is a function of speed. It is seen in Figure 2.5, that the pneumatic power developed which is dependent on speed is relatively constant over the operating speed range of 750 rpm to 1,500 rpm of the device. To simplify the speed loop design, this mechanical input power and torque will be neglected during controller design. An inherent feature of this input power is that it will go to zero twice during every wave period.

The PI controller zero frequency is set to cancel the pole of the system by setting $\omega_{i_speed} = B/J$. Due to the assumption that tracking of i_{q_m} is ideal and for stability purposes, the speed loop bandwidth is set ten times lower than the current loops. This sets the cut off frequency to 20 Hz.

The closed loop transfer function of these current control loops becomes:

$$TF_{speed_closed_loop}(s) = \frac{\omega}{\omega^*} = \frac{\frac{k_{p_speed}}{s} k_m \, 1/J}{1 + \frac{k_{p_speed}}{s} k_m \, 1/J} \tag{4.16}$$

$$TF_{speed_closed_loop}(s) = \frac{\omega}{\omega^*} = \frac{k_{p_speed} \, k_m \, 1/J}{s + k_{p_speed} \, k_m \, 1/J} \tag{4.17}$$

The cut-off frequency of $k_{p_speed} \, k_m \, 1/J$ is thus set to 20 Hz by setting k_{p_speed} to 5240.

A full PWM averaged model of the machine converter was developed in Simulink using the SimPowerSystems library, and the resulting schematic diagram is shown in Figure 4.6.

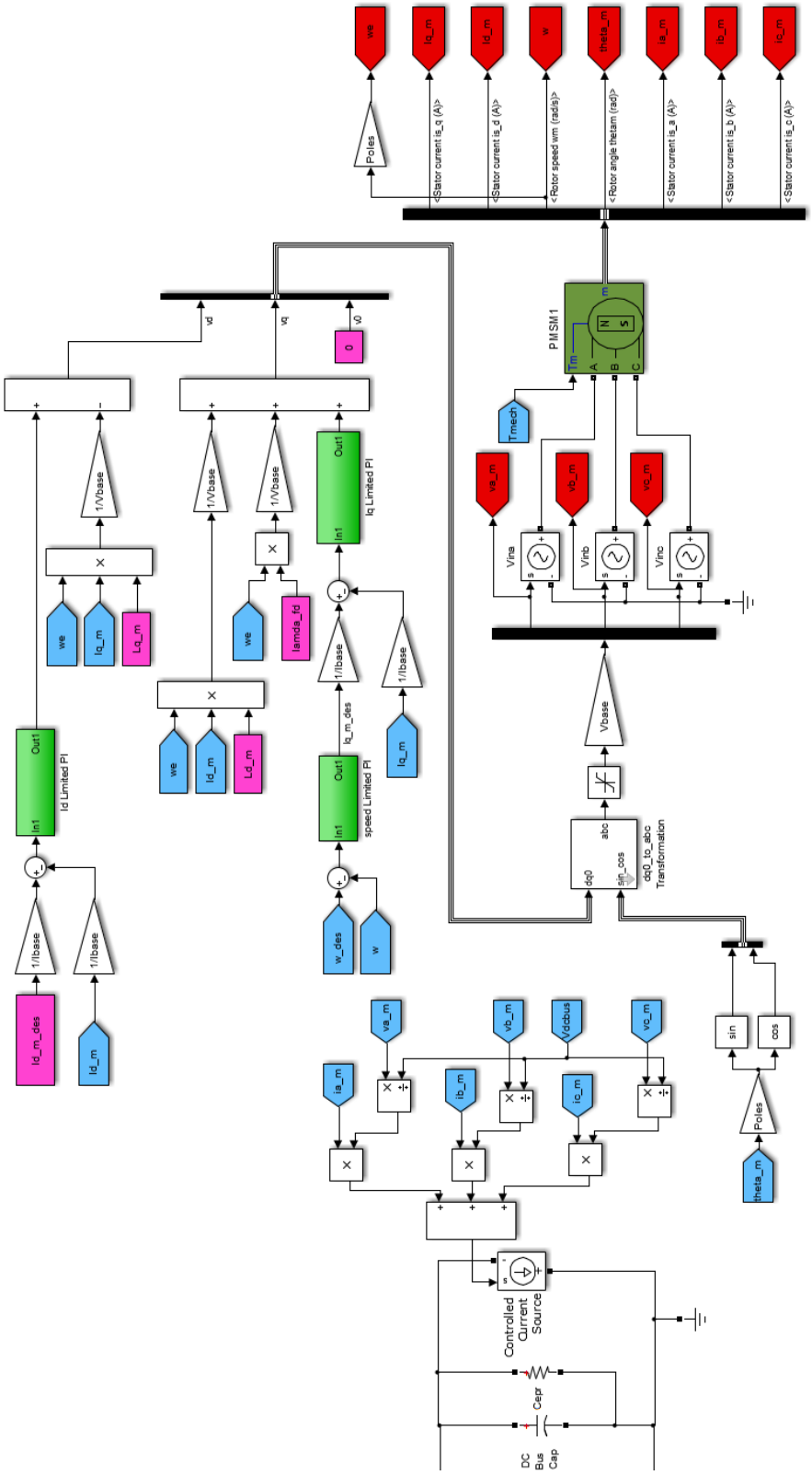


Figure 4.6: Simulink schematic of the machine-side converter

4.6.4 Grid-side converter model

4.6.4.1 Current loop

The inverter connection to the grid is modelled as a series resistor and inductor connected to an infinite bus. The grid parameters are shown in Table XIII.

Table XIII: Grid connection model parameters

Parameter	Value
R_g	5 mΩ
L_g	0.4 mH
V_{ll} rms	400 V
Frequency	50 Hz

The grid circuit for one phase may be represented by equation (4.18).

$$V_a = -R_g I_a - L_g \frac{dI_a}{dt} + V_{agrid} \tag{4.18}$$

where V_a is the per phase output voltage from the inverter and V_{agrid} is the corresponding voltage of the stiff grid.

Transforming voltage equations for the three phases into the *d-q* reference frame [66] produces equations (4.19) and (4.20).

$$v_{d_g}(t) = -R_g\, i_{d_g}(t) - L_g\, \frac{d}{dt}\, i_{d_g}(t) + \omega_g(t)\, L_g\, i_{q_g}(t) + v_{dgrid}(t) \tag{4.19}$$

$$v_{q_g}(t) = -R_g\, i_{q_g}(t) - L_g\, \frac{d}{dt}\, i_{q_g}(t) - \omega_g(t)\, L_g\, i_{d_g}(t) + v_{qgrid}(t) \tag{4.20}$$

The term $\omega_g(t)$ describes the frequency of the grid in rad/s. The quadrature component of the grid voltage $v_{qgrid}(t)$ is zero if the *d*-axis of the reference frame is aligned to the phase voltage using an appropriate phase locked loop voltage sensing system.

The inverter voltages $v_{d_g}(t)$ and $v_{q_g}(t)$ in equations (4.19) and (4.20) may be set using PWM switching in an ideal inverter. The grid-side converter is controlled to maintain the dc-link voltage at a desired level using PI controllers. Any current fed onto the dc-link from the machine is outputted to the grid or to an energy storage system to maintain a constant dc-link capacitor voltage. A PI controller uses a voltage error to thus create a reference *d*-axis current which is directly proportional to output power as shown in equation (4.27), while the *q*-axis current can provide any desired reactive power requirements. The controller to the PWM inverter controls the terminal voltages to produce given *d* and *q*-axis currents. The equations (4.19) and (4.20) are rearranged in terms of and *d* and *q*-axis current derivatives.

$$\frac{d}{dt}\, i_{d_g} = \frac{1}{L_g}\left(v_{dgrid} - R_g\, i_{d_g} + \omega_g\, L_g\, i_{q_g} - v_{d_g}\right) \tag{4.21}$$

$$\frac{d}{dt}\, i_{q_g} = \frac{1}{L_g}\left(-R_g\, i_{q_g} - \omega_g\, L_g\, i_{d_g} - v_{q_g}\right) \tag{4.22}$$

Again a field oriented control scheme is used where the maximum output voltage amplitude to one phase from the PWM converter is half the dc-bus voltage. This creates the desired full sine wave voltage without distortion. As described in Section 4.6.4, a triangular waveform with magnitude 1 is assumed and the gain of the control voltage is effectively $V_{dc_link}/2$. The output of the controller thus is a per unit value allowing ease of scaling.

The equations of (4.19) and (4.20) again contain cross coupled terms complicating controller design. These terms are cancelled by feeding forward the grid currents and frequency and using appropriate scaling as described in equations (4.23)and (4.24).

$$v_{d_g} = v'_{d_g} + \omega_g\, L_g\, i_{q_g} + v_{dgrid} \tag{4.23}$$

$$v_{q_g} = v'_{q_g} - \omega_g\, L_g\, i_{d_g} \tag{4.24}$$

The full system with controllers is shown in Figure 4.7.

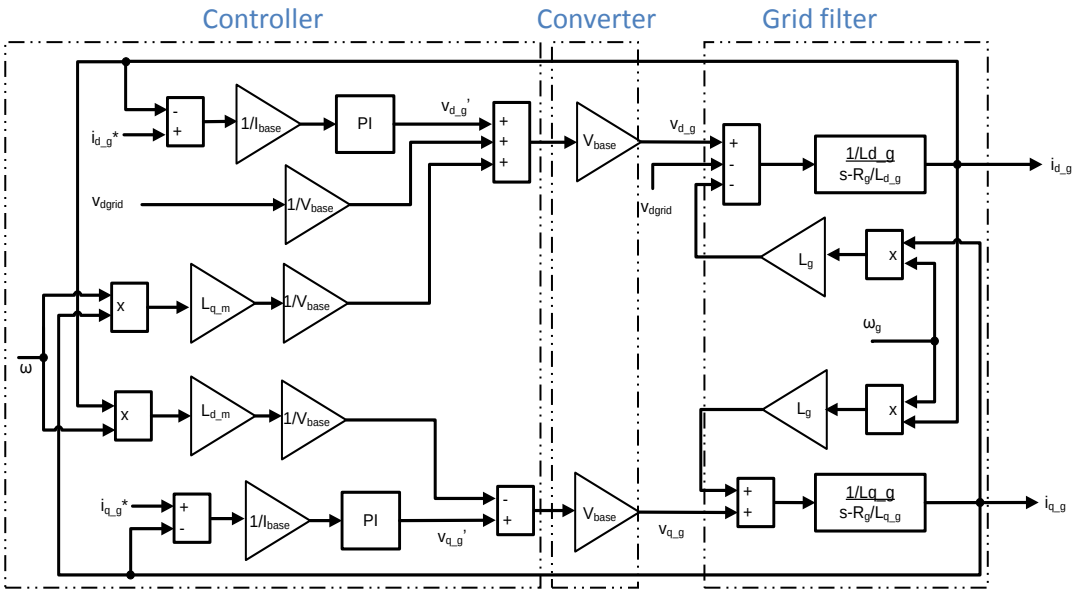


Figure 4.7: Block diagram of grid filter and controller

By using Laplace transforms and cancelling fed forward cross coupled terms, the system may be represented by the following equations:

$$V_{d_g}'(s) = \left(R_g + sL_g\right) I_{d_g}(s) \tag{4.25}$$

$$V_{q_g}'(s) = \left(R_g + sL_g\right) I_{q_g}(s) \tag{4.26}$$

The gains of the PI controllers that control the *d-q* axis currents for the grid side converter are named $\omega_{i_g_cur}$ and $k_{p_g_cur}$. As before, by using classical control design the pole of the system is cancelled by the zero of the PI controller by setting $\omega_{i_g_cur} = R_g/L_g$.

The control loop then describes a first order system with $\omega_{cg} = \frac{1}{I_{base}} k_{p_g_cur} V_{base}\, 1/L_g$ as the cut-off frequency. By choosing an appropriate value for ω_{cg} the PI gain $k_{p_g_cur}$ may be determined. Choosing a cut-off frequency of 200 Hz, produces a $k_{p_g_cur}$ of 1.29. This cut-off frequency of the current loop is an order of magnitude smaller than the switching frequency of the PWM converter and the impact of PWM switch and frequency harmonics is neglected. The PI controllers in both channels are designed

assuming that the inverter is ideal, and that the gain of the converter of $V_{dc_link}/2$ is constant. In reality this will change as the dc-link voltage is changed, but typically over a relatively small range. Control of this dc-link voltage is described in the following section.

4.6.4.2 Voltage loop

The current i_{d_g} produces real power out, while i_{q_g} can be controlled to meet reactive power requirements according to equation (4.28). The quadrature component of the grid voltage $v_{qgrid}(t)$ is zero as the *d*-axis of the reference frame is aligned to the phase voltage. Since the amplitude of the grid voltage is constant, v_{dgrid} is constant.

$$P(t) = \frac{3}{2} i_{d_g}(t) v_{dgrid} \tag{4.27}$$

$$Q(t) = \frac{3}{2} i_{q_g}(t) v_{dgrid} \tag{4.28}$$

The equations that govern the dc-link voltage and current are given in equations (4.29) and (4.30) only taking account of the grid-side converter, and assuming the modulation index of the converter is a constant over a relatively small range. The converter is to operate in buck mode only, where power is exported to the grid. Also switching harmonics losses and the losses in the converter and inductor are neglected.

$$I_{dc_link} = \frac{3}{2\sqrt{2}} i_{d_g} \tag{4.29}$$

$$V_{dc_link} = \frac{1}{sC} I_{dc_link} \tag{4.30}$$

The voltage strategy in this chapter consists of setting a desired voltage for the dc-bus, $V_{dc_link}*$, and the system responding to produce this voltage using a PI controller as shown in Figure 4.8. This is similar to the control scheme implemented in [66]

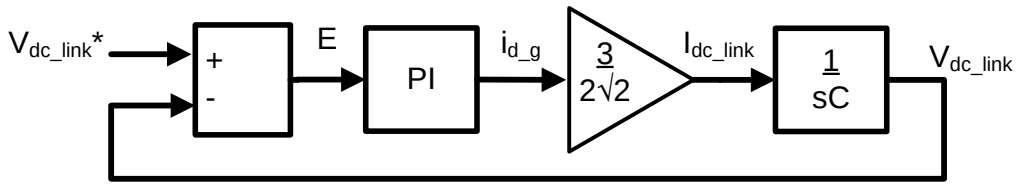


Figure 4.8: Dc-link voltage control strategy

This control scheme produces the following open loop transfer function in equation (4.31) for the system. This assumes that this tracking of i_{d_g} is ideal. This control of i_{d_g} is described in the previous section.

$$\begin{aligned} TF_{volt_open_loop}(s) &= \frac{V_{dc_link}}{V_{dc_link}\ *} \\ &= \frac{k_{p_g_volt}\left(s + \omega_{i_g_volt}\right)}{s} \frac{3}{2\sqrt{2}} \frac{1}{sC} \end{aligned} \tag{4.31}$$

Due to the assumption that tracking of i_{d_g} is ideal and for stability purposes, the voltage loop bandwidth is set ten times lower than the current loop. This sets the cut off frequency at 20 Hz. Utilising a desired phase margin of 80° allows the PI gains to be evaluated by solving equations (4.32) and (4.33).

$$\left|TF_{volt_open_loop}(j\omega_c)\right| = 1 \tag{4.32}$$

$$\angle TF_{volt_open_loop}(j\omega_c) = 80° \tag{4.33}$$

This results in values of 4.3 for $k_{p_g_volt}$ and 46.8 for $\omega_{i_g_volt}$.

A full PWM averaged model of the machine converter was developed in Simulink using the SimPowerSystems library, and the resulting schematic is shown in Figure 4.9.

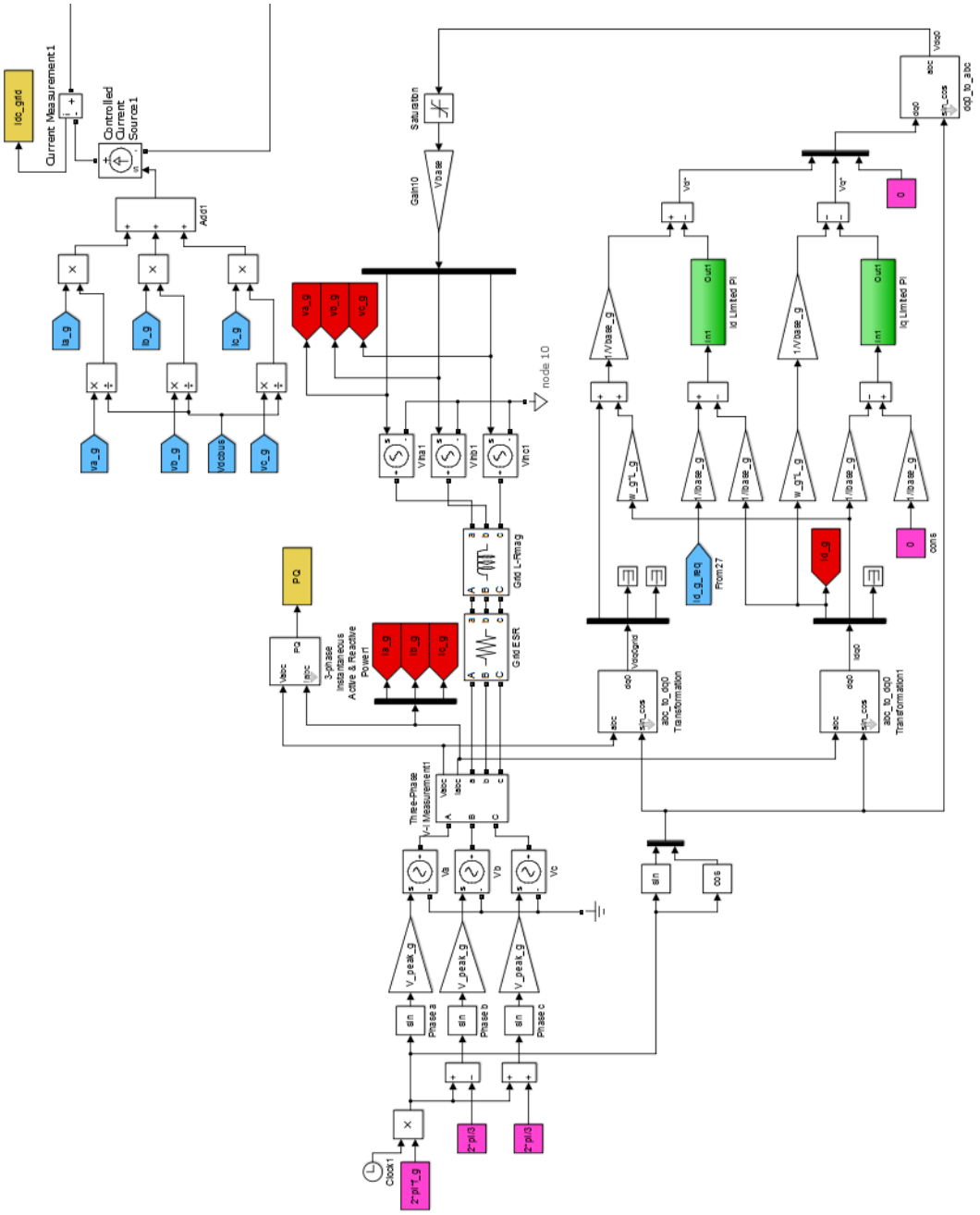


Figure 4.9: Simulink schematic of the grid-side converter

4.6.5 Supercapacitor (SC) converter and control

Equivalent circuit models for SCs have been examined in [67], [68], and [69]. They include the RC model, parallel-branch model, transmission-line model, and the multi-branch model. This chapter uses the classical RC model shown in Figure 4.10 which includes the most important parameters, while still allowing processing power to simulate the rest of the system. The equivalent series resistance, R_{esr}, limits the charge/discharge current of the device and contributes to internal heating. The parallel

resistance, R_{epr}, simulates the energy loss due to self-discharge and also governs the steady state voltage distribution across each device in a series connected module.

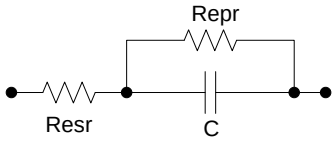


Figure 4.10: SC equivalent circuit used

In order to decouple the SCs from the system and allow full control over their operation, a bi-directional dc-dc converter was used. The SC module was placed on the low-voltage side of the converter in order to obtain full use of the SCs' voltage and energy range [70]. Also, modules tend to be available with low voltage ratings. The proposed system can be seen in Figure 4.1.

One of the objectives of this chapter was to power up the system from rest. To estimate the capacity of SCs needed, the following equations were used.

$$W_{turbine} = \frac{1}{2} J {\omega_m}^2 \tag{4.34}$$

$$W_{SC} = \frac{1}{2} C \left({V_{max}}^2 - {V_{min}}^2 \right) \tag{4.35}$$

The set point speed for the system is 1,100 rpm and the total inertia of coupled masses is 100 kg m^2. From this, the total kinetic energy stored in the system from rest (neglecting friction) is 665 kJ.

The BMOD0063 P125 SC module, from Maxwell Technologies, was chosen for this project. The standard voltage rating is 125 V, and the capacitance is 63 F. Using equation (4.35), the energy available from the module when fully charged is around 370 kJ. Therefore two such modules in series give 740 kJ. This should provide the required energy level and have enough excess energy to overcome heating losses in parasitic elements and friction losses in the turbine. Given the capacitance tolerance of the module, voltage balancing is required. It is common practice to choose the minimum voltage at half the maximum value and then to add a 20% safety margin to the

required energy value (to ensure that energy requirements are still satisfied near SCs' end of life). With this in mind the energy of two such modules in series gives 591 kJ at 80% capacitance. While this may not be enough to speed the turbine up to 1,100 rpm, as the speed increases more and more input torque will be experienced and aid in the acceleration to the set speed where normal operation can occur.

The voltage range of 125 V – 250 V is also high enough for the bi-directional dc-dc converter to operate when connected to the 690 V dc-bus. The specifications of a single BMOD0063 P125 module are shown in Table XIV.

Table XIV: Parameters of the SC module [54]

The BMOD0063 P125 module from Maxwell Technologies Inc.	
Capacitance (F)	63
Rated voltage (V)	125
Surge voltage (V)	135
Operating temperature range	-40°C to +65°C
Capacitance tolerance	+20% / -0%
Cycle life (cycles)	1,000,000
R_{esr}, DC (mΩ)	18
Mass (kg)	59.5
Max continuous current (A)	150
Max peak current, 1 second (A)	750

It is specified in [54] that, after 30 days, 50% of the initial voltage remains. The parallel resistance shown in the equivalent circuit in Figure 4.10 is thus calculated to be about 120 kΩ, using equation (4.36). This module employs Maxwell's Voltage Management System (VMS), assumed ideal for this chapter.

$$R_{epr} = \frac{-(t_2 - t_1)}{ln\left(\frac{V_2}{V_1}\right) C} \tag{4.36}$$

The capacitance of the SC module is quoted at dc and this rapidly reduces to a very low value beyond 100 Hz [71]. Therefore, the SCs cannot significantly attenuate the voltage ripple generated by switch mode converters and filtering is required. It is recommended in [71] to use a low valued inductance in series with the SCs, to attenuate this ripple and

to increase lifetime. Selection of this filter inductance is important as it operates in both buck and boost mode. Minimisation of this device using variable switching frequency is examined in [72], while an extra filter stage comprising of a low value inductance is shown in [71]. This work used an averaged PWM SimPowerSystems model to simulate the time periods under investigation, and filtering of the high frequency effects with an inductor was not needed.

The maximum output power transfer theorem dictates that the available power from SCs is given by equation (4.37).

$$P_{max} = \frac{1}{4}\frac{V^2}{R_{esr}} \tag{4.37}$$

This is calculated to be 109 kW for the sized SC system at the minimum operating voltage. Clearly it is much lower than this limit in practice for the lifetime reasons outlined above and also to ensure the temperature of the module remains within specified limits. From the data above, the maximum output power ranges from 73.5 kW to 167 kW for a maximum of one second, or 18 kW to 36.5 kW corresponding to the rated maximum continuous current.

The operating voltage of the SC module during WEC operation was chosen at half the usable energy range which is 197.6 V. Using (4.38), the maximum voltage of the SC modules when charged at rated current for three seconds and with 80% capacitance was checked to ensure ratings would not be exceeded during LVRT. This was found to be 239 V.

$$I_c = C\frac{dV}{dt} \tag{4.38}$$

A PI controller was utilised to achieve the desired SC current necessary to balance the power flows of the system.

4.7 Turbine start-up control scheme

As seen in Figure 4.1 the system topology consists of the generator connected to the grid via full-rated back-to-back PWM voltage-source converters.

The control strategy used for the motoring sequence consists of first setting i_d to zero in the grid-side converter to prevent active power flow through the device. Also, as flux weakening mode will not be used in the PMSM, i_d is set to zero in the machine-side converter.

The machine-side converter controls the speed of the turbine using cascaded speed/current loops. The limit for the inner current loop is initially set to ensure that the current rating of the converter is not exceeded.

The dc-link voltage is maintained at the desired set point by controlling the SC current. As the machine accelerates due to i_q, the input power increases and the current drawn from the SC module increases. Once the current rating of the SC module is reached, it is maintained at this value and control of the dc-link voltage is now achieved using the machine current i_q. This controlled current sets the limit of the inner current loop.

Obtained plots for this scheme are shown in the results section. Total energy flows in the circuit are also observed.

4.8 Low-voltage ride-through (LVRT) control scheme

Due to the use of a full rated back-to-back converter, the grid and machine frequencies are decoupled. Also, this topology allows control of active and reactive power to and from the gird via the use of the currents i_{d_g} and i_{q_g}.

The grid code states that the renewable energy source should provide active power in proportion to the retained grid voltage, but for a turbine operated at constant speed, the output power profile corresponds to the fluctuating response of the Wells turbine to the input pneumatic power. In order to supply a fixed power in proportion to the retained voltage, the current i_{d_g} is fixed during the low-voltage event according to equation (4.27) shown again in equation (4.39).

$$P(t) = \frac{3}{2}\, i_{d_g}(t) v_{dgrid}(t) \tag{4.39}$$

Due to difficulties in predicting input energy over a three second period in highly variable sea-states, this parameter is calculated using worst case conditions to ensure the turbine speed rating is not exceeded during the fault. Also it is important to ensure that the turbine will not decelerate below the minimum operational speed limit during

low energy or high stall events. A significant amount of reactive power needs to be generated according to the grid code.

The grid-side current i_{q_g} is evaluated to maximise reactive power ensuring that limits for current or inverter voltage are not exceeded according to equations (4.40) and (4.41).

$$\hat{\imath}_a(t) = \sqrt{i_{d_g}(t)^2 + i_{q_g}(t)^2} \tag{4.40}$$

$$\hat{V}_{inv}(t) = \hat{V}_a(t) + \left(i_{d_g}(t) + j\, i_{q_g}(t)\right)\left(R_g + jX_g\right) \tag{4.41}$$

This method allows for a clear prediction of output power and reactive power from the WEC for all low-voltage events.

The desired dc-link voltage is achieved by controlling the machine current i_{q_m}, while the supercapacitor module is used to control turbine speed ensuring limits are not exceeded.

In this simulation, a three phase fault is analysed resulting in the most severe voltage profile which the system has to endure. The case where SCs are not used (with no control over turbine speed) is shown, followed by the same conditions using the SC module. Sea-state data is used to give a typical turbine torque input during the event.

4.9 Results

4.9.1 Turbine start-up utilising supercapacitors (SCs)

Results from the start-up control strategy using SCs are illustrated in Figure 4.11 and Figure 4.12.

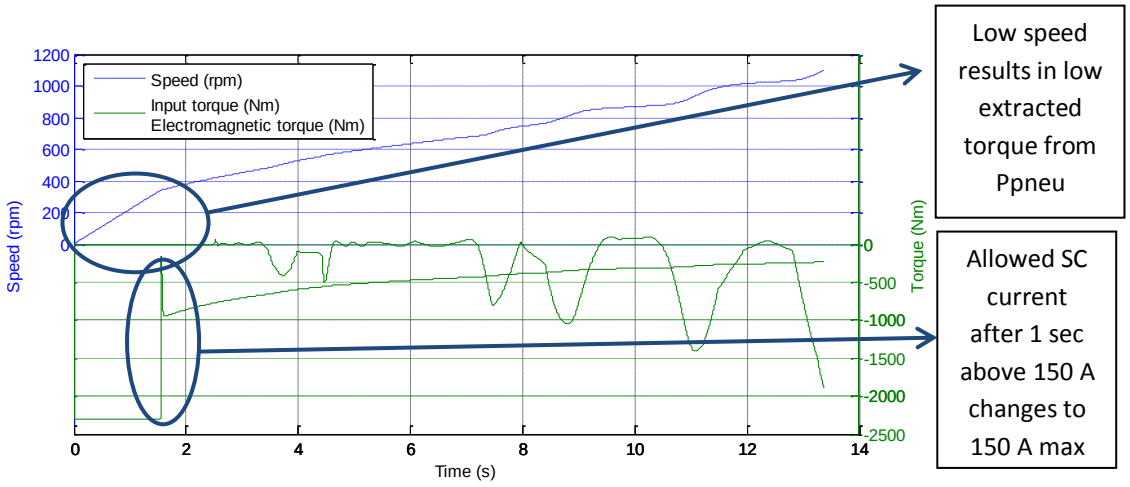


Figure 4.11: Speed, input torque and electromagnetic torque versus time during turbine start-up with typical sea-state data

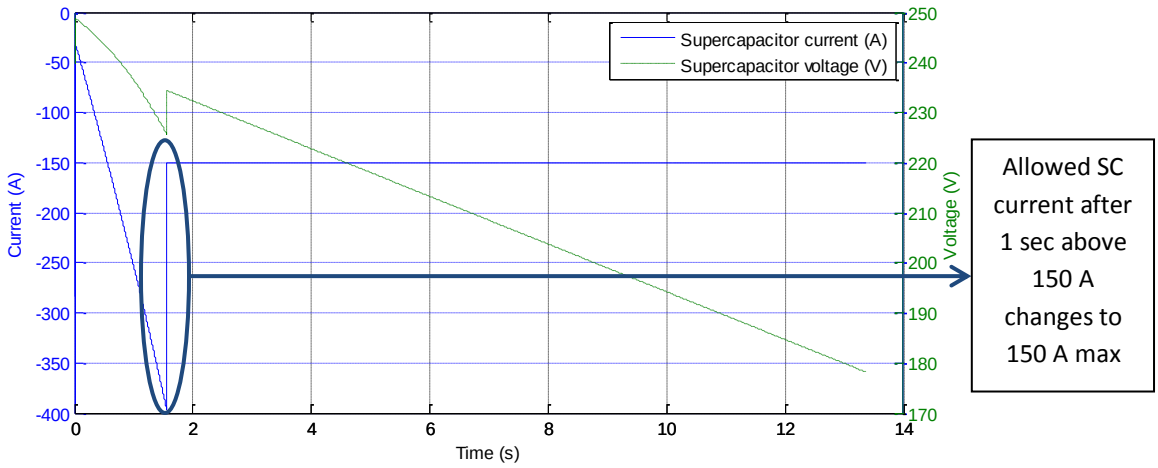


Figure 4.12: SC voltage and current during turbine start-up

It can be seen in Figure 4.11 and Figure 4.12 that it takes 13.75 seconds to accelerate the turbine to the set speed from rest. Initially the PM machine accelerates at rated torque (rated i_{q_m}), until the SC current limit comes into effect. As expected, the additional turbine input torque from the WEC's pneumatic power increases as the speed increases. It is specified in Table XIV that the continuous rated current can be exceeded for one second up to a value of 750 A. This was taken into account before control of the dc-link voltage was taken over by the machine quadrature current i_{q_m} from the supercapacitor module.

Two tests were carried out. In the first test, the input torque was set to zero, and in the second test, real sea-state data was used to produce an accurate input torque during start-up. The first test demonstrates worst case conditions as low input wave energy events occur in all sea-states and a low energy event may occur after the start signal. The energy values are shown in Table XV.

Table XV: Energy supplied and lost in the system during turbine start-up (assuming an ideal converter)

	Motoring without P_{pneu}	**Motoring with P_{pneu}**
Time taken (s)	26.60	13.37
	Energy at full speed (J)	
	665,288	665,296
	Energy supplied (J)	
Supercapacitor	755,423	453,543
P_{pneu}	0	257,323
	Energy lost (J)	
Turbine friction	51,165	18,495
Generator R_s	15,561	14,454
Supercapacitor R_{esr}	23,275	12,556
Dc-bus capacitor R_{epr}	127	64
Supercapacitor R_{epr}	8	5

It is noted that the energy of the rotating turbine is approximately equal to the energy supplied by the SCs plus turbine, minus losses. The small difference is due to the energy stored in the inductances of the machine and rounding of values.

4.9.2 Low-voltage ride-through utilising supercapacitors (SCs)

Plots from the LVRT analysis are shown in Figure 4.13, Figure 4.14, Figure 4.15, Figure 4.17, Figure 4.18, and Figure 4.19. The transient is simulated for four seconds, and voltage collapse begins at 0.75 seconds. The low-voltage event mirrors the worst case conditions shown in the grid code requirement of Figure 4.2 and lasts three seconds. The grid voltage profile is given in Figure 4.13.

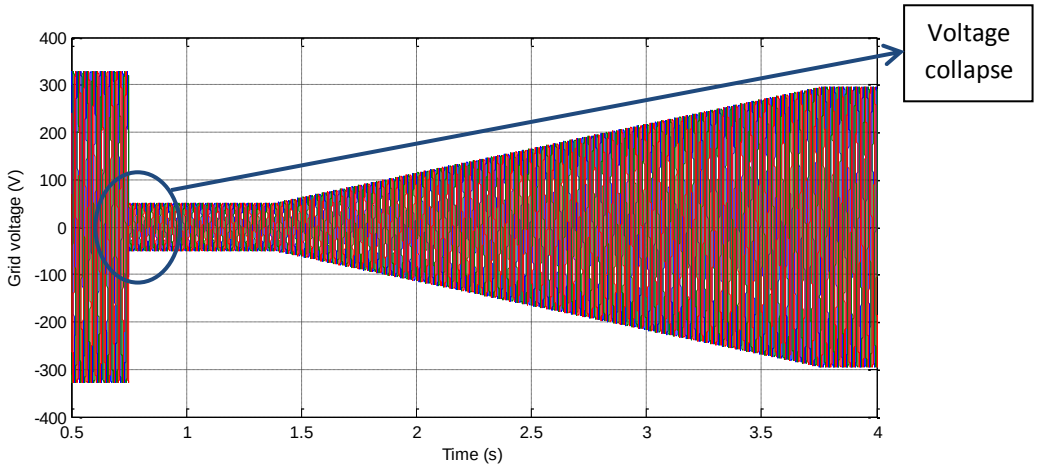


Figure 4.13: Grid voltage during LVRT event

The output grid current, power and reactive power are seen in Figure 4.14 and Figure 4.15 respectively. Active power in proportion to the retained voltage is achieved while maximum reactive power is output while satisfying current and converter voltage ratings.

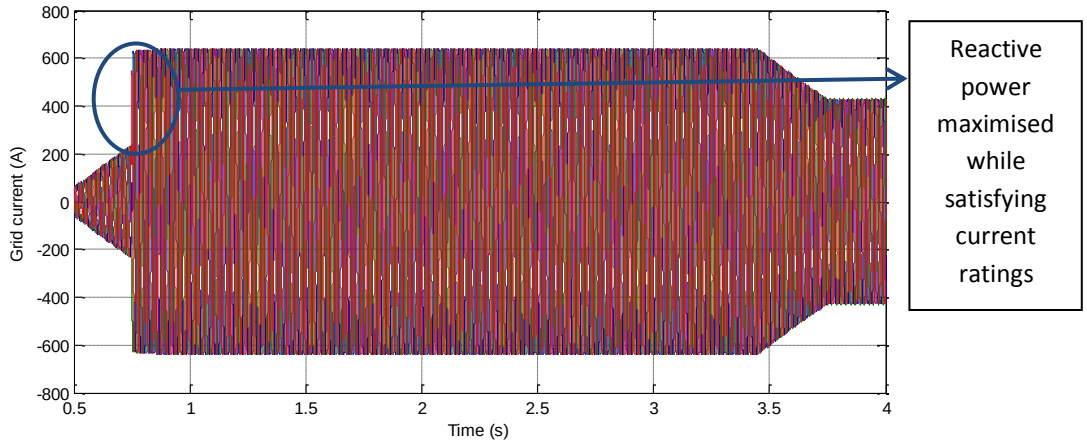


Figure 4.14: Grid current during LVRT event

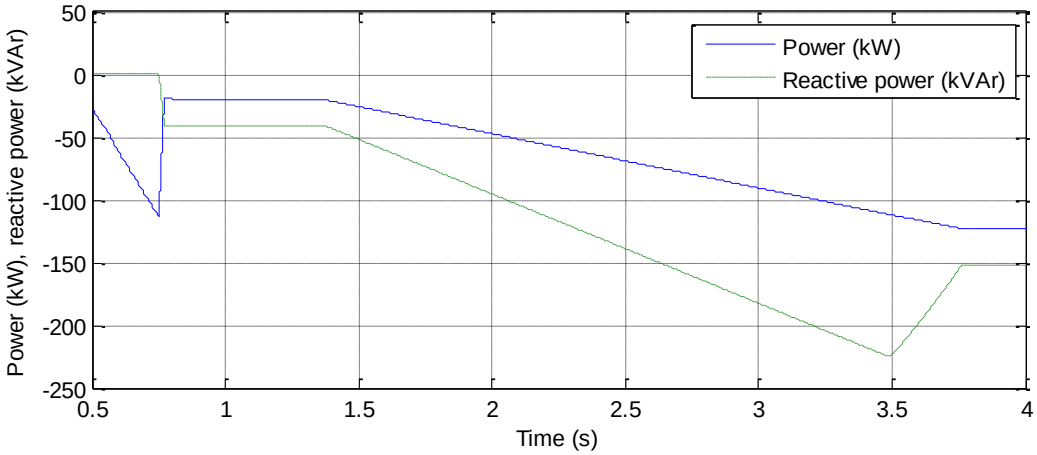


Figure 4.15: Grid power and reactive power during LVRT event

The converter voltage output is seen in Figure 4.16. Maximum voltage rating is encountered before 3.5 seconds, and as active power is still increasing in proportion to the retained voltage the reactive power current drops to ensure the voltage rating isn't breached in accordance with equations (4.40) and (4.41).

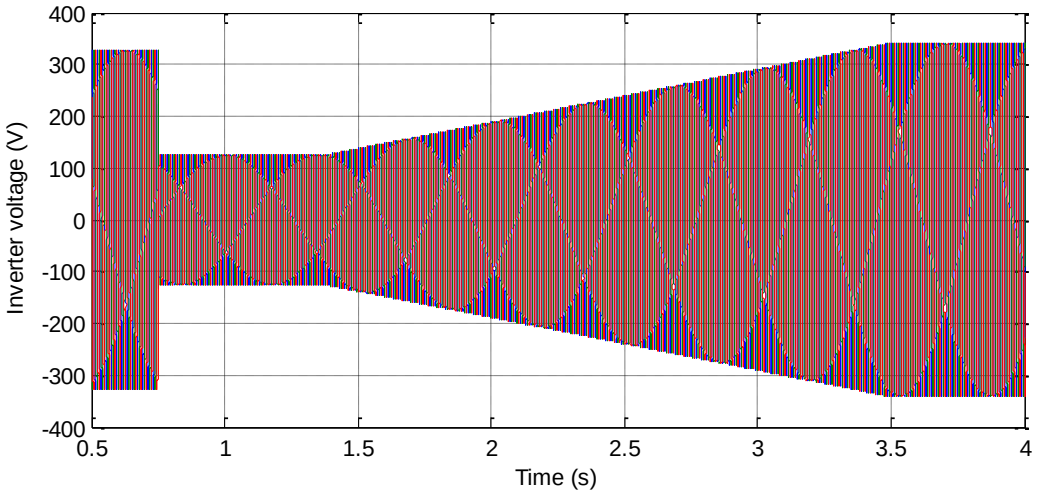


Figure 4.16: Inverter voltage during LVRT event

Figure 4.17 illustrates the corresponding turbine speed and input torque for the case without supercapacitor (SC) energy storage. It is seen that a significant over-speed occurs.

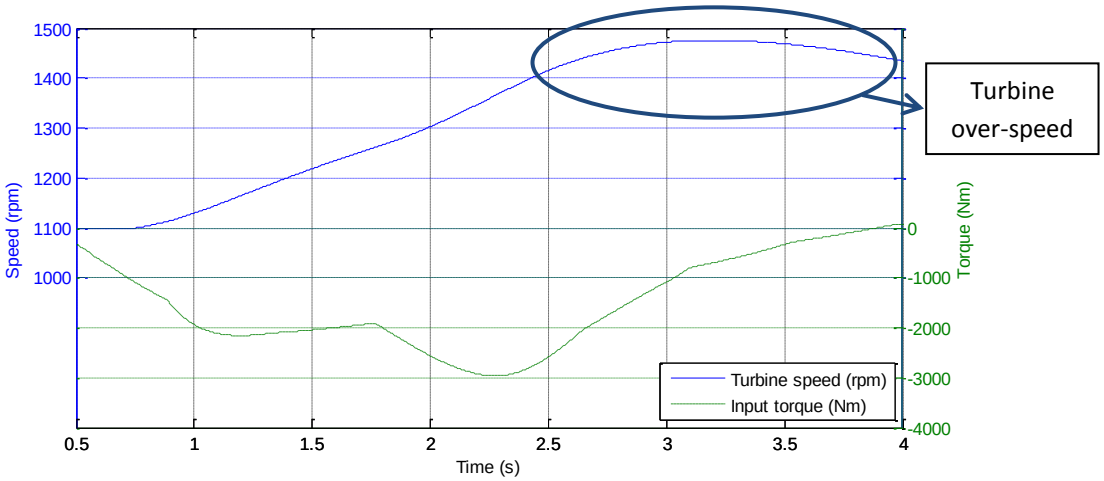


Figure 4.17: Turbine speed and input torque during LVRT event without SCs

Figure 4.18 and Figure 4.19 demonstrates the situation in which the SC module is employed. The SC current and voltage ratings are satisfied, and turbine speed remains within limits. The same input wave data is applied in both tests, and stall is seen to occur in Figure 4.18 as turbine speed is reduced. As the speed increases for the case without SC energy storage in Figure 4.17, this turbine stall effect does not occur to the same degree. This is because at increased speed stall begins to occur at a larger input torque.

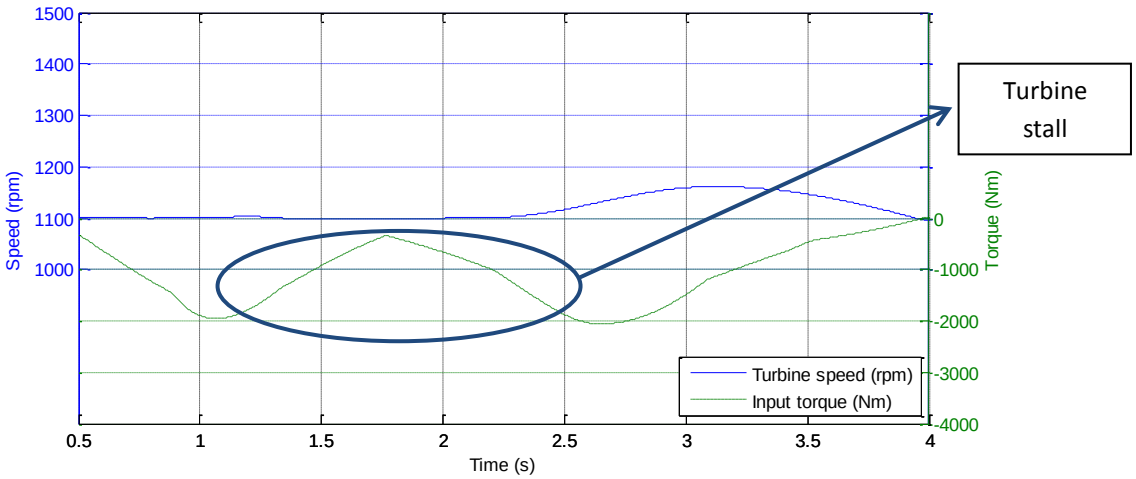


Figure 4.18: Turbine speed and input torque during LVRT event with SCs

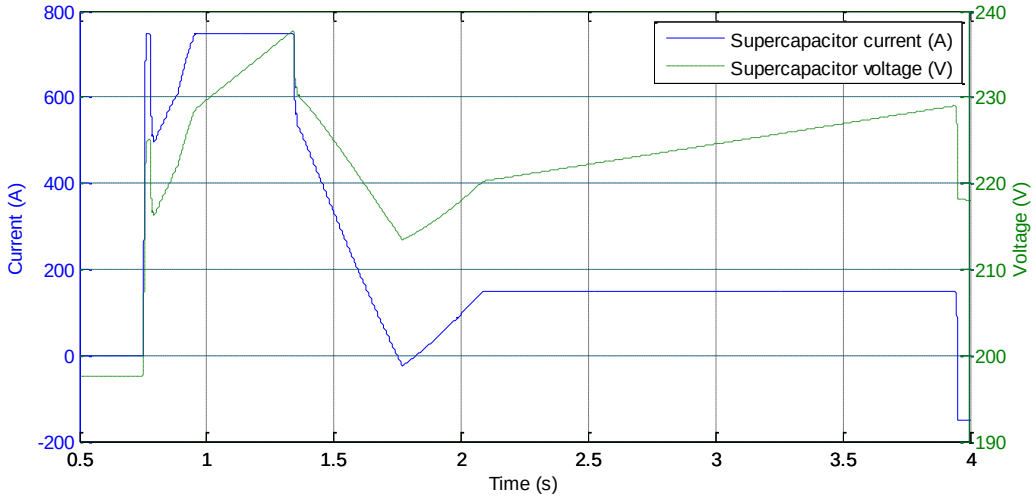


Figure 4.19: SC voltage and current during LVRT event

4.10 Conclusions

This chapter reviewed the use of SC energy storage in renewable energy systems. It was shown that a significant increase in SC cycle lifetime needs to be demonstrated before the application of power smoothing with SC modules over every wave period can be considered for future WEC prototypes.

Two applications of SCs were shown using a full sized WEC SimPowerSystems model, namely turbine start-up and low-voltage ride through (LVRT). The control requirements of the generator power take-off (PTO) system were highlighted. This consisted of SC energy storage coupled to the dc-link of a back-to-back converter via a dc-dc power converter.

By employing SCs to power-up the turbine, starting surge for a wave farm can be minimised. Also, by contributing towards LVRT, future grid codes may be satisfied and redundancy is built into the system.

Electrical power is needed in offshore WECs for lighting, communications, equipment monitoring, and control purposes. Heating and ventilation equipment may also need to be powered. Thus, some form of energy storage is needed and due to the high energy density values of batteries, as seen in Section 1.6, these seem ideal devices for this application. Employing SC energy storage to operate during these high power events would complement this battery system and could extend the battery lifetime.

A high-voltage Li-ion battery is investigated in the next chapter and the safety and practical aspects of implementing a high power energy storage system to a power converter and grid are explored in the emerging field of microgrid research.

Chapter 5 Integration and testing of a high-voltage lithium-ion battery into a microgrid

5.1 Introduction

As part of a microgrid development research project with a view to investigating pulsating power phenomena in electrical power systems, a 15 kW power converter and high-voltage (HV) lithium-ion (Li-ion) battery were integrated. This took place at the Hydraulics and Maritime Research Centre (HMRC), UCC, in Cork, Ireland. The microgrid itself currently consists of a diesel generator, load bank, electronic load, and wind-turbine emulator rig, under the supervisory control of a Programmable Logic Controller (PLC) system.

This chapter details the following

1. The integration of this battery and power converter system into the microgrid.
2. The design and development of the local controls and safety features.
3. The implementation of software, networking, and modelling requirements for the system.

The internal Li-ion battery model in SimPowerSystems in Matlab/Simulink is then compared to data obtained from step and full charge/discharge tests of the battery. A new piecewise equation is then proposed and fitted to the discharge profile to describe voltage versus state of charge (SOC).

5.1.1 Motivation

The previous chapters detail work carried out with SC energy storage with a focus on possible applications in an offshore WEC, as well as integrating SC and turbine inertia energy storage in a variable speed scheme for offshore WECs. This chapter focuses on the potential of Li-ion battery energy storage.

Li-ion batteries are gaining market share in EV and renewable applications and are currently employed in the Nissan Leaf, Mitsubishi iMieV, Ford Fusion, and Chevy Volt. The maximum state of charge for the Li-ion battery in the Nissan Leaf is recommended

to be set to 80% to extend battery life [73]. A recent NREL publication provides more data on battery degradation in plug-in electric vehicles (PEVs) subject to ambient conditions, size and usage patterns [74].

It's shown in Chapter 1 that Li-ion batteries could also achieve a high cycle life, into the millions, by reducing the DOD they operate over. Other ways of improving battery performance have been explored in [42] [43] [44], where SCs are used to assist high power events, increase battery lifetime, and improve efficiency. It is proposed in [75] to use a battery to help smooth out the slow-varying power components in a stand-alone wave energy plant and to use a SMES system for the fast-varying components. This concept could also be applied to a system incorporating battery and SC energy storage technology.

With the increased proportion of renewable generation and smaller generators on the grid, many systems are of yet not well integrated with nearby renewables or to the external grid. Also, overall system performance is not optimised for efficient, reactive and sustainable operations in the event of power outages or periods of high stress on the grid [45]. This has led to an increased focus on microgrids to help manage these areas encompassing local generation and local loads.

The two modes of operation for a microgrid are islanding mode and grid connected mode [76]. During islanding mode, the main role of energy storage is to perform an energy balance and during grid connected mode the main role of employed energy storage is to prevent propagation of the renewable source intermittency and load fluctuations to the grid [76] [77]. While suitable energy storage options in the high power range for standard power systems would comprise of pumped hydro storage, compressed air storage etc., for microgrids where power levels are in the range of a few megawatts, battery, supercapacitors and flywheels are more suitable options [76]. An outline of some of the research and development of microgrids in Europe, the United States, Japan, and Canada is given in [78].

While the previous chapters explored modelling and SC testing, the safety, communications and control requirements of an energy storage system build (and associated power converter) have yet to be addressed. This chapter gives a better understanding of these requirements and explores Li-ion battery technology in the emerging field of microgrid research.

5.1.2 Battery overview

The 5 kW h air-cooled Li-ion battery pack is manufactured by LG Chem Power Inc. The battery has a continuous power rating of 10 kW and a peak rating of 65 kW. It has a maximum operating voltage of 410 V, a minimum of 260 V and a nominal voltage of 360 V. The battery is made up of 96, 15 A h "P1" cells developed by LG-Chem utilising Li-ion polymer technology. It is specified in [79] that these "P1" cells have a specific energy of 150 Wh/kg and energy density of 300 Wh/L. These cells are arranged in 6 modules with cell balancing control available from the battery management system (BMS). Full specifications are given in Appendix I.

The battery consists of a large metal casing with an air inlet filter and an outlet fan. A low-voltage connector is utilised for signalling, safety and fan power control. The high-voltage connector to the main battery incorporates an inbuilt high voltage interlock loop (HVIL) safety feature. A ground strap is connected to the chassis of the unit. An extra layer of safety when performing work on, or transporting the battery, is provided by a Manual Service Disconnect (MSD) device.

Figure 5.1, Figure 5.2, and Figure 5.3 show the battery in its transport plastic casing, as well as the location of connectors, fan and MSD.

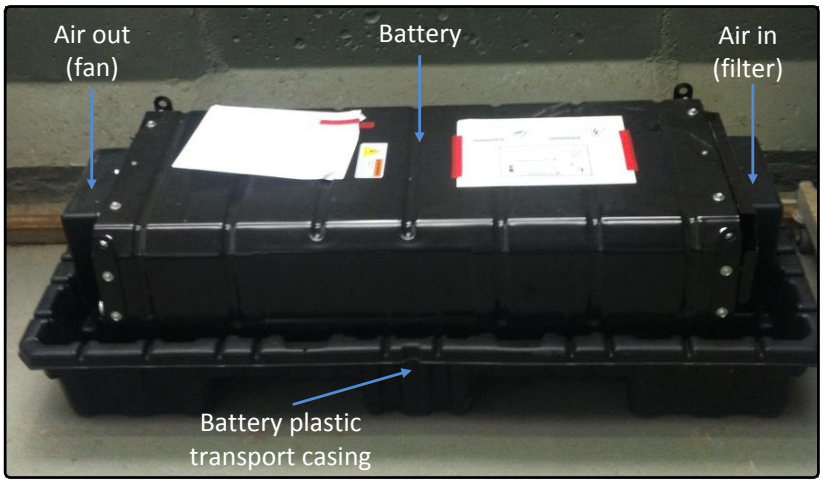


Figure 5.1: Li-ion battery

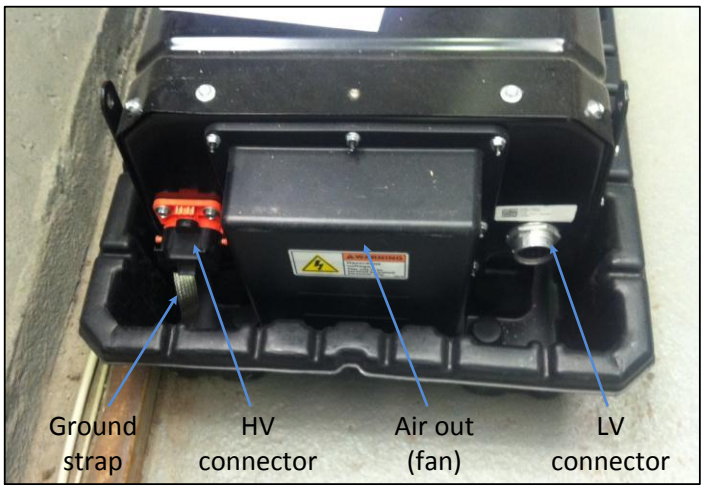


Figure 5.2: Battery side with high and low voltage connectors

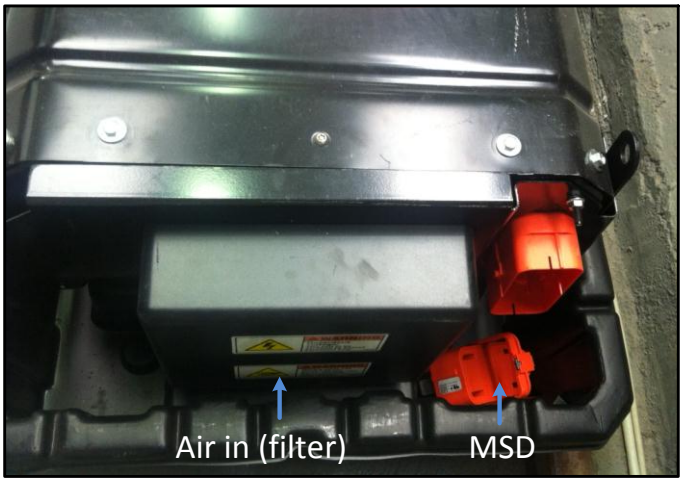


Figure 5.3: Battery side with MSD

5.1.3 Power converter overview

A 15 kW power converter with control of three phase ac channels and active neutral, and two dc-channels was purchased from Triphase NV, Belgium.

The converter uses real-time Ethernet (the EtherCat fieldbus) from a Linux-based industrial PC to control the IGBT based converter. This converter can operate in the switching range of 8 to 16 kHz. The Linux based industrial PC is programmed via Ethernet from an engineering PC. Control and programming are carried out in the Matlab/Simulink environment, with some proprietary Simulink toolboxes created by

Triphase also required. The inverter circuit connects to the grid, and the dc circuit connects to the battery via LC filters (or optional LCL filters).

A brief overview diagram of the electrical circuit with the active neutral ignored is shown in Figure 5.4.

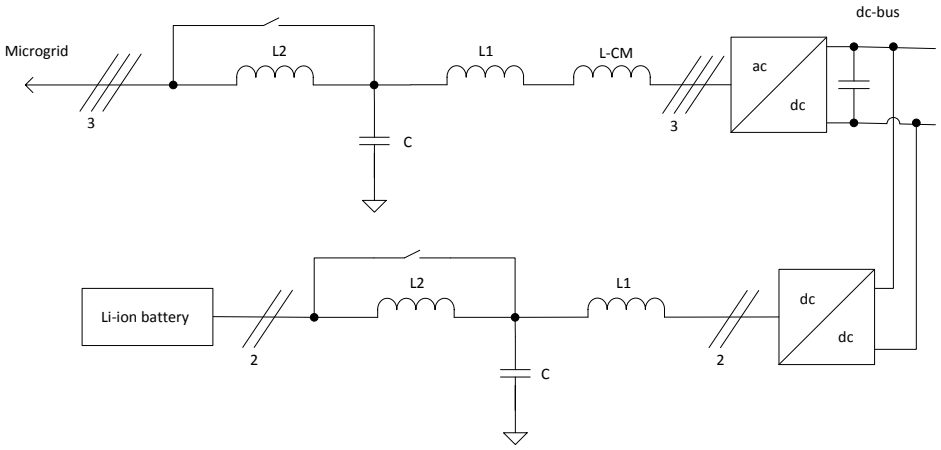


Figure 5.4: Power converter electrical circuit overview

Some of the main specifications of the power converter and filters are shown below.

Table XVI: Triphase power converter specifications

Parameter	Value	Unit
Sample PWM frequency	8	kHz
Bus capacitance	600	µF
L1 (filter inductance)	2.3	mH
C (filter capacitance)	10	µF
L2 (optional filter inductance)	0.93	mH
C-CM (ac common mode filter effective capacitance)	0.68	µF
L-CM (ac common mode filter inductance)	20	mH

5.2 Objectives

An overview of the system with the main power and communication lines are shown in Figure 5.5.

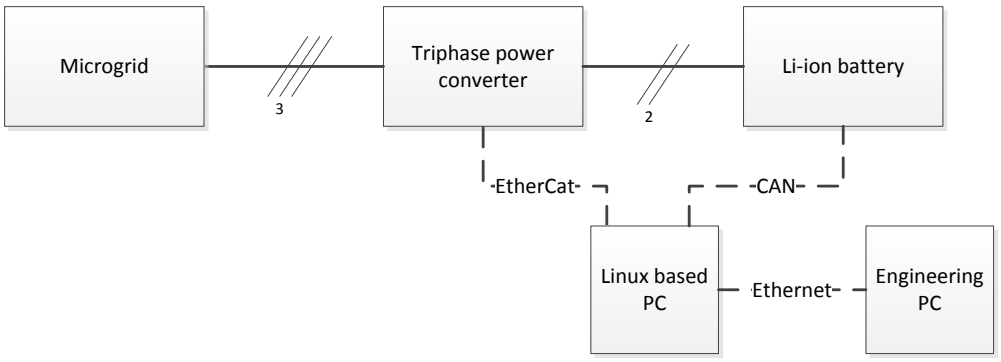


Figure 5.5: Overview of microgrid to battery connection with the main power and communication lines

This chapter aims to explore some of the design, safety and cost requirements of implementing a high power energy storage system through a power converter to a microgrid/grid. This technology is applicable to the development of offshore renewable systems.

The validity of the internal Li-ion battery model in SimPowerSystems in Matlab/Simulink, used to estimate battery parameters such as voltage and state of charge is also examined.

5.3 Device operation

The safety features included are examined before initial testing is carried out, or final designs created.

5.3.1 Safety features of the lithium-ion (Li-ion) battery

The Li-ion battery is a high-voltage product and inherently contains hazardous material. The battery manufacturer has implemented many safety features for personnel and equipment. Some of these safety features are:

- An internal battery management system (BMS) with contactors. This only allows the internal contactors to operate and enable high voltage at the external terminals if multiple conditions are met. These conditions include:
    - All connectors are in place.
    - The high-voltage interlock loop (HVIL) is shorted. This is wired alongside the high voltage connector.
    - Individual cell and overall battery voltages and temperatures are within limits.

    - Receipt of the specified CAN message over the CAN fieldbus.
    - Internal battery electronics are powered (12 V).
- Safe operating conditions for the internal battery cells are maintained under control of the BMS which maintains the internal temperature between limits via fan control, as well as carrying out voltage balancing.
- A manual service disconnect (MSD) containing a 125 A fuse as part of the internal battery circuit. This battery MSD needs to be installed to allow the internal battery contactors to operate. A guideline of "last in, first out" is specified for the MSD to prevent accidental high-voltage exposure. This means that removal of the MSD should be carried out first when performing work on the system, and that the reinsertion of the MSD should be carried out last when finished this work and before powering up the microgrid/battery system.
- The battery contains a solid grounding point to the chassis
- Cables with robust shielding and insulation.
- A lockable well-insulated high-voltage connection point to the battery.
- Clear warning labels on the battery.
- The user manuals comprehensively cover safety and include a "material safety data" section detailing fire fighting measures.

Additional safety work/features carried out initially include:

- The protective casing the battery was shipped in consists of a hard, plastic shell with removable top. This provided safe housing for the battery during preliminary testing before the final system was built.
- Safety labelling was added to, and the safety section of the manual was made available with the battery.
- A Class D fire extinguisher for combustible metals was installed beside the battery system.

5.3.2 Lithium-ion (Li-ion) battery

To operate the battery some specific low voltage signals need to be powered and integrated. The following table of signals describes the low voltage requirements for the Deutsch 18-pin low voltage connector (HD34_24_18PE).

Table XVII: Low voltage connector pin-out

Pin #	Description	Voltage	Current (typical)	In-Rush	Note
2	Vehicle CAN HI	0 - 5 V			Communications
3	Vehicle CAN LO	0 - 5 V			Communications
6	Fan Power (+)	8 - 16 V	8 A		
8	Fan Power (-)	0 V			
9	VBATT	8 - 16 V	1.7 A		
10	Vehicles PSR (ignition)	8 - 16 V	0.9 A	4 A	4A power supply required
11	Ground				

Using shielded twisted pair cables, the CAN cable network is set up, with the battery end pin-out specified in Table XVIII. Other devices connected to the CAN fieldbus utilise standard 9-pin D-sub connectors with the pin-out shown in Table XVIII. These devices include a purchased CAN monitor and the Linux based target PC which operate the IGBT power converter.

Table XVIII: D-sub 9-pin connector pin-out

Pin #	Description
2	CAN L (twisted pair)
3	Ground
5	Shield
7	CAN H (twisted pair)

The CAN network requires 120 Ω terminations at two ends. One is an internal termination in the battery while the other termination was added beside the Linux based industrial PC CAN connection.

5.3.3 Controller Area Network (CAN)

The battery communications to and from the BMS operate via the controller area network (CAN) fieldbus. More specifically, the battery communicates under the J1939 CAN automotive broadcast standard from the Society of Automotive Engineers (SAE). This is a high-level protocol defining how communication between equipment occurs on the CAN bus. Any unit on the bus is permitted to transmit a message to the network when the bus is idle. This protocol operates under the CAN 2.0 B standard which uses the extended frame format. Therefore, every message includes a 29 bit identifier which

defines the message priority and which device is communicating. The message data is contained in the 8 bytes that follow the identifier.

Data is sent under a Parameter Group Number (PGN) which uniquely identifies the Parameter Group (PG) being transmitted in the messages. The battery operates using "Proprietary B" PGNS (in the range of 00FF00 to 00FFFF), where messages and data lengths and groupings etc. are defined by the manufacturer.

The battery broadcasts messages to the bus at 250 kbit/s and with a typical update rate for most messages of 20 ms. A command message must be sent to the battery to activate the contactors once all battery hardware conditions are met. It is recommended to send this message repetitively at 20 ms.

The following messages are read from the battery:

- Hybrid Battery Data 1.
    - Discharge power available.
    - Charge power available.
    - Voltage level.
    - Current flow.
- Hybrid Battery Data 2.
    - Fast update state of charge.
    - Highest cell voltage.
    - Lowest cell voltage.
    - Cell voltage differential status.
- Hybrid Battery Data 3.
    - Highest cell temperature.
    - Lowest cell temperature.
    - Cell temperature differential status.
- Hybrid Battery Control.
    - High-voltage bus contactor command.
    - Power-down command.
    - Active isolation test command.

Each data set is interpreted using provided resolution, offset, and data ranges for each set of bytes in the CAN messages.

An example of a CAN message and its interpretation is given in Table XIX.

Table XIX: CAN message example sent from the Li-ion battery

PGN	Byte 0	Byte 1	Byte 2	Byte 3	Byte 4	Byte 5	Byte 6	Byte 7
FF922	6D	00	5E	00	BA	1C	FF	7C

FF92 is the PGN for the Hybrid Battery Data 1 message which has the following parameters.

- Discharge power available = 2 bytes (start position 1).
- Charge power available = 2 bytes (start position 3).
- Voltage level = 2 bytes (start position 5).
- Current level = 2 bytes (start position 7).

For example, the following given parameters are utilised to interpret the voltage level data.

- Resolution: 0.05 V/bit, 0 offset.
- Data range: 0 to 3,212.75 V.

Therefore, using bytes 5 and 6 above produce 1CFF in hexadecimal. This is equal to 7,423 in decimal, which when multiplied by the resolution of 0.05 V/bit gives 371.15 V.

5.3.4 Initial battery testing

Initial testing of the battery was carried out utilising:

- The resistive load of the microgrid. This is a 400 V, 10 kW, three-phase device. This load sinks 0 to 10 kW in discrete 0.5 kW steps at three phase 400 V ac.
- A Xantrex 600 V, 10 A power supply.
- A USB CAN monitor from Kvaser with galvanic isolation and associated software (the Kvaser Leaf Light HS (high speed)). This device is also able to send CAN messages to the bus.
- A 20 A low voltage dc power supply was utilised to power the internal battery electronics and fan.
- A switch across the high voltage interlock loop (HVIL).

To ensure that current ratings of cables and resistors would not be exceeded, initial battery testing was carried out across two of the resistor phases. This meant an

equivalent series resistance of 32 Ω across the battery at the 10 kW setting, and an equivalent resistance of 635 Ω at the 0.5 kW setting. Assuming a constant nominal 360 V dc battery voltage, this equates to discharge times for the 3.6 kW h battery of 540 minutes at the 10 kW setting, and almost 18 hours at the 0.5 kW setting.

The following plots were produced from two charge/discharge tests.

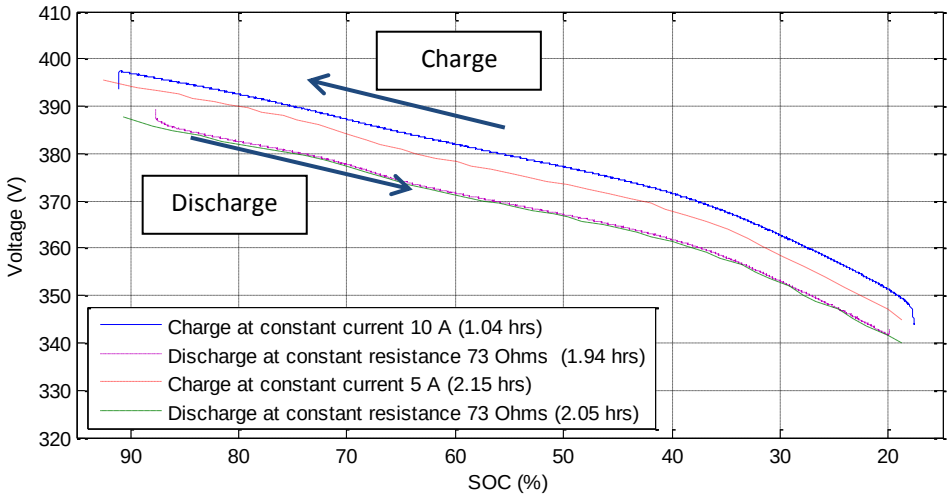


Figure 5.6: Li-ion battery voltage over approximately 20% to 90% state of charge (SOC)

5.3.5 Power converter operation

The power converter operates in real-time via a Matlab/Simulink real-time model. Converter Simulink models were provided by the manufacturer. These models facilitated testing of the in-built sensors, allowed full operation of the converter, and a simulation model was given to examine control operation.

The dc-bus is activated via a command that operates a contactor connecting to the microgrid. This charges the dc-bus through a diode bridge and a pre-charge resistor which is then automatically shorted out. Control of the dc-bus voltage is achieved once the model is activated, and the three-phase connection to the grid is closed and enabled. A timed pre-charge resistor across the capacitance of the grid side filter is automatically implemented in control. Resolved *d*-*q* axis components of currents are used, where the *d* component is in phase with grid voltage and the *q* component is in quadrature with it. The *d*-axis component of grid current controls the dc-bus voltage to the specified 660 V level, while the *q*-axis component can be used to specify a desired reactive current demand from the grid conductors.

The dc-dc converters to the battery are utilised in constant-current control to both source and sink power from the battery to the grid.

The power converter cabinet provides external circuit breakers to the three main circuits of the IGBT based power converter:

- The circuit to charge the dc-bus using the diode bridge rectifier powered directly from the three phase microgrid.
- The circuit used to control the dc-bus voltage and provide reactive power to the grid via PWM operation of IGBT switches.
- The dc circuit providing connection to the high voltage battery terminals.

Indicator lamps on the front of the converter show the status of the following:

  - If auxiliaries within the cabinet are receiving power.
  - If the dc-bus is activated.
  - If the real-time code is running.

Safety information, status of contactors and meters are also provided at the user engineering PC via the Ethercat fieldbus. This fieldbus standard operates over CAT 5E Ethernet cables between the Triphase power converter cabinet, the engineering PC, and the real-time Linux based target PC.

The interpretation of data sent on the CAN bus from the battery is achieved with the Triphase power converter target PC. This contains an interpretation file with data specified by an .xml file on the engineering PC, allowing the Matlab real-time model to read and send CAN data on the fieldbus. The proprietary battery PGN codes are defined in the .xml file. Assigned for each CAN PGN ID in the .xml file are the CAN bus period of data transfer, the order of data within a message, the size of a CAN message, and which CAN standard length is utilised.

The following figure shows the layout of the Triphase power converter cabinet before integration into the microgrid.

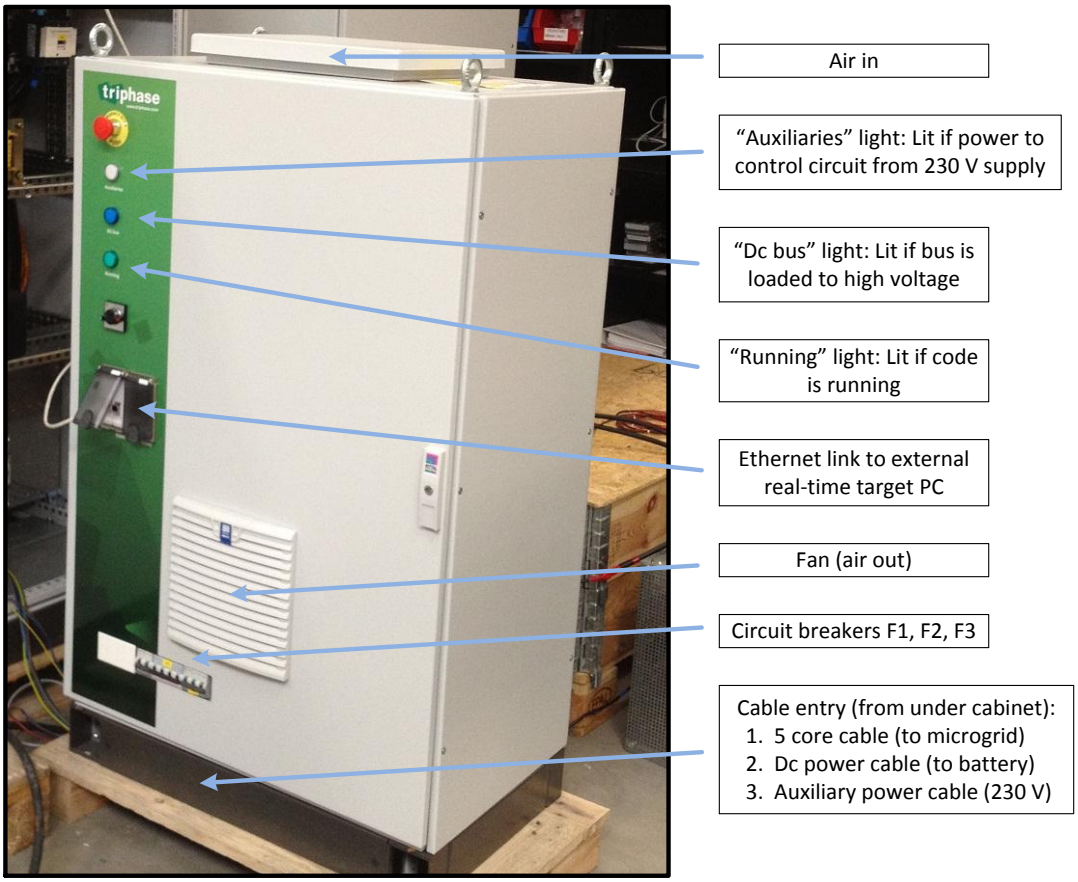


Figure 5.7: Triphase power converter cabinet layout

5.4 Integration of the power converter and battery to the microgrid

5.4.1 Floating the battery and isolation

During initial testing an isolation issue was identified which caused the BMS to trip the high-voltage supply to the external high-voltage terminals. This would prevent full testing of the battery in conjunction with the power converter. The BMS detects high voltage isolation faults between HV+ and the chassis, or HV- and the chassis, with an impedance monitoring circuit operating every five seconds. The Triphase power converter has paths to earth through the neutral. The earth has paths to the battery through the Triphase dc-dc converter, and the inverter also uses Y capacitors to ground.

Access to the internal battery circuitry or software was not advised. To resolve this problem the entire battery pack was floated and all connections to the battery were treated as potentially hazardous.

5.4.1.1 Isolation of the CAN cabling

A PCAN repeater device (part number IPEH-004038) was purchased from PEAK systems to isolate the CAN cabling connected to the battery from the rest of the system. This provides galvanic isolation up to 5 kV between two high-speed CAN buses and between the CAN channels and the repeater power supply.

5.4.1.2 The low voltage power supply

An industrial grade 12 V power supply with isolation from Tracopower was used to power the low voltage signals of the battery. This power supply included remote power on/off operation which allows the battery management system (BMS) to be reset.

The power supply was din-rail mountable with dual colour status indicator LEDs to help with diagnostics during initial testing and with double output terminals for ease of wiring.

5.4.1.3 Battery housing and floating supports

An enclosure was designed to protect the high-voltage battery in the industrial environment of the microgrid. This was made out of the robust and durable CUBIC system including metal frame and coverings. The CUBIC system comprises of standard modular sized pieces which aid in design and construction.

The system was designed to be substantially drip-proof, with ventilation openings on vertical surfaces on both sides of the housing. There was space for cable management to the battery inside the enclosure. A door was placed on the MSD side of the battery for ease of access to this safety device, with a door interlock utilised. The battery was placed on non-conducting supports, with a normally closed contactor providing grounding to the battery chassis when the microgrid system is powered down. The enclosure was to be raised off the ground for ease of manoeuvrability with the aid of a pallet truck.

5.4.2 The battery panel

A panel was designed to be incorporated on top of the battery enclosure to enclose the significantly increased amount of electronics needed for isolation due to the floating of the battery and the treatment of all signals as potentially hazardous.

As well as the 12 V power supply and CAN repeater, there was a requirement to include in the design an emergency stop system, visual indications of the battery status, fusing

and fault protection, and terminal blocks to help with cable management and connections.

The design also attempted to separate, with a clear boundary, all hazardous voltages and potentially hazardous equipment from safe equipment and cabling.

This battery panel was made out of the robust CUBIC system. Following on from testing with the isolation systems in place, the design of all battery local controls were finalised through consultation, with emphasis on clear labelling, neatness and feedback to the overall supervisory system in the PLC.

This is shown in the drawing of Figure 5.8.

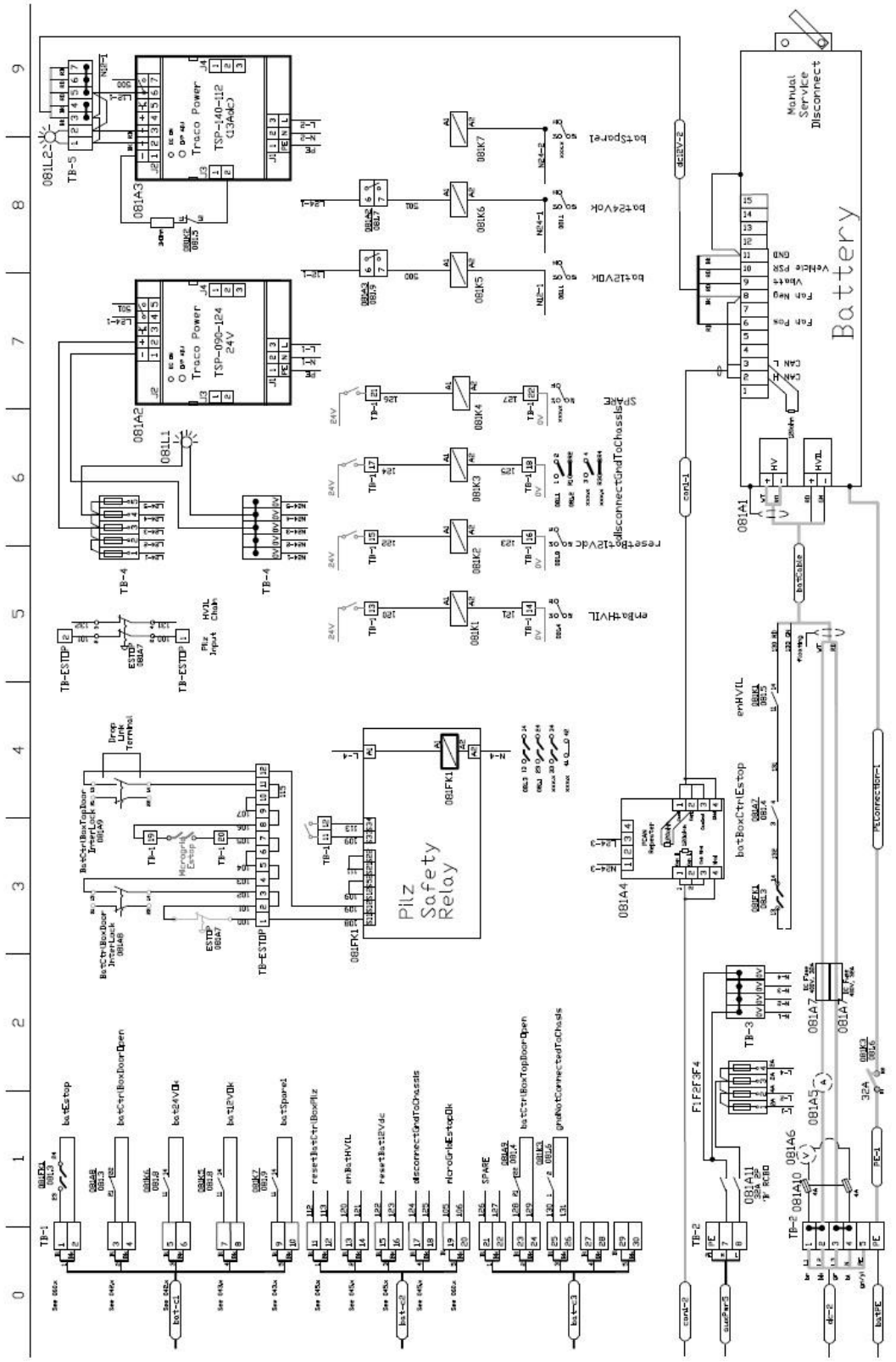


Figure 5.8: Electrical drawing of the battery electronics of the battery panel enclosure

The purposes of the components in the above drawing are outlined in Table XX.

Table XX: Explanation of items in the electrical drawing of the battery panel enclosure

Item #	Item Description	Further Information
081A2	24 V supply	Powers local relays and the PCAN repeater.
081A3	12 V supply	The low-voltage power supply for the battery and also powers a relay informing the PLC of its status.
081A4	PCAN Repeater	Isolates the CAN bus of the battery from the CAN bus of the Target PC.
081A5	-50 A to +50 A dc analogue ammeter	A visual indication of the current to or from the battery.
081A6	0 V to 500 V dc analogue voltmeter	A visual indication of the voltage on the battery terminals and if the internal contactors are closed.
081A7	32 A, 410 V, dc fuses	Current protection on the dc positive and dc negative high power cable to the Triphase cabinet.
081A8	Door interlock	A switch detecting if the battery enclosure door is open. This is part of an E-stop chain that shuts the system down if open. A secondary output provides a status signal to the PLC.
081A9	Door interlock	A switch detecting if the door to the control circuitry is open. This is part of an E-stop chain that shuts the system down if open. A secondary output provides a status signal to the PLC. A drop-link terminal is provided to bypass the E-stop chain if required to have the door open during testing.
081A10	4A high voltage fuses.	Fuses to protect the analogue voltmeter.
081A11	32A 2 pole, B type RCBO	RCBO (residual-current circuit breaker with overload protection) on the auxiliary power input. This is for circuit and user protection.
081A12	E-stop	An emergency stop button on the front of the panel providing an industry standard mechanism of shutting the complete system down if required by personnel.
081L1	24 V green lamp, 22mm	A visual indication of the status of the 24 V supply and status of auxiliary power to the control panel.
081L2	12 V green lamp, 22mm	A visual indication of the status of the 12V supply to the battery.
081FK1	Pilz safety relay	Provides a reliable mechanism for opening the HVIL circuit as well as the rest of the system E-stop chain.
081K1	enHVIL 24V relay	Operated by the PLC, this allows independent control over opening and closing the HVIL circuit.
081K2	reset12Vdc 24V relay	Operated by the PLC, this allows the 12 V dc supply to the battery to be reset and reset the BMS.
081K3	gndToChassis 24V relay	This allows the battery chassis to be grounded at system shut down or E-stop event.
081K4	Spare relay	This is in the battery panel and activated by the Microgrid panel.
081K5	Dc12Vok 12V relay	This signals to the PLC whether the 12 V supply is operational.
081K6	Dc24Vok 24V relay	This signals to the PLC whether the 24 V supply is operational.
081K7	batSpare1 relay	This spare relay in the battery panel is powered locally.

The build of the battery enclosure was undertaken by professional electrical wiring contractors and photographs of the integrated system are shown in the results section.

5.4.3 Cabling and cable terminations

Details of the cables drawn internally in the battery box are given in Table XXI.

Table XXI: Cables from the battery to the battery panel

Cable Tag	Type	Connection
dc12V-2	3 red, 2 black, 2.5 mm^2	TB-5
batCable	2 core, 16 mm^2 (large insulation, shield taped off,)	- to TB-2 3 + to 081A5 Rd to 081K1 Gr to 081FK1
earth	1 core, 25 mm^2	TB-2 6
can1-1	4 core, 24AWG, shielded	081A4

Cabling from the battery panel to the external equipment is detailed below.

Table XXII: Cables from the battery panel to the microgrid system

Cable Tag	Type	Connection
auxPwr5	3 core	TB-2
can1-2	5 core, L1YCY	081A4
dc-2	5 core, sylflex, 10 mm^2 conductors	TB-2
bat-c1	5 pairs	TB-1
bat-c2	5 pairs	TB-1
bat-c3	5 pairs	TB-1
Earth	1 pair, 25 mm^2	TB-2 6

The terminations of earths and shields are described in Table XXIII.

Table XXIII: Groundings of cables from the panel box to the system

Cable Tag	Type	Connection
auxPwr5	Armour	On microgrid panel, not on battery panel.
auxPwr5	Internal earth	Terminated in earth terminal in battery panel.
dc-2	Sylflex shield	Shield grounded at Triphase, shield hanging at battery panel.
dc-2	Internal earth	Terminated in normal terminal in battery panel and not connected to other earths at this point, terminated in earth terminal at Triphase.
bat-c1	Overall shield	Earthed at microgrid panel, hanging at battery panel.
bat-c1	Individual shields	Earthed at microgrid panel, hanging at battery panel.
bat-c2	Overall shield	Earthed at microgrid panel, hanging at battery panel.
bat-c2	Individual shields	Earthed at microgrid panel, hanging at battery panel.
bat-c3	Overall shield	Earthed at microgrid panel, hanging at battery panel.
bat-c3	Individual shields	Earthed at microgrid panel, hanging at battery panel.
25 mm^2 earth	Cable	Grounded at both microgrid panel and battery panel.

5.4.4 Microgrid control

Overall control of the complete microgrid is achieved by a PLC system operated by an engineering PC in a control room. Here the power converter and battery system signals described above were integrated with the rest of the microgrid software. The opening and closing of contactors to the various items on the grid are carefully controlled and monitored by this system.

Images of the completed system are shown in the results section.

5.5 Battery modelling and characterisation

5.5.1 Battery charge and discharge tests

The internal battery model available in SimPowerSystems in the Matlab/Simulink platform was utilised to compare performance data of the high-voltage Li-ion battery. This model is developed in [80] and is similar to the Shepherd model [81]. The model uses parameters for response time, nominal voltage and rated capacity to give an approximation of the full voltage versus state of charge charge/discharge curves.

The model makes the following assumptions:

- The internal resistance is constant during charge and discharge and does not vary with current.
- The model parameters are deduced from the discharge curve and a step test and assumed to also apply to charging.
- The capacity of the battery does not change with current amplitude.
- The model does not take account of temperature.
- The self-discharge of the battery is not taken into account
- The battery has no memory effect.

The discharge model for a Li-ion battery is based on the following equation:

$$V_{batt} = E_0 - R\,i - K\frac{Q}{Q-it}it - K\frac{Q}{Q-it}i^* + Ae^{-B\cdot it} \quad (5.1)$$

Polarisation voltage

Polarisation resistance

where V_{batt} = battery voltage (V), E_0 = battery constant voltage (V), R = internal resistance (Ω), i = battery current (A), i^* = filtered current (A), K = polarisation constant (V/(A h)) or polarisation resistance (Ω), Q= battery capacity (A h), A = exponential zone amplitude (V), B = exponential zone time constant inverse (A h)$^{-1}$.

The term concerning the polarisation voltage helps to better represent the open circuit voltage behaviour which varies non-linearly with state of charge, and the term concerning the polarisation resistance [81] is modified. The particularity of the model is the use of a filtered current, i^*, flowing through the polarisation resistance, which helped solve a Simulink algebraic loop problem. This filter is represented by $\frac{1}{T_r/3\,s+1}$ in Simulink.

The charge model is based on equation (5.2).

$$V_{batt} = E_0 - R\cdot i - K\frac{Q}{it - 0.1\cdot Q}\cdot i^* - K\frac{Q}{Q-it}\cdot it + Ae^{-B\cdot it} \quad (5.2)$$

The primary advantage of this battery model is the simplicity of extracting the dynamic model parameters from the discharge curve of the battery and a step test. Only three points from this curve are required to obtain most of the parameters, while a step test is

used to obtain the response time and battery internal resistance. These three points are:

1. Full voltage at 100% state of charge.
2. The voltage at the end of the initial exponential voltage drop-off region of the discharge curve, and the corresponding capacity at that point.
3. The end of the nominal zone voltage after which voltage drops off rapidly, and again the corresponding battery capacity at that point.

The method of extracting the parameters for equations (5.1) and (5.2) from these three points is discussed in [80].

The battery was cycled through complete discharge and charge cycles at a demanded current of 10 A. From this, the parameters of the model were obtained and the experimental discharge curves were compared with model performance.

Plots of tests are obtained using the logging capability of the Triphase software inbuilt into Simulink.

5.5.2 Battery step test

To obtain the response time of the battery and the internal resistance, a step test of the battery current was performed and the resulting battery voltage was plotted. During this step test, the dc-bus voltage was also plotted to allow a comparison of the power converter dynamics in the test setup.

5.6 Results

5.6.1 The battery and power converter integrated into the microgrid

Photographs of the final integrated microgrid system are shown in Figure 5.9, Figure 5.10, Figure 5.11, and Figure 5.12. These include the built battery enclosure for the high voltage Li-ion battery, the incorporated panel with the battery control electronics, as well as the microgrid panel and Triphase IGBT based power converter panel.



Figure 5.9: Front view of the high voltage battery enclosure including panel with associated control electronics



Figure 5.10: Battery panel internal view



Figure 5.11: Battery enclosure internal view



Figure 5.12: Microgrid panel and Triphase panel installations

5.6.2 Test plots

Full functionality tests were performed on the integrated system. The resultant plots from two tests are given.

5.6.2.1 Examine standard operation with q axis current set to 10A

In this plot the set-point dc-bus voltage was 660 V. Neutral switching was not enabled and the *q*-axis grid current set-point was 10 A peak. This would result in the current lagging the grid voltage.

In the plot below, channel 1 measures the dc-bus voltage, channel 2 measures the grid voltage on phase a, channel 3 measures the inverter current on phase a before filtering, and channel 4 measures grid phase a current after filtering. The current probes used a conversion factor of 10 A per volt.

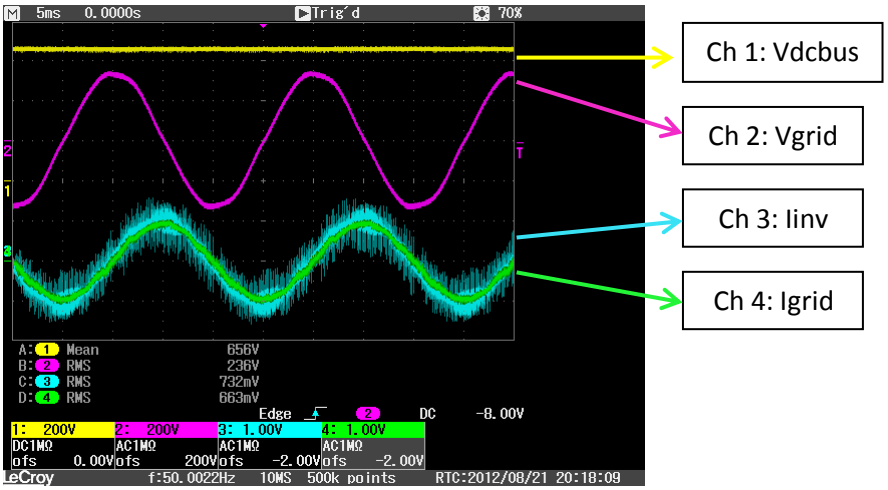


Figure 5.13: Standard operation of the Triphase IGBT based power converter with the set-point for Iinv_q at 10 A

As the *d*-axis current is only feeding dc-bus capacitance losses, the *q*-axis current is equal to the grid phase current. This is seen in Figure 5.13 where the phase current has a peak of 10 A.

5.6.2.2 Examine standard operation with current from battery raised from 0 to 5 A

Again, the dc-bus voltage set-point was 660 V. Neutral switching was not enabled and the *q*-axis grid current set-point was 0 A. The overall current from the battery was changed from 0 to 5 A through two channels, with a rate limiter in the model of 5 A/s on each channel.

In Figure 5.14, channel 1 measure the dc-bus voltage, channel 2 measures the battery voltage, channel 3 measures the phase a grid current (after filtering), and channel 4 measures the current supplied to the Li-ion battery.

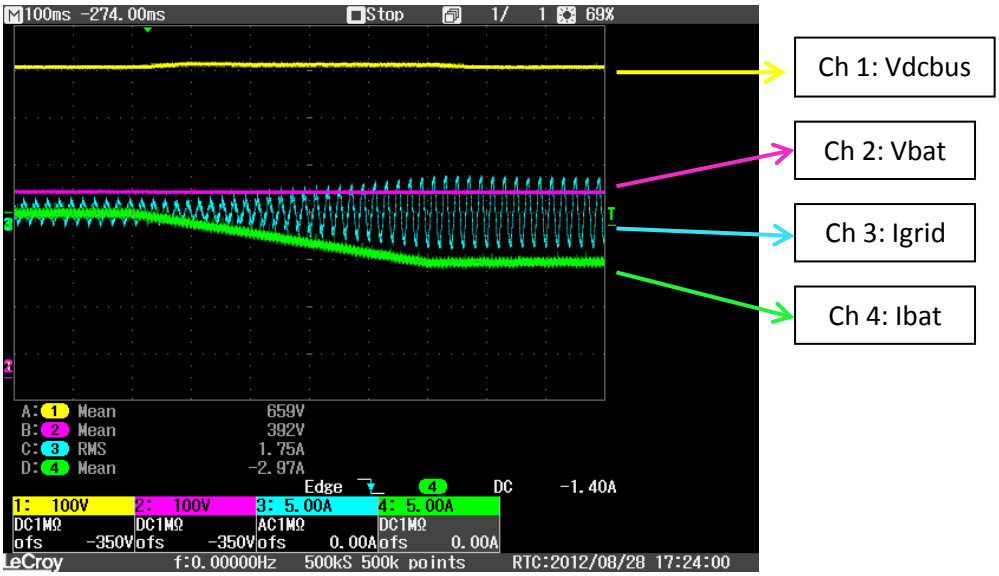


Figure 5.14: Power converter and battery standard operation with current from the battery raised from 0 to 5 A

The above figure shows the change of battery current from 0 to 5 A occur over 500 ms, consistent with a rate limit of 5 A/s over two channels (effectively 10 A/s). The dc-bus voltage is also seen to rise as the exported battery current to it increases.

5.6.3 Charge/discharge curves

The model sample time for the charge/discharge tests was 125 µs, corresponding to the PWM frequency. The logging decimation was set at 200, giving a sample time of 25 ms for plotting. The BMS measures of state of charge (SOC) and voltage were recorded and these plots are shown.

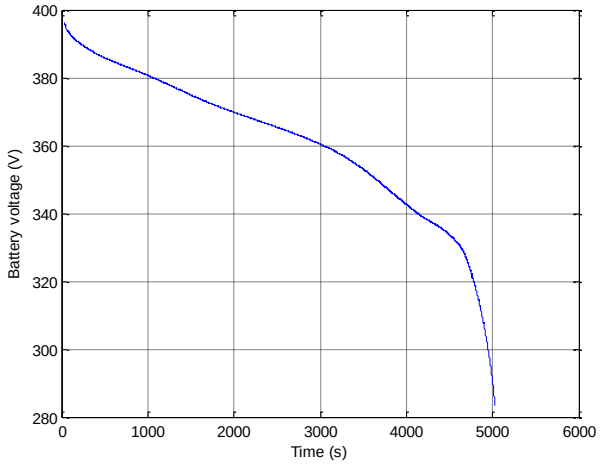


Figure 5.15: Battery voltage during complete discharge at 10 A recorded from the BMS

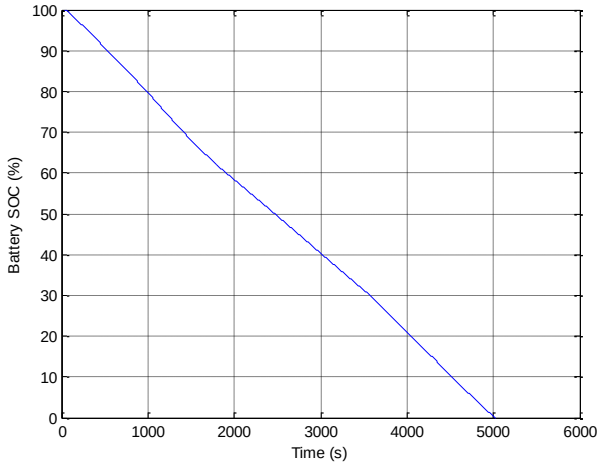


Figure 5.16: Battery SOC during complete discharge at 10 A recorded from the BMS

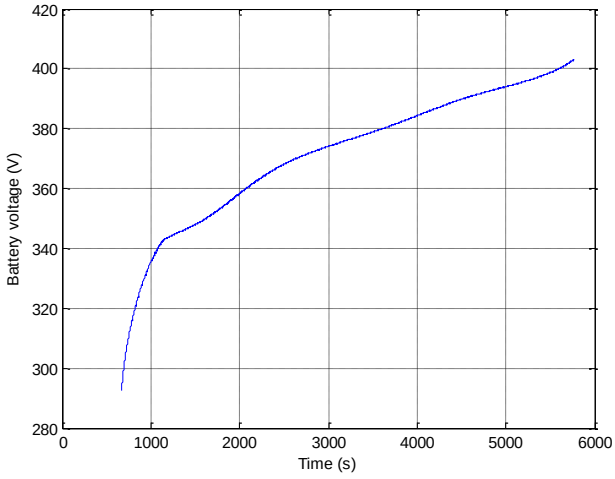


Figure 5.17: Battery voltage during complete charge at 10 A recorded from the BMS

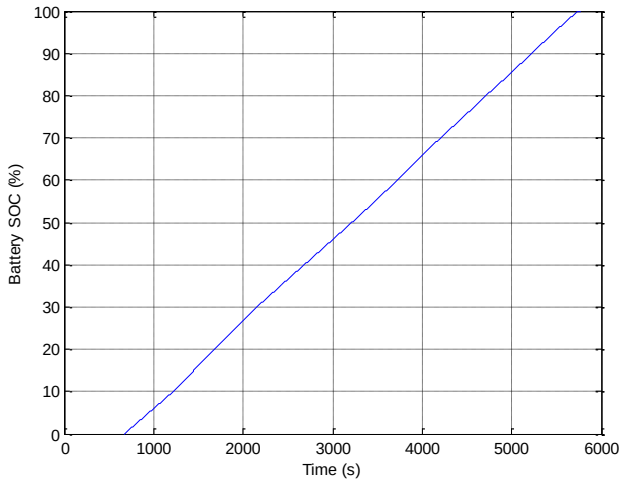


Figure 5.18: Battery SOC during complete charge at 10 A recorded from the BMS

As discussed in Section 5.5.1 the following parameters are to be deduced from the discharge test:

- V_{full}
- Q_{exp}
- V_{exp}
- Q_{nom}
- V_{nom}
- Q

These parameters are usually extrapolated at a discharge rate of 0.2 C [80], where C is the charge/discharge rate of the battery and 1 C is the charge/discharge rate equal to the capacity of the battery in one hour. In this case, it was approximately 0.67 C (approximately 10 A from 15 A h cells). The current readings from the BMS are used in calculations instead of the demanded values, this slight discrepancy in measured values between the Triphase power converter and the BMS is illustrated in Figure 5.19. Table XXIV shows the parameter extrapolation. With the values for rated capacity and nominal voltage inserted into the inbuilt SimPowerSystems model in Matlab/Simulink, corresponding values for the other points are produced and these are also shown in Table XXIV.

Table XXIV: Parameter extrapolation from the battery discharge curve for the battery model

Parameter	Discharge curve extrapolated value	Matlab produced value
Time at 100% SOC	65.1 s	
Time at 0% SOC	5020.8 s	
Average current	-10.6 A	
Q	14.6 A h	14.6 A h (input)
V_{full}	394.2 V	385.4 V
V_{exp}	387.2 V	357.8 V
Time at V_{exp}	400 s	
Q_{exp}	0.99 A h	0.72 A h
V_{nom}	331.2 V	331.2 V (input)
Time at V_{nom}	4600 s	
Q_{nom}	13.34 A h	13.19 A h

The SimPowerSystems battery model also produced a series resistance value of 0.23 Ω.

5.6.4 Step test

The final model parameters of response time and equivalent series resistance were measured using a step test. The SOC for the step test was 90%. A current step from 0 to -10 A was applied and the battery was discharged to 80% SOC. No current was demanded for 10 minutes, and then the current was stepped to 10 A. The battery was then charged to 90% SOC, and 0 A was demanded again for 10 minutes.

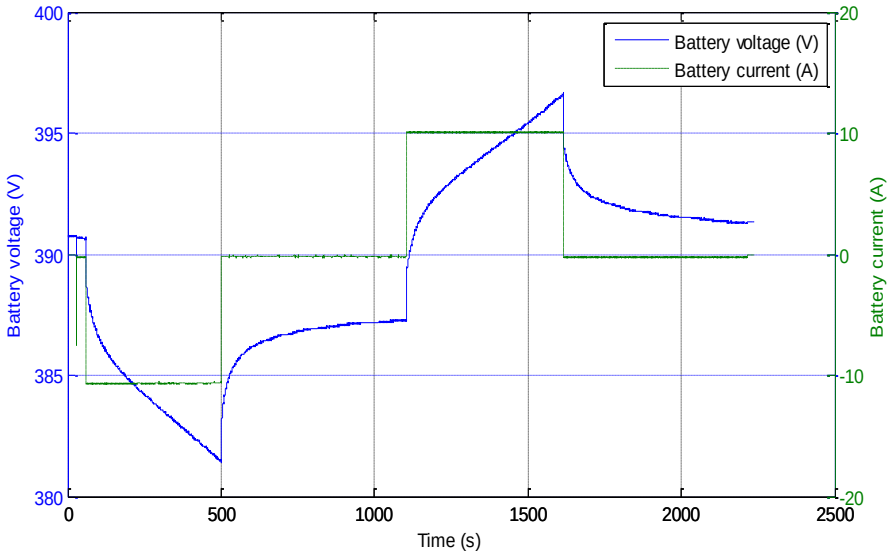


Figure 5.19: Voltage versus time for battery step test

The current readings from the BMS are plotted above instead of the demanded values from the power converter. A small discrepancy is seen here with 10.65 A drawn during discharge and 10.1 A measured by the BMS during charge.

5.6.4.1 Battery internal resistance

The battery internal resistance is found from the above plot using voltages at the beginning of the steps and the voltage at the next sample.

Table XXV: Evaluation of battery resistance

Parameter	Voltage (V)
$V_{min_with_R}$	381.4
V_{min}	383.2
V_{diff_min}	1.8
$V_{max_with_R}$	396.6
V_{max}	394.8
V_{diff_max}	1.8

These two readings give a difference of 1.8 V at an average of 10.38 A. Therefore, the equivalent series resistance of the battery is 0.17 Ω. The battery datasheet gives a resistance of 0.29 Ω, and the SimPowerSystems model produces a battery resistance of 0.23 Ω using the inputs of rated capacity and nominal voltage from the discharge curve.

5.6.4.2 Battery response time

The response time is the time taken for the battery to reach 95% of the final steady state terminal voltage value after a current step back to 0 A. Values are extrapolated from the step test where discharge current from the battery is stepped from 10 A to 0 A. Table XXVI shows the evaluation of the battery response time. The minimum voltage is taken after the initial voltage change, due to the voltage drop across the battery internal resistance.

Table XXVI: Evaluation of battery response time

	Voltage (V)	Time (s)
V_{min}	383.2	502.6
V_{end}	387.3	1104
V_{diff}	4.1	
0.95 (V_{diff})+V_{min}	387.095	902.6
Battery response time		400

The dc-bus responses at these two steps of battery current are shown below.

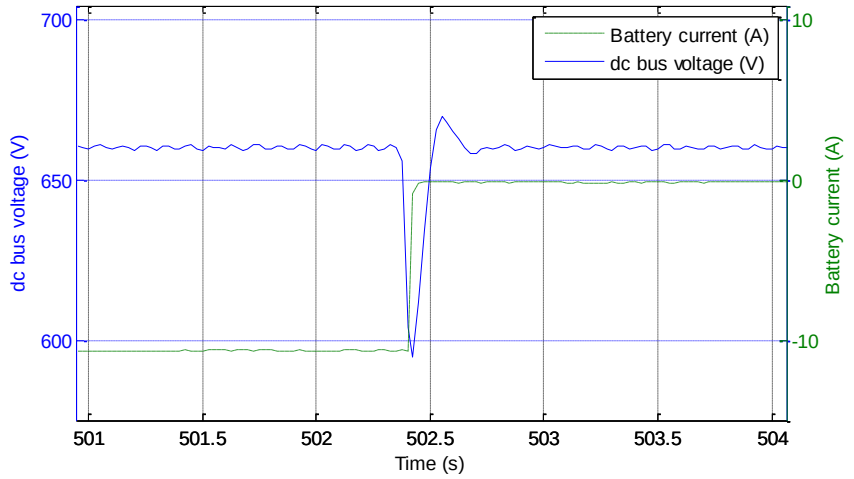


Figure 5.20: Dc-bus voltage response to a step in battery current from -10 A (discharge) to 0 A

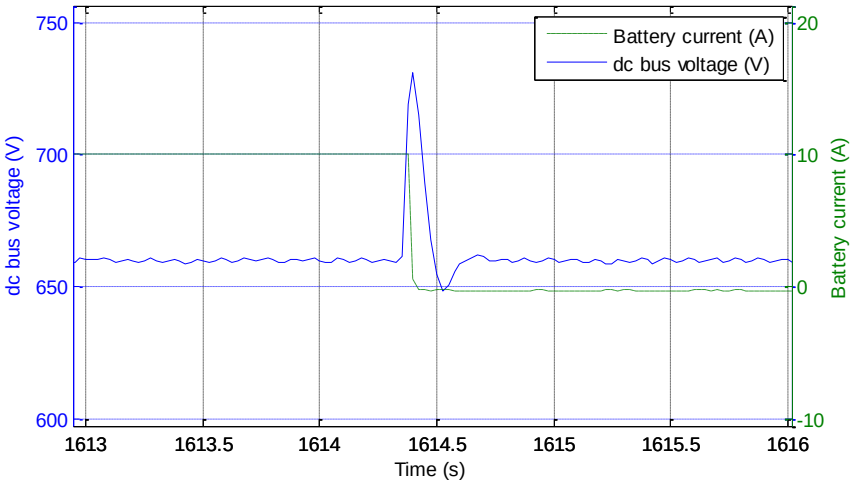


Figure 5.21: Dc-bus voltage response to a step in battery current from 10 A (charge) to 0 A

For the step change at about 500 s, there is an approximate 10 A step at the V_{min} of 383.2 V. Using the conservation of power gives a current step of 5.8 A on the dc-bus voltage of 660 V. The dc-bus reaches a minimum voltage of 594.9 V and overshoots back to 669.8 V. This minimum drop represents an almost 10 % drop in bus voltage.

For the step change at about 1,600 s, there is a 10 A step at the V_{max} of 394.8 V. Using the conservation of power, gives a step in current on the dc-bus voltage of 660 V of 6 A.

The dc-bus reaches a maximum voltage of 730.9 V and overshoots back to 648.5 V. This maximum peak represents a rise in bus voltage of over 10%.

The parameters E_0, K, A, in equation (5.1) were evaluated as 391.4 V, 0.207 V/Ah (or Ω), and 4.72 V respectively, and B was approximated as $3/Q_{exp}$.

5.6.5 Model performance

With the complete set of data points calculated above entered into the SimPowerSystems model in Matlab, a discharge curve over the full state of charge of the battery was produced at a measured constant current discharge of 10.6 A. This is shown in Figure 5.22 with the experimental curve.

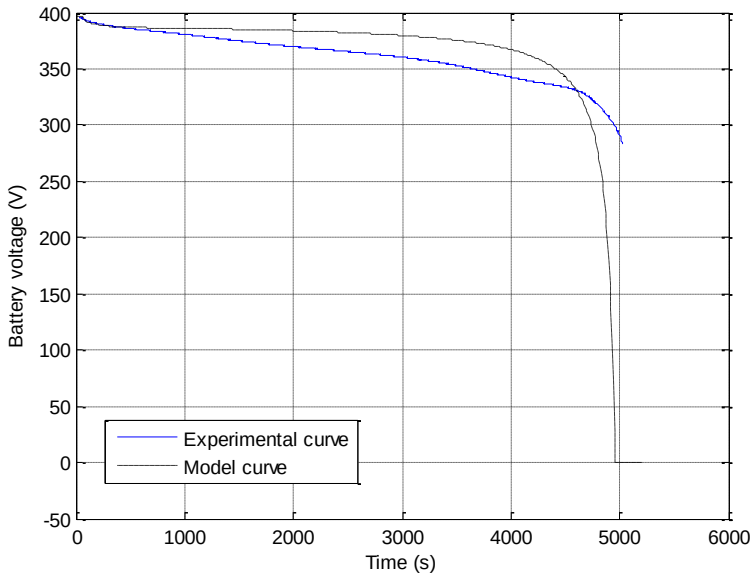


Figure 5.22: Battery voltage during complete discharge comparing experimental profile to model profile

While the model curve discharges to zero, the BMS sets its SOC to a value where voltage limits are satisfied and the battery will not be damaged. Before the voltage drop-off near zero SOC, the largest deviation in performance was about 7.1% at 3,850 s. The measured experimental curve displays a larger rate of voltage decline. The battery model in [80] is developed for a range of battery types, each based on similar mathematical models. A comparison of the voltage profile from discharge of a low-voltage NiMH battery to the developed mathematical model is given in the paper and a similar shape to Figure 5.22 is observed as shown in Figure 5.23.

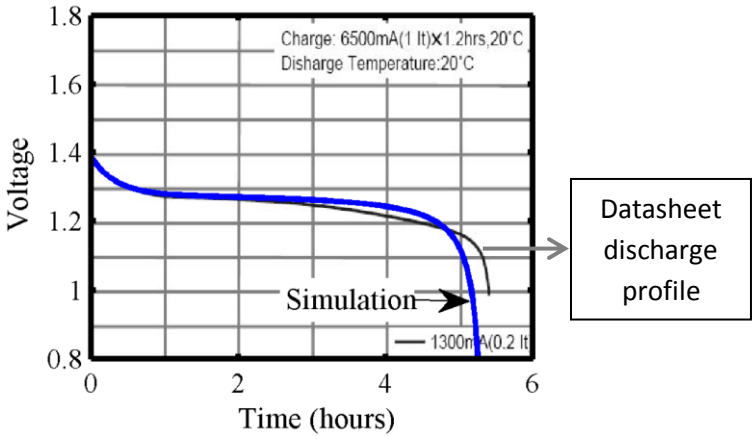


Figure 5.23: Simulation and datasheet results from discharge of a 1.2 V NiMH battery (HHR650D from Panasonic) [80]

The inbuilt model response time of 30 seconds for all Li-ion batteries, is much shorter than the calculated 400 seconds response time used in this work. This might demonstrate a difference in comparing models based on individual cells to those incorporating a large number of cells in a module. The propagation of charge between cells as well as the effect of voltage balancing by the BMS seems obvious reasons for the response time increase.

Adding the charge curve to the comparison work and plotting the battery voltage versus state of charge produces the following figure.

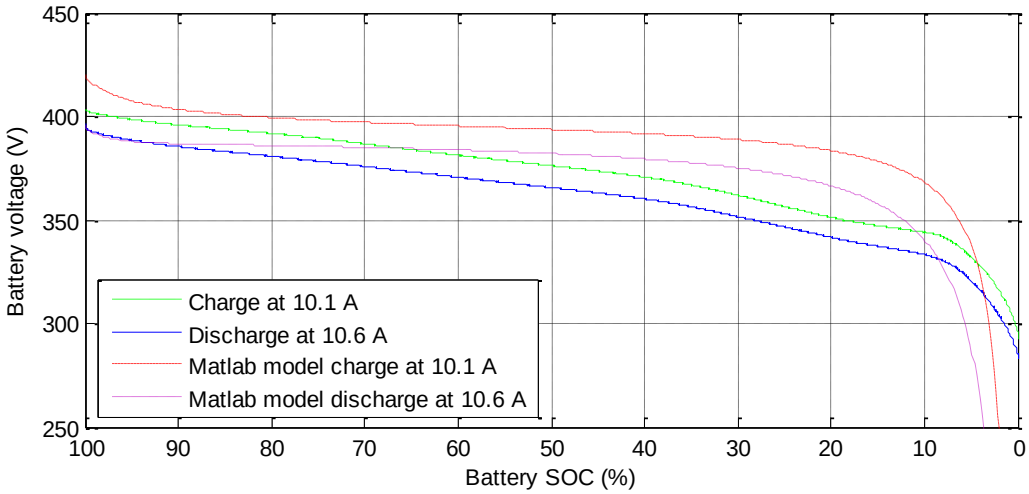


Figure 5.24: Battery voltage versus SOC for charge and discharge tests comparing model performance to experimental data

The discharge model closely matches the tested discharge profile near 100% SOC. The model is based on two sets of parameters near this area of the curve. The third set of parameters is found from the knee of the above curve and the two curves diverge, crossing at this point. The charge profiles do not match as closely, but 100% SOC occurs at the end of the discharge test. It is also assumed in the model that the charge and discharge battery models are the same.

5.6.6 Creation of piecewise equation to describe discharge profile

It is seen in Figure 5.24 that the experimental discharge profile for the high voltage Li-ion battery consists of three main sections over the state of charge of the battery: a small initial exponential voltage decay, a linear region, and an exponential drop-off near low capacity. The high voltage battery is integrated into a microgrid and was initially designed for the EV market. Inbuilt safety features prevent battery voltage from deviating from high or low voltage limits, and it is expected that operation will mainly occur over the linear region. The Matlab battery model examined previously shows a large deviation from the experimental discharge profile over this linear range, and the exponential drop off near zero SOC also does not closely correlate with the experimental profile, as seen in Figure 5.24. A simple piecewise equation is proposed to better describe this battery discharge profile for the application of interest.

This piecewise equation is shown in equations (5.3), (5.4), and (5.5):

100% to 90% SOC: $$V_{batt}(SOC) = V_{90\%} - R\,i + A_{init}\left(e^{-\frac{90-SOC}{8}} - 1\right) \quad (5.3)$$

90% to 8% SOC: $$V_{batt}(SOC) = V_{90\%} - R\,i + K_{new}(90 - SOC) \quad (5.4)$$

8% to 0% SOC: $$V_{batt}(SOC) = V_{0\%} - R\,i + A_{end}\left(1 - e^{-\frac{SOC}{5}}\right) \quad (5.5)$$

where $V_{90\%}$ (V), and $V_{0\%}$ (V), are the measured voltages at 90% and 0% SOC respectively. A_{init} (V) and A_{end} (V) are the exponential zone amplitudes, and K_{new} (V/SOC%) describes the slope of the linear operating region.

The equations are created as functions of SOC to aid plotting but as the measured discharge profile is obtained from a constant current discharge these equations could be related to time and energy, also the measured values of $V_{90\%}$ and $V_{0\%}$ included the voltage drop due to the internal resistance.

The used time constants in the above equations allowed the slopes of the exponential regions of the voltage profile to tie in with the linear portion of the piecewise curve.

The voltage points on the discharge curve used to evaluate parameters were, $V_{100\%}$ = 394.2 V, $V_{90\%}$ = 385.45 V, $V_{8\%}$ = 330.47 V, and $V_{0\%}$ = 284.9 V. This produced values of A_{init} = 3.51 V, A_{end} = 57.1 V, K_{new}=-0.67 V/SOC%.

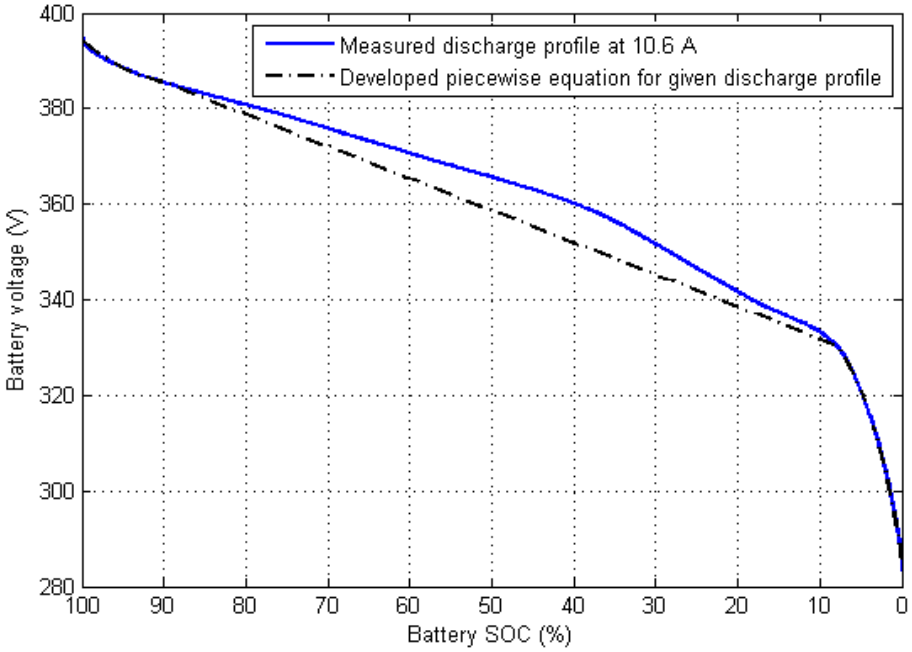


Figure 5.25: Battery voltage versus SOC for piecewise fitted equation with discharge profile

The largest deviation of voltage from the curves occurs over the linear portion where at 37.5% SOC, a 2.3% deviation occurs. This is a large improvement over the previous model. Further work is required to test this piecewise equation at various currents and evaluate if good model performance is maintained. Initial estimates show that if these evaluated curves are applied to the charge profile at 10 A, the new curve will be stepped up by a factor of $R\left(i_{charge} + i_{discharge}\right) = 3.73\ V$. It is seen in Figure 5.26 that this charge profile does not accurately represent the charge profile of the battery and further work is required.

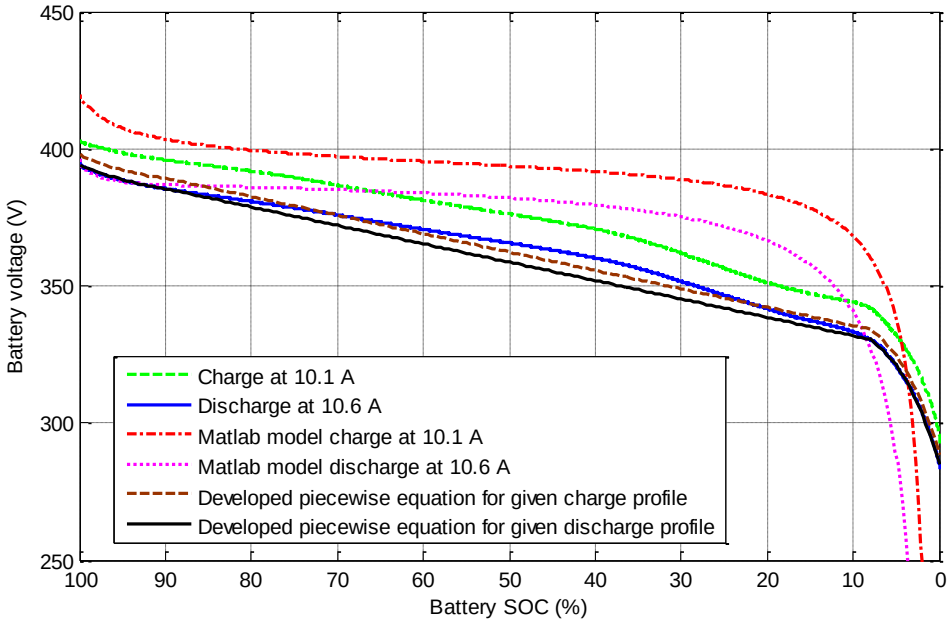


Figure 5.26: Battery voltage versus SOC for charge and discharge tests comparing model performance to experimental data to piecewise equation

5.7 Conclusions

Li-ion batteries are gaining market share in EV and renewable applications and are currently employed in the Nissan Leaf, Mitsubishi iMieV, Ford Fusion, and Chevy Volt. It's shown in Chapter 1 that Li-ion batteries could achieve a high cycle life, into the millions, by reducing the DOD over which they operate. Other ways of improving battery performance have been explored in [42] [43] [44], where SCs are used to assist high power events, increase battery lifetime, and improve efficiency.

While the previous chapters explored modelling and SC testing for the application of energy storage in an offshore WEC, the safety, communications and control requirements of an energy storage system build (and associated power converter) have yet to be addressed. This chapter gives a better understanding of these requirements and explores Li-ion battery technology in the emerging field of microgrid research. Li-ion batteries have been shown to be an energy storage technology suitable for operation with microgrids and their two modes of operation: grid connected mode and islanding mode.

This work integrated a 15 kW power converter and battery system into a microgrid. Equipment and personnel safety, communications with different standards (for example CAN and EtherCat fieldbus), and coordinating operation with an overall supervisory PLC

control system, were paramount throughout the build. The battery system was floated and the unique design included isolation devices built into the battery panel and CUBIC battery enclosure.

The associated power converter allows real-time control of currents to and from the battery, as well as allowing reactive power injection into the grid.

The standard Li-ion battery model available in the SimPowerSystems Matlab/Simulink software package, was utilised in comparison work, which is based on [80]. The experimental discharge profile was seen to have a larger slope, but the model produced similar values and the discharge profile only differed by a maximum of 7.1% from the experimental plot before the voltage drop-off near zero SOC.

The in-built model response time of 30 seconds for all Li-ion batteries, is much shorter than the calculated 400 seconds response time used in this work. This might demonstrate a difference in comparing models based on individual cells to those incorporating a large number of cells in a module.

A new piecewise model was proposed and fitted to the voltage discharge profile, to better describe the voltage over the linear region of operation. A maximum deviation of 2.3% occurred but it was found that when used to describe the charge profile, a relatively fixed voltage deviation over the SOC was observed. Further work is required to improve this model.

Further work with this energy storage system would be to validate wave energy control schemes and power flows. While the system is currently part of a microgrid, it is built in the Hydraulics and Maritime Research Centre, Cork, Ireland which is dedicated primarily to ocean energy research. The versatility of the complete microgrid build should facilitate this work.

Chapter 6 Conclusions

6.1 Conclusion summary

The motivation for the research was outlined in Chapter 1. The benefits of utilising energy storage in an offshore WEC application were described in terms of power smoothing, low-voltage ride-through, and ancillary services. A review of the energy storage mechanisms inherent to various wave energy converter technologies was undertaken and presented.

Electrical energy storage technologies are then compared with a focus on batteries, capacitors and supercapacitors (SCs). Robust technology with high cycle lifetimes is a requirement for devices employed in offshore WECs, due to the long desired intervals of typically 5 years for non-routine disruptive maintenance. Batteries can meet this requirement if operated within specified limits, provided they are oversized sufficiently to achieve the desired DOD figure. SCs have high cycle lifetimes, high charge/discharge efficiencies, and a very high power density in comparison with batteries, and appear ideal for a WEC application.

In Chapter 2, a developed Simulink model of a full-scale OWC WEC is utilised to compare five different variable speed strategies that make use of the high-inertia Wells turbine. Each strategy is optimised for the sea-state under consideration and compared in terms of efficiency, power smoothing and speed limit constraints. The chosen variable speed strategy consisted of two parts where part one related generator torque to a power of speed and part two prevented over speed. The developed control equation allowed this strategy to operate in different sea-states without alteration. This strategy was enhanced with the use of a switched controller to overcome the chattering seen at the equation boundary, with a hysteretic band of 80 rpm. The efficiency of the examined sea-state with the model was 55% comparing input pneumatic power to output electrical power for an ideal generator taking account of friction. The results of this altered strategy in terms of power smoothing were a measured standard deviation of 0.23 pu, where pneumatic power had a standard deviation of 1 pu. The peak to average

electrical power was 4.6, while the peak to average value of input pneumatic power was 18.6 for the examined sea-state.

The altered variable speed strategy produced a power profile with occasional peaks. It was proposed to further smooth this power utilising SC energy storage connected via a power electronic dc-dc converter, to the direct current (dc) bus of the back-to-back converter which couples the generator to the grid. This is shown in Chapter 3. The strategy attempts to maintain the SCs at their lowest operational voltage (half rated voltage) to make available the SC energy capacity for absorbing power peaks. Once the generator power exceeds a predetermined value (dependent on the sea-state), the SCs prevent any excess power flowing to the grid and absorb the difference. A voltage hysteresis band prevents rapid charging and discharging cycles occurring. This SC energy storage strategy was found to reduce the grid peak to average power ratio to 2.2 for the sea-state under examination. The standard deviation of electrical power to the grid reduced to 0.18 pu (pneumatic power had a standard deviation of 1 pu). This application test predicted around 980,000 cycles would be performed on the SC energy storage device over the desired 5 year period. Previous available results of cycle lifetime testing reached at most 150,000 and data of up to 450,000 tested cycles is available without *y*-axis scaling.

Chapter 3 goes on to describe single sample testing of SCs carried out to validate the cycle lifetime figures quoted in datasheets, to investigate suitability for an offshore WEC power smoothing application. The temperature effect on this cycle lifetime figure was investigated by carrying out lifecycle tests at rated temperature. Application testing also took place. 10 million cycles have been carried out at ambient temperature, 9 million power cycles at rated temperature (and testing is on-going), and 1 million cycles for the application test at ambient temperature. These figures far exceed manufacturer's specifications. Linear trends estimate cycle lifetimes to be 26.6 million for the standard test SC, 12.8 million for the test at rated temperature, and 6.7 million for the application test at ambient temperature.

An Arrhenius degradation was assumed to create an equation for expected time of life based on operation temperature. A temperature increase of approximately 15°C halves lifetime based on single sample testing at 65°C and 26°C on small capacitance SCs. This is a reasonable correlation to the usual 10°C rule of thumb which is based on SCs maintained at a constant voltage. These results suggest that SCs are a very suitable

energy storage technology for power smoothing in offshore WECs with typical long desired intervals for non-routine disruptive maintenance of 5 years.

In Chapter 4 a more complete model of the system was created in Simulink with the SimPowerSystems library. A permanent magnet generator and back-to-back converter were modelled with an integrated SC system. Applications for an offshore OWC WEC were investigated and these included turbine start-up and low-voltage ride-through. The control requirements of this system and power converters were highlighted. By employing SCs to power up the turbine, starting surge for a wave farm can be minimised. Also, by contributing towards LVRT, future grid codes may be satisfied and redundancy is built into the system.

Electrical power is needed in offshore WECs for lighting, communications, equipment monitoring, and control purposes. Heating and ventilation may also need power. Thus, some form of energy storage is needed and batteries seem ideal devices for this application. Employing SC energy storage to operate during these high power events would complement this battery system and could extend the battery lifetime.

As part of a microgrid development research project with a view to investigating pulsating power phenomena in electrical power systems, a 15 kW power converter and high-voltage lithium-ion (Li-ion) battery were integrated. Li-ion batteries are gaining market share in EV and renewable applications. This work highlighted the safety, communications and control requirements of an energy storage system build. The battery system was floated and the unique design included isolation devices built into the battery panel and enclosure.

The Li-ion battery model available in Simulink was utilised in comparison work. The model produced similar values to experimental tests, but the module itself was seen to exhibit a larger slope in voltage during discharge than the model predicted. The in-built model response time of 30 seconds for all Li-ion batteries is much shorter than the calculated 400 seconds response time used in this work. This might demonstrate a difference in comparing models based on individual cells to those incorporating a large number of cells in a module.

A new piecewise equation was proposed and fitted to the Li-ion discharge profile, to better describe the voltage over the linear region of operation. A maximum deviation of 2.3% occurred but it was found that when the equation with parameters evaluated was

used to describe the charge profile, a relatively fixed voltage deviation over the SOC was observed. Further work is required to improve this model.

6.2 Future work

The variable speed strategies should eventually be tested on a scaled prototype to get a better understanding of efficiencies and losses as well as practical issues, to allow refinement of any chosen variable speed strategy in a market WEC device employing a Wells turbine as part of the PTO mechanism.

Other applications of SCs which can be explored for an offshore WEC are regenerative breaking of the turbine during normal or emergency shutdown.

It is planned to continue testing the SC operating at rated temperature until failure and to submit the results of this updated experimental data to the IEEE transactions on industrial electronics, or a similar journal, for publication.

Lifetime analysis of SC modules should be clarified and investigated, to see if differences exist between modules incorporating inbuilt voltage balancing circuits and single SCs. Lower voltage testing seems to extend SC lifetime at constant voltage, and future work could clarify if similar lifetime increases occur for power cycling. Time constraints of testing would be an issue and a detailed plan of available time to test would need to be drawn up before committing to such a long project.

The SC equipment and test setups created could also be used to test Li-ion battery cells and compare power cycling lifetime at rated and ambient temperature. These high energy devices would require significantly longer time to test, and a more aggressive lifetime test could be considered where a significant depth of discharge would be utilised. Comparative testing of a Li-ion battery for the same WEC application as considered for SCs would provide WEC developers with detailed energy storage data.

The developed battery and microgrid test setup would allow detailed analysis of a HV battery module. Additional battery testing at different C rates and step testing at various SOCs would help create a more detailed dynamic battery model and allow further comparison of battery module performance to battery cell performance.

Further work with the microgrid project will be completed. The energy storage system could be used to validate wave energy control schemes and power flows as well as microgrid analysis.

Appendix A Examination of power loss due to I^2R in a WEC with and without energy storage

Sea waves are combinations of many different wave frequencies and amplitudes and are not constant sine waves. When the sea waves are analysed in a given location, a certain number of states called sea-states are defined with dominant periods and wave heights. To help examine the reduction of I^2R losses in the transmitted grid power due to power smoothing in an offshore wave energy converter (WEC) with an on-board energy storage device, sea waves with a perfect sine wave profile will be assumed as the input power to the device and analysed.

A.1 Normal peak to average input power analysis

A.1.1 Grid power and energy with and without an energy storage device for power smoothing

The power in the sea wave assuming a monochromatic source with a single frequency wave is given in (A.1):

$$P_{wave}(t) = A\sin(\omega t) \tag{A.1}$$

where the frequency is defined as:

$$\omega = 2\pi f \tag{A.2}$$

The wave energy converter under examination in this thesis, an offshore oscillating water column (OWC) of the backward bent duct buoy (BBDB) design, converts this input power from the sea water into pneumatic power. Assuming conversion with a constant efficiency k_{pneu}, the pneumatic input power to the device is:

$$P_{pneu}(t) = k_{pneu}\,P_{wave}(t) = k_{pneu}\,A\sin(\omega t) \tag{A.3}$$

If the conversion efficiency from pneumatic power to mechanical power is assumed to be a constant k_{mech}, and the characteristic feature of a Wells turbine is noted, where the input wave power is rectified so that the rotational power is always in one direction, then the mechanical power on the turbine is given in (A.4).

$$P_{mech}(t) = \left|k_{mech}\, P_{pneu}(t)\right| = \left|k_{mech}\, k_{pneu}\, A\sin(\omega t)\right| \tag{A.4}$$

Finally, if the conversion efficiency of the mechanical power of the turbine to electrical output power (including the efficiency of the back-to-back converter) is assumed as a constant k_{elec}, this gives the resultant power to the electrical grid as:

$$P_{grid}(t) = |k_{elec}\, P_{mech}(t)| = \left|k_{elec}\, k_{mech}\, k_{pneu}\, A\sin(\omega t)\right| \tag{A.5}$$

Let the conversion efficiencies be encapsulated by one term.

$$k_{wec} = k_{elec}\, k_{mech}\, k_{pneu} \tag{A.6}$$

The grid power can now be written as:

$$P_{grid}(t) = |k_{wec}\, A\sin(\omega t)| \tag{A.7}$$

A plot of this grid power and input wave power over time is shown in Figure A.1 for a normalised lossless device (k_{wec} = 1, A = 1 pu) with a wave period of 10 seconds. This power to the grid has a value of zero twice in every wave period.

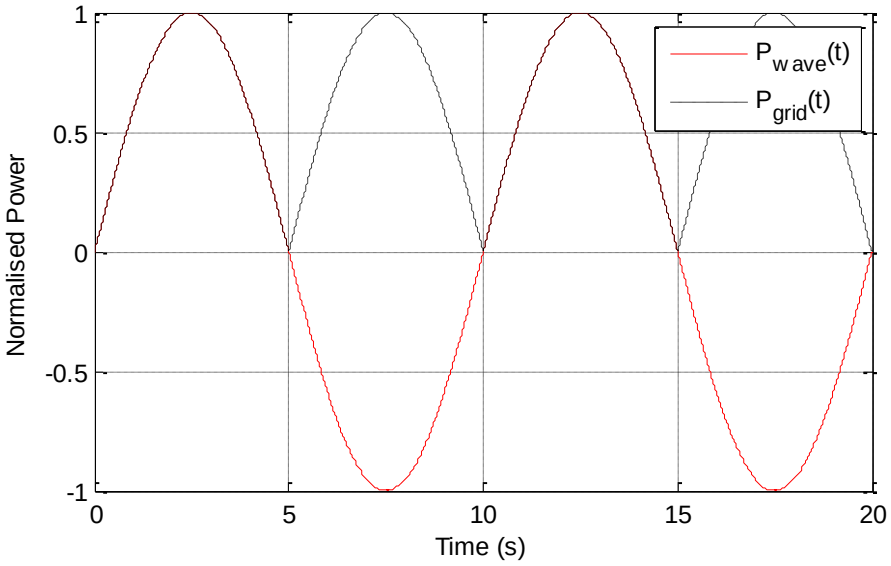


Figure A.1: Wave power and resultant grid power over time for an idealised wave

If an ideal energy storage device was implemented in the WEC which could smooth this input power completely, the power to the grid would simply be the average of the above equation, found by integrating over half an ocean wave period and dividing by this time value.

$$P_{grid_with_ES} = \frac{\int_0^{\frac{1}{2f}} P_{grid}(t)\, dt}{\frac{1}{2f}} \tag{A.8}$$

$$\begin{aligned} P_{grid_with_ES} &= \frac{\left[-k_{wec}\frac{A}{\omega}\cos(2\pi f t)\right]_0^{\frac{1}{2f}}}{\frac{1}{2f}} \\ &= \frac{k_{wec}\left(-\frac{A}{\omega}\cos(\pi) + \frac{A}{\omega}\cos(0)\right)}{\frac{1}{2f}} \\ &= \frac{k_{wec}\left(\frac{A}{\omega} + \frac{A}{\omega}\right)}{\frac{1}{2f}} = \frac{k_{wec}(4Af)}{2\pi f} \end{aligned} \tag{A.9}$$

$$P_{grid_with_ES} = \frac{k_{wec} 2A}{\pi} \tag{A.10}$$

Assuming the power to and from the energy storage device which produces the smooth output grid power has an associated efficiency factor k_{ES}, by which the smoothed grid power is reduced, and also assuming k_{ES} is a constant term, gives the following revised equation for power to the grid utilising an energy storage device.

$$P_{grid_with_ES} = \frac{k_{ES} k_{wec} 2A}{\pi} \tag{A.11}$$

Therefore, the power processed by the energy storage device is derived from (A.12).

$$P_{grid_with_ES} = P_{grid}(t) + P_{ES}(t) \tag{A.12}$$

Assuming positive power is power out of the energy storage system (ESS).

$$P_{ES}(t) = P_{grid_with_ES} - P_{grid}(t) \tag{A.13}$$

$$P_{ES}(t) = \frac{k_{ES} k_{wec} 2A}{\pi} - |k_{wec} A \sin(\omega t)| \tag{A.14}$$

$$P_{ES}(t) = k_{wec} \left(\frac{k_{ES} 2A}{\pi} - |A \sin(\omega t)| \right) \tag{A.15}$$

A plot of this power from the energy storage device and the grid average power is shown in Figure A.2 for a lossless system.

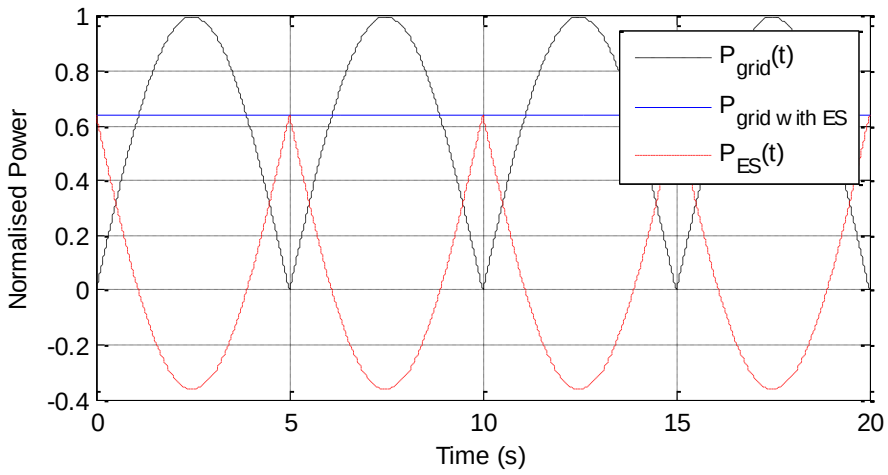


Figure A.2: Plot of power from an idealised energy storage device and grid power before and after power smoothing

A.1.2 Net flow of energy to the energy storage system

Clearly there should be no net flow of power to the energy storage device if the energy storage device efficiency is 100% and the energy in should equal the energy out. Therefore integrating over one half period produces:

$$E_{ES} = \int_0^{\frac{1}{2f}} k_{wec}\left(\frac{k_{ES}2A}{\pi} - |A\sin(\omega t)|\right)dt \tag{A.16}$$

$$E_{ES} = \int_0^{\frac{1}{2f}} k_{wec}\left(\frac{k_{ES}2A}{\pi} - A\sin(\omega t)\right)dt \tag{A.17}$$

$$E_{ES} = \left[k_{wec}\left(\frac{k_{ES}2A}{\pi}t + \frac{A}{2\pi f}\cos(2\pi f t)\right)\right]_0^{\frac{1}{2f}} \tag{A.18}$$

$$\begin{aligned} E_{ES} = k_{wec}\Big(&\frac{k_{ES}A}{\pi f} - \frac{k_{ES}2A0}{\pi} + \frac{A}{2\pi f}\cos\left(2\pi f\,\frac{1}{2f}\right) \\ &- \frac{A}{2\pi f}\cos(2\pi f 0)\Big) \\ &= k_{wec}\left(\frac{k_{ES}A}{\pi f} + \frac{A}{2\pi f}\cos(\pi) - \frac{A}{2\pi f}\cos(0)\right) \\ &= k_{wec}\left(\frac{k_{ES}A}{\pi f} - \frac{A}{2\pi f} - \frac{A}{2\pi f}\right) \\ &= k_{wec}\left(\frac{k_{ES}A}{\pi f} - \frac{A}{\pi f}\right) \end{aligned} \tag{A.19}$$

$$E_{ES} = k_{wec}\left(\frac{A(k_{ES}-1)}{\pi f}\right) \tag{A.20}$$

If k_{ES} = 1 then the total net flux of energy through the energy storage device evaluates to zero. In a practical system k_{ES} < 1.

$$E_{ES} = \frac{-Ak_{wec}(1-k_{ES})}{\pi f} \tag{A.21}$$

This is the energy lost over one half ocean wave period from which the average power lost can be found by dividing by one half period.

$$P_{ES_loss_avg} = \frac{-(1-k_{ES})k_{wec}2A}{\pi} \tag{A.22}$$

A.1.3 Transmission I^2R losses from output grid power with and without energy storage for power smoothing

To investigate if a power source with a fluctuating power output has a higher power loss than a constant power output, the I^2R losses will be analysed.

Evaluating losses for variable output power with no energy storage:

$$P_{grid_without_ES}(t) = |k_{wec} A \sin(\omega t)| \tag{A.23}$$

$$\begin{aligned} P_{grid_without_ES}(t) &= V_{grid}(t) I_{grid_without_ES}(t) \\ &= |k_{wec} A \sin(\omega t)| \end{aligned} \tag{A.24}$$

While the grid voltage and current are ac quantities, dc quantities (representing RMS values) will be assumed for $V_{grid}(t)$ and $I_{grid}(t)$ so as not to confuse these sine waves with the ocean wave sine wave profile. Assuming a constant grid voltage ($V_{grid}(t) = V_{grid}$) gives:

$$I_{grid_without_ES}(t) = \frac{|k_{wec} A \sin(\omega t)|}{V_{grid}} \tag{A.25}$$

$$\begin{aligned} P_{grid_without_ES_loss}(t) &= I_{grid_without_ES}(t)^2 R \\ &= \left(\frac{|k_{wec} A \sin(\omega t)|}{V_{grid}} \right)^2 R \end{aligned} \tag{A.26}$$

The average power loss over one half period is:

$$P_{grid__without_ES_loss_avg} = \frac{E_{grid_without_ES_loss}}{\frac{1}{2f}} \tag{A.27}$$

$$E_{grid_without_ES_loss} = \int_0^{\frac{1}{2f}} P_{grid_without_ES_loss} dt \tag{A.28}$$

$$
\begin{aligned}
E_{grid_{without_{ES_{loss}}}} &= \int_0^{\frac{1}{2f}} \left(\frac{|k_{wec} A \sin(\omega t)|}{V_{grid}}\right)^2 R\, dt \\
&= \int_0^{\frac{1}{2f}} \left(\frac{k_{wec} A \sin(\omega t)}{V_{grid}}\right)^2 R\, dt \\
&= \int_0^{\frac{1}{2f}} \frac{{k_{wec}}^2 A^2 \sin^2(\omega t)}{{V_{grid}}^2} R\, dt \\
&= \left[\frac{{k_{wec}}^2 A^2 R}{{V_{grid}}^2}\left(\frac{1}{2\omega}\right)\left(\omega t - \frac{1}{2}\sin(2\omega t)\right)\right]_0^{\frac{1}{2f}} \\
&= \left[\frac{{k_{wec}}^2 A^2 R}{{V_{grid}}^2}\left(\frac{t}{2} - \frac{1}{4\omega}\sin(2\omega t)\right)\right]_0^{\frac{1}{2f}} \\
&= \frac{{k_{wec}}^2 A^2 R}{{V_{grid}}^2}\left(\frac{1/2f}{2} - \frac{1}{8\pi f}\sin\left(4\pi f \frac{1}{2f}\right)\right) \\
&- \frac{{k_{wec}}^2 A^2 R}{{V_{grid}}^2}\left(\frac{0}{2} - \frac{1}{8\pi f}\sin(4\pi f 0)\right) \\
&= \frac{{k_{wec}}^2 A^2 R}{{V_{grid}}^2}\left(\frac{1}{4f} - \frac{1}{8\pi f}\sin(2\pi)\right) \\
&- \frac{{k_{wec}}^2 A^2 R}{{V_{grid}}^2}\left(-\frac{1}{8\pi f}\sin(0)\right)
\end{aligned}
\tag{A.29}
$$

$$
E_{grid_without_ES_loss} = \frac{{k_{wec}}^2 A^2 R}{{V_{grid}}^2}\left(\frac{1}{4f}\right) \tag{A.30}
$$

$$
E_{grid_without_ES_loss} = \frac{1}{4}\frac{{k_{wec}}^2 A^2 R}{f\,{V_{grid}}^2} \tag{A.31}
$$

$$
P_{grid_without_ES_loss_avg} = \frac{1}{2}\frac{{k_{wec}}^2 A^2 R}{{V_{grid}}^2} \tag{A.32}
$$

A plot of this power loss assuming unity voltage and an arbitrary value of 0.2 Ω for R is shown in Figure A.3.

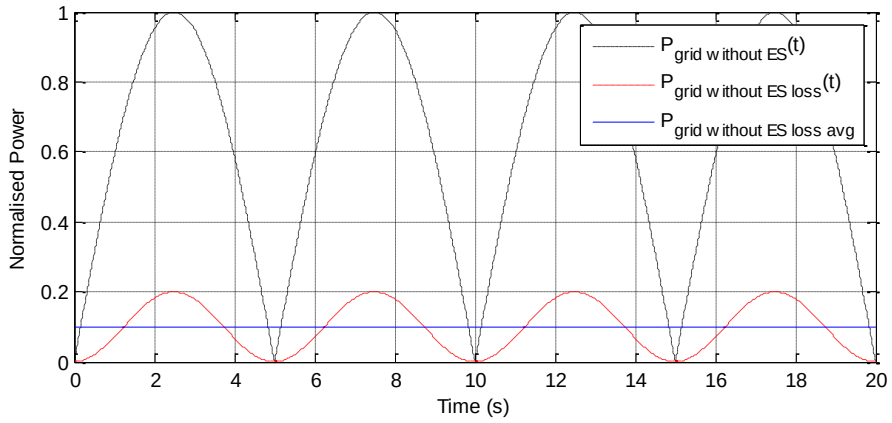


Figure A.3: I^2R power loss without an energy storage device assuming unity voltage and an arbitrary value of 0.2 Ω for R

Investigating the smoothed case which utilises energy storage:

$$P_{grid_with_ES} = \frac{k_{ES}k_{wec}2A}{\pi} \tag{A.33}$$

Assuming a constant voltage, then:

$$P_{grid_with_ES} = V_{grid}I_{grid_with_ES} = \frac{k_{ES}k_{wec}2A}{\pi} \tag{A.34}$$

$$I_{grid_with_ES} = \frac{k_{ES}k_{wec}2A}{\pi V_{grid}} \tag{A.35}$$

The transmission line losses due to I^2R are:

$$P_{grid_with_ES_loss} = {I_{grid_with_ES}}^2 R = \left(\frac{k_{ES}k_{wec}2A}{\pi V_{grid}}\right)^2 R \tag{A.36}$$

$$P_{grid_with_ES_loss} = \frac{4{k_{ES}}^2}{\pi^2}\frac{{k_{wec}}^2 A^2 R}{{V_{grid}}^2} \tag{A.37}$$

The power loss for the case without an energy storage system is repeated in (A.38).

$$P_{grid_without_ES_loss_avg} = \frac{1}{2}\frac{{k_{wec}}^2 A^2 R}{{V_{grid}}^2} \tag{A.38}$$

Comparing these two powers, the power loss due to I^2R of the transmitted smoothed power output which utilises energy storage compared to the unsmoothed case is:

$$\frac{4{k_{ES}}^2}{\pi^2} : \frac{1}{2} \tag{A.39}$$

$$0.81{k_{ES}}^2 : 1 \tag{A.40}$$

This difference of power losses is plotted in Figure A.4.

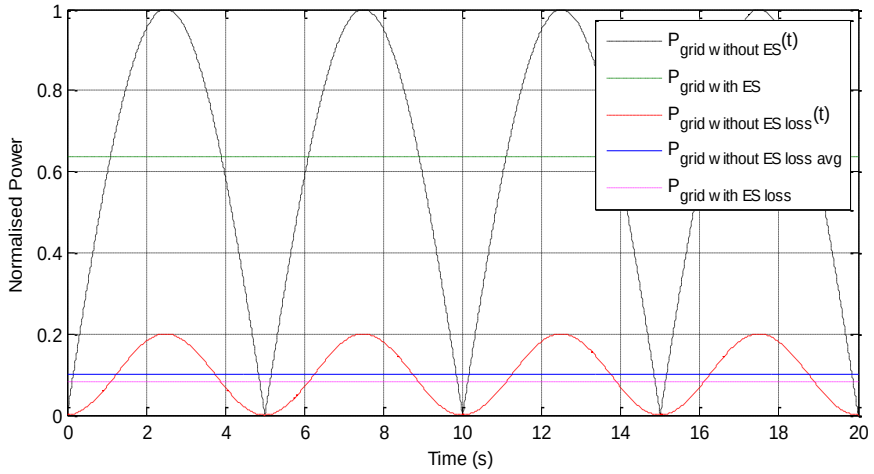


Figure A.4: Comparing power loss due to I^2R of grid power output with and without energy storage assuming unity voltage and an arbitrary value of 0.2 Ω for *R*

This shows that the less efficient the energy smoothing device, the lower the power losses. This is true, but it also lowers the transmitted power.

A.1.4 Net output grid power with and without energy storage for power smoothing taking account of transmission I^2R losses

Comparing both cases to the amount of power transmitted after losses leads to the following analysis. For the smoothed output power case which utilises an energy storage device:

$$P_{grid_with_ES_net} = P_{grid_with_ES} - P_{grid_with_ES_loss} \tag{A.41}$$

$$P_{grid_with_ES} = \frac{k_{ES}k_{wec}2A}{\pi} \tag{A.42}$$

$$P_{grid_with_ES_loss} = \frac{4{k_{ES}}^2}{\pi^2}\frac{{k_{wec}}^2A^2R}{{V_{grid}}^2} \tag{A.43}$$

$$\begin{aligned} P_{grid_with_ES_net} &= \frac{k_{ES}k_{wec}2A}{\pi} - \frac{4{k_{ES}}^2}{\pi^2}\frac{{k_{wec}}^2A^2R}{{V_{grid}}^2} \\ &= \frac{{V_{grid}}^2\pi k_{ES}k_{wec}2A}{\pi^2{V_{grid}}^2} - \frac{4{k_{ES}}^2}{\pi^2}\frac{{k_{wec}}^2A^2R}{{V_{grid}}^2} \\ &= \frac{{V_{grid}}^2\pi k_{ES}k_{wec}2A - 4{k_{ES}}^2{k_{wec}}^2A^2R}{{V_{grid}}^2\pi^2} \end{aligned} \tag{A.44}$$

$$P_{grid_with_ES_net} = \frac{2k_{ES}k_{wec}A\left({V_{grid}}^2\pi - 2k_{ES}k_{wec}AR\right)}{{V_{grid}}^2\pi^2} \tag{A.45}$$

For the unsmoothed power case where no energy storage system is used produces:

$$P_{grid_without_ES_net} = P_{grid_without_ES_avg} - P_{grid_without_ES_loss_avg} \tag{A.46}$$

$$P_{grid_without_ES_loss_avg} = \frac{1}{2}\frac{{k_{wec}}^2 A^2 R}{{V_{grid}}^2} \tag{A.47}$$

$$P_{grid_without_ES_avg} = \frac{k_{wec} 2A}{\pi} \tag{A.48}$$

$$\begin{aligned} P_{grid_without_ES_net} &= \frac{k_{wec} 2A}{\pi} - \frac{1}{2}\frac{{k_{wec}}^2 A^2 R}{{V_{grid}}^2} \\ &= \frac{{V_{grid}}^2 \pi k_{wec} 4A - \pi^2 {k_{wec}}^2 A^2 R}{2{V_{grid}}^2 \pi^2} \end{aligned} \tag{A.49}$$

$$P_{grid_without_ES_net} = \frac{2k_{wec} A\left({V_{grid}}^2 \pi - \frac{1}{4}\pi^2 k_{wec} AR\right)}{{V_{grid}}^2 \pi^2} \tag{A.50}$$

Comparing to the case with energy storage utilised:

$$P_{grid_with_ES_net} = \frac{2k_{ES} k_{wec} A\left({V_{grid}}^2 \pi - 2k_{ES} k_{wec} AR\right)}{{V_{grid}}^2 \pi^2} \tag{A.51}$$

$$P_{diff} = P_{grid_with_ES_net} - P_{grid_without_ES_net} \tag{A.52}$$

If $P_{diff} > 0$, then the case where an energy storage system with an associated efficiency is used, is demonstrated to increase the effective power to the grid by a reduction in I^2R losses.

$$P_{diff} = \frac{2k_{ES}k_{wec}A\left({V_{grid}}^2\pi - 2k_{ES}k_{wec}AR\right) - 2k_{wec}A\left({V_{grid}}^2\pi - \frac{1}{4}\pi^2 k_{wec}AR\right)}{{V_{grid}}^2\pi^2} \quad \text{(A.53)}$$

Case where $k_{ES} = 1$ gives the same results as shown previously in (A.40).

$$P_{diff} = \left[\frac{1}{2} - \frac{4}{\pi^2}\right]\frac{{k_{wec}}^2A^2R}{{V_{grid}}^2} \quad \text{(A.54)}$$

For the case where $k_{ES} \neq 1$:

$$\begin{aligned} P_{diff} &= \frac{2k_{ES}k_{wec}A{V_{grid}}^2\pi - 4{k_{ES}}^2{k_{wec}}^2A^2R - 2k_{wec}A{V_{grid}}^2\pi + \frac{1}{2}\pi^2{k_{wec}}^2A^2R}{{V_{grid}}^2\pi^2} \\ &= \frac{2k_{ES}k_{wec}A - 2k_{wec}A}{\pi} + \frac{\frac{1}{2}{k_{wec}}^2A^2R - \frac{4}{\pi^2}{k_{ES}}^2{k_{wec}}^2A^2R}{{V_{grid}}^2} \end{aligned} \quad \text{(A.55)}$$

$$P_{diff} = \frac{2k_{wec}A}{\pi}(k_{ES} - 1) + \left(\frac{1}{2} - \frac{4{k_{ES}}^2}{\pi^2}\right)\frac{{k_{wec}}^2A^2R}{{V_{grid}}^2} \quad \text{(A.56)}$$

This is a difficult function to assess as wave amplitude and voltage are contained in the formula, and these are difficult to compare.

To find case for when P_{diff} is positive or when it is 0 , solve (A.56) for k_{ES}.

$$0 = \frac{2k_{wec}Ak_{ES}}{\pi} - \frac{2k_{wec}A}{\pi} + \frac{1}{2}\frac{{k_{wec}}^2A^2R}{{V_{grid}}^2} - \frac{4{k_{ES}}^2}{\pi^2}\frac{{k_{wec}}^2A^2R}{{V_{grid}}^2} \quad \text{(A.57)}$$

$$\frac{4}{\pi^2}\frac{{k_{wec}}^2 A^2 R}{{V_{grid}}^2}{k_{ES}}^2 - \frac{2k_{wec}Ak_{ES}}{\pi} + \left(\frac{2k_{wec}A}{\pi} - \frac{1}{2}\frac{{k_{wec}}^2 A^2 R}{{V_{grid}}^2}\right) = 0 \quad \text{(A.58)}$$

$$ax^2 + bx + c = 0 \quad \text{(A.59)}$$

$$x = \frac{-b \pm \sqrt{b^2 - 4ac}}{2a} \quad \text{(A.60)}$$

$$k_{ES} = \frac{\frac{2k_{wec}A}{\pi} \pm \sqrt{\left(\frac{2k_{wec}A}{\pi}\right)^2 - 4\left(\frac{4}{\pi^2}\frac{{k_{wec}}^2 A^2 R}{{V_{grid}}^2}\right)\left(\frac{2k_{wec}A}{\pi} - \frac{1}{2}\frac{{k_{wec}}^2 A^2 R}{{V_{grid}}^2}\right)}}{2\left(\frac{4}{\pi^2}\frac{{k_{wec}}^2 A^2 R}{{V_{grid}}^2}\right)} \quad \text{(A.61)}$$

$$k_{ES} = \frac{\frac{2k_{wec}A}{\pi} \pm \sqrt{\left(\frac{2k_{wec}A}{\pi}\right)^2 - \left(\frac{8}{\pi^2}\frac{{k_{wec}}^3 A^3 R}{{V_{grid}}^2}\right)\left(\frac{4}{\pi} - \frac{k_{wec}AR}{{V_{grid}}^2}\right)}}{\left(\frac{8}{\pi^2}\frac{{k_{wec}}^2 A^2 R}{{V_{grid}}^2}\right)} \quad \text{(A.62)}$$

Evaluating for $k_{wec} = A = V = 1$ and $R = 0.2$ gives $k_{ES} = 0.960347$. Putting in more realistic values (assuming A is twice the voltage value for now), $V = 230$, $R = 0.2$, $k_{wec} = 0.3$ gives $k_{ES} = 0.999922$! This gives an indication of how efficient the energy storage device needs to be in order to benefit from decreased I^2R power losses from a smoother power output.

If equation (A.56) is divided across by A, to give a per unit measure of the power difference between the case of utilising energy storage and not, some interesting terms are produced:

$$\frac{P_{diff}}{A} = \frac{2k_{wec}}{\pi}(k_{ES} - 1) + \left(\frac{1}{2} - \frac{4}{\pi^2}{k_{ES}}^2\right){k_{wec}}^2 \frac{A}{{V_{grid}}^2/R} \tag{A.63}$$

Let:

$$r = \frac{A}{{V_{grid}}^2/R} \tag{A.64}$$

The term $\frac{P_{diff}}{A}$ is the difference in power per unitised to wave amplitude input. The ratio term r is the max input power available normalised to the short circuit power of the grid, generally this term is very small but it is a figure of merit.

The above equation is compared for two cases of r, $r = 0.5$ and $r = 0.001$, representing a weak grid and a strong grid. It is assumed that $k_{wec} = 1$ and the two cases are plotted for a range of values for k_{ES} shown in Figure A.5.

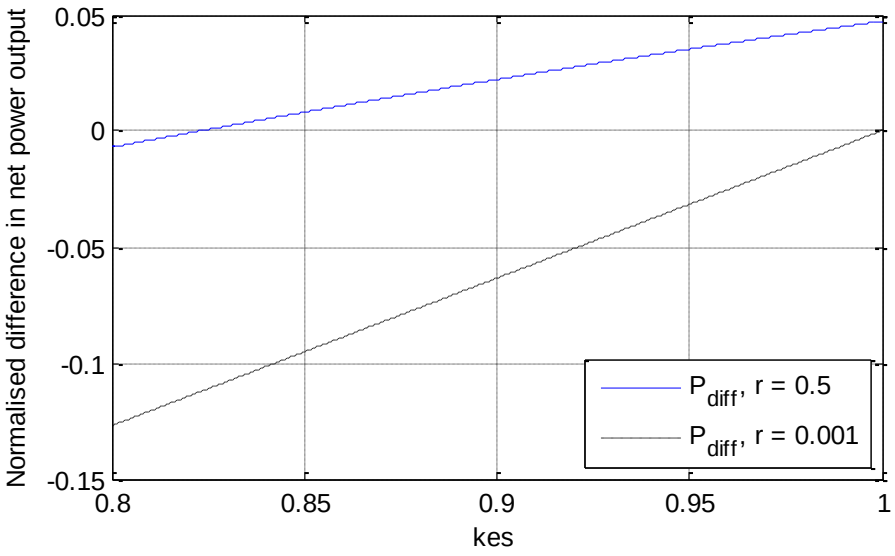


Figure A.5: Normalised difference in net power output for cases where energy storage is and isn't used to smooth the grid output power and taking into account the resultant power loss due to I^2R in the transmitted power

This shows that if the power is into a weak grid with a low short circuit power, then the benefit of lowering the transmitted I^2R power losses increases, taking into account the efficiency of the energy storage system.

A.2 Large peak to average input wave power profile analysis

A.2.1 Transmission I^2R losses from output grid power with and without energy storage used for power smoothing

It should be noted that the power input in a real WEC has a larger peak to average value than this analysis assumed, and that there are more benefits to energy storage systems.

If the input power profile contains one wave period at normal power, and no power input for the next four periods, the previous equations change as follows:

$$P_{grid_without_ES_avg} = \frac{k_{wec}\left(\frac{A}{\omega}+\frac{A}{\omega}\right)}{\frac{5}{2f}} = \frac{k_{wec}(4Af)}{10\pi f} \tag{A.65}$$

This is analogous to on for one half period, off for four half periods, so dividing equation (A.48) by five half periods instead of one produces.

$$P_{grid_without_ES_avg} = \frac{k_{wec}2A}{5\pi} \tag{A.66}$$

And losses are, from (A.32):

$$P_{grid_without_ES_loss_avg} = \frac{1}{10}\frac{{k_{wec}}^2A^2R}{{V_{grid}}^2} \tag{A.67}$$

For the smoothed power case which utilises an energy storage device, from (A.11):

$$P_{grid_with_ES} = V_{grid}I_{grid_with_ES} = \frac{k_{ES}k_{wec}2A}{5\pi} \tag{A.68}$$

A plot of grid power with and without energy storage used for this large peak to average profile is shown in Figure A.6 for $k_{ES} = k_{wec} = 1$ over two ocean wave periods.

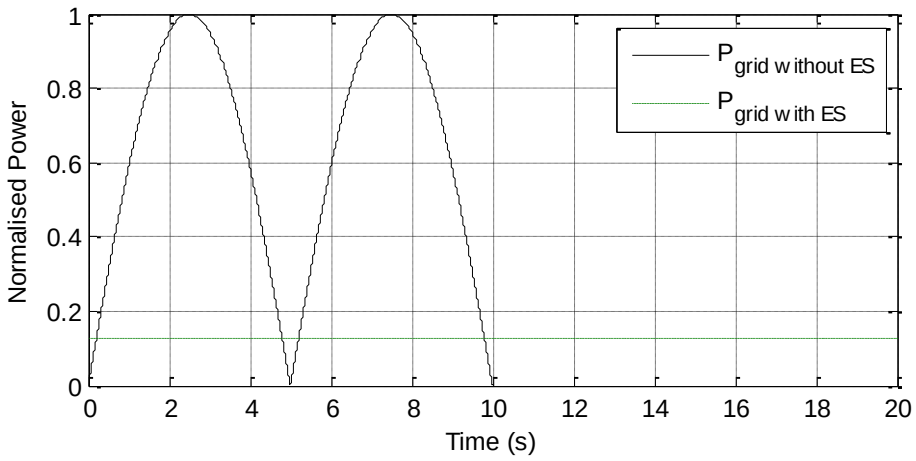


Figure A.6: Grid power with and without energy storage employed for a large peak to average profile

Assuming a constant voltage, then transmission line I^2R losses for the case with energy storage is:

$$P_{grid_with_ES_loss} = {I_{grid_with_ES}}^2 R = \left(\frac{k_{ES}k_{wec}2A}{5\pi V_{grid}}\right)^2 R \tag{A.69}$$

$$P_{grid_with_ES_loss} = \frac{4{k_{ES}}^2}{25\pi^2}\frac{{k_{wec}}^2 A^2 R}{{V_{grid}}^2} \tag{A.70}$$

and average transmission line I^2R losses for the case without energy storage is repeated in (A.71):

$$P_{grid_without_ES_loss_avg} = \frac{1}{10}\frac{{k_{wec}}^2 A^2 R}{{V_{grid}}^2} \tag{A.71}$$

Comparing these two powers, the power loss due to I^2R of the smoothed power output which utilises energy storage compared to the unsmoothed case is:

$$\frac{4{k_{ES}}^2}{25\pi^2}:\frac{1}{10} \tag{A.72}$$

$$0.16{k_{ES}}^2:1 \tag{A.73}$$

This shows that the less efficient the energy smoothing device, the lower the power loss due to I^2R in the transmitted power. This is true, but it also lowers the transmitted power.

A.2.2 Net output grid power with and without energy storage used for power smoothing taking account of transmission I^2R losses

Comparing both cases to the amount of power transmitted after losses leads to the following analysis. For the smoothed power case which utilises an energy storage device the net power transmitted is:

$$P_{grid_with_ES_net} = P_{grid_with_ES} - P_{grid_with_ES_loss} \tag{A.74}$$

$$P_{grid_with_ES} = \frac{k_{ES}k_{wec}2A}{5\pi} \tag{A.75}$$

$$P_{grid_with_ES_loss} = \frac{4{k_{ES}}^2}{25\pi^2}\frac{{k_{wec}}^2A^2R}{{V_{grid}}^2} \tag{A.76}$$

$$\begin{aligned} P_{grid_with_ES_net} &= \frac{k_{ES}k_{wec}2A}{5\pi} - \frac{4{k_{ES}}^2}{25\pi^2}\frac{{k_{wec}}^2A^2R}{{V_{grid}}^2} \\ &= \frac{5{V_{grid}}^2\pi k_{ES}k_{wec}2A}{25\pi^2{V_{grid}}^2} - \frac{4{k_{ES}}^2}{25\pi^2}\frac{{k_{wec}}^2A^2R}{{V_{gid}}^2} \\ &= \frac{10{V_{grid}}^2\pi k_{ES}k_{wec}A - 4{k_{ES}}^2{k_{wec}}^2A^2R}{25{V_{grid}}^2\pi^2} \end{aligned} \tag{A.77}$$

$$P_{grid_with_ES_net} = \frac{20k_{ES}k_{wec}A\left({V_{grid}}^2\pi - \frac{2}{5}k_{ES}k_{wec}AR\right)}{50{V_{grid}}^2\pi^2} \tag{A.78}$$

For the unsmoothed power case where an energy storage system is not used:

$$P_{grid_without_ES_net} = P_{grid_without_ES_avg} - P_{grid_without_ES_loss_avg} \tag{A.79}$$

$$P_{grid_without_ES_loss_avg} = \frac{1}{10}\frac{{k_{wec}}^2A^2R}{{V_{grid}}^2} \tag{A.80}$$

$$P_{grid_without_ES_avg} = \frac{k_{wec}2A}{5\pi} \tag{A.81}$$

$$P_{grid_without_ES_net} = \frac{k_{wec}2A}{5\pi} - \frac{1}{10}\frac{{k_{wec}}^2A^2R}{{V_{grid}}^2} \tag{A.82}$$

$$P_{grid_without_ES_net} = \frac{{V_{grid}}^2\pi k_{wec}4A - \pi^2{k_{wec}}^2A^2R}{10{V_{grid}}^2\pi^2} \tag{A.83}$$

$$P_{grid_without_ES_net} = \frac{20k_{wec}A\left({V_{grid}}^2\pi - \frac{1}{4}\pi^2k_{wec}AR\right)}{50{V_{grid}}^2\pi^2} \tag{A.84}$$

The net power to the grid with an energy storage device is repeated in (A.85).

$$P_{grid_with_ES_net} = \frac{20k_{ES}k_{wec}A\left({V_{grid}}^2\pi - \frac{2}{5}k_{ES}k_{wec}AR\right)}{50{V_{grid}}^2\pi^2} \quad \text{(A.85)}$$

$$P_{diff} = P_{grid_with_ES_net} - P_{grid_without_ES_net} \quad \text{(A.86)}$$

$$P_{diff} = \frac{20k_{ES}k_{wec}A\left({V_{grid}}^2\pi - \frac{2}{5}k_{ES}k_{wec}AR\right) - 20k_{wec}A\left({V_{grid}}^2\pi - \frac{1}{4}\pi^2k_{wec}AR\right)}{50{V_{grid}}^2\pi^2} \quad \text{(A.87)}$$

Case where $k_{ES} = 1$ confirms the result shown previously in (A.73).

$$P_{diff} = \frac{20k_{wec}A{V_{grid}}^2\pi - 8{k_{wec}}^2A^2R}{50{V_{grid}}^2\pi^2} + \frac{-20k_{wec}A{V_{grid}}^2\pi + 5{k_{wec}}^2A^2\pi^2R}{50{V_{grid}}^2\pi^2} \quad \text{(A.88)}$$

$$P_{diff} = \frac{5{k_{wec}}^2A^2\pi^2R - 8{k_{wec}}^2A^2R}{50{V_{grid}}^2\pi^2} \quad \text{(A.89)}$$

$$P_{diff} = \left(\frac{{k_{wec}}^2A^2R}{{V_{grid}}^2}\right)\frac{5\pi^2 - 8}{50\pi^2} \quad \text{(A.90)}$$

$$P_{diff} = \left(\frac{{k_{wec}}^2A^2R}{{V_{grid}}^2}\right)\left(\frac{1}{10} - \frac{4}{25\pi^2}\right) \quad \text{(A.91)}$$

For the case where $k_{ES} \neq 1$:

$$P_{diff} = \frac{20k_{ES}k_{wec}A{V_{grid}}^2\pi - 20k_{wec}A{V_{grid}}^2\pi}{50{V_{grid}}^2\pi^2} + \frac{5{k_{wec}}^2A^2\pi^2R - 8{k_{ES}}^2{k_{wec}}^2A^2R}{50{V_{grid}}^2\pi^2} \quad \text{(A.92)}$$

$$P_{diff} = \frac{2}{5\pi}k_{ES}k_{wec}A - \frac{2}{5\pi}k_{wec}A + \left(\frac{{k_{wec}}^2A^2R}{{V_{grid}}^2}\right)\left(\frac{1}{10} - \frac{4{k_{ES}}^2}{25\pi^2}\right) \quad \text{(A.93)}$$

$$P_{diff} = \frac{2}{5\pi}k_{wec}A(k_{ES} - 1) + \left(\frac{1}{10} - \frac{4{k_{ES}}^2}{25\pi^2}\right)\left(\frac{{k_{wec}}^2A^2R}{{V_{grid}}^2}\right) \quad \text{(A.94)}$$

This is a difficult function to assess as wave amplitude and voltage are contained in the formula, and these are difficult to compare.

To find the case for when P_{diff} is positive or when it is 0, solve (A.95) for k_{ES}.

$$0 = \frac{2}{5\pi}k_{wec}Ak_{ES} - \frac{2}{5\pi}k_{wec}A + \frac{1}{10}\frac{{k_{wec}}^2A^2R}{{V_{grid}}^2} - \frac{4{k_{ES}}^2}{25\pi^2}\frac{{k_{wec}}^2A^2R}{{V_{grid}}^2} \quad \text{(A.95)}$$

$$\frac{4}{25\pi^2}\frac{{k_{wec}}^2A^2R}{{V_{grid}}^2}{k_{ES}}^2 - \frac{2}{5\pi}k_{wec}Ak_{ES} + \left(\frac{2}{5\pi}k_{wec}A - \frac{1}{10}\frac{{k_{wec}}^2A^2R}{{V_{grid}}^2}\right) = 0 \quad \text{(A.96)}$$

$$ax^2 + bx + c = 0 \quad \text{(A.97)}$$

$$x = \frac{-b \pm \sqrt{b^2 - 4ac}}{2a} \tag{A.98}$$

$$k_{ES} = \frac{\frac{2}{5\pi}k_{wec}A \pm \sqrt{\left(\frac{2}{5\pi}k_{wec}A\right)^2 - 4\left(\frac{4}{25\pi^2}\frac{{k_{wec}}^2A^2R}{{V_{grid}}^2}\right)\left(\frac{2}{5\pi}k_{wec}A - \frac{1}{10}\frac{{k_{wec}}^2A^2R}{{V_{grid}}^2}\right)}}{2\left(\frac{4}{25\pi^2}\frac{{k_{wec}}^2A^2R}{{V_{grid}}^2}\right)} \tag{A.99}$$

$$k_{ES} = \frac{\frac{2}{5\pi}k_{wec}A \pm \sqrt{\left(\frac{2}{5\pi}k_{wec}A\right)^2 - \left(\frac{8}{25\pi^2}\frac{{k_{wec}}^3A^3R}{{V_{grid}}^2}\right)\left(\frac{4}{5\pi} - \frac{1}{5}\frac{k_{wec}AR}{{V_{grid}}^2}\right)}}{\left(\frac{8}{25\pi^2}\frac{{k_{wec}}^2A^2R}{{V_{grd}}^2}\right)} \tag{A.100}$$

Evaluating for $k_{wec} = A = V = 1$ and $R = 0.2$ gives $k_{ES} = 0.861835$, in the previous analysis of an ideal sine wave it was 0.9603. Putting in more realistic values (assuming A is twice the voltage value for now), $V = 230$, $R = 0.2$, $k_{wec} = 0.3$ gives $k_{ES} = 0.999657$. In the previous analysis of an ideal sine wave it was 0.999922. These figures demonstrate the larger the peak to average power, the greater the benefit of smoothing the output power and reducing the I^2R losses in the transmitted power.

If equation (A.94) is divided across by A as before, some interesting terms are produced:

$$\frac{P_{diff}}{A} = \frac{2}{5\pi}k_{wec}(k_{ES} - 1) + \left(\frac{1}{10} - \frac{4{k_{ES}}^2}{25\pi^2}\right){k_{wec}}^2\left(\frac{A}{{V_{grid}}^2/R}\right) \tag{A.101}$$

Again let:

$$r = \frac{A}{{V_{grid}}^2 / R} \tag{A.102}$$

The term $\frac{P_{diff}}{A}$ is the difference in power per unitised to wave amplitude input. The ratio term r is the max input power available normalised to the short circuit power of the grid, generally this term is very small but it is a figure of merit. Again the above equation is compared for two cases of r, $r = 0.5$ and $r = 0.001$, representing a weak grid and a strong grid. $k_{wec} = 1$ is assumed and the two cases are plotted for a range of values for k_{ES} shown in Figure A.7.

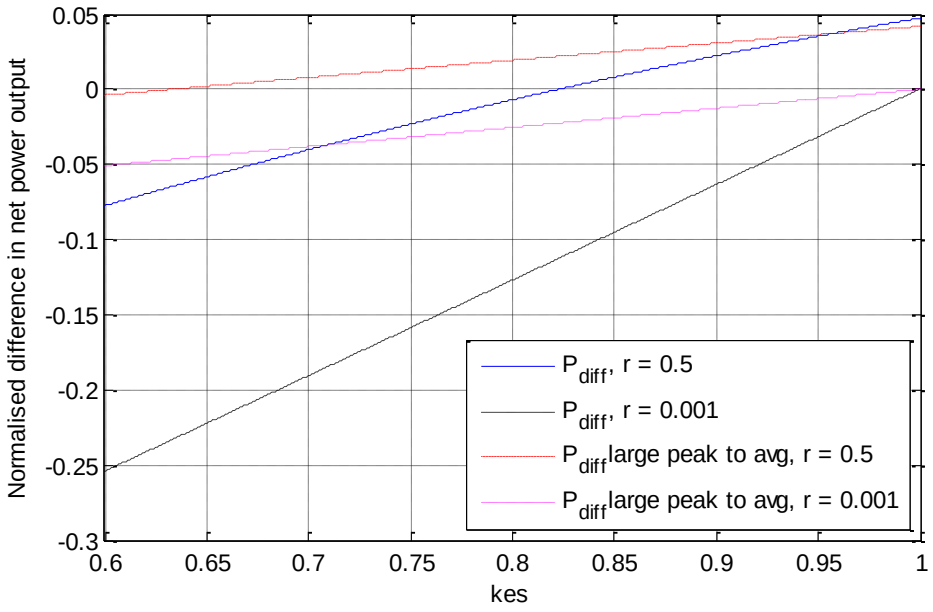


Figure A.7: Normalised difference in net power output for cases where energy storage is and isn't used. Also taking into account the resultant power loss due to I^2R in the transmitted power, and comparing with large peak to average input power

This shows that if the power is into a weak grid with a low short circuit power, then the benefit of lowering the transmitted I^2R power losses increases, taking into account the efficiency of the energy storage system. In this case where the peak to average power has been increased the benefit of energy storage is enhanced.

Appendix B Derivation of PI anti-integral control block equations

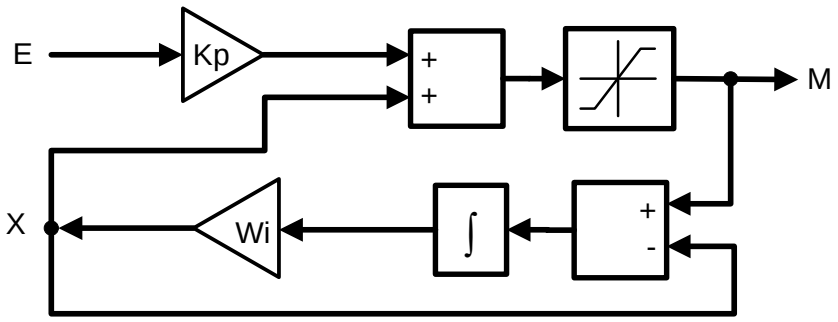


Figure B.1: PI model block

From Figure B.1, the following equations can be determined for the controller when not in saturation.

$$M = K_p E + X \tag{B.1}$$

$$(M - X)\frac{W_i}{s} = X \tag{B.2}$$

$$\frac{W_i}{s} M = X\left(1 + \frac{W_i}{s}\right) \tag{B.3}$$

$$X = \frac{\frac{W_i}{s} M}{\left(1 + \frac{W_i}{s}\right)} \tag{B.4}$$

$$M = K_p E + \frac{\frac{W_i}{s} M}{\left(1 + \frac{W_i}{s}\right)} \tag{B.5}$$

$$M\left(1-\frac{\frac{W_i}{s}}{\left(1+\frac{W_i}{s}\right)}\right)=K_pE \tag{B.6}$$

$$M=\frac{K_pE}{\left(1-\frac{\frac{W_i}{s}}{\left(1+\frac{W_i}{s}\right)}\right)} \tag{B.7}$$

$$M=\frac{\left(1+\frac{W_i}{s}\right)K_pE}{\left(1+\frac{W_i}{s}-\frac{W_i}{s}\right)} \tag{B.8}$$

$$M=E\left(K_p+\frac{K_pW_i}{s}\right) \tag{B.9}$$

$$K_i=K_pW_i \tag{B.10}$$

When the controller is in saturation the output is limited to M_{max} or M_{min} and the value of X will then also saturate at this output limit. This describes the anti-integral windup feature of the controller.

Appendix C Derivation of strategy F: ω^{β} control equation from [26]

The oscillations in electrical power output from an OWC WEC can easily be absorbed by a large electrical grid, but may introduce unacceptable disturbances into a small isolated grid. The capability of storing kinetic energy in and releasing it from a flywheel, is a way of smoothing the oscillations in electrical power delivered to the grid. However, this has to be associated with a control law that allows the rotational speed to oscillate. For this reason one should avoid a control law curve:

$$P_e = f(\omega) \tag{C.1}$$

part of which exhibits an infinite slow (infinite derivative). The maximum allowed slope depends on what the grid accepts in terms of power oscillation and on the inertia of the rotating parts, as will be shown in what follows.

The dynamics of the rotor can be written as:

$$P_n(t) - P_e(t) = J\omega\frac{d\omega}{dt} \tag{C.2}$$

$$P_n = \omega T_n \tag{C.3}$$

$$P_e = \omega T_e \tag{C.4}$$

where J is the inertia of the rotating parts (turbine and generator), T_n is the aerodynamic torque on the turbine rotor and T_e is the electromagnetic torque on the generator rotor (bearing friction is ignored here). In this analysis it is J=595 kg m^2.

The electrical grid (especially in the case of a small isolated grid) may impose constraints on what concerns maximum allowable values for the time-derivative of the electrical

power delivered to the grid. A simple algorithm, accounting for such restriction is derived in [26] in order to complement the optimal control law.

From the grid viewpoint, the most unfavourable situation is expected to occur when the turbine torque sharply drops due to rotor blade stalling. Let us assume, in the worst scenario that T_n has dropped to zero and write:

$$-P_e = J\omega\frac{d\omega}{dt} \tag{C.5}$$

From which we obtain:

$$-f(\omega) = J\omega\frac{d\omega}{dt} \tag{C.6}$$

$$-\frac{dP_e}{dt} = \frac{d\left(J\omega\frac{d\omega}{dt}\right)}{dt} \tag{C.7}$$

$$-\frac{dP_e}{dt} = \frac{d\big(-f(\omega)\big)}{dt} \tag{C.8}$$

$$-\frac{dP_e}{dt} = \frac{-df(\omega)}{d\omega}\frac{d\omega}{dt} \tag{C.9}$$

$$\frac{-f(\omega)}{J\omega} = \frac{d\omega}{dt} \tag{C.10}$$

$$-\frac{dP_e}{dt} = \frac{-df(\omega)}{d\omega}\left(\frac{-f(\omega)}{J\omega}\right) \tag{C.11}$$

$$-\frac{dP_e}{dt} = \frac{1}{J\omega}\frac{df(\omega)}{d\omega}f(\omega) \tag{C.12}$$

We may specify:

$$-\frac{dP_e}{dt} \leq A \tag{C.13}$$

And consider the limiting case when:

$$-\frac{dP_e}{dt} = A \tag{C.14}$$

We obtain an ordinary differential equation:

$$AJ\omega = f(\omega)\frac{df(\omega)}{d\omega} \tag{C.15}$$

Let ω_{max} be the maximum value the rotation speed is allowed to take (for mechanical and/or electrical reasons). In order to avoid overspeeding, the control law should prescribe

$$f(\omega) = P_{max}, \qquad \omega \geq \omega_{max} \tag{C.16}$$

where P_{max} is a value to be prescribed close to the peak power of the turbine at its maximum speed. The solution of the differential equation subject to the following boundary condition:

$$f(\omega_{max}) = P_{max} \tag{C.17}$$

Is:

$$\frac{d}{d\omega}f^2(\omega) = 2f(\omega)\frac{df(\omega)}{d\omega} \tag{C.18}$$

$$\frac{1}{2}\frac{d}{d\omega}f^2(\omega) = f(\omega)\frac{df(\omega)}{d\omega} \tag{C.19}$$

$$\frac{1}{2}\frac{d}{d\omega}f^2(\omega) = AJ\omega \tag{C.20}$$

$$\frac{d}{d\omega}f^2(\omega) = 2AJ\omega \tag{C.21}$$

$$f^2(\omega) = \int 2AJ\omega \, d\omega \tag{C.22}$$

$$f^2(\omega) = AJ\omega^2 + c \tag{C.23}$$

$${P_{max}}^2 = AJ{\omega_{max}}^2 + c \tag{C.24}$$

$${P_{max}}^2 - AJ{\omega_{max}}^2 = c \tag{C.25}$$

$${P_e}^2 = AJ\omega^2 + {P_{max}}^2 - AJ{\omega_{max}}^2 \tag{C.26}$$

$${P_e}^2 = {P_{max}}^2 - AJ({\omega_{max}}^2 - \omega^2) \tag{C.27}$$

$$P_e = f(\omega) = \left[{P_{max}}^2 - AJ({\omega_{max}}^2 - \omega^2)\right]^{\frac{1}{2}} \tag{C.28}$$

This is the equation of a hyperbola in the (ω, P_e) plane, whose axis coincide with the axes of coordinates, passing through the points (ω_{max}, P_{max}) and $(\omega_0, 0)$, where:

$$\omega_0 = \left[{\omega_{max}}^2 - \frac{{P_{max}}^2}{AJ}\right]^{\frac{1}{2}} \tag{C.29}$$

Four regulation curves $P_e = f(\omega)$ are shown in [26] for $P_{max} = 570$ kW, $\omega_{max} = 1500$ rpm, and $AJ = 100, 50, 30, 20$ MW kg m^2/s.

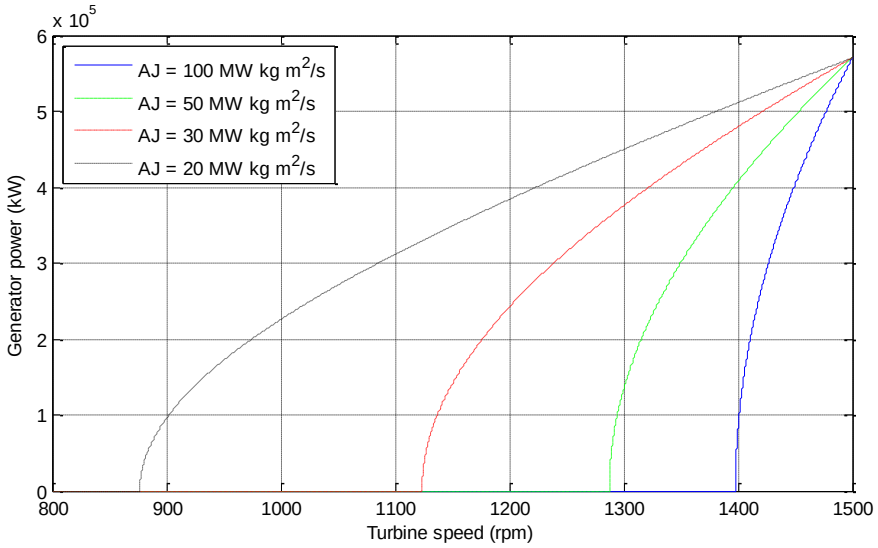


Figure C.1: Regulation curves for several values of AJ MW kg m^2/s, where A = $|dP_e/dt|$ is the maximum value of the time-derivative of the electrical power allowed by the grid.

As should be expected, the slope of the curve increases with the product AJ. Obviously a larger slope allows more electrical energy to be produced; this may be achieved by increasing the rotational inertia J and/or the value of the electrical power time-derivative $|dP_e/dt| = A$ allowed by the grid.

This graph is true for any rotational device where a limit is specified on $\frac{dP_e}{dt}$ and the case is considered where the input torque on the turbine developed from the ocean waves drops to zero.

Appendix D BCAP0005 P270 supercapacitor (SC) datasheet from Maxwell Technologies

DATASHEET
HC POWER SERIES ULTRACAPACITORS

BCAP0005 P270 BCAP0050 P270
BCAP0010 P270 BCAP0100 P270
BCAP0025 P270 BCAP0150 P270

TYPICAL FEATURES AND BENEFITS

- Ultra-low internal resistance
- Two pin radial lead
- Resistant against reverse polarity
- 500,000 cycles, 10 year life capability
- RoHS compliant
- Proprietary material science and packaging technology

EXAMPLE APPLICATIONS

- Consumer electronics
- Industrial and automation
- Portable power tools
- Renewable energy systems
- Short term UPS (uninterruptible power supply) and telecom systems

PRODUCT SPECIFICATIONS

CAPACITANCE	BCAP0005	BCAP0010	BCAP0025	BCAP0050	BCAP0100	BCAP0150
Nominal capacitance	5 F	10 F	25 F	50 F	100 F	150 F
Capacitance tolerance	±20%		-0% / +20%			
VOLTAGE						
Rated voltage	2.7 V DC					
Surge voltage	2.85 V DC					
RESISTANCE						
ESR, DC	200 mΩ	80 mΩ	42 mΩ	20 mΩ	15 mΩ	14 mΩ
ESR, AC	110 mΩ	60 mΩ	28 mΩ	15 mΩ	9 mΩ	8 mΩ
Resistance tolerance	Max.					
TEMPERATURE						
Operating temperature range	-40°C to +65°C					
Storage temperature range	-40°C to +70°C					
Temperature characteristics						
Capacitance change	Within ± 5% of initial measured value at 25°C (at -40°C)					
Internal resistance change	Within ± 50% of initial measured value at 25°C (at -40°C)					
POWER						
Pd	1,900 W/kg	2,700 W/kg	2,800 W/kg	3,100 W/kg	2,300 W/kg	1,700 W/kg
Pmax	3,100 W/kg	7,500 W/kg	9,000 W/kg	8,600 W/kg	8,100 W/kg	6,500 W/kg
ENERGY						
Energy density (Emax)	2.2 Wh/kg	2.5 Wh/kg	3.6 Wh/kg	3.6 Wh/kg	4.0 Wh/kg	4.3 Wh/kg
LIFESPAN						
Shelf life	After 1,000 hours storage at 65°C without load shall meet specification for endurance					
Endurance After 1,000 hours application of rated voltage at 65°C. Within % of initial specified value.						
Capacitance change	Within 30% of initial value					
Internal resistance change	Within 100% of initial value					
Life test After 10 years at rated voltage and 25°C. Within % of initial specified value.						
Capacitance change	Within 30% of initial value					
Internal resistance	Within 100% of initial value					

DATASHEET
HC POWER SERIES ULTRACAPACITORS

BCAP0005 P270 BCAP0050 P270
BCAP0010 P270 BCAP0100 P270
BCAP0025 P270 BCAP0150 P270

PRODUCT SPECIFICATIONS (cont.)

CYCLES	BCAP0005	BCAP0010	BCAP0025	BCAP0050	BCAP0100	BCAP0150
Capacitors cycled between specified voltage and half rated voltage under constant current at 25°C (500,000 cycles).						
Capacitance change	Within 30% of initial value					
Internal resistance	Within 100% of initial value					
CURRENT						
Leakage current (Ic) After 72 hours at 25°C. Initial leakage current can be higher.	0.015 mA	0.03 mA	0.045 mA	0.075 mA	0.26 mA	0.5 mA
Maximum continuous current Assuming 15°C temperature rise above ambient temperature.	1.6 A	3.5 A	4.9 A	7.1 A	8.2 A	9.1 A
Maximum peak current	3.4 A	7.5 A	16.5 A	33.7 A	54.0 A	65.3 A
Short circuit current (Isc)	13.5 A	33.8 A	64.3 A	135.0 A	180.0 A	193.0 A
CONNECTION						
Terminal	Radial lead	Radial lead	Radial lead	Radial lead	Snap in	Snap in
SIZE						
Dimensions	See drawings					
Weight	2.3g	4.0g	7.2g	14.0g	25.0g	35.0g

MARKINGS

Modules are marked with the following information: Rated capacitance, rated voltage, product number, name of manufacturer, negative terminal, serial number.

ADDITIONAL TECHNICAL INFORMATION

Capacitance and ESR, DC measured per document no. 1007239, available at www.maxwell.com.

I_c = leakage current after 72 hours at 25°C

Isc = short circuit current (maximum peak current)

R_{th} = thermal resistance

$$Emax = \frac{\frac{1}{2} CV^2}{3{,}600 \times mass} \qquad Pmax = \frac{\frac{V^2}{4R\ (1khz)}}{mass} \qquad Pd = \frac{\frac{0.12V^2}{R\ (DC)}}{mass}$$

$$\text{Maximum Peak Current (1 sec)} = \frac{\frac{1}{2} V}{R(DC) + \frac{1}{C}}$$

Appendix E Matlab code used for supercapacitor (SC) #11 (standard testing)

```
% Created by: Dónal Murray
% Date created: 26th March 2010
% Date modified: 2nd February 2011

% This file carries out repeated cycling tests on supercapacitors
% by operating a power supply, load, multimeter and temperature
% sensor using GPIB. Constant current control is used. Data is
% then saved to files every predetermined number of cycles.

clear all
% Note that even though variables are set at the beginning of this
% program for GPIB control of current, voltage, and resistance
% values, the actual number must be used in the code.


% Get Simulation time
%%%%%%%%%%%%%%%%%%%%%%%%%%%%%%%%%%%%%%%%%%%%%%%%%%%%FINISHED BLOCK OF CODE
number_of_simulated_days = input ('Please enter the number of days
that you expect \nthe simulation to last (as a decimal):');
if isempty(number_of_simulated_days)
    error('Error: No amount of days defined');
    %fclose('all');
end
one_minute = 60;
one_hour = 60 * one_minute;
one_day = 24 * one_hour;
simulation_time = one_day * number_of_simulated_days; %in seconds
%%%%%%%%%%%%%%%%%%%%%%%%%%%%%%%%%%%%%%%%%%%%%%%%%%%%FINISHED BLOCK OF CODE
%Variable of use: simulation_time


% Key variables chosen for testing
%%%%%%%%%%%%%%%%%%%%%%%%%%%%%%%%%%%%%%%%%%%%%%%%%%%%FINISHED BLOCK OF CODE
max_voltage_cycled_to =             2.7;
min_voltage_cycled_to =             1.35;
cycles_between_char_tests =         100;
number_of_char_tests_in_a_row =     5;
cycles_between_char_tests_var =     cycles_between_char_tests -
number_of_char_tests_in_a_row;
number_of_param_readings_per_file = 300;
charge_and_discharge_current =      1.6;
%%%%%%%%%%%%%%%%%%%%%%%%%%%%%%%%%%%%%%%%%%%%%%%%%%%%FINISHED BLOCK OF CODE


load('cycle_number.mat', 'cycle_number');
%Variables used to help with code operation
cycle_num_fixed = cycle_number;
meas_voltage_multi_meter = 0;
```

```
resettable_variable = 1;
safety_error_voltage = 0.5;
safety_error_temp = 33;

% Begin communicating with GPIB equipment
%%%%%%%%%%%%%%%%%%%%%%%%%%%%%%%%%%%%%%%%%%%%FINISHED BLOCK OF CODE
temp_sens = gpib('ni',0,2);  %Locate the temperature sensing
%device at GPIB address 2
fopen(temp_sens);            %Begin communications with the device
pow_sup = gpib('ni',0,5);
fopen(pow_sup);
prog_load = gpib('ni',0,1);
fopen(prog_load);
multi_meter = gpib('ni',0,3);
fopen(multi_meter);
%%%%%%%%%%%%%%%%%%%%%%%%%%%%%%%%%%%%%%%%%%%%FINISHED BLOCK OF CODE


% Set parameters for equipment and then turn them on
%%%%%%%%%%%%%%%%%%%%%%%%%%%%%%%%%%%%%%%%%%%%FINISHED BLOCK OF CODE
fprintf(pow_sup,'Curr 0.05');
fprintf(pow_sup,'Volt 0');
fprintf(prog_load,'CCCR 1');    %Enable CC mode (2 is for CC mode)
fprintf(prog_load,'Iset 0');
fprintf(prog_load,'Rset 20');   %For completeness sake
fprintf(multi_meter,'Conf:Volt:dc 10, 0.0001'); %Sets the
%multimeter to dc voltmeter mode and the range too
fprintf(multi_meter,'Trig:Del 0');
fprintf(multi_meter,'Inp:Imp:Auto Off');%To change input R to 10 M
%if off, and 10 G if on
fprintf(multi_meter,'Zero:Auto Off'); %Should double the reading
%speed of dc voltage when off
fprintf(pow_sup,'Outp on');     %Turn on the power supply
fprintf(pow_sup,'Volt 0.2');
pause(1)
fprintf(pow_sup,'Volt 0.4');
pause(1)
fprintf(pow_sup,'Volt 0.6');
pause(1)
fprintf(pow_sup,'Volt 0.8');
pause(1)
fprintf(pow_sup,'Volt 1.0');
pause(1)
fprintf(pow_sup,'Volt 1.2');
pause(1)
fprintf(pow_sup,'Volt 1.4');
pause(1)
fprintf(pow_sup,'Volt 1.6');
pause(1)
fprintf(pow_sup,'Volt 1.8');
pause(1)
fprintf(pow_sup,'Volt 2.0');
pause(1)
fprintf(pow_sup,'Volt 2.2');
pause(1)
fprintf(pow_sup,'Volt 2.4');
pause(1)
fprintf(pow_sup,'Volt 2.8');
fprintf(prog_load,'Load on');   %Turn on the load
%%%%%%%%%%%%%%%%%%%%%%%%%%%%%%%%%%%%%%%%%%%%FINISHED BLOCK OF CODE
```

```
% The main loop for the program
tic;
time_to_fin_counter = 0;        %Iniitialise the variable, put in
%earlier
total_time = toc;               %Used to compare with
%time_to_fin_counter to check code simulation time

while(time_to_fin_counter < simulation_time)

% 95 cycles without writing to files or performing
%characterisation tests
%%%%%%%%%%%%%%%%%%%%%%%%%%%%%%%%%%%%%%%%%%%%%%%%%%%%%%%%%%%%%%%%FINISHED BLOCK OF CODE
    for cycle_test_array_pos = 1:cycles_between_char_tests_var
        cycle_number = cycle_number+1;

%%%%%%%%%%%%%%%%%%%%%%%%%%%%%%%%%%%%%%%%%%%%%%%%%%%%%%%%%%%%%%%%FINISHED BLOCK OF CODE
        fprintf(pow_sup,'Curr 1.6');
        while(meas_voltage_multi_meter < max_voltage_cycled_to)
            fprintf(multi_meter,'Init')
            fprintf(multi_meter,'Fetc?')
            meas_voltage_multi_meter_str = fscanf(multi_meter);
            meas_voltage_multi_meter =
str2double(meas_voltage_multi_meter_str);
            if (meas_voltage_multi_meter < safety_error_voltage)
                break
            end
        end
        fprintf(pow_sup,'Curr 0');
%%%%%%%%%%%%%%%%%%%%%%%%%%%%%%%%%%%%%%%%%%%%%%%%%%%%%%%%%%%%%%%%FINISHED BLOCK OF CODE

%%%%%%%%%%%%%%%%%%%%%%%%%%%%%%%%%%%%%%%%%%%%%%%%%%%%%%%%%%%%%%%%FINISHED BLOCK OF CODE
        fprintf(prog_load,'Iset 1.6');
        while(meas_voltage_multi_meter > min_voltage_cycled_to)
            fprintf(multi_meter,'Init')
            fprintf(multi_meter,'Fetc?')
            meas_voltage_multi_meter_str = fscanf(multi_meter);
            meas_voltage_multi_meter =
str2double(meas_voltage_multi_meter_str);
        end;
        fprintf(prog_load,'Iset 0');
%%%%%%%%%%%%%%%%%%%%%%%%%%%%%%%%%%%%%%%%%%%%%%%%%%%%%%%%%%%%%%%%FINISHED BLOCK OF CODE
        if (meas_voltage_multi_meter < safety_error_voltage)
            break
        end

        fprintf(temp_sens,'Meas? 3');
        meas_temp_str = fscanf(temp_sens);
        meas_temp = str2double(meas_temp_str);

        if (meas_temp > safety_error_temp)
            break
        end

    end
%%%%%%%%%%%%%%%%%%%%%%%%%%%%%%%%%%%%%%%%%%%%%%%%%%%%%%%%%%%%%%%%FINISHED BLOCK OF CODE

    if (meas_voltage_multi_meter < safety_error_voltage)
        break
    end
```

```
    if (meas_temp > safety_error_temp)
        break
    end


    for char_test_array_pos = 1:number_of_char_tests_in_a_row
        cycle_number = cycle_number+1

% Charge to max voltage
%%%%%%%%%%%%%%%%%%%%%%%%%%%%%%%%%%%%%%%%%%%%%%%%%%%%%%%%%%%%%%%%FINISHED BLOCK OF CODE
        fprintf(pow_sup,'Curr 1.6');
        while(meas_voltage_multi_meter < max_voltage_cycled_to)
            fprintf(multi_meter,'Init')
            fprintf(multi_meter,'Fetc?')
            meas_voltage_multi_meter_str = fscanf(multi_meter);
            meas_voltage_multi_meter =
str2double(meas_voltage_multi_meter_str);
            if (meas_voltage_multi_meter < safety_error_voltage)
                break
            end
        end
        fprintf(pow_sup,'Curr 0');
%%%%%%%%%%%%%%%%%%%%%%%%%%%%%%%%%%%%%%%%%%%%%%%%%%%%%%%%%%%%%%%%FINISHED BLOCK OF CODE

% Wait 5 seconds
%%%%%%%%%%%%%%%%%%%%%%%%%%%%%%%%%%%%%%%%%%%%%%%%%%%%%%%%%%%%%%%%FINISHED BLOCK OF CODE
        five_counter = 0;
        time1 = toc;
        while(five_counter < 5)
            fprintf(multi_meter,'Init')
            fprintf(multi_meter,'Fetc?')
            meas_voltage_multi_meter_str = fscanf(multi_meter);
            meas_voltage_multi_meter =
str2double(meas_voltage_multi_meter_str);

            fprintf(temp_sens,'Meas? 3');
            meas_temp_str = fscanf(temp_sens);
            meas_temp = str2double(meas_temp_str);

            if (meas_temp > safety_error_temp)
                break
            end

            the_time = clock;
            elapsed_time = toc;
            voltage_and_elapsed_time_and_temp_and_date =
[meas_voltage_multi_meter meas_temp elapsed_time the_time];
            file_out =
sprintf('SC11_voltages_for_cycle.%d.dat',cycle_number);
            save('-append', file_out,
'voltage_and_elapsed_time_and_temp_and_date', '-ascii');
            five_counter = toc - time1;
        end
%%%%%%%%%%%%%%%%%%%%%%%%%%%%%%%%%%%%%%%%%%%%%%%%%%%%%%%%%%%%%%%%FINISHED BLOCK OF CODE

        if (meas_temp > safety_error_temp)
            break
        end
```

```
        fprintf(multi_meter,'Conf:Volt:dc 10, 0.00001');
        fprintf(multi_meter,'Init')
        fprintf(multi_meter,'Fetc?')
        meas_Vmultimeter_2_str = fscanf(multi_meter);
        meas_Vmultimeter_2 = str2double(meas_Vmultimeter_2_str);
        fprintf(multi_meter,'Conf:Volt:dc 10, 0.0001');

% Discharge to min voltage
%%%%%%%%%%%%%%%%%%%%%%%%%%%%%%%%%%%%%%%%%%%%%%%%%%%%%%%%%%%%%%%%FINISHED BLOCK OF CODE
        time2 = toc;
        fprintf(prog_load,'Iset 1.6');
        while(meas_voltage_multi_meter > min_voltage_cycled_to)
            fprintf(temp_sens,'Meas? 3');
            meas_temp_str = fscanf(temp_sens);
            meas_temp = str2double(meas_temp_str);

            if (meas_temp > safety_error_temp)
                break
            end

            the_time = clock;
            elapsed_time = toc;

            fprintf(multi_meter,'Init')
            fprintf(multi_meter,'Fetc?')
            meas_voltage_multi_meter_str = fscanf(multi_meter);
            meas_voltage_multi_meter =
str2double(meas_voltage_multi_meter_str);

            voltage_and_elapsed_time_and_temp_and_date =
[meas_voltage_multi_meter meas_temp elapsed_time the_time];
            save('-append', file_out,
'voltage_and_elapsed_time_and_temp_and_date', '-ascii');
        end;
        fprintf(prog_load,'Iset 0');
%%%%%%%%%%%%%%%%%%%%%%%%%%%%%%%%%%%%%%%%%%%%%%%%%%%%%%%%%%%%%%%%FINISHED BLOCK OF CODE

        if (meas_temp > safety_error_temp)
            break
        end


% Wait 5 seconds
%%%%%%%%%%%%%%%%%%%%%%%%%%%%%%%%%%%%%%%%%%%%%%%%%%%%%%%%%%%%%%%%FINISHED BLOCK OF CODE
        time3 = toc;
        fprintf(temp_sens,'Meas? 6');
        meas_temp_str_at_6 = fscanf(temp_sens);
        meas_temp_at_6 = str2double(meas_temp_str_at_6);

        if (meas_temp_at_6 > safety_error_temp)
            break
        end

        fprintf(temp_sens,'Meas? 5');
        meas_temp_str_at_5 = fscanf(temp_sens);
        meas_temp_at_5 = str2double(meas_temp_str_at_5);

        if (meas_temp_at_5 > safety_error_temp)
            break
        end
```

```
        fprintf(temp_sens,'Meas? 4');
        meas_temp_str_at_4 = fscanf(temp_sens);
        meas_temp_at_4 = str2double(meas_temp_str_at_4);

        if (meas_temp_at_4 > safety_error_temp)
            break
        end

        fprintf(temp_sens,'Meas? 3');
        meas_temp_str_at_3 = fscanf(temp_sens);
        meas_temp_at_3 = str2double(meas_temp_str_at_3);

        if (meas_temp_at_3 > safety_error_temp)
            break
        end

        five_counter = 0;
        while(five_counter < 5)
            fprintf(multi_meter,'Init')
            fprintf(multi_meter,'Fetc?')
            meas_voltage_multi_meter_str = fscanf(multi_meter);
            meas_voltage_multi_meter_after =
str2double(meas_voltage_multi_meter_str);

            fprintf(temp_sens,'Meas? 3');
            meas_temp_str = fscanf(temp_sens);
            meas_temp = str2double(meas_temp_str);

            if (meas_temp > safety_error_temp)
                break
            end

            the_time = clock;
            elapsed_time = toc;
            voltage_and_elapsed_time_and_temp_and_date =
[meas_voltage_multi_meter_after meas_temp elapsed_time the_time];
            save('-append', file_out,
'voltage_and_elapsed_time_and_temp_and_date', '-ascii');
            five_counter = toc - time3;
        end
%%%%%%%%%%%%%%%%%%%%%%%%%%%%%%%%%%%%%%%%%%%%%%%%%%%%FINISHED BLOCK OF CODE

        if (meas_temp > safety_error_temp)
            break
        end

        fprintf(multi_meter,'Conf:Volt:dc 10, 0.00001');
        fprintf(multi_meter,'Init')
        fprintf(multi_meter,'Fetc?')
        meas_Vmultimeter_4_str = fscanf(multi_meter);
        meas_Vmultimeter_4 = str2double(meas_Vmultimeter_4_str);
        fprintf(multi_meter,'Conf:Volt:dc 10, 0.0001');

        the_time = clock;
        elapsed_time = toc;
        voltage_and_elapsed_time_and_temp_and_date =
[meas_Vmultimeter_4 meas_temp_at_3 elapsed_time the_time];
        save('-append', file_out,
'voltage_and_elapsed_time_and_temp_and_date', '-ascii');
```

```
        td = (time3 - time2);
        Equiv_series_resistance = (meas_Vmultimeter_4 -
meas_voltage_multi_meter) / charge_and_discharge_current
        Capacitance = (charge_and_discharge_current * td /
(meas_Vmultimeter_2 - meas_Vmultimeter_4))
        the_time = clock;
        td_voltages_ESR_C_temps_time = [cycle_number
Equiv_series_resistance Capacitance meas_temp_at_3 meas_temp_at_4
meas_temp_at_5 meas_temp_at_6 time3 time2 meas_Vmultimeter_2
meas_Vmultimeter_4 meas_voltage_multi_meter the_time];

        if (resettable_variable >
number_of_param_readings_per_file)
            resettable_variable = 1;
            cycle_num_fixed = cycle_number;
        end
        resettable_variable = resettable_variable + 1;

        file_out =
sprintf('SC11_parameters_for_cycle.%d.dat',cycle_num_fixed);
        save('-append', file_out, 'td_voltages_ESR_C_temps_time',
'-ascii');

%        time_elapsed_start = time2 - time1
        if (meas_voltage_multi_meter < safety_error_voltage)
            break
        end
    end

    save('cycle_number.mat', 'cycle_number');
    time_to_fin_counter = toc - total_time;

    if (meas_temp > safety_error_temp)
        break
    end
    if (meas_temp_at_6 > safety_error_temp)
        break
    end
    if (meas_temp_at_5 > safety_error_temp)
        break
    end
    if (meas_temp_at_4 > safety_error_temp)
        break
    end
    if (meas_temp_at_3 > safety_error_temp)
        break
    end

end

meas_temp
meas_temp_at_6
meas_temp_at_5
meas_temp_at_4
meas_temp_at_3

save('cycle_number.mat', 'cycle_number');

%Turn off devices
```

```
fprintf(prog_load,'Load off');
fprintf(pow_sup,'Outp off');

%Delete and clear the GPIB variables
%When you no longer need to communicate the GPIB created variable,
%you should disconnect it from the instrument, remove it from
%memory, and remove it from the MATLAB workspace.
fclose(temp_sens);
delete(temp_sens)
clear temp_sens

fclose(pow_sup);
delete(pow_sup)
clear pow_sup

fclose(prog_load);
delete(prog_load)
clear prog_load

fclose(multi_meter);
delete(multi_meter)
clear multi_meter
```

Appendix F Matlab code used for supercapacitor (SC) #16 (thermal testing)

```
% Created by: Dónal Murray
% Date created: 27th May 2010
% Date modified: 12th July 2011
% Date started testing: 12th July 2011

% Last major update: New SC. Previously testing using DAcq unit
%only to read temp

% This file carries out repeated power cycling tests using
%constant current control on supercapacitors by operating a power
%supply, load, multimeter and temperature sensor using GPIB.
% Data is then saved to files %every predetermined number of
cycles. This is carried out at high temperature using the oven in
the pcb room.
% Test 2: SC16: 65 degrees C = rated operating temperature for the
SCs under consideration

clear all

% Get Simulation time
%%%%%%%%%%%%%%%%%%%%%%%%%%%%%%%%%%%%%%%%%%%%%%%%%%%%FINISHED BLOCK OF CODE
number_of_simulated_days = input ('Please enter the number of days
that you expect \nthe simulation to last (as a decimal):');
if isempty(number_of_simulated_days)
    error('Error: No amount of days defined');
end
one_minute = 60;
one_hour = 60 * one_minute;
one_day = 24 * one_hour;
simulation_time = one_day * number_of_simulated_days; %in seconds
%%%%%%%%%%%%%%%%%%%%%%%%%%%%%%%%%%%%%%%%%%%%%%%%%%%%FINISHED BLOCK OF CODE


% Key variables chosen for testing
%%%%%%%%%%%%%%%%%%%%%%%%%%%%%%%%%%%%%%%%%%%%%%%%%%%%FINISHED BLOCK OF CODE
max_voltage_cycled_to =             2.7;
min_voltage_cycled_to =             1.35;
cycles_between_char_tests =         100;
number_of_char_tests_in_a_row =     5;
cycles_between_char_tests_var =     cycles_between_char_tests -
number_of_char_tests_in_a_row;
number_of_param_readings_per_file = 300;
charge_and_discharge_current =      1.6;
%%%%%%%%%%%%%%%%%%%%%%%%%%%%%%%%%%%%%%%%%%%%%%%%%%%%FINISHED BLOCK OF CODE


% Variables used to help with code operation
```

```
%%%%%%%%%%%%%%%%%%%%%%%%%%%%%%%%%%%%%%%%%%%%FINISHED BLOCK OF CODE
load('cycle_number.mat', 'cycle_number');
cycle_num_fixed = cycle_number;
meas_voltage_multi_meter = 0;
resettable_variable = 1;
safety_error_voltage = 0.5;
safety_error_temp = 69;
safety_error_temp_room = 30;
%%%%%%%%%%%%%%%%%%%%%%%%%%%%%%%%%%%%%%%%%%%%FINISHED BLOCK OF CODE


% Begin communicating with GPIB equipment
%%%%%%%%%%%%%%%%%%%%%%%%%%%%%%%%%%%%%%%%%%%%FINISHED BLOCK OF CODE
pow_sup = gpib('agilent',7,10);       %Locate the temperature
%sensing device at GPIB address 3
fopen(pow_sup);              %Begin communications with the device
pause(1)
prog_load = gpib('agilent',7,4);
fopen(prog_load);
pause(1)
multi_meter = gpib('agilent',7,28);
fopen(multi_meter);
%%%%%%%%%%%%%%%%%%%%%%%%%%%%%%%%%%%%%%%%%%%%FINISHED BLOCK OF CODE


% Initialise some variables
%%%%%%%%%%%%%%%%%%%%%%%%%%%%%%%%%%%%%%%%%%%%FINISHED BLOCK OF CODE
meas_temp_top = 10;     %101
meas_temp_leg = 10;     %102
meas_temp_body = 10;    %103
meas_temp_room = 10;    %104
meas_temp_chamber = 10; %105
%%%%%%%%%%%%%%%%%%%%%%%%%%%%%%%%%%%%%%%%%%%%FINISHED BLOCK OF CODE


% Set parameters for equipment and then turn it on
%%%%%%%%%%%%%%%%%%%%%%%%%%%%%%%%%%%%%%%%%%%%FINISHED BLOCK OF CODE
fprintf(pow_sup,'Curr 0.05');
fprintf(pow_sup,'Volt 0');
pause(1)

fprintf(prog_load,'Chan 3');        %This is the module number
%used in the load
fprintf(prog_load,'Input Off');     %Ensure device is off while
%values are being set
fprintf(prog_load,'Mode:Curr');     %Enable current mode
fprintf(prog_load,'Curr:Rang 4');   %The value 4 is the largest
%integer current value the device will see.
fprintf(prog_load,'Curr 0');        %Set the current value to 0
initially
pause(1)

fprintf(multi_meter,'conf:volt:dc 10, 0.0001, (@106)'); %Sets the
%multimeter to dc voltmeter mode and the range too
fprintf(multi_meter,'zero:auto on, (@106)'); %Should double the
%reading speed of dc voltage when off, %Check this
fprintf(multi_meter,'input:impedance:auto off, (@106)'); %To
%change input R to 10 M if off, and 10 G if on
```

```
fprintf(multi_meter,'Rout:Mon (@106)'); %Puts the multi_meter in
%monitor mode on channel 6 which allows quick readings of the
voltage.
fprintf(multi_meter,'Rout:Mon:State ON');
pause(1)

fprintf(pow_sup,'Outp on');      %Turn on the power supply
fprintf(pow_sup,'Volt 0.2');
pause(1)
fprintf(pow_sup,'Volt 0.4');
pause(1)
fprintf(pow_sup,'Volt 0.6');
pause(1)
fprintf(pow_sup,'Volt 0.8');
pause(1)
fprintf(pow_sup,'Volt 1.0');
pause(1)
fprintf(pow_sup,'Volt 1.2');
pause(1)
fprintf(pow_sup,'Volt 1.4');
pause(1)
fprintf(pow_sup,'Volt 1.6');
pause(1)
fprintf(pow_sup,'Volt 1.8');
pause(1)
fprintf(pow_sup,'Volt 2.0');
pause(1)
fprintf(pow_sup,'Volt 2.2');
pause(1)
fprintf(pow_sup,'Volt 2.4');
pause(1)
fprintf(pow_sup,'Volt 2.8');
pause(1)
fprintf(prog_load,'Input On');  %Turn on the load
pause(10)
%%%%%%%%%%%%%%%%%%%%%%%%%%%%%%%%%%%%%%%%%%%%%%%%%%%%FINISHED BLOCK OF CODE


%%%%%%%%%%%%%%%%%%%%%%%%%%%%%%%%%%%%%%%%%%%%%%%%%%%%%%%%%%%%%%%%%%%%%%%%%%%
%%%%%%%%%%%%%%%%%%%%%%%%%%%%%%%%%%%%%%%%%%%%%%%%%%%%%%%%%%%%%%%%%%%%%%%%%%%
% THE MAIN LOOP OF THE PROGRAM
%%%%%%%%%%%%%%%%%%%%%%%%%%%%%%%%%%%%%%%%%%%%%%%%%%%%%%%%%%%%%%%%%%%%%%%%%%%
%%%%%%%%%%%%%%%%%%%%%%%%%%%%%%%%%%%%%%%%%%%%%%%%%%%%%%%%%%%%%%%%%%%%%%%%%%%
tic;
time_to_fin_counter = 0;         %Initialise the variable, put in
%earlier
total_time = toc;                %Used to compare with
%time_to_fin_counter to check code simulation time

while(time_to_fin_counter < simulation_time)

    % 95 cycles without writing to files or performing
%characterisation tests
    %%%%%%%%%%%%%%%%%%%%%%%%%%%%%%%%%%%%%%%%%%%%%%%%%%%%FINISHED BLOCK OF CODE
    for cycle_test_array_pos = 1:cycles_between_char_tests_var
        cycle_number = cycle_number + 1;


        % Charge SCs to rated Voltage
        %%%%%%%%%%%%%%%%%%%%%%%%%%%%%%%%%%%%%%%%%%%%%%%%%%%%FINISHED BLOCK OF CODE
        safety_time = toc;
```

```
        seven_counter = 0;
        fprintf(pow_sup,'Curr 1.6');
        while(meas_voltage_multi_meter < max_voltage_cycled_to &
seven_counter < 7)

            fprintf(multi_meter,'Rout:Mon:Data?');
            meas_voltage_multi_meter_str = fscanf(multi_meter);
            meas_voltage_multi_meter =
str2double(meas_voltage_multi_meter_str);
            if (meas_voltage_multi_meter < safety_error_voltage)
                break
            end

            seven_counter = toc - safety_time;
        end
        fprintf(pow_sup,'Curr 0');
        %%%%%%%%%%%%%%%%%%%%%%%%%%%%%%%%%%%%%%%%FINISHED BLOCK OF CODE


        % Safety checks on voltage and temperature
        %%%%%%%%%%%%%%%%%%%%%%%%%%%%%%%%%%%%%%%%FINISHED BLOCK OF CODE
        if (meas_voltage_multi_meter < safety_error_voltage)
            break
        end

%         fprintf(multi_meter,'Meas:Temp? tc,k,(@101)');
%         meas_temp_str_top = fscanf(multi_meter);
%         meas_temp_top = str2double(meas_temp_str_top);
%         if (meas_temp_top > safety_error_temp)
%             break
%         end
%
%         fprintf(multi_meter,'conf:volt:dc 10, 0.0001, (@105)');
%         fprintf(multi_meter,'zero:auto on, (@105)'); %Check this
%on and off to compare results
%         fprintf(multi_meter,'input:impedance:auto off, (@105)');
%         fprintf(multi_meter,'Rout:Mon (@105)');
%         fprintf(multi_meter,'Rout:Mon:State ON');
        %%%%%%%%%%%%%%%%%%%%%%%%%%%%%%%%%%%%%%%%FINISHED BLOCK OF CODE


        % Discharge SCs to rated Voltage
        %%%%%%%%%%%%%%%%%%%%%%%%%%%%%%%%%%%%%%%%FINISHED BLOCK OF CODE
        safety_time = toc;
        seven_counter = 0;
        fprintf(prog_load,'Curr 1.6');
        while(meas_voltage_multi_meter > min_voltage_cycled_to &
seven_counter < 7)
            fprintf(multi_meter,'Rout:Mon:Data?');
            meas_voltage_multi_meter_str = fscanf(multi_meter);
            meas_voltage_multi_meter =
str2double(meas_voltage_multi_meter_str);

            seven_counter = toc - safety_time;
        end;
        fprintf(prog_load,'Curr 0');
        %%%%%%%%%%%%%%%%%%%%%%%%%%%%%%%%%%%%%%%%FINISHED BLOCK OF CODE


        % Safety checks on voltage and temperature
```

```
        %%%%%%%%%%%%%%%%%%%%%%%%%%%%%%%%%%%%%%%%%%%%FINISHED BLOCK OF CODE
        if (meas_voltage_multi_meter < safety_error_voltage)
            break
        end
        fprintf(multi_meter,'Meas:Temp? tc,k,(@101)');
        meas_temp_str_top = fscanf(multi_meter);
        meas_temp_top = str2double(meas_temp_str_top);
        if (meas_temp_top > safety_error_temp)
            break
        end

        fprintf(multi_meter,'conf:volt:dc 10, 0.0001, (@106)');
        fprintf(multi_meter,'zero:auto on, (@106)'); %Check this
%on and off to compare results
        fprintf(multi_meter,'input:impedance:auto off, (@106)');
        fprintf(multi_meter,'Rout:Mon (@106)');
        fprintf(multi_meter,'Rout:Mon:State ON');
        %%%%%%%%%%%%%%%%%%%%%%%%%%%%%%%%%%%%%%%%%%%%FINISHED BLOCK OF CODE


    end
    %%%%%%%%%%%%%%%%%%%%%%%%%%%%%%%%%%%%%%%%%%%%%%%%FINISHED BLOCK OF CODE


    % Safety checks on voltage and temperature
    %%%%%%%%%%%%%%%%%%%%%%%%%%%%%%%%%%%%%%%%%%%%%%%%FINISHED BLOCK OF CODE
    if (meas_voltage_multi_meter < safety_error_voltage)
        break
    end
    if (meas_temp_top > safety_error_temp)
        break
    end
    %%%%%%%%%%%%%%%%%%%%%%%%%%%%%%%%%%%%%%%%%%%%%%%%FINISHED BLOCK OF CODE


    % 5 cycles performing characterisation tests
    %%%%%%%%%%%%%%%%%%%%%%%%%%%%%%%%%%%%%%%%%%%%%%%%FINISHED BLOCK OF CODE
    for char_test_array_pos = 1:number_of_char_tests_in_a_row
        cycle_number = cycle_number + 1


        % Charge to max voltage
        %%%%%%%%%%%%%%%%%%%%%%%%%%%%%%%%%%%%%%%%%%%%FINISHED BLOCK OF CODE
        safety_time = toc;
        seven_counter = 0;
        fprintf(pow_sup,'Curr 1.6');
        while(meas_voltage_multi_meter < max_voltage_cycled_to &
seven_counter < 7)

            fprintf(multi_meter,'Rout:Mon:Data?');
            meas_voltage_multi_meter_str = fscanf(multi_meter);
            meas_voltage_multi_meter =
str2double(meas_voltage_multi_meter_str);
            if (meas_voltage_multi_meter < safety_error_voltage)
                break
            end

            seven_counter = toc - safety_time;
        end
        fprintf(pow_sup,'Curr 0');
```

```
        %%%%%%%%%%%%%%%%%%%%%%%%%%%%%%%%%%%%%%%%FINISHED BLOCK OF CODE


        time1 = toc;


        % Safety checks on voltage
        %%%%%%%%%%%%%%%%%%%%%%%%%%%%%%%%%%%%%%%%FINISHED BLOCK OF CODE
        if (meas_voltage_multi_meter < safety_error_voltage)
            break
        end
        %%%%%%%%%%%%%%%%%%%%%%%%%%%%%%%%%%%%%%%%FINISHED BLOCK OF CODE


        % Wait 5 seconds
        %%%%%%%%%%%%%%%%%%%%%%%%%%%%%%%%%%%%%%%%FINISHED BLOCK OF CODE
        five_counter = 0;
        while(five_counter < 5)
            fprintf(multi_meter,'Rout:Mon:Data?');
            meas_voltage_multi_meter_str = fscanf(multi_meter);
            meas_voltage_multi_meter =
str2double(meas_voltage_multi_meter_str);
%             if (meas_voltage_multi_meter < safety_error_voltage)
%                 break
%             end

            the_time = clock;
            elapsed_time = toc;
            voltage_and_elapsed_time_and_temp_and_date =
[meas_voltage_multi_meter meas_temp_top elapsed_time the_time];
            file_out =
sprintf('SC16_voltages_for_cycle.%d.dat',cycle_number);
            save('-append', file_out,
'voltage_and_elapsed_time_and_temp_and_date', '-ascii');
            five_counter = toc - time1;
        end
        %%%%%%%%%%%%%%%%%%%%%%%%%%%%%%%%%%%%%%%%FINISHED BLOCK OF CODE


        % Safety checks on voltage, include temperature?
        %%%%%%%%%%%%%%%%%%%%%%%%%%%%%%%%%%%%%%%%FINISHED BLOCK OF CODE
        if (meas_voltage_multi_meter < safety_error_voltage)
            break
        end
        %%%%%%%%%%%%%%%%%%%%%%%%%%%%%%%%%%%%%%%%FINISHED BLOCK OF CODE


%         fprintf(multi_meter,'conf:volt:dc 10, 0.00001, (@106)');
        fprintf(multi_meter,'Rout:Mon:Data?');
        meas_Vmultimeter_2_str = fscanf(multi_meter);
        meas_Vmultimeter_2 = str2double(meas_Vmultimeter_2_str);
%         fprintf(multi_meter,'conf:volt:dc 10, 0.0001, (@106)');


        % Discharge to min voltage
        %%%%%%%%%%%%%%%%%%%%%%%%%%%%%%%%%%%%%%%%FINISHED BLOCK OF CODE
        safety_time = toc;
        seven_counter = 0;
        time2 = toc;
        fprintf(prog_load,'Curr 1.6');
```

```
        while(meas_voltage_multi_meter > min_voltage_cycled_to &
seven_counter < 7)

            the_time = clock;
            elapsed_time = toc;

            fprintf(multi_meter,'Rout:Mon:Data?');
            meas_voltage_multi_meter_str = fscanf(multi_meter);
            meas_voltage_multi_meter =
str2double(meas_voltage_multi_meter_str);

            voltage_and_elapsed_time_and_temp_and_date =
[meas_voltage_multi_meter meas_temp_top elapsed_time the_time];
            save('-append', file_out,
'voltage_and_elapsed_time_and_temp_and_date', '-ascii');

            seven_counter = toc - safety_time;
        end;
        fprintf(prog_load,'Curr 0');
        %%%%%%%%%%%%%%%%%%%%%%%%%%%%%%%%%%%%%%%%FINISHED BLOCK OF CODE


        time3 = toc;

        % Safety checks on voltage, include temperature?
        %%%%%%%%%%%%%%%%%%%%%%%%%%%%%%%%%%%%%%%%FINISHED BLOCK OF CODE
        if (meas_voltage_multi_meter < safety_error_voltage)
            break
        end
        %%%%%%%%%%%%%%%%%%%%%%%%%%%%%%%%%%%%%%%%FINISHED BLOCK OF CODE


        % Wait 5 seconds
        %%%%%%%%%%%%%%%%%%%%%%%%%%%%%%%%%%%%%%%%FINISHED BLOCK OF CODE
        fprintf(multi_meter,'Meas:Temp? tc,k,(@105)');
        meas_temp_str_chamber = fscanf(multi_meter);
        meas_temp_chamber = str2double(meas_temp_str_chamber);
        if (meas_temp_chamber > safety_error_temp)
            break
        end
        pause (0.2)

        fprintf(multi_meter,'Meas:Temp? tc,k,(@104)');
        meas_temp_str_room = fscanf(multi_meter);
        meas_temp_room = str2double(meas_temp_str_room);
        if (meas_temp_room > safety_error_temp)
           %consider putting in different room temp here of 30,
           %need to be sure thermocouple reader doesn't latch to a
           %diff channel though
            break
        end
        pause (0.2)

        fprintf(multi_meter,'Meas:Temp? tc,k,(@103)');
        meas_temp_str_body = fscanf(multi_meter);
        meas_temp_body = str2double(meas_temp_str_body);
        if (meas_temp_body > safety_error_temp)
            break
        end
        pause (0.2)
```

```
        fprintf(multi_meter,'Meas:Temp? tc,k,(@102)');
        meas_temp_str_leg = fscanf(multi_meter);
        meas_temp_leg = str2double(meas_temp_str_leg)
        if (meas_temp_leg > safety_error_temp)
            break
        end
        pause (0.2)

        fprintf(multi_meter,'Meas:Temp? tc,k,(@101)');
        meas_temp_str_top = fscanf(multi_meter);
        meas_temp_top = str2double(meas_temp_str_top)
        if (meas_temp_top > safety_error_temp)
            break
        end
        pause (0.2)

        fprintf(multi_meter,'conf:volt:dc 10, 0.0001, (@106)');
        fprintf(multi_meter,'zero:auto on, (@106)'); %Check this
%on and off to compare results
        fprintf(multi_meter,'input:impedance:auto off, (@106)');
        fprintf(multi_meter,'Rout:Mon (@106)');
        fprintf(multi_meter,'Rout:Mon:State ON');

        five_counter = 0;
        while(five_counter < 5)
            fprintf(multi_meter,'Rout:Mon:Data?');
            meas_voltage_multi_meter_str = fscanf(multi_meter);
            meas_voltage_multi_meter_after =
str2double(meas_voltage_multi_meter_str);
%       if (meas_voltage_multi_meter_after < safety_error_voltage)
%       break
%       end
            the_time = clock;
            elapsed_time = toc;
            voltage_and_elapsed_time_and_temp_and_date =
[meas_voltage_multi_meter_after meas_temp_top elapsed_time
the_time];
            save('-append', file_out,
'voltage_and_elapsed_time_and_temp_and_date', '-ascii');
            five_counter = toc - time3;
        end
        %%%%%%%%%%%%%%%%%%%%%%%%%%%%%%%%%%%%FINISHED BLOCK OF CODE


        % Measure last voltage, work out parameters, and write to
        %file
        %%%%%%%%%%%%%%%%%%%%%%%%%%%%%%%%%%%%FINISHED BLOCK OF CODE
%        fprintf(multi_meter,'conf:volt:dc 10, 0.00001, (@106)');
        fprintf(multi_meter,'Rout:Mon:Data?');
        meas_Vmultimeter_4_str = fscanf(multi_meter);
        meas_Vmultimeter_4 = str2double(meas_Vmultimeter_4_str);
%        fprintf(multi_meter,'conf:volt:dc 10, 0.0001, (@106)');

        the_time = clock;
        elapsed_time = toc;
        voltage_and_elapsed_time_and_temp_and_date =
[meas_Vmultimeter_4 meas_temp_top elapsed_time the_time];
        save('-append', file_out,
'voltage_and_elapsed_time_and_temp_and_date', '-ascii');
```

```
        if (meas_voltage_multi_meter < safety_error_voltage)
            break
        end
        if (meas_temp_top > safety_error_temp)
            break
        end

        td = (time3 - time2);
        Equiv_series_resistance = (meas_Vmultimeter_4 -
meas_voltage_multi_meter) / charge_and_discharge_current
        Capacitance = (charge_and_discharge_current * td /
(meas_Vmultimeter_2 - meas_Vmultimeter_4))
        the_time = clock;
        td_voltages_ESR_C_temps_time = [cycle_number
Equiv_series_resistance Capacitance meas_temp_top meas_temp_leg
meas_temp_body meas_temp_room meas_temp_chamber time3 time2
meas_Vmultimeter_2 meas_Vmultimeter_4 meas_voltage_multi_meter
the_time];

        if (resettable_variable >
number_of_param_readings_per_file)
            resettable_variable = 1;
            cycle_num_fixed = cycle_number;
        end
        resettable_variable = resettable_variable + 1;

        file_out =
sprintf('SC16_parameters_for_cycle.%d.dat',cycle_num_fixed);
        save('-append', file_out, 'td_voltages_ESR_C_temps_time',
'-ascii');
        %%%%%%%%%%%%%%%%%%%%%%%%%%%%%%%%%%%%%%%%%%%%FINISHED BLOCK OF CODE


%         time_elapsed_start = time2 - time1

    end
    %%%%%%%%%%%%%%%%%%%%%%%%%%%%%%%%%%%%%%%%%%%%%%%%FINISHED BLOCK OF CODE


    save('cycle_number.mat', 'cycle_number');
    time_to_fin_counter = toc - total_time;


    % Safety checks on voltage and temperature
    %%%%%%%%%%%%%%%%%%%%%%%%%%%%%%%%%%%%%%%%%%%%%%%%%%%%FINISHED BLOCK OF CODE
    if (meas_temp_chamber > safety_error_temp)
        break
    end
    if (meas_temp_room > safety_error_temp)
        break
    end
    if (meas_temp_body > safety_error_temp)
        break
    end
    if (meas_temp_leg > safety_error_temp)
        break
    end
    if (meas_temp_top > safety_error_temp)
        break
```

```
    end
    %%%%%%%%%%%%%%%%%%%%%%%%%%%%%%%%%%%%%%%%FINISHED BLOCK OF CODE

end


% Output temperatures, for error debugging purposes
%%%%%%%%%%%%%%%%%%%%%%%%%%%%%%%%%%%%%%%%%%%FINISHED BLOCK OF CODE
pause(1)
meas_temp_chamber
meas_temp_room
meas_temp_body
meas_temp_leg
meas_temp_top
pause(1)
%%%%%%%%%%%%%%%%%%%%%%%%%%%%%%%%%%%%%%%%%%%%FINISHED BLOCK OF CODE


save('cycle_number.mat', 'cycle_number');
pause(1)


% Turn off devices
%%%%%%%%%%%%%%%%%%%%%%%%%%%%%%%%%%%%%%%%%%%%FINISHED BLOCK OF CODE
fprintf(prog_load,'Input Off');
fprintf(pow_sup,'Outp off');
pause(1)
%Delete and clear the GPIB variables
%When you no longer need to communicate the GPIB created variable,
%you should disconnect it from the instrument, remove it from
%memory, and remove it from the MATLAB workspace.

fclose(pow_sup);
delete(pow_sup)
clear pow_sup
pause(1)

fclose(prog_load);
delete(prog_load)
clear prog_load
pause(1)

fclose(multi_meter);
delete(multi_meter)
clear multi_meter
%%%%%%%%%%%%%%%%%%%%%%%%%%%%%%%%%%%%%%%%%%%%FINISHED BLOCK OF CODE
```

Appendix G Matlab code used for supercapacitor (SC) #26 (application testing)

```
% File_name: SC_power_wave_demand_GPIB_loop_revised.m
% Author: Dónal Murray
% Creation date: 15th June 2010
% Last edit date: 15th April 2011

% This file carries out application power profile cycling tests on
% a supercapacitor by operating a power supply, load, multimeter
% and temperature sensor using GPIB. Constant current control is
% used.
% The file applies a power profile to a supercapacitor based on
% Simulink modelling of a full scale system which uses a SC bank
% for power smoothing. Characterisation tests are carried out
% every predetermined number of cycles and data is then saved to
% files.

% Safey checks:
clear all;


% Get Simulation time
%%%%%%%%%%%%%%%%%%%%%%%%%%%%%%%%%%%%%%%%%%%%%%%%%%%%FINISHED BLOCK OF CODE
number_of_simulated_days = input ('Please enter the number of days
that you expect \nthe simulation to last (as a decimal):');
if isempty(number_of_simulated_days)
    error('Error: No amount of days defined');
end
one_minute =        60;
one_hour =          60 * one_minute;
one_day =           24 * one_hour;
simulation_time =   one_day * number_of_simulated_days; %in
%seconds
%%%%%%%%%%%%%%%%%%%%%%%%%%%%%%%%%%%%%%%%%%%%%%%%%%%%%%%%FINISHED BLOCK OF CODE


% Current and Resistances
%%%%%%%%%%%%%%%%%%%%%%%%%%%%%%%%%%%%%%%%%%%%%%%%%%%%%%%%FINISHED BLOCK OF CODE
SC_maximum_current = 2.7;   %although its 3.4, examination shows
%never above 2.65 so this allows more use of energy range taking
%hysteresis values below into account.
SC_minimum_current = -2.14; %although its -3.4, examination shows
%never above 2.1
%Recheck these values after a while as increased ESR slightly
%affects energy range.
SC_ESR = 0.12;  %0.105; %Estimate based on a bit more than initial
%value - consider updating every now and again
%%%%%%%%%%%%%%%%%%%%%%%%%%%%%%%%%%%%%%%%%%%%%%%%%%%%%%%%FINISHED BLOCK OF CODE
```

```
% Voltages
%%%%%%%%%%%%%%%%%%%%%%%%%%%%%%%%%%%%%%%%%%%%FINISHED BLOCK OF CODE
Hyst_reset_const =        1.2;
SC_min_voltage =          1.35;
SC_min_voltage_hyst =     SC_min_voltage -
SC_minimum_current*SC_ESR;
SC_min_voltage_reset =    SC_min_voltage -
Hyst_reset_const*(SC_minimum_current*SC_ESR);
SC_minimum_voltage =      SC_min_voltage; %This variable changes in
%value to help with hysteresis point

max_voltage_cycled_to = 2.7;
SC_max_voltage =          2.669; %Check the difference in voltage
%reached after 0.1 second at maximum current with normal C, then
%subtract from 2.7 (with implemented sample time in mind).
SC_max_voltage_hyst =     SC_max_voltage -
SC_maximum_current*SC_ESR;
SC_max_voltage_reset =    SC_max_voltage -
Hyst_reset_const*(SC_maximum_current*SC_ESR);
SC_maximum_voltage =      SC_max_voltage;
%%%%%%%%%%%%%%%%%%%%%%%%%%%%%%%%%%%%%%%%%%%%FINISHED BLOCK OF CODE

sample_time =             0.10875; %how long it should take is 393.5
%actually 0.108754165 scaled at 21.13513


% Key variables chosen for testing
%%%%%%%%%%%%%%%%%%%%%%%%%%%%%%%%%%%%%%%%%%%%FINISHED BLOCK OF CODE
number_of_char_tests_in_a_row =      5; %5
number_of_param_readings_per_file = 300;
charge_and_discharge_current =      1.6;
meas_voltage_multi_meter =          0;

Number_of_iterations_before_char_test = 3; %3
resettable_variable =               0.5;
safety_error_voltage =              0.5;
safety_error_temp =                 33;
%%%%%%%%%%%%%%%%%%%%%%%%%%%%%%%%%%%%%%%%%%%%FINISHED BLOCK OF CODE


% Begin communicating with GPIB equipment
%%%%%%%%%%%%%%%%%%%%%%%%%%%%%%%%%%%%%%%%%%%%FINISHED BLOCK OF CODE
pow_sup =       gpib('agilent',7,8);     %Locate the device at GPIB
%address 8 with Agilent gpib controller at address 7
fopen(pow_sup);                  %Begin communications with the device
prog_load =     gpib('agilent',7,6);
fopen(prog_load);
multi_meter =   gpib('agilent',7,4);
fopen(multi_meter);
%%%%%%%%%%%%%%%%%%%%%%%%%%%%%%%%%%%%%%%%%%%FINISHED BLOCK OF CODE


% Load the power profile and cycle numbers
%%%%%%%%%%%%%%%%%%%%%%%%%%%%%%%%%%%%%%%%%%%%FINISHED BLOCK OF CODE
SC_power_demand_revised2;       %Load the array of power values
total_number_of_array = 3619;   %Set the end array number for the
%array

load('pow_profile_cyc_num.mat', 'pow_profile_cycle_num')
```

```
%Load the cycle number used to track cycles of power profile
load('char_test_cyc_num.mat', 'char_test_cycle_num');
%Load the cycle number used to track characterisation test cycles
cycle_num_fixed = char_test_cycle_num; %Used to write the cycle
number to the name of the parameter file
%%%%%%%%%%%%%%%%%%%%%%%%%%%%%%%%%%%%%%%%%%%%%%%%%%%%FINISHED BLOCK OF CODE

% Initialise some variables
%%%%%%%%%%%%%%%%%%%%%%%%%%%%%%%%%%%%%%%%%%%%%%%%%%%%FINISHED BLOCK OF CODE
meas_temp_at_3 = 10;
meas_temp_at_4 = 10;
meas_temp_at_5 = 10;
meas_temp_at_6 = 10;
%%%%%%%%%%%%%%%%%%%%%%%%%%%%%%%%%%%%%%%%%%%%%%%%%%%%FINISHED BLOCK OF CODE


% Setup the GPIB equipment:
%%%%%%%%%%%%%%%%%%%%%%%%%%%%%%%%%%%%%%%%%%%%%%%%%%%%FINISHED BLOCK OF CODE
fprintf(pow_sup,'Sour:Curr 0.1');  %Value used to put device into
%CC mode
fprintf(pow_sup,'Sour:Volt 0');

fprintf(prog_load,'Chan 4');        %This is the module number
%used in the load
fprintf(prog_load,'Input Off');     %Ensure device is off while
%values are being set
fprintf(prog_load,'Mode:Curr');     %Enable Current mode
fprintf(prog_load,'Curr:Rang 4');   %The value 4 is the largest
%integer current value the device will see.
fprintf(prog_load,'Curr 0');        %Set the current value to 0
%initially

fprintf(multi_meter,'conf:volt:dc 10, 0.0001, (@105)');
%Sets the multimeter to dc voltmeter mode and the range too
fprintf(multi_meter,'zero:auto on, (@105)'); %Check this on and
%off to compare results
fprintf(multi_meter,'input:impedance:auto off, (@105)'); %To
%change input R to 10 M if off, and 10 G if on
%fprintf(multi_meter,'Rout:chan:delay:auto off, (@105)'); %Check
%this fprintf(multi_meter,'Rout:scan (@105)');
fprintf(multi_meter,'Rout:Mon (@105)'); %Puts the multi_meter in
%monitor mode on channel 5 which allows quick readings of the
%voltage.
fprintf(multi_meter,'Rout:Mon:State ON');
%%%%%%%%%%%%%%%%%%%%%%%%%%%%%%%%%%%%%%%%%%%%%%%%%%%%FINISHED BLOCK OF CODE


%%%%%%%%%%%%%%%%%%%%%%%%%%%%%%%%%%%%%%%%%%%%%%%%%%%%FINISHED BLOCK OF CODE
fprintf(pow_sup,'Outp on');          %Turn on the power supply
fprintf(pow_sup,'Sour:Volt 0.2');
pause(1)
fprintf(pow_sup,'Sour:Volt 0.4');
pause(1)
fprintf(pow_sup,'Sour:Volt 0.6');
pause(1)
fprintf(pow_sup,'Sour:Volt 0.8');
pause(1)
fprintf(pow_sup,'Sour:Volt 1.0');
pause(1)
fprintf(pow_sup,'Sour:Volt 1.2');
pause(1)
```

```
fprintf(pow_sup,'Sour:Volt 1.4');
pause(1)
fprintf(pow_sup,'Sour:Volt 1.6');
pause(1)
fprintf(pow_sup,'Sour:Volt 1.8');
pause(1)
fprintf(pow_sup,'Sour:Volt 2.0');
pause(1)
fprintf(pow_sup,'Sour:Volt 2.2');
pause(1)
fprintf(pow_sup,'Sour:Volt 2.4');
pause(1)
fprintf(pow_sup,'Sour:Volt 2.8');
pause(1)                        %The above code was used to ensure
%no major current values were encountered while the power supply
%changed from voltage to current mode. And did this, no matter
%what the voltage on the SCs were.
fprintf(prog_load,'Input On');  %Turn on the load
pause(12);                      %Allow time for power supply to
%change to constant current mode and to make sure to get about 0.5
% V so as no error if starting from 0 V
fprintf(pow_sup,'SOUR:Curr 0'); %Set the current value to zero
%again.
%%%%%%%%%%%%%%%%%%%%%%%%%%%%%%%%%%%%%%%%%%%%%%%%%%%%%%%%FINISHED BLOCK OF CODE


%The main loop for the program
tic;
time_to_fin_counter = 0;        %Initialise the variable
total_time = toc;               %This is used to check the
%simulation time

while(time_to_fin_counter < simulation_time)

%%%%%%%%%%%%%%%%%%%%%%%%%%%%%%%%%%%%%%%%%%%%%%%%%%%%%%%%FINISHED BLOCK OF CODE
    for power_profile_cycle_number =
1:Number_of_iterations_before_char_test
        for power_array_pos = 1:total_number_of_array
            time_start = toc;%Need to ensure each sample lasts
%correct time
            SC_power = SC_power_demand(power_array_pos);

            fprintf(multi_meter,'Rout:Mon:Data?');
            meas_voltage_multi_meter_str = fscanf(multi_meter);
            meas_voltage_multi_meter =
str2double(meas_voltage_multi_meter_str);

            %Safety check
            if (meas_voltage_multi_meter < safety_error_voltage)
                break
            end

            SC_current = SC_power / meas_voltage_multi_meter;

            if(meas_voltage_multi_meter > SC_min_voltage_reset)
%used as hysteresis thing
                    SC_minimum_voltage = SC_min_voltage;
            end;
```

```
            if(meas_voltage_multi_meter < SC_max_voltage_reset)
%used as hysteresis thing
                SC_maximum_voltage = SC_max_voltage;
            end;

            if(SC_current < 0)
                fprintf(pow_sup,'SOUR:Curr 0');
                if(meas_voltage_multi_meter < SC_minimum_voltage)
                    SC_minimum_voltage = SC_min_voltage_hyst;
%used as hysteresis thing
                    SC_demand_current = 0;
                elseif(SC_current < SC_minimum_current)%This might
%be excess code and should never be used but it is a safety check.
                    SC_demand_current = -SC_minimum_current; %As
%current value evaluated was -ve, need to change it to a positive
%value to allow it to work with the pow_sup.
                else
                    SC_demand_current = -SC_current;
                end
                fprintf(prog_load,'Curr %4.3f',SC_demand_current);
%Set's the number outputted to a value correct to three decimal
%places, and the width of the number is at least 4 characters.
%Check this 3 decimal places thing

            else
                fprintf(prog_load,'Curr 0');
                if(meas_voltage_multi_meter > SC_maximum_voltage)
                    SC_maximum_voltage = SC_max_voltage_hyst;
%used as hysteresis thing
                    SC_demand_current1 = 0;
                elseif(SC_current > SC_maximum_current)
                    SC_demand_current1 = SC_maximum_current;
                else
                    SC_demand_current1 = SC_current;
                end
                fprintf(pow_sup,'Sour:Curr
%4.3f',SC_demand_current1);

            end;

            time_end = 0;

            while(time_end < sample_time) %Used to ensure that the
%sample time was the same every time.
                time_end = toc - time_start;
            end
            %time_end
        end
        if (meas_voltage_multi_meter < safety_error_voltage)
            break
        end

        fprintf(multi_meter,'Meas:Temp? tc,k,(@104)');
        meas_temp_str_at_6 = fscanf(multi_meter);
        meas_temp_at_6 = str2double(meas_temp_str_at_6);

        if (meas_temp_at_6 > safety_error_temp)
            break
        end
```

```
        fprintf(multi_meter,'Meas:Temp? tc,k,(@103)');
        meas_temp_str_at_5 = fscanf(multi_meter);
        meas_temp_at_5 = str2double(meas_temp_str_at_5);

        if (meas_temp_at_5 > safety_error_temp)
            break
        end

        fprintf(multi_meter,'Meas:Temp? tc,k,(@102)');
        meas_temp_str_at_4 = fscanf(multi_meter);
        meas_temp_at_4 = str2double(meas_temp_str_at_4);

        if (meas_temp_at_4 > safety_error_temp)
            break
        end

        fprintf(multi_meter,'Meas:Temp? tc,k,(@101)');
        meas_temp_str_at_3 = fscanf(multi_meter);
        meas_temp_at_3 = str2double(meas_temp_str_at_3);

        if (meas_temp_at_3 > safety_error_temp)
            break
        end

        fprintf(multi_meter,'conf:volt:dc 10, 0.0001, (@105)');
        fprintf(multi_meter,'zero:auto on, (@105)'); %Check this
%on and off to compare results
        fprintf(multi_meter,'input:impedance:auto off, (@105)');
        fprintf(multi_meter,'Rout:Mon (@105)');
        fprintf(multi_meter,'Rout:Mon:State ON');

    end

    fprintf(multi_meter,'Rout:Mon:Data?');
    meas_voltage_multi_meter_str = fscanf(multi_meter);
    meas_voltage_multi_meter =
str2double(meas_voltage_multi_meter_str);

    if (meas_voltage_multi_meter < safety_error_voltage)
        break
    end
    if (meas_temp_at_6 > safety_error_temp)
        break
    end
    if (meas_temp_at_5 > safety_error_temp)
        break
    end
    if (meas_temp_at_4 > safety_error_temp)
        break
    end
    if (meas_temp_at_3 > safety_error_temp)
        break
    end
    %%%%%%%%%%%%%%%%%%%%%%%%%%%%%%%%%%%%%%%%%%%%%%%%%%%%FINISHED BLOCK OF CODE
    fprintf(prog_load,'Curr 0');
    pow_profile_cycle_num = pow_profile_cycle_num+1;
    %cycletime = toc - total_time
```

```
  % The following code is used to carry out characterisation
%tests.
    for char_test_array_pos = 1:number_of_char_tests_in_a_row
        char_test_cycle_num = char_test_cycle_num + 1;

% Charge to max voltage
%%%%%%%%%%%%%%%%%%%%%%%%%%%%%%%%%%%%%%%%%%%%%%%%%%%%%%%%FINISHED BLOCK OF CODE
        fprintf(pow_sup,'SOUR:Curr 1.6');
        while(meas_voltage_multi_meter < max_voltage_cycled_to)
            fprintf(multi_meter,'Rout:Mon:Data?');
            meas_voltage_multi_meter_str = fscanf(multi_meter);
            meas_voltage_multi_meter =
str2double(meas_voltage_multi_meter_str);
            if (meas_voltage_multi_meter < safety_error_voltage)
                break
            end
        end
        fprintf(pow_sup,'SOUR:Curr 0');
%%%%%%%%%%%%%%%%%%%%%%%%%%%%%%%%%%%%%%%%%%%%%%%%%%%%%%%%FINISHED BLOCK OF CODE

        if (meas_voltage_multi_meter < safety_error_voltage)
            break
        end

% Wait 5 seconds
%%%%%%%%%%%%%%%%%%%%%%%%%%%%%%%%%%%%%%%%%%%%%%%%%%%%%%%%FINISHED BLOCK OF CODE
        five_counter = 0;
        time1 = toc;
        while(five_counter < 5)
            fprintf(multi_meter,'Rout:Mon:Data?');
            meas_voltage_multi_meter_str = fscanf(multi_meter);
            meas_voltage_multi_meter =
str2double(meas_voltage_multi_meter_str);
            if (meas_voltage_multi_meter < safety_error_voltage)
                break
            end

            the_time = clock;
            elapsed_time = toc;
            voltage_and_elapsed_time_and_date =
[meas_voltage_multi_meter elapsed_time the_time];
            file_out =
sprintf('SC11_voltages_for_cycle.%d.dat',char_test_cycle_num);
            save('-append', file_out,
'voltage_and_elapsed_time_and_date', '-ascii');
            five_counter = toc - time1;
        end
%%%%%%%%%%%%%%%%%%%%%%%%%%%%%%%%%%%%%%%%%%%%%%%%%%%%%%%%FINISHED BLOCK OF CODE

        if (meas_voltage_multi_meter < safety_error_voltage)
            break
        end

        fprintf(multi_meter,'conf:volt:dc 10, 0.00001, (@105)');
        fprintf(multi_meter,'Rout:Mon:Data?');
        meas_Vmultimeter_2_str = fscanf(multi_meter);
        meas_Vmultimeter_2 = str2double(meas_Vmultimeter_2_str);
        fprintf(multi_meter,'conf:volt:dc 10, 0.0001, (@105)');
```

```
% Discharge to min voltage
%%%%%%%%%%%%%%%%%%%%%%%%%%%%%%%%%%%%%%%%%%%%%%%%%%%%%%%%FINISHED BLOCK OF CODE
        time2 = toc;
        fprintf(prog_load,'Curr 1.6');
        while(meas_voltage_multi_meter > SC_min_voltage)
            the_time = clock;
            elapsed_time = toc;

            fprintf(multi_meter,'Rout:Mon:Data?');
            meas_voltage_multi_meter_str = fscanf(multi_meter);
            meas_voltage_multi_meter =
str2double(meas_voltage_multi_meter_str);

            voltage_and_elapsed_time_and_date =
[meas_voltage_multi_meter elapsed_time the_time];
            save('-append', file_out,
'voltage_and_elapsed_time_and_date', '-ascii');
        end;
        fprintf(prog_load,'Curr 0');
        if (meas_voltage_multi_meter < safety_error_voltage)
            break
        end
%%%%%%%%%%%%%%%%%%%%%%%%%%%%%%%%%%%%%%%%%%%%%%%%%%%%%%%%FINISHED BLOCK OF CODE

% Wait 5 seconds
%%%%%%%%%%%%%%%%%%%%%%%%%%%%%%%%%%%%%%%%%%%%%%%%%%%%%%%%FINISHED BLOCK OF CODE
        time3 = toc;
        fprintf(multi_meter,'Meas:Temp? tc,k,(@104)');
        meas_temp_str_at_6 = fscanf(multi_meter);
        meas_temp_at_6 = str2double(meas_temp_str_at_6);

        if (meas_temp_at_6 > safety_error_temp)
            break
        end

        fprintf(multi_meter,'Meas:Temp? tc,k,(@103)');
        meas_temp_str_at_5 = fscanf(multi_meter);
        meas_temp_at_5 = str2double(meas_temp_str_at_5);

        if (meas_temp_at_5 > safety_error_temp)
            break
        end

        fprintf(multi_meter,'Meas:Temp? tc,k,(@102)');
        meas_temp_str_at_4 = fscanf(multi_meter);
        meas_temp_at_4 = str2double(meas_temp_str_at_4);

        if (meas_temp_at_4 > safety_error_temp)
            break
        end

        fprintf(multi_meter,'Meas:Temp? tc,k,(@101)');
        meas_temp_str_at_3 = fscanf(multi_meter);
        meas_temp_at_3 = str2double(meas_temp_str_at_3);

        if (meas_temp_at_3 > safety_error_temp)
            break
        end

        fprintf(multi_meter,'conf:volt:dc 10, 0.0001, (@105)');
```

```
        fprintf(multi_meter,'zero:auto on, (@105)'); %Check this
%on and off to compare results
        fprintf(multi_meter,'input:impedance:auto off, (@105)');
        fprintf(multi_meter,'Rout:Mon (@105)');
        fprintf(multi_meter,'Rout:Mon:State ON');


        five_counter = 0;
        while(five_counter < 5)
            fprintf(multi_meter,'Rout:Mon:Data?');
            meas_voltage_multi_meter_str = fscanf(multi_meter);
            meas_voltage_multi_meter_after =
str2double(meas_voltage_multi_meter_str);

            the_time = clock;
            elapsed_time=toc;
            voltage_and_elapsed_time_and_date =
[meas_voltage_multi_meter_after elapsed_time the_time];
            save('-append', file_out,
'voltage_and_elapsed_time_and_date', '-ascii');
            five_counter = toc - time3;
        end
%%%%%%%%%%%%%%%%%%%%%%%%%%%%%%%%%%%%%%%%%%%%%%%%%%%%FINISHED BLOCK OF CODE


        fprintf(multi_meter,'conf:volt:dc 10, 0.00001, (@105)');
        fprintf(multi_meter,'Rout:Mon:Data?');
        meas_Vmultimeter_4_str = fscanf(multi_meter);
        meas_Vmultimeter_4 = str2double(meas_Vmultimeter_4_str);
        fprintf(multi_meter,'conf:volt:dc 10, 0.0001, (@105)');

        the_time = clock;
        elapsed_time = toc;
        voltage_and_elapsed_time_and_date =
[meas_voltage_multi_meter_after elapsed_time the_time];
        save('-append', file_out,
'voltage_and_elapsed_time_and_date', '-ascii');

        td = (time3 - time2);
        Equiv_series_resistance = (meas_Vmultimeter_4 -
meas_voltage_multi_meter) / charge_and_discharge_current
        Capacitance = (charge_and_discharge_current * td /
(meas_Vmultimeter_2 - meas_Vmultimeter_4))
        the_time = clock;
        td_voltages_ESR_C_temps_time = [ char_test_cycle_num
Equiv_series_resistance Capacitance meas_temp_at_3 meas_temp_at_4
meas_temp_at_5 meas_temp_at_6 td meas_Vmultimeter_2
meas_Vmultimeter_4 meas_voltage_multi_meter the_time];

        if (resettable_variable >
number_of_param_readings_per_file)
            resettable_variable = 0.5;
            cycle_num_fixed = char_test_cycle_num;
        end
        resettable_variable = resettable_variable + 1;
        file_out =
sprintf('SC11_parameters_for_cycle.%d.dat',cycle_num_fixed);
        save('-append', file_out, 'td_voltages_ESR_C_temps_time',
'-ascii');
    end
```

```
    time_to_fin_counter = toc - total_time
    %toc %this is total time (including total_time)
    save('char_test_cyc_num.mat', 'char_test_cycle_num') %Write
%the cycle_num to file
    save('pow_profile_cyc_num.mat', 'pow_profile_cycle_num')
%Write the cycle_num to file

    if (meas_voltage_multi_meter < safety_error_voltage)
        break
    end

    if (meas_temp_at_6 > safety_error_temp)
        break
    end
    if (meas_temp_at_5 > safety_error_temp)
        break
    end
    if (meas_temp_at_4 > safety_error_temp)
        break
    end
    if (meas_temp_at_3 > safety_error_temp)
        break
    end

end
save('char_test_cyc_num.mat', 'char_test_cycle_num') %Write the
%cycle_num to file
save('pow_profile_cyc_num.mat', 'pow_profile_cycle_num')
%Write the cycle_num to file

fprintf(prog_load,'Curr 0');
fprintf(pow_sup,'SOUR:Curr 0');
meas_temp_at_3
meas_temp_at_4
meas_temp_at_5
meas_temp_at_6
meas_voltage_multi_meter


finish_message=input ('The program has finished\nPlease press
enter to exit:');

%Turn off devices
fprintf(prog_load,'Input Off');
fprintf(pow_sup,'Outp off');

%Delete and clear the GPIB variables
%When you no longer need to communicate to the GPIB created
variable, you should disconnect it from the instrument, remove it
%from memory, and remove it from the MATLAB workspace.
fclose(pow_sup);
delete(pow_sup)
clear pow_sup

fclose(prog_load);
delete(prog_load)
clear prog_load
```

```
fclose(multi_meter);
delete(multi_meter)
clear multi_meter

%Description of file: This file calls a power profile from the
%file SC_power_demand_revised2. This is a scaled power profile
%that was obtained from a Simulink model. This Simulink model used
%sea-state 6 data at full scale on a turbine model and averaged
%power model with an altered Falcao speed control strategy. The
%power profile was the power signal sent to the SC before
%voltage limits or current limits of the SC module came into
%effect. This module smoothed power by absorbing the power peaks
%and then outputting a set 150,000 W to the grid until the SC
%voltage reached its minimum again. This power was then scaled
%down to 1:22 which is applicable to an individual SC of 5 F 2.7
%V.

%To ensure the power profile is outputted at the correct time, the
%code uses a sample time of 0.1066 second to output GPIB values to
%the equipment. Once the code has been executed, a while loop
%waits until 0.1066 seconds has been reached for that sample. The
%GPIB equipment operates in constant current mode, and this
%current value is calculated from dividing the power value by the
%instantaneous voltage of the SC. Once the voltage limits have
%been reached the SC stops outputting or absorbing current that
%would result in this voltage limit being exceeded.

%While a current is being outputted or absorbed, the voltage at
%the SC terminals will be different to the true voltage of the SC
%due to the ESR of the SC. This will mean that once the voltage
%limit has been reached, the SC current will go to zero, but then
%the voltage limit will no longer be reached and it will then
%allow a non-zero current value again. This ringing will continue
%until the SC true voltage is outside the limit. To prevent
%this ringing, hysteresis is introduced that will change the
%voltage limit to a value outside the range of the SC true
%voltage.

%The power profile last about 385 seconds. After 3 repetitions the
%file will carry out 5 characterisation tests to measure
%capacitance and ESR. The cycle number for the power profile and
%the characterisation tests are obtained from a file and outputted
%to a file, to remove the need for the user to change these values
%manually. The user only has to enter in the expected amount of
%time desired for the experiment.
```

Appendix H Derivation of the inertia of a Wells turbine with NACA 0015 turbine blades

Wells turbine consists of a cylindrical disc piece (approx.) with a number of blades attached as shown below in Figure H.1. The Wells turbine examined in this thesis is a full scale aluminium turbine with nine NACA 0015 blades.

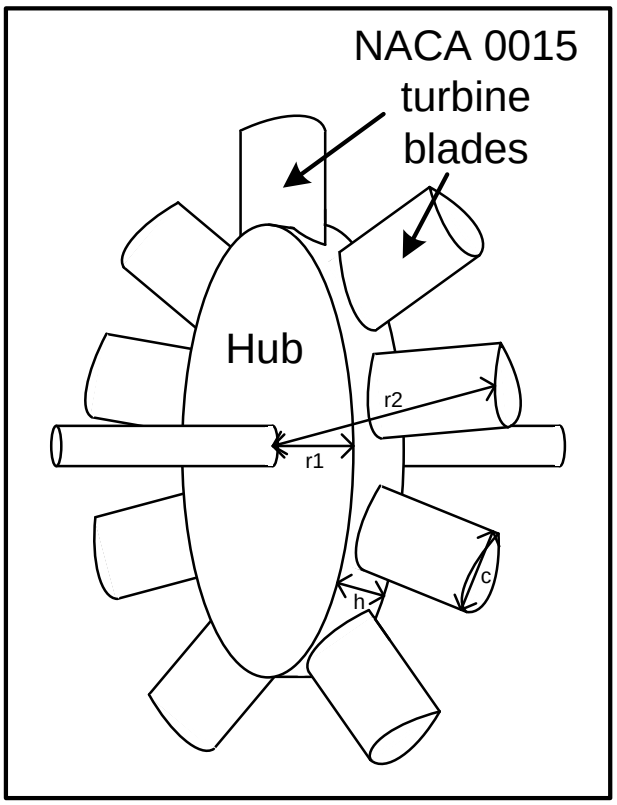


Figure H.1: Wells turbine

NACA 0015 blades are aerofoils whose shapes described in the four digits 0015, were developed by the National Advisory Committee for Aeronautics (NACA). The first two digits describe the camber, in this case the digits 00 indicate no camber is present and the aerofoil is symmetrical. The last two digits are the maximum percentage thickness as a fraction of chord length.

The equation for the shape of the aerofoil is shown in equation (H.1):

$$y_t = \frac{t}{0.2}c\left[0.2969\sqrt{\frac{x}{c}} - 0.126\left(\frac{x}{c}\right) - 0.3516\left(\frac{x}{c}\right)^2 + 0.2843\left(\frac{x}{c}\right)^3 - 0.1015\left(\frac{x}{c}\right)^4\right] \quad \text{(H.1)}$$

where c is chord length (shown above in Figure H.1), x is the position along the chord from 0 to c, y_t is the half thickness at a given value of x, and t is the maximum thickness as a fraction of chord length. This profile is shown below in Figure H.2.

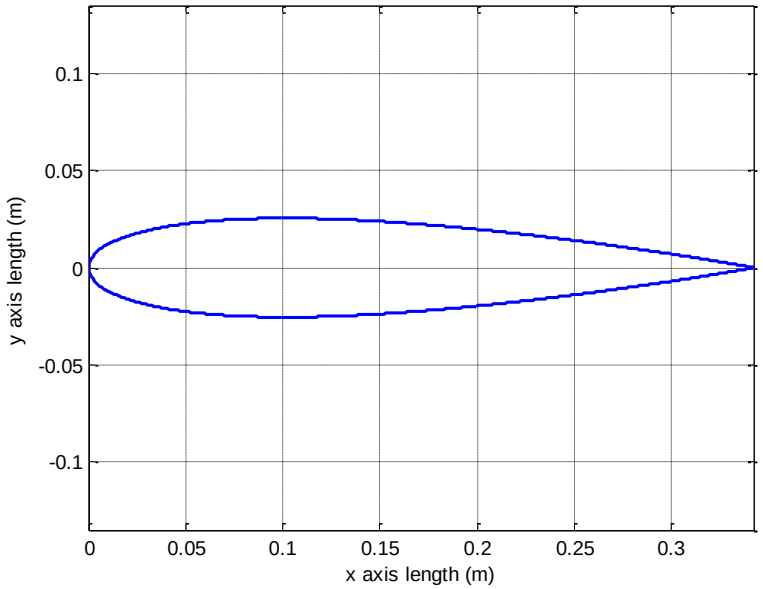


Figure H.2: Profile of the NACA0015 turbine blade

To calculate the inertia and mass of this Wells turbine, the inertia of the individual components will first be calculated before calculating the total inertia.

The inertia of the hub is obtained from the equation governing the inertia of a cylinder rotating about a centre axis as shown below.

$$J = \frac{m{r_1}^2}{2} \quad \text{(H.2)}$$

The mass of the aluminium cylinder is found using equation (H.3).

$$m = \rho V \tag{H.3}$$

Where ρ is the density of the material (in this case it is aluminium), and V is the volume of the cylinder. The volume is found using equation (H.4).

$$V = \pi {r_1}^2 h \tag{H.4}$$

The inertia of an individual blade is obtained utilising the equation describing the inertia of a rectangular bar mass rotating around an axis.

$$J = \frac{m}{3}({r_1}^2 + {r_2}^2 + r_1 r_2) \tag{H.5}$$

Where r_1 and r_2 are the distances from the near side and the far side of the rectangular mass to the axis point.

To calculate the mass of the aluminium blade, the volume is calculated using the area of the blade cross-section and its length.

$$V = 2(r_2 - r_1)\int_0^c y_t \, dx \tag{H.6}$$

The total inertia is then calculated according to:

$$J_{total} = J_{hub} + 9J_{blade} \tag{H.7}$$

Using the following values:

- $r_1 = 0.66$ m
- $r_2 = 1$ m
- $\rho_{alu} = 2{,}762$ kg/m^3
- $h = 0.025$ m
- $c = 0.34$ m

The total inertia of the full scale turbine is calculated to be 91 kg m^2 and the total mass is 195 kg. If the material density used is 8,000 kg/m^3 corresponding to steel, then the overall inertia increases to 263 kg m^2 and the mass is 564 kg.

Appendix I High-voltage lithium-ion (Li-ion) battery specifications

Requirements	Power and Energy Hybrid Functions	SoC (%)	Temp	Event Duration (sec)	Pack Performance	Units
Cells					**96**	Cells
Parallel					1	Cells
Series					96	Cells
Voltage Limits						
	V Max Operating				410	V
	V Min Operating				260	V
	V Nom				360	V
Power						
Regen		50	25°C			
	Peak, BoL			10	61	kW
				5	72	kW
Discharge		50	25°C			
	Peak, BoL			10	60	kW
				5	61	kW
Energy						
			25°C			
Total Pack	100% SoC, BoL				5.1	kW h
Usable	30-70% SoC, BoL				3.6	kW h
Peak Current			25°C			
Charge, BoL				10	150	Amp
Discharge, BoL				10	200	Amp

Bibliography

1. Lee, R., *The outlook for population growth.* Science, 2011. 333(6042): p. 569-573.
2. Change, I.P.O.C., *Climate change 2007: the physical science basis.* Agenda, 2007. 6: p. 07.
3. The European Commission. Climate action [cited 2012 12th December]; Available from: http://ec.europa.eu/clima/policies/package/index_en.htm.
4. European Commission, *Directive 2009/28/EC of the European Parliament and of the Council of 23 April 2009 on the promotion of the use of energy from renewable sources and amending and subsequently repealing Directives 2001/77/EC and 2003/30.* Official Journal of the European Union, 2009: p. 16-62.
5. Department of Communications, Energy and Natural Resources *Strategy for Renewable Energy: 2012 - 2020*. 2012.
6. Eurelectric, *Hydro in Europe: Powering Renewables. Synopsis report.*, September 2011.
7. European Wind Energy Association, *Wind in Power.* 2011 European Statistics, 2012.
8. REN21 *Renewables 2012 Global Status Report*.
9. Gunn, K. and C. Stock-Williams, *Quantifying the global wave power resource.* Renewable Energy, August 2012. 44: p. 296-304.
10. European Ocean Energy Association *Oceans of Energy–European Ocean Energy Roadmap 2010-2050, EU-OEA, Brussels, Belgium*. 2010.
11. O'Sullivan, D., D. Murray, J. Hayes, M. Egan, and A. Lewis, *The Benefits of Device Level Short Term Energy Storage in Ocean Wave Energy Converters.*
12. Alcorn, R. and W. Beattie, *Power quality assessment from the LIMPET wave-power station.* Proceedings of the 11th international offshore and polar engineering conference, 2001. 1: p. 17-22.
13. Rahm, M., O. Svensson, C. Boström, R. Waters, and M. Leijon, *Experimental results from the operation of aggregated wave energy converters.* Renewable Power Generation, IET, 2012. 6(3): p. 149-160.
14. Tissandier, J., A. Babarit, and A. Clément, *Study of the smoothing effect on the power production in an array of SEAREV wave energy converters.* ISOPE-2008: Eighteenth (2008) International Offshore and Offshore and Polar Engineering Conference Proceedings, July 2008: p. 374-381.
15. Molinas, M., O. Skjervheim, B. Sørby, P. Andreasen, S. Lundberg, and T. Undeland, *Power smoothing by aggregation of wave energy converters for minimizing electrical energy storage requirements.* Proceedings of the 7th European Wave and Tidal Energy Conference, 2007: p. 3-8.
16. Salter, S.H., *World progress in wave energy—1988.* International journal of ambient energy, 1989. 10(1): p. 3-24.
17. Falcão, A.F.O., *Wave energy utilization: A review of the technologies.* Renewable and Sustainable Energy Reviews, 2010. 14(3): p. 899-918.

18. The European Marine Energy Centre (EMEC) Ltd. [cited 2013 March]; Available from: www.emec.org.uk/marine-energy/wave-developers.
19. Czech, B. and P. Bauer, *Wave Energy Converter Concepts: Design Challenges and Classification.* Industrial Electronics Magazine, IEEE, 2012. 6(2): p. 4-16.
20. O'Sullivan, D., D. Mollaghan, A. Blavette, and R. Alcorn, *Dynamic characteristics of wave and tidal energy converters & a recommended structure for development of a generic model for grid connection, a report prepared by HMRC-UCC for the OES-IA Annex III.* Available: www.iea-oceans.org, 2010.
21. Cashman, D.P., D.L. O'Sullivan, M.G. Egan, and J.G. Hayes, *Modelling and analysis of an offshore oscillating water column wave energy converter.* Proceedings of 8th European Wave and Tidal Energy Conference, 2009: p. 924-933.
22. Waveplam *Report on the state of the art analysis, a cautiously optimistic review of the technical status of wave energy technology*. Available at www.waveplam.eu/files/downloads/SoA.pdf, February 2009.
23. O'Sullivan, D., J. Griffiths, M.G. Egan, and A.W. Lewis, *Development of an electrical power take off system for a sea-test scaled offshore wave energy device.* Renewable Energy, 2011. 36(4): p. 1236-1244.
24. Falcão, A.F.O., *The shoreline OWC wave power plant at the Azores.* Proceedings of the Fourth European Wave Energy Conference, Aalborg, Denmark, 2000: p. 42-48.
25. Heath, T., T. Whittaker, and C. Boake, *The design, construction and operation of the LIMPET wave energy converter (Islay, Scotland).* 4th European Wave Energy Conference, 2000: p. 49-55.
26. Falcão, A.F.O., *Control of an oscillating-water-column wave power plant for maximum energy production.* Applied Ocean Research, 2002. 24(2): p. 73-82.
27. Boake, C. *Islay LIMPET Wave Power Plant, Publishable Report*. 1 November 1998 to 30 April 2002, The Queesn's University of Belfast. Contract JOR3-CT98-0312, 2003.
28. Henderson, R., *Design, simulation, and testing of a novel hydraulic power take-off system for the Pelamis wave energy converter.* Renewable Energy, 2006. 31(2): p. 271-283.
29. Falcão, A.F.O., *Modelling and control of oscillating-body wave energy converters with hydraulic power take-off and gas accumulator.* Ocean engineering, 2007. 34(14): p. 2021-2032.
30. Faiz, J. and M. Ebrahimi-Salari, *Comparison of the performance of two direct wave energy conversion systems: Archimedes wave swing and power buoy.* Journal of Marine Science and Application, 2011. 10(4): p. 419-428.
31. Valério, D., M.J. Mendes, P. Beirão, and J. Sá da Costa, *Identification and control of the AWS using neural network models.* Applied Ocean Research, 2008. 30(3): p. 178-188.
32. The Maritime Journal. *The quiet life of a seabed Oyster*. 15 Nov 2011 March 2013]; Available from: http://www.maritimejournal.com/news101/marine-renewable-energy/the-quiet-life-of-a-seabed-oyster.
33. Molinas, M., O. Skjervheim, P. Andreasen, T. Undeland, J. Hals, T. Moan, and B. Sorby, *Power electronics as grid interface for actively controlled wave energy converters.* International Conference on Clean Electrical Power, 2007. ICCEP'07, 2007: p. 188-195.
34. Carrasco, J.M., L.G. Franquelo, J.T. Bialasiewicz, E. Galván, R.C.P. Guisado, M.A.M. Prats, J.I. León, and N. Moreno-Alfonso, *Power-electronic systems for the grid integration of renewable energy sources: A survey.* Industrial Electronics, IEEE Transactions on, 2006. 53(4): p. 1002-1016.

35. Wu, F., X. Zhang, and P. Ju, *Application of the battery energy storage in wave energy conversion system.* International Conference on Sustainable Power Generation and Supply, 2009. SUPERGEN'09, 2009: p. 1-4.
36. Luongo, C.A., *Superconducting storage systems: An overview.* Magnetics, IEEE Transactions on, 1996. 32(4): p. 2214-2223.
37. Ali, M.H., B. Wu, and R.A. Dougal, *An overview of SMES applications in power and energy systems.* Sustainable Energy, IEEE Transactions on, 2010. 1(1): p. 38-47.
38. Amjad, S., S. Neelakrishnan, and R. Rudramoorthy, *Review of design considerations and technological challenges for successful development and deployment of plug-in hybrid electric vehicles.* Renewable and Sustainable Energy Reviews, 2010. 14(3): p. 1104-1110.
39. Glavin, M., P.K.W. Chan, S. Armstrong, and W. Hurley, *A stand-alone photovoltaic supercapacitor battery hybrid energy storage system.* 13th Power Electronics and Motion Control Conference, 2008. EPE-PEMC 2008, Sept 2008: p. 1688-1695.
40. Weeren, D., H. Joosten, R. Scrivens, and A. Schneuwly, *Ultracapacitors double operational life of wave measurement buoys*, in *Case study by Maxwell Technologies, available at www.maxwell.com.* 2009.
41. Saft batteries *Saft batteries Data sheet. Synerion 48E Li-ion module. Available at www.saftbatteries.com.*
42. Camara, M.B., H. Gualous, F. Gustin, and A. Berthon, *Design and new control of DC/DC converters to share energy between supercapacitors and batteries in hybrid vehicles.* Vehicular Technology, IEEE Transactions on, 2008. 57(5): p. 2721-2735.
43. Laldin, O., M. Moshirvaziri, and O. Trescases, *Predictive Algorithm for Optimizing Power Flow in Hybrid Ultracapacitor/Battery Storage Systems for Light Electric Vehicles.* 2011.
44. Kuperman, A., I. Aharon, S. Malki, and A. Kara, *Design of a Semi-Active Battery-Ultracapacitor Hybrid Energy Source.* Power Electronics, IEEE Transactions on, 2011. 28(2): p. 806-815.
45. Van Broekhoven, S., N. Judson, S. Nguyen, and W. Ross, *Microgrid Study: Energy Security for DoD Installations*, in *Technical report 1164. Lincoln Laboratory. Massachusetts Institute of Technology.* 2012, DTIC.
46. Douglas, H. and P. Pillay, *Sizing ultracapacitors for hybrid electric vehicles.* 31st Annual Conference of IEEE Industrial Electronics Society, 2005. IECON 2005, Nov 2005: p. 1599-1604.
47. O'Sullivan, D.L. and A.W. Lewis, *Generator Selection and Comparative Performance in Offshore Oscillating Water Column Ocean Wave Energy Converters.* Energy Conversion, IEEE Transactions on, 2011. 26(2): p. 603-614.
48. Curran, R., T. Whittaker, and T. Stewart, *Aerodynamic conversion of ocean power from wave to wire.* Energy conversion and management, 1998. 39(16): p. 1919-1929.
49. Justino, P.A.P. and A.F.O. Falcão, *Rotational speed control of an OWC wave power plant.* Journal of Offshore Mechanics and Arctic Engineering, 1999. 121: p. 65-70.
50. Duquette, J., D. O'Sullivan, S. Ceballos, and R. Alcorn, *Design and construction of an experimental wave energy device emulator test rig.* Proceedings of the 8th European Wave and Tidal Energy Conference, 2009: p. 443-452.
51. O'Sullivan, D. and A. Lewis, *Generator selection for offshore oscillating water column wave energy converters.* 13th Power Electronics and Motion Control Conference, 2008. EPE-PEMC 2008, 2008: p. 1790-1797.

52. Maxwell Technologies *Product guide, Maxwell Technologies BOOSTCAP ultracapacitors. Available at www.maxwell.com. Document 1014627.1*. 2009.
53. Maxwell Technologies, *Application note: Boostcap energy storage modules life duration estimation. Available at www.maxwell.com. Document 1012839*, 2007.
54. Maxwell Technologies *Data sheet. HTM Heavy Transportation Series 125 V module. BMOD0063 P125. Available at www.maxwell.com. Document 1014696.2*. 2009.
55. Lajnef, W., J.M. Vinassa, O. Briat, H. El Brouji, and E. Woirgard, *Monitoring fading rate of ultracapacitors using online characterization during power cycling.* Microelectronics Reliability, 2007. 47(9): p. 1751-1755.
56. Paul, K., M. Christian, V. Pascal, C. Guy, R. Gerard, and Z. Younes, *Constant power cycling for accelerated ageing of supercapacitors.* 13th European Conference on Power Electronics and Applications, 2009. EPE'09, 2009: p. 1-10.
57. El Brouji, H., O. Briat, J.M. Vinassa, N. Bertrand, and E. Woirgard, *Comparison between changes of ultracapacitors model parameters during calendar life and power cycling ageing tests.* Microelectronics Reliability, 2008. 48(8): p. 1473-1478.
58. Wavenet *Results from the work of the European thematic network on wave energy*. ERK5-CT-1999-20001, March 2003.
59. Linzen, D., S. Buller, E. Karden, and R.W. De Doncker, *Analysis and evaluation of charge-balancing circuits on performance, reliability, and lifetime of supercapacitor systems.* Industry Applications, IEEE Transactions on, 2005. 41(5): p. 1135-1141.
60. Alcicek, G., H. Gualous, P. Venet, R. Gallay, and A. Miraoui, *Experimental study of temperature effect on ultracapacitor ageing.* 2007 European Conference on Power Electronics and Applications, 2007: p. 1-7.
61. Bohlen, O., J. Kowal, and D.U. Sauer, *Ageing behaviour of electrochemical double layer capacitors: Part I. Experimental study and ageing model.* Journal of power sources, 2007. 172(1): p. 468-475.
62. Harrison, G.P. and A.R. Wallace, *Sensitivity of wave energy to climate change.* Energy Conversion, IEEE Transactions on, 2005. 20(4): p. 870-877.
63. Eirgrid *Eirgrid grid code, version 3.2*. 2008.
64. Mueller, M., H. Polinder, and N. Baker, *Current and novel electrical generator technology for wave energy converters.* IEEE International Electric Machines & Drives Conference, 2007. IEMDC'07, 2007. 2: p. 1401-1406.
65. Mohan, N., *Advanced electric drives: analysis, control and modeling using simulink.* Year 2001 edition: Minnesota Power Electronics Research & Education (MNPERE).
66. Pena, R., J. Clare, and G. Asher, *Doubly fed induction generator using back-to-back PWM converters and its application to variable-speed wind-energy generation.* IEE Proceedings - Electric Power Applications, 1996. 143: p. 231-241.
67. Shi, L. and M. Crow, *Comparison of ultracapacitor electric circuit models.* 2008 IEEE Power and Energy Society General Meeting-Conversion and Delivery of Electrical Energy in the 21st Century, 2008: p. 1-6.
68. Wei, T., X. Qi, and Z. Qi, *An improved ultracapacitor equivalent circuit model for the design of energy storage power systems.* International Conference on Electrical Machines and Systems, 2007. ICEMS, 2007: p. 69-73.
69. Yao, Y., D. Zhang, and D. Xu, *A study of supercapacitor parameters and characteristics.* International Conference on Power System Technology, 2006. PowerCon 2006, 2006: p. 1-4.
70. Li, W., G. Joós, and C. Abbey, *A parallel bidirectional dc/dc converter topology for energy storage systems in wind applications.* Conference Record of the 2007

IEEE Industry Applications Conference, 2007. 42nd IAS Annual Meeting, 2007: p. 179-185.

71. Basu, S. and T.M. Undeland, *A novel design scheme for improving ultra-capacitor lifetime while charging with switch mode converters.* Power Electronics Specialists Conference, 2008. PESC 2008. IEEE, 2008: p. 2325-2328.
72. Wei, T., S. Wang, and Z. Qi, *A supercapacitor based ride-through system for industrial drive applications.* International Conference on Mechatronics and Automation, 2007. ICMA 2007, 2007: p. 3833-3837.
73. Nissan, *2011 Nissan Leaf Owner's Manual*.
74. Wood, E., J. Neubauer, A.D. Brooker, J. Gonder, and K.A. Smith, *Variability of Battery Wear in Light Duty Plug-In Electric Vehicles Subject to Ambient Temperature, Battery Size, and Consumer Usage: Preprint*, 2012, National Renewable Energy Laboratory (NREL), Golden, CO.
75. Muthukumar, S., S. Kakumanu, S. Sriram, and V. Jayashankar, *Energy storage considerations for a stand-alone wave energy plant.* 2005 IEEE International Conference on Electric Machines and Drives, 2005: p. 193-198.
76. Zhou, H., T. Bhattacharya, D. Tran, T.S.T. Siew, and A.M. Khambadkone, *Composite energy storage system involving battery and ultracapacitor with dynamic energy management in microgrid applications.* Power Electronics, IEEE Transactions on, 2011. 26(3): p. 923-930.
77. Serban, I. and C. Marinescu. *A look at the role and main topologies of battery energy storage systems for integration in autonomous microgrids*. in *Optimization of Electrical and Electronic Equipment (OPTIM), 2010 12th International Conference on*. 2010. IEEE.
78. Hatziargyriou, N., H. Asano, R. Iravani, and C. Marnay, *Microgrids.* Power and Energy Magazine, IEEE, 2007. 5(4): p. 78-94.
79. Darcy, E., *Technical report. NASA. Li-Ion Pouch Cell Designs; Performance and Issues for Crewed Vehicle Applications.* April 2011.
80. Tremblay, O. and L.-A. Dessaint, *Experimental validation of a battery dynamic model for EV applications.* World Electric Vehicle Journal, 2009. 3: p. 13-16.
81. Shepherd, C.M., *Design of primary and secondary cells II. An equation describing battery discharge.* Journal of the Electrochemical Society, 1965. 112(7): p. 657-664.